A MACHINE VISION SYSTEM FOR IN-SITU QUALITY INSPECTION IN METAL POWDER-BED ADDITIVE MANUFACTURING

A Dissertation
Presented to
The Academic Faculty

by

Masoumeh Aminzadeh

In Partial Fulfillment
Of the Requirements for the Degree
Doctor of Philosophy in Mechanical Engineering

Georgia Institute of Technology

December 2016

A MACHINE VISION SYSTEM FOR IN-SITU QUALITY INSPECTION IN METAL POWDER-BED ADDITIVE MANUFACTURING

Approved by:

Dr. Thomas Kurfess,
PhD Committee Chair
Mechanical Engineering
Georgia Institute of Technology

Dr. Richard Cowan
Mechanical Engineering
Georgia Institute of Technology

Dr. David Rosen
Mechanical Engineering
Georgia Institute of Technology

Dr. Chen Zhou
Industrial Engineering
Georgia Institute of Technology

Dr. H. Jerry Qi
Mechanical Engineering
Georgia Institute of Technology

Date Approved: September 29, 2016

To my Beloved Family, especially my Dearest Mom

ACKNOWLEDGEMENTS

I would like to thank the following people for making this thesis possible:

My family, including my dearest Mom, Athareh, Vajiheh, and Mohammad, Your support, encouragement and prayers are invaluable.

My Advisor: Prof. Thomas R. Kurfess. Your guidance and inspiration has been critical to the contents of this study as well as my formation as a doctoral student.

My committee members: Prof. David Rosen, Dr.'s Jerry H. Qi, Richard Cowan, and Chen Zhou, for your erudite comments that have gone a long way in improving the quality of this study.

Funding Agencies: Edison Welding Institute, for funding this research, setting up the in-house SLM machine, and providing the equipment and support for conducting this work.

My friends and labmates: who made working at Georgia Tech a pleasant experience.

There are of course many more whose critical role directly or indirectly in the success of this project is deeply appreciated.

TABLE OF CONTENTS

ACKNOWLEDGEMENTS iv

LIST OF TABLES ix

LIST OF FIGURES x

SUMMARY xxvii

CHAPTER I: INTRODUCTION 1

1.1 Research Motivation 1

1.2 Research Goals & Contributions 6

1.3 Thesis Organization 8

CHAPTER II: BACKGROUND 10

2.1 Additive Manufacturing 10

2.2 Defects in Metal AM and Defect Formation Mechanism 13

2.3. Quality Monitoring and Control in AM 25

2.3.1 Real-Time Process Control 27

2.3.2 In-Situ Quality Inspection and Defect Detection in Powder-Bed AM 30

2.4 Past and Concurrent Work on In-Situ Detection of Defects and Geometry in Metal Powder-Bed AM 31

2.4.1 Thermal Imaging for In-Situ Defect Inspection 32

2.4.2 Applications of Visible-Light Imaging and Machine Vision in In-Situ Inspection in Metal Powder-Bed AM 35

2.5 Terminology and Principles of Machine Vision for Automated Visual Inspection 49

2.5.1. Image segmentation 50
2.5.2 Feature Extraction 52
2.5.3. Classification or Identification 54
2.5.4 Remarks on Application of MV in AVI 54
2.5 Conclusions from Literature Review and Background 55
CHAPTER III: PROBLEM FORMULATION AND THE AVI FRAMEWORK 59
3.1 Layout of the Machine Vision System for AVI in Metal Powder-Bed AM 59
3.2 Formulation of the Problem to Be Solved in This Dissertation: The AVI System for Detection of Geometric Objects and Assessment (Detection and Identification) of Porosity from In-Situ, Layerwise Visible-Light Camera Images of Inconel 625 Parts made by Laser Powder-Bed Fusion Process 64
3.3 Segmentation of Fused Geometric Objects 65
3.4 Detection and Identification of Pores 65
3.5 Development and Modification of Imaging Setup 67
3.6 Development of Image Database of Porosity 68
3.7 Measures and Evaluation Metrics 68
3.8 Application of the Designed AVI System in This Dissertation to Outside the Scope of This Dissertation 70
3.9 Overview of the Material and its Organization in Chapters IV to VII to Address the Formulated Problem of This Dissertation 72
CHAPTER IV: SYSTEM SETUP AND MEASUREMENTS 74
4.1. Visual Camera Imaging Setup 74
4.2 Imaging Setup for Visualizing Porosity 80

4.3 Further Discussion of Imaging and Different Aspects for Improving the Clarity of Camera Images 87

CHAPTER V: DEVELOPMENT OF DEFECT IMAGE DATABASE 95

CHAPTER VI: DETECTION OF FUSED OBJECTS 108

6.1 Example of a Noisy Low-Contrast Image 109

6.2 Camera Images of the Build Layer by the Camera Setup at EWI- Dataset before Modification 113

6.3 Camera Images of the Build Layer by the Camera Setup at EWI- Dataset after Modification 123

6.3.1 Initial Analysis and Algorithm Trials 124

6.3.2 Image Segmentation Algorithms for Detection of the Fused Geometric Objects from Camera Images 133

6.3.3 Application of the Algorithm to Other geometries 139

6.4 Assessment of Imaging Characteristics and an Achievable Segmentation Precision 141

6.5 Evaluation of the Performance and Precision of the Segmentation Algorithms of Fused Geometric Objects 145

6.5.1 Pixel-Wise Segmentation Error 146

6.5.2 Point-To-Point Segmentation Error 148

6.6 Calculation of Synthetic Parameters using Model-Based Image Processing Algorithms 154

CHAPTER VII: DETECTION OF PORES 161

7.1 Automated Inspection of In-Situ Camera Images 161

7.2 Detection of Individual Pores 162

7.3 Discussion on Image Characteristics and Algorithm Design and Evaluation for Detection of Pores 185

CHAPTER VIII: IDENTIFICATION OF POROUS REGIONS 188

8.1 Description of Bayesian Classifier 189

8.2 Feature Extraction 192

8.3 Identification of Porous versus Non-Porous Layers using Bayesian 217

CHAPTER IX: CONCLUSION 226

9.1 Contributions 227

9.2 Limitations and Application to Outside of the Scope of This Thesis 233

9.3 Extensions and Recommendations for Future Work 234

APPENDIX A: DESCRIPTION OF THE UTILIZED IMAGE PROCESSING ALGORITHMS 237

REFERENCES 248

VITA 257

LIST OF TABLES

Table 1- Processing levels of the online defect and error detection system and its subsystems 62

Table 2- Various considered pairs of process parameters with their assigned numbers .. 96

Table 3- Energy level of the 35 pairs of process parameters shown in Table 2. 96

Table 4- Results and performance of Bayesian identification for different combination of features and for selection of optimal threshold (* shows two cases of non-optimal thresholds for the finally selected set of features). 220

LIST OF FIGURES

Figure 1- Illustration of L-PBF process [46] 13

Figure 2- Illustration of laser powder fusion. 13

Figure 3- Examples of various types of defects that occur in metal powder-bed AM. (a) pores (sometimes, in this document, generally referred to as defects), (b) geometric errors, (c) undesirable surface characteristics in terms of surface roughness and quality of fusion [31]. 14

Figure 4- SEM images of parts made by L-PBF at different levels of energy [48]: (a) sufficient energy, (b) low energy, (c) high energy. 16

Figure 5- Porosity due to insufficient energy: (a) and (b) Respectively, microscopic image and SEM image of a part made by L-PBF that encounters lack of fusion in the layer [50], (c) Microscopic image of lack of fusion between layers [51]. 16

Figure 6- Microscopic image showing pores formed due to insufficient energy. 16

Figure 7- Porosity due to excessive energy in AM parts: (a) Microscopic image of a cross-section of a built part that show pores [6] (the cross section was obtained by cutting the part), (b) SEM image of parts built with excessive energy that contain small spherical gas pores [48, 51]. 18

Figure 8- Variation of porosity (a measure of porosity) with respect to scan speed at constant level of energy. (a) porosity monotonically increasing with decrease in level of energy, (b) a non-monotonic trend for porosity variation with scan speed and introducing the 4 zones of process parameters. 19

Figure 9- Graph illustrating the 4 zones in the laser power – scan speed space. 19

Figure 10- Nonuniform powder fusion and defects formed at sharp corners: (a) [5] , (b) [9] 21

Figure 11- (a) A schematic view of heat transfer from melt pool to its surroundings for first and second scan paths [5], (b) An example of a resulted elevated edge [60], (c)

elevated edges at the contour of a circular object [12], (d) a defect caused by disrupted heat transfer at the boundary of the object [9]. 22
Figure 12- Defect in making a bridge due to overhang [9]..... 22
Figure 13- Example image of darkly etching regions formed due to oxidation [51] 24
Figure 14- CT scans of porosity in parts made by L-PBF. Images illustrate the effect of scan strategy on formation of pores at different scan speeds. [63]..... 24
Figure 15- Flowchart of the AM process on the current commercial AM machines. 25
Figure 16- Flowchart of AM process with online quality monitoring and control..... 27
Figure 17- An example of comparison of melt pool mapping (left) with microscopic image of the layer (right) from [6]..... 33
Figure 18- Generated pores and crack [13]..... 34
Figure 19- IR imaging for detection of pores [30], top: visual images of layers, bottom: IR imaging results after selected thresholding..... 35
Figure 20- An example image captured from powder deposition and illustration of how abrupt changes correlate to damaged coater [31]. 38
Figure 21- Schematic view of the imaging setup developed in [31] and an example image of the build platform illustrating the perspective effects. 38
Figure 22- (a) Illustration of imaging system used in [12] with the camera mounted outside the machine, (b) illustration of perspective effects in images captured from build platform before corrections, (c) an example image of a EBM build after correction of perspective effects and intensity rescaling for better visualization. 39
Figure 23- (a) Camera image (after intensity rescaling) of the build, (b) camera image after powder deposition, (c) result of thresholding of (b) that signify elevated edges. 40
Figure 24- Examples of camera images (after intensity rescaling) from EBM parts from the imaging setup in [32]. 41

Figure 25- High resolution camera images taken from parts made with different process parameters. Vs is scan velocity, P is laser powder, h is hatch spacing. For more details, see [52]. 42
Figure 26- Comparison of selected high resolution (top) images vs. images taken from microscopy (bottom) see [52] for more details. 43
Figure 27- Photomicrograph from selected test specimens [80]. 43
Figure 28- (a) the geometry made using LBM in [85], (b) a representative image captured from the cross section of the part during build using the high-resolution imaging setup, and a close-up of the marked region in the image. 44
Figure 29- Examples of micrographs captured in [85] to visualize defects. 45
Figure 30- (a) A schematic view of the front view of the machine illustrating the location of camera with respect to the build platform, (b) an example of a raw image captured by the oblique camera and the resultant perspective effect. 46
Figure 31- Images captured by imaging setup developed in [86]. 46
Figure 32- (a) the SLM machine used in [87] with a standard stereo microscope imaging mounted on it, (b) image captured from the left microscope from a built turbine blade on the machine after powder removal. 48
Figure 33- Examples of image segmentation. 51
Figure 34- The procedure for detection and identification of defects. 53
Figure 35- A schematic diagram of setup for in-situ defect inspection system (inclusion of light source is only for illustration, it's not to specify light source location). 60
Figure 36 - A schematic diagram of the AVI system including two subsystems of geometric error identification and defect identification. 61
Figure 37- Flowchart of an online AVI system for detection of defects and geometric errors. 63

Figure 38- Layout for AVI system for detection and identification of defects (pores) in powder-bed AM (L-PBF) for the purpose of this dissertation. 65
Figure 39- The custom SLM machine built at EWI. 75
Figure 40- Close-up of the build chamber and its components. 76
Figure 41- Example of image with the setup using 2 megapixel camera and square LED mounted at an angle from the build. 77
Figure 42- An example of image taken with the setup with 8 megapixel camera and ring illumination mounted around the camera. 78
Figure 43- Example of image with the setup using 8 megapixel camera and high-intensity square LED mounted at an angle from the build. 79
Figure 44- Example of image with the setup using 8 megapixel camera and adjusted level of intensity for square LED mounted at an angle from the build. 80
Figure 45- Images of the same build layer: (a) captured by a standard microscope with the resolution of 7 µm/pixel, (b) captured by visual camera in the imaging setup using the LED spot light at an angle (Figure 40) with the resolution of 7 µm/pixel, (c) captured by visual camera in the imaging setup using the ring LED perpendicular to the build and around the camera with the resolution of 7 µm/pixel. 81
Figure 46- Image of the new imaging setup with movable ring LED mounted at a fixture on the coater at a selected height above the build platform. 85
Figure 47- (a) An example image captured from a porous surface by the setup with movable ring LED (Figure 46), (b) corresponding microscopic image of the part. 86
Figure 48- Three example of effect of illumination angle (or build location in FoV) on the camera image. Each row shows a different part (with different process parameters). First column in each row shows the microscopic image correspondent to the same part in that row. Second column shows camera images captured when the part is nearly below the camera. Third column is the camera image captured when the part is near the left margin

of the FoV of the camera. The illumination lights up the part from the right side of the image from above. 88
Figure 49- An example of camera image (left) with respect to microscopic image (right) that show comparison of depth of focus and focus sharpness between camera and microscope. 91
Figure 50- (a) Zoomed-in views of the top parts of images in Figure 49, (b) Zoomed-in views of the top parts of the images in another examplar build. In each row, the left image is camera image and the right image is the corresponding microscopic image. 92
Figure 51- Example of an image taken from a smooth surface that has caused saturation. Left: microscopic image, right: camera image. 93
Figure 52- An example of image that local image saturation has covered some surface features with respect to microscope. Left: microscope, right: camera. 93
Figure 53- Energy levels of the 35 pairs of process parameters in Table 2. The bottom left of the graph corresponds to process parameter pair number 1, and the upper right corresponds to process parameter pair number 35. The dashed square shows the process parameter pairs used for experiments in this research. 97
Figure 54- Images captured from high-resolution camera at the new setting in comparison with microscopic images. Each row shows a build with different process parameters. The left image in each row is the camera image and the right image is the corresponding microscopic image. 99
Figure 55- More examples of microscopic images in comparison with camera images that were captured with blue color setting. 100
Figure 56- Microscopic images of different builds at various energy levels: (a) the build with process parameters numbered as 1 (numberings are based on Table 2), (b) the build with process parameters numbered as 12, (c) the build with process parameters numbered

as 13, (d) the build with process parameters numbered as 9, (e) the build with process parameters numbered as 15, (f) the build with process parameters numbered as 25..... 102
Figure 57- Examples of builds associated with different process parameters. 103
Figure 58- Visual identification of porous surfaces versus non-porous surfaces and marking their corresponding process parameters. 105
Figure 59- Illustration of three feasible zones of builds in process parameter space based on part properties from [48]. The marked square represents the region that relatively matches with the chart in Figure 58. 106
Figure 60- Microscopic images of (a) from the surface of a porous layer corresponding to Zone III, (b) (cut and polished) cross section of a part built with Zone III parameters [50], (c) cross section of a part built with Zone II parameters [50]. 107
Figure 61- An image of a layer made with laser powder-bed AM [12] 110
Figure 62- Results of attempting some of the image segmentation techniques applied to Figure 61 for detection of fused objects. (a) Optimal Otsu thresholding, (b) local thresholding by local standard deviation, (c) Canny edge detection, (d) Canny edge detection with manually selected parameters after about 10 trials. 111
Figure 63- Histogram of the original image (left), histogram after Wiener filtering (right). 112
Figure 64- a) Result of thresholding by histogram study, b) after clearing the border items and applying opening by reconstruction, c) after closing, d) superimposing with the original image. 113
Figure 65- Image of the powder layer during build of a block- setup at EWI..... 114
Figure 66- Result of converting Figure 65 to gray scale and applying a 3×3 median filter. 115
Figure 67- (a) Histogram of Figure 66, (b) normalized histogram of the whole image in contrast with that of image of powder regions..... 116

Figure 68- Result of bi-level thresholding of Figure 66. 117
Figure 69- Different steps to remove the laser spot: (a) thresholding of dominantly red regions, (b) dilation of the results to make sure about the connectivity of the laser spot boundary, (d) morphological filling of the enclosed regions to fill in the laser spot, (d) selection of the largest object, (e) results after erosion to restore the size of the segmented laser spot, (f) superimposing the result on the original image. 118
Figure 70- Result of thresholding to segment the square after removal of the laser spot119
Figure 71- Segmentation of the solid square: (a) Result of implementing “fill” operation to Figure 70, (b) after implementing the correlation by the top-neighborhood mask and applying the neighborhood threshold, (c) after filing operation, (d) after applying the erosion by the complement of the top-neighborhood mask to restore the size. 121
Figure 72- Results of implementing the designed segmentation algorithms to several of the test images. 123
Figure 73- Example of an image captured from the build at the setup after modifying camera and illumination. 124
Figure 74- (a) Result of conversion of Figure 73 to gray-scale image (white noisy dots in the image should be removed to avoid their interference with segmentation results), (b) Result of conversion to gray image and applying a median filter of size 7×7 to Figure 73. 125
Figure 75- Results of implementation of several representative common image segmentation techniques to image in Figure 74 (b): (a) Optimal Otsu thresholding, (b) Canny edge detection (automatic), (c) Canny edge detection with manually selected parameters. 126
Figure 76- Histograms and normalized histograms of the fused region versus the powder region and versus the whole image. 127

Figure 77- The two pairs of thresholds selected at the wider and narrower band of histogram of the fused powder. 128
Figure 78- Result of thresholding Figure 74 (b) by the thresholds selected by histogram comparison, i.e. 20 and 125. 129
Figure 79- Segmentation of fused region: (a) and (b) correlation by bottom neighborhood mask respectively: binary image by itself and overlapped on the original image (Figure 73), (c) and (d) erosion by the complement mask, respectively: binary image by itself and the overlapped with the original image, (e) overlap of the boundary of the segmentation results with the original image. 131
Figure 80- Examples of application of segmentation of fused regions based on applying one set of thresholds at the far extents of the fused region histogram, i.e. 20 and 125. . 131
Figure 81- (a) Result of thresholding of by a different threshold (by narrow threshold bands of the powder region to segment more of the fused region (30 and 100)), (b) and (c) the resulted errors in final segmentation. 132
Figure 82- The flowchart representing the stages of the algorithm, designed and described in this subsection, for segmentation of the fused geometric object from camera images meant for inspection of geometry. 134
Figure 83- Result of median filtering and thresholding applied to the gray scale image of Figure 73. 135
Figure 84- Result of segmentation of regions encompassing all fused regions: (a) binary image, (b) binary image plotted on the original image, (c) the gray scale image encompassing the fused. 136
Figure 85- Thresholding of segmented regions in Figure 84 (c) by the new set of thrseholds of 25 and 100 (a wider band of segmentation). 136
Figure 86- Result of segmentation of fused objects using an initial approximation. 137
Figure 87- Implementation of the algorithm to three of the design images. 138

Figure 88- Examples of the result of the implementation of the segmentation algorithm implemented to the test images. 139
Figure 89- Examples of results of implementation of the developed algorithm to segmentation of the fused objects of geometries other than square object, (a) a T- cross-sectional object, (b) a hollow object. 140
Figure 90- Application of the developed image processing algorithms for a circle: (a) the image of the cross section of the part in powder layer, (b) the result of segmentation of the circular cross section using the developed algorithm (shown by solid, yellow line), (c) the comparison of the true circle, true cross section, (blue) with the segmented geometric object (red), (d) the point-to-point boundary error calculated radially throughout the circumference versus all angles. 141
Figure 91- (a) original image, (b) the dark spots in powder region, (c) non-uniformity within fused region due to non-optimal scanning and non-uniform illumination. 142
Figure 92- Illustration of the small dark regions in the powder which exactly have the intensity of the fused region that interfere with segmentation of the fused region and its boundary. 143
Figure 93- Illustration of intensity distribution of the fused and powder regions (21×21 pixels regions): (a) a selection from a general (bright) region of the fused object (b) a selection from a general region of the powder, (c) a selection from a non-well-illuminated (dark) region of the fused object, (d) a selection from a dark spot or a non-well-illuminated region of the powder. 144
Figure 94- An example of a fused object. (a) The original image with the fused object segmented manually, regarded as the true fused object (the error of the manual segmentation of the square object is assumed to be negligible), (b) the result of algorithm in segmenting the fused object, (c) overlap of the result of segmentation algorithm with

the true fused object; white regions belong to both, the green regions only belong to the true fused object, the pink regions only belong to the algorithm segmentation result. .. 147
Figure 95- Second example of a fused object. (a) The original image with the fused object segmented manually, regarded as the true fused object (the error of the manual segmentation of the square object is assumed to be negligible), (b) the result of algorithm in segmenting the fused object, (c) overlap of the result of segmentation algorithm with the true fused object; white regions belong to both, the green regions only belong to the true fused object, the pink regions only belong to the algorithm segmentation result. .. 147
Figure 96- Calculation of the point-to-point error between the boundaries of the true square (the white line) and the segmented square (the pink line) in example image in Figure 92. See description in the text..... 148
Figure 97- Calculation of the point-to-point error between the boundaries of the true square (the green line) and the segmented square (the pink line) in example image in Figure 95. See description in the text..... 149
Figure 98- Another example of the result of segmentation of the fused object and illustration of the corresponding pixel-wise segmentation error and point-to-point error. (a) True square, (b) Segmentation result, (c) True square and segmentation results plotted on the same figure (the green regions belong to the true square, the pink regions belong to the segmented square, and the white regions belong to both.), (d) The boundaries of true square (green) and segmented square (pink) plotted again each other (see description in text), (e) Point-to-point error..... 150
Figure 99- Original image and segmentation results for the image one of the two cases that lead to maximum local point-to-point error of over 40. (a) Original image, the red square shows the region of maximum point-to-point error. Description of other parts is the same as in Figure 96..... 152

Figure 100- Distributions of maximum of local point-to-point error in each image for 50 images in terms of pixel and micron. 153
Figure 101- Examples of failure of Hough transform to detect the sides of the fused object from the detected boundary. The yellow solid line shows the detected boundary, the green dashed lines show the detected lined by Hough, and the (yellow and red) points show the beginning and end of each detected line. (a) No line segment from the lateral sides are detected by Hough, (b) and (c) The bottom line is only detected by Hough, (d) No line segment from the left side is detected by Hough. 156
Figure 102- Example of results of application of Hough to extract sides of the fused object in Figure 99 (a): (a) dilation with mask size of 11, (b) dilation with mask size of 15. The two adjacent yellow lines show the band of variation of the boundary captured by dilation (an 11-pixel-wide and a 15-pixel-wide band for corresponding images). 158
Figure 103- Zoomed-in views of some sections of Figure 100 for result of dilation with mask sizes of (a) 11 pixels, (b) 15 pixels. No line segment was detected without dilation on these sides. Mask size of 15 pixels leads to detection of lines covering about 90% of the boundary points. 158
Figure 104- Results of application of Hough transform after dilation with mask size of 15 pixels applied to the images in Figure 99. 159
Figure 105- Large view of results of application of Hough transform: (a) without dilation; despite the precise boundary segmentation, the lateral line is not detected by Hough, (b) with dilation of mask size 15 (the two yellow lines show the 15-pixel-wide band to capture variation of the boundary that was considered by dilation). 160
Figure 106- Two example camera images that show a smooth pore-less layer (left) and a porous layer (right). Squares mark examples of darkly-etched regions that are of the same color as pores and sometimes have same characteristic of pores after segmentation, and circles mark examples of true pores. 163

Figure 107- Example image of a porous layer..... 166
Figure 108- Result of thresholding of wiener-filtered gray-scale image of Figure 105 with different thresholds. The thresholds are: (a) 0.32, (b) 0.35, (c) 0.4, (d) 0.43. 167
Figure 109- Pores manually segmented from the camera image and isolated in the new image for examining the intensity distribution of pores. 167
Figure 110- Histograms of pores segmented from camera image in comparison with histogram of regions that contain no pore..... 168
Figure 111- Application of reconstruction to segment pores from the camera image: (a) marker, (b) mask, (c) result of reconstruction, (d) removal of long, horizontal, narrow objects. 170
Figure 112- Example images of (a) a smooth surface (Zone II), and (b) a porous surface (Zone III). It is clearly seen that Zone II surface shows larger darkly etching regions due to higher energy and temperature. 171
Figure 113- (a) Example of the porous layer (Zone III), (b) segmentation result of reconstruction, (c) result after implementing rule-based identification on geometric features. 172
Figure 114- Histogram of the geometric features of the segmented objects in Figure 109 that majorly consist of true pores: (a) orientation, (b) eccentricity, (c) thickness of long horizontal objects. 173
Figure 115- Histogram of the geometric features of the segmented objects in Figure 109 that majorly consist of long horizontal scan markings: (a) orientation, (b) eccentricity, (c) thickness of the long horizontal objects. 174
Figure 116- Results of application of pore detection algorithm to Figure 110 (a): (a) and (b) result of thresholding of wiener-filtered gray-scale image of Figure 110 (a) with thresholds: (a) 0.35, (b) 0.41; (c) reconstructing of image in part (b) as a mask and image in part (a) as a marker; (d) the distribution and histogram of the area of the segmented

objects in Figure 114 (c); (e) image after removal of objects with an area larger than 100 pixels and smaller than 50 micron equivalent diameter ; (f) and (g) the distribution and histogram of the eccentricity and orientation of the objects in Figure 114 (e); (h) the image after removal of horizontal objects (within ± 150 from horizontal line and with eccentricity larger than 0.9 and thickness smaller than 10 pixels). 176
Figure 117- (a) application of reconstruction using a mask made by a higher threshold (0.42), (b) application of region-growing with the similarity parameter of 0.06..... 178
Figure 118- Microscopic image of a layer in Zone III corresponding to the camera image in Figure 105 with the results of pore segmentation using region-growing after manual parameter optimization. 179
Figure 119- Result of error between the area of detected pores in camera with respect to that of microscope for various selection of the mask parameter in reconstruction operation. 180
Figure 120- Result of error between the area of detected pores in camera with respect to that of microscope for various selection of the similarity parameter in region-growing operation. 180
Figure 121- Examples of application of the segmentation algorithm to other layers. Each row shows an individual layer with the original image on the left and the segmentation results on the right..... 181
Figure 122- Comparison of pore detection in camera image with the true pores detected from microscopic image: (a) camera image, (b) result of pore segmentation with reconstruction, (c) microscopic image, (d) pores detected from microscopic image using manually adjusted region-growing. 182
Figure 123- Comparison of pore detection in camera image with the true pores detected from microscopic image. See description of Figure 120. 183

Figure 124- Comparison of pore detection in camera image with the true pores detected from microscopic image. See description of Figure 120. 183
Figure 125- Comparison between the area of segmented pores from camera image and microscope image calculated for 10 randomly selected images. 184
Figure 126- Percentage relative error between the area of segmented pores from camera image and microscope image calculated for 10 randomly selected images. 184
Figure 127- Example images of (a) a smooth surface, and (b) a porous surface. 189
Figure 128- Example images of (a) a smooth, non-porous surface, and (b) a porous surface. 193
Figure 129- Application of local thresholding to images in Figure 126. 194
Figure 130- Zoomed-in views of small cropped portions of the two images in Figure 127. 194
Figure 131- Results of local thresholding applied to (a) and (b) two examples of high-energy, smooth surfaces (zone II), (c) and (d) low-energy, porous layers (Zone III). ... 196
Figure 132- The probability distribution of the black areas in local thresholding results for all camera images of Zone II (high-energy, non-porous: HE) and Zone III (low-energy, porous: LE) layers. 196
Figure 133- Result of using Bayesian network to identify Zone III (LE) versus Zone II (HE) using area as the only feature: (a) output of Bayesian, (b) Bayesian output after binarizing. 198
Figure 134- Pdf's of area for porous (Zone III) and non-porous (Zone II and I combined). 199
Figure 135- Result of Bayesian network to identify Zone III versus Zone II and I using area as the only feature: (a) output of Bayesian, (b) Bayesian output after binarizing using optimal threshold of 0.6. 200

Figure 136- Performance of Bayesian network, using area as the only feature, for various values of thresholds: (a) average of $TPR + TNR$, (b) Figure of Merit (F1). 201
Figure 137- Pdf's of area for porous (Zone III) versus non-porous, Zone II and Zone I individually. 201
Figure 138- Pdf's of number of intensity changes for Zone III (porous) versus Zone II and Zone I individually. 203
Figure 139- Output of Bayesian network to identify Zone III versus Zone II and I using two features of area and number of intensity changes. True value of 1 represents Zone III, true value of 0 represents Zones I & II. 203
Figure 140- Performance of Bayesian network, using two features of area and number of intensity changes, for various values of thresholds: (a) average of $TPR + TNR$, (b) Figure of Merit (F1). 204
Figure 141- Results of local thresholding for several examples of (only) non-porous layers: (a) Zone II, (b) Zone I. 205
Figure 142- Results of local thresholding for several examples of porous layers, Zone III. 205
Figure 143- Two patterns generated to simulate regions belonging to Zone I (left) for non-porous versus Zone III (right) for porous layers..... 206
Figure 144- fft of images in Figure 141 in the x-y frequency plane while the color represents the z value of each component, i.e. amplitude at that frequency pair..... 207
Figure 145- fft of Figure 141 (a): (a) the y-z view, (b) x-z view. 209
Figure 146- fft of 1D signals corresponding to a square wave and a constant value. Square wave represents the variation of the 2D image (Figure 141 (a)) along y direction and the constant function represents the variation of the 2D image along x direction. .. 209
Figure 147- fft of the two images in Figure 141 in y-z view. Left fft corresponds to left image in Figure 141 and similarly for the right image and fft. 210

Figure 148- fft of the two images in Figure 141 in x-z view. 211
Figure 149- Four cases of 1D signals in each row on left with their corresponding Fourier transform on the right. "_f" denotes the fft of the corresponding signal. 212
Figure 150- Two sample images of Zone I (left) and Zone III (right) after applying local thresholding..... 213
Figure 151- fft of images in Figure 148 next to each other in yz view..... 213
Figure 152- fft of images in Figure 148 next to each other in xz view..... 213
Figure 153- pdf of each of the 5 frequency features for regions belonging to the three different Zones. 217
Figure 154- pdf of the two features, area and number of intensity changes, represented here for comparison. 217
Figure 155- Performance of Bayesian, using the final optimal features, in terms of Figure of Merit, for various values of threshold. 222
Figure 156- Performance of Bayesian, using the final optimal features, in terms of sensitivity and specificity, for various values of threshold. 222
Figure 157- Performance of Bayesian, using the final optimal features, in terms of precision and NPV, for various values of threshold. 223
Figure 158- Two examples of porous regions (in each row): (a) original image, (b) result of pore segmentation from Chapter VIII, result of local thresholding applied to the region that was identified as porous using Bayesian network developed in this Chapter. 224
Figure 159- Two examples of non-porous regions (in each row): (a) original image, (b) gray-scale image, (c) result of pore segmentation from Chapter VIII, (d) result of local thresholding applied to the region that was identified as non-porous using Bayesian network developed in this Chapter. The segmented objects that could be FPs were removed using Bayesian identification. 225
Figure 160- Mechanics of cross-correlation of mask w with image f. 238

Figure 161- final result of cross-correlation of the filter w with the image f shown in Figure 158. 239
Figure 162- Result of dilation of image A by mask B. 240
Figure 163- Result of erosion of image A by mask B. 241
Figure 164- Illustration of the mechanics and final results of opening operation. 242
Figure 165- Illustration of the mechanics and final results of closing operation..... 242
Figure 166- Procedure and steps for morphological reconstruction [106]: (a) mask, (b) marker, (c) iterative procedure for step 3 described above, (d) final result of reconstruction. 243
Figure 167- Illustration of region-growing algorithm. From left to right: image containing the seed number, image containing a grown region resulted from finding and connecting the seed number neighboring pixels that satisfied a specified similarity predicate to the seed point or to the grown region at the previous step, the image containing the final result where adding any neighboring pixels would no longer satisfy the similarity predicate. 244
Figure 168- Parametric representation of a line in x-y space with respect to r and θ.... 246
Figure 169- Example of application of Hough transform to extract lines: (a) an image containing of 3 points in x-y space that lie on a line, approximately with r = 89 and $\theta = 30o$ (b) locus of the lines passing through each of the three points in parameter space r-θ 247

SUMMARY

Metal powder-bed fusion is an additive manufacturing (AM) process which enables fabrication of functional metal parts with near-net-shape geometries. The drawback to the metal powder-bed AM processes is lack of precision and the high chances of defect formation. Over the past two decades much research has been conducted on real-time process control and thermal monitoring in order to produce parts of higher quality. Despite partial improvements, defects may still occur during the process, leading to defective parts and low geometric precision.

This work addresses the efficacy and development of in-situ quality inspection for powder-bed AM (more specifically laser powder-bed fusion, L-PBF) using high-resolution visual images. For the first time, an imaging setup and the required machine vision (MV) algorithms are developed, implemented, and evaluated to inspect the part cross sectional geometry and to provide an assessment of porosity, in metal powder-bed AM, by direct visualization of porosity. An imaging setup is developed to produce images in-situ from each layer that visualize the fused objects in the layer of powder and the surface quality in terms of fusion and formed defects. A framework for an imaging-based inspection system is developed that consists of two subsystems: one for extraction of fused geometric objects in the layer of powder and detection of geometric errors, and the other for detection of defects (pores) and identifying defective (porous) regions.

Appropriate image processing algorithms are designed and implemented for detection of fused geometric objects and estimation of the geometric parameters. Geometric objects are detected with a boundary point-to-point (root-mean-square) error of 81 microns. Image processing algorithms are also developed to detect porosity directly from the camera images of the layers. Information about location, shape, and size

of defects can be inferred from them. In addition to detection of individual pores, a high-level, intelligent approach is proposed and implemented to provide a qualitative assessment of porosity by identifying defective regions. For this purpose, a statistical Bayesian framework is developed and trained based on specific features extracted from the image of subregions of the layers. The Bayesian network is designed to maximize the Figure of Merit and leads to precision of 89% and negative predictive value of 83%.

This work is the first work on development of an extensive[1] MV system for metal powder-bed AM using visible-light images. In addition to offering an efficient MV-based inspection system, this work also provides an infrastructure for developing more precise and confident imaging and detection systems for powder-bed AM for visible-light camera images. It also offers a foundation for developing MV systems for powder-bed AM that use other sources of 2D measurements such as height maps, microscopic images, stereo imaging, etc. Although the algorithms in this work mainly focused on geometric errors and defects (in form of porosity), the work on identification of porous regions can be generalized to assess roughness of the layer, quality of fusion, level of input energy, and process calibration.

[1] "Extensive" in terms of that is follows a substantial framework consisting of three processing levels (including high-level MV) and addresses both geometry and part porosity.

CHAPTER I

INTRODUCTION

1.1 Research Motivation

AM is a layerwise manufacturing technique with the ability to make near-net-shape parts. The capability of making complicated geometries, lower raw material usage, no requirement of tooling, and consequently reduced cost and lead manufacturing time are its important advantages over conventional manufacturing methods such as machining, forging, and casting. These benefits have made AM a very convenient cost-efficient method for rapid prototyping and even manufacturing functional parts [1-3]. With the development of production techniques for high density metal parts from one-component metallic powders in 1999, a trend of producing individual metal parts for mass customization started, extending the application to a large variety of functional parts and components in automotive and aerospace industries [4]. Selective Laser Sintering (SLS) and Selective Laser Melting (SLM) are two important types of such techniques that use a high-power laser to sinter or melt specified regions of a layer of metal powder spread on a platform, a process also known as L-PBF. If the fusion energy is provided by an electron beam instead of laser, the process is called electron beam melting (EBM). L-PBF and EBM are two forms of metal powder-bed (fusion) AM.

Despite important advantages of metal powder-bed fusion, conventional methods such as machining are still a method of preference for high-precision applications and where certain solid defect-free parts are required [3, 5]. Due to the nature of powder fusion in L-PBF (as well as EBM) processes, the parts built suffer from lower precision (than the conventional high-precision processes) and high chances of formation of defects in the layers. For large-scale applications in many critical industries such as aerospace,

where precision and part quality are very important, it is necessary to prevent formation of defects and/or repair formed defects as early as possible in the build process. This important objective can be achieved by online quality monitoring and control.

Past studies on quality monitoring in L-PBF were centered on process control where process parameters are controlled to monitor the physical phenomena in laser powder fusion. Much research has been done to investigate the causes of defect formation in L-PBF. The majority of this research is on the study of the laser powder fusion (the process underlying laser powder-bed fusion, L-PBF) and the behavior of the associated physical phenomena and properties such as the temperature and area of the heat-affected zone (HAZ) and melt pool. It has been observed that irregularities associated with HAZ and melt pool behavior and properties can cause defect formation. The objective of process control is to maintain these physical phenomena and behavior in a desired manner by adjusting laser power and scan speed so as to avoid defect formation. Much work on this area has led to improvement of part quality and the ability of successfully fabricating parts that would otherwise have failed [6-10].

Studies showed that even when process control was performed precisely and no irregularities in HAZ or melt pool were observed, various types of defects still formed. Some researchers investigated the correlation of melt pool irregularities with formed defects by mapping infra-red (IR) measurements on the workpiece and realized that there are many instances that defects form with no corresponding HAZ or melt pool irregularity and there are many cases of irregular melt pool behavior that do not lead to defect formation [11]. These results imply that mere process control does not guarantee build of defect-free parts.

Alternatively, a very efficient method of online quality control in AM, is the in-situ automated detection of defects, which is the objective of this research. Automated defect detection provides several important benefits to the AM. The results of defect

detection can be used in corrective actions to correct the defects in-situ so as to fix defects as well as to prevent from further propagation. Study of results of detected defects can also help identify defect causes and process errors that are responsible for formation of defects. Appropriate process control actions can then be taken. Early identification of defective parts also prevents cost and material waste by stopping the process from building a whole defective part. In-situ detection of defects also allows for more reliable 3D part quality assessment by providing in-depth layerwise information. A 3D model of the part that provides information about the true internal structure of the part can also be used for simulation, modeling, and evaluation purposes.

Past study on monitoring defects in L-PBF has been done mostly for the purpose of understanding the defects and the defect formation mechanism and the causes of defect formation. Various sensors including high-resolution visual camera, IR and thermal camera, (offline) CT scanner, and acoustic sensors have been used for defect detection. For work that addressed detection of defects, the defects were detected mostly by manual examination or 1D signal processing of the measurements to detect only existence of a defect. Among the large number of work on thermal monitoring for process control, there are several researches aimed to detect defects by thermal imaging. However, most of these works are only limited to detection of existence of defects and the results are very approximate. A few works on defect monitoring suggested that the results of detection can help in corrective actions; however, their detection results did not provide sufficient information for identity, characteristic, and location of defects [11-14]. No work on detection of geometric errors was found reported. Detailed study of these researches will be addressed in Background Chapter. Development of an in-situ inspection system for metal powder-bed AM that can detect defects and provide information about defect location, shape, and size is a very important research objective and the past research in this area is very preliminary.

Machine vision systems have widely been used for automated visual inspection (AVI) in a variety of manufacturing and industrial applications such as material and surface inspection (sheets, wood, glass, ceramics, tiles, concrete, etc.), weld inspection, electronics, textile, and manufacturing of consumer products [15-30]. In AVI, images that visualize surface and part features are analyzed automatically using a computer to detect flaws and defects. Although there is a variety of work on thermal imaging for inspection in L-PBF, as mentioned before, there is very little research conducted on visible-light imaging-based inspection in metal powder-bed AM. Recently and mostly concurrent with this research, very preliminary image processing algorithms have been used to monitor some aspects of the process such as quality of powder distribution or elevated edges from visual images [31-33]. Image analyses performed so far in quality inspection in metal powder-bed AM have been limited to simple intensity thresholding.

Visual images are a 2D source of information that visualize the powder layer and have the capability to visualize the fused part surface features. So, theoretically, clear visual images analyzed by effective machine vision algorithms, have the efficacy to provide a very useful means for in-situ quality inspection in powder-bed AM both for detection of geometric errors and defects . However, visual images as well as machine vision have not been used for inspection of defects in metal powder-bed AM and in fact application of machine vision for this task is very challenging. Some of the challenging factors obstructing the effective application of machine vision in metal powder-bed AM are stated as follows.

Challenging factors obstructing the effective application of machine vision in metal powder-bed AM:

1) Defects of interest in metal powder-bed AM can be as small as 100 microns or even smaller. Capturing high-quality images in situ that visualize

defects has not been reported previously, as seen in literature, and can be very challenging.

2) Although geometric objects are larger and can be visualized more easily, the very low contrast between the fused object and the powder, the non-uniformity of the background (powder area) and the fused object, and process irregularities such as melt pool spatters on powder region, make efficient detection of fused objects very challenging.

3) Even for images that visualize defects, the very low contrast between defect and background, a large variety of irregular forms, shapes, and sizes of defects, and non-uniformity of background due to its usually irregular texture, itching, oxidation, or existing random noise pose a strong challenge against efficient defect detection.

4) There is no prior work on detection of geometric objects and part defects (pores) from metal powder-bed AM. Therefore, there is no work to provide a starting point and guideline for selecting, parameterizing, and combining the more effective algorithms among all existing algorithms for object detection.

5) There is no prior developed database of metal AM defects that provides a large set of possible patterns for defects to be used in pattern matching or feature-based identification techniques.

The objective of this research is to resolve or alleviate the above challenges and develop an automated quality inspection system based on machine vision that detects the geometric fused objects and defects (porosity) in each layer in L-PBF. Based on the 2D nature of the analysis, the result of detection can provide information about defect location, shape, and size. This will be elaborated more in next section.

1.2 Research Goals & Contributions

The goal of this research is to study the efficacy of using visual camera images for in-situ inspection of part, in terms of geometric aspects and part quality (assessment of porosity), in metal powder-bed AM (or more specifically L-PBF). This work is aimed to alleviate or resolve the challenges mentioned in Section 1.1 and develop an imaging setup and sets of machine vision algorithms that detects fused geometric objects and provides an assessment of part quality in terms of porosity (or lack of fusion) from high-resolution camera images. An imaging setup is developed to capture measurements, in form of high-resolution visible-light images, at each layer during the build process that visualize fused objects and defects. Appropriate machine vision algorithms are developed with the capability to efficiently extract geometric objects, detect and identify porosity, and provide information about pores characteristics such as size, location, and shape from images in each layer during L-PBF process. The system output information is comprehensive and sufficient enough to be used for in-situ corrective actions or in-depth 3D part quality assessment. Additionally, this AVI will provide information about the geometry of fused objects that can be used for detection of geometric errors and tolerance issues.

Tasks

This research goal can be expanded into the following tasks:

1. (Major contribution into) Development/modification of an imaging setup that visualize a level of information that can be used for an assessment of part quality in terms of geometry and porosity.
2. Develop a MV-based inspection system for detection of fused geometric objects and porosity:

a. Development of a framework for inspection of geometric errors and defects in powder-bed AM based on metrology and machine vision principals.
b. Development and evaluation of image processing algorithms for extraction and detection of fused geometric objects in powder bed.
c. Development of image processing algorithms that detect porosity.

3. Develop high-level machine vision algorithms for more confident detection and for a reliable qualitative assessment of porosity :
    a. Extraction and analysis of discriminating features for subregions of layers with acceptable or bad quality of fusion, or porous and non-porous subregions.
    b. Development of a statistical Bayesian network for identification of defective regions based on statistical texture identification.
4. Develop an image database of porosity for design and evaluation of porosity detection and identification algorithms.
5. Identify metrics for evaluation of algorithms.

To make the above research feasible, the following task was also performed as:

6. Resolve some of the major issues with in-situ imaging of AM part detailed features; contribute into development of an imaging setup that visualizes fused objects and provides a level of information of fused object surface features including porosity that can be used for an assessment of part quality in terms of porosity.

Contributions

Based on the discussion, in previous section as well as the Background Chapter, on the research gaps in the existent literature, this research has the following contributions:

1. Provided a solution to the issue against in-situ imaging of detailed surface features in AM parts and developed the imaging setup that visualizes detailed surface features including porosity in layers n AM parts during build.
2. Developed image segmentation algorithms that detect the fused geometric objects from camera images with a performance quantified as 81 micron point-to-point boundary error.
3. Designed and implemented model-based segmentation algorithms to extract the geometric parameters with precision of within 1^{o} for angles of lines and a maximum error of 50 μm for locations of verities, verified for square objects.
4. Designed and implemented image segmentation algorithms for detection of porosity, from porous layers, that matches the true porosity area, seen by microscopic, with 15% root-mean-square error, with specificity and sensitivity of 100% for object larger than 100 microns equivalent diameter.
5. Developed an intelligent identification algorithm using Bayesian approach to identify porous regions (corresponding to Zone III in laser parameter space) from non-porous regions. The performance of the identification was improved by incorporating frequency features in addition to spatial features. Using a measure to maximize Figure of Merit, the identification was performed with sensitivity of 89%, specificity of 82% that led to precision of 89% and negative predictive value (NPV) of 83%.

Detailed explanation of the contributions is given in Chapter IX.

1.3 Thesis Organization

This research will be more established and detailed in the following chapters. Chapter II familiarizes the reader with AM, AM defects and their formation mechanism and provides a more detailed literature review on the state-of-the-art in quality inspection and control in metal AM. It also provides background knowledge on automated visual inspection and machine vision and provides introductory knowledge of several image processing definitions of concepts and algorithms. Chapter III formulates the problem of design of an AVI for L-PBF using machine vision principals from 2D optical measurements. The described AVI system is divided into detection of fused objects and detection and identification of defects. Chapter IV describes the system and imaging setup; it provides an overview of the development stages of the imaging setup. Chapter V describes developing a database for images of porosity to be used for developing machine vision algorithms for assessment of porosity. In Chapter VI, detection of fused geometric objects is addressed and appropriate image processing algorithms are developed to detect the geometric objects from camera images. Chapter VII addresses the detection of porosity where image processing algorithms are developed to detect individual pores from camera images. The developed algorithms are quantified, assessed and verified based on the quantification measures. In Chapter VIII, a Bayesian network is developed and implemented to identify potentially porous regions and to provide more reliable detection of defects through probabilistic information. The developed Bayesian identifier is quantitatively evaluated in terms of FPs and FNs. Finally, Chapter IX gives the conclusions of this research. It discusses in detail the contributions of this research as well as the limitations and provides the scopes of the future work. At the end, Appendix A provides a description and basics of some of the image processing algorithms used in this dissertation.

CHAPTER II

BACKGROUND

This chapter will first provide a description of AM and AM defects and mechanism of defect formation. It will then provide a review of the past work regarding online quality monitoring and control in AM. Background knowledge on application and design of machine vision systems will also be given in this chapter. Conclusion of this chapter will then identify the gap in the past research based on the literature review and establishes the motivation for conducting this research as was discussed in the Introduction Chapter.

2.1 Additive Manufacturing

Additive Manufacturing (AM) is defined as "process of joining materials to make objects from 3D model data, usually layer upon layer, as opposed to subtractive manufacturing methodologies." AM is also referred to as additive fabrication, additive processes, additive techniques, additive layer manufacturing, layered manufacturing, and freeform fabrication. The primary applications of additive fabrication are design/modeling, fit and function prototyping, and direct part production [1, 34].

AM is largely an emerging technology that shows promise for energy, aerospace, medical and commercial sectors. Its ability to build up objects directly makes it a good alternative to conventional machining, forging, molding and casting for rapidly making highly customized parts [35, 36]. According to the industry report by Wohlers Associates [34], by 2015 the sale of additive manufacturing products and services could reach $3.7 billion worldwide, and by 2019, exceed $6.5 billion. Around the world, AM is changing the way organizations design and manufacture products. When used correctly, it can save

impressive amounts of time and money. From a raw materials and environmental perspective, AM creates a minimum of manufacturing byproduct (waste). From a bill of materials perspective, cost savings of more than 75 percent can accrue from using AM rather than conventional methods. AM production of simple parts also improves the production speed by about 40 percent [37].Remanufacturing parts through advanced AM and surface treatment processes can also return end-of-life products to as-new condition, using only 2−25% of the energy required to make new parts [38-40]. Companies maintain that AM has helped trim weeks, even months, of design, prototyping, and manufacturing time, while avoiding costly errors and enhancing product quality [1, 34].

There is a variety of AM techniques. Initially techniques such as stereolithography [2], fused deposition modeling [41], and laminated object manufacturing (LOM) allowed for manufacture of parts made of plastic, polymer, wax, and similar materials [3, 42]. With the invention of selected laser sintering (SLS) [43] and its commercialization in 1992, and later on Selective Laser Melting (SLM) [44], build of a large variety of metallic parts and components was made possible, extending the application to a large variety of parts and components in automotive and aerospace industries [4]. SLS as well as SLM use a high-power laser to sinter or melt specified regions of a layer of metal powder spread on a platform, a process also known as laser powder-bed fusion (L-PBF). Similar metal powder-bed fusion technology where the input energy is provided by electron beam instead of laser is called Electron Beam Melting (EBM). Both EBM and L-PBF are powder-bed fusion processes that fuse selected regions on a powder bed and the only major difference is the source of input energy. On the contrary to techniques such as stereolithography and FDM, L-PBF does not require support structures that allows for the construction of previously impossible geometries. Similar concept of laser metal powder fusion has earlier been used in laser powder deposition which is the implementation of laser cladding for fabrication of true

parts [45]. While laser powder deposition moves and controls a powder feeding nuzzle with a mounted central laser beam all over predefined paths to fabricate a layer, L-PBF directs laser beam using a mirror scanner to selectively fuse the powder layered on a powder bed. Although, some of the techniques and discussions in this research are implementable to other sorts of AM, the focus of this research is metal powder-bed AM, mainly L-PBF. The developed vision system and setup, however, can easily be implemented to EBM as well as L-PBF. Since the machine and the setups being used in this research is L-PBF process, the majority of the discussion is on L-PBF, an important AM process conveniently aimed for fast fabrication of large complex geometries.

Figure 1 shows an illustration of a L-PBF machine and its components. A layer of metal powder of a certain depth is spread on a platform by a coater (powder layering). The laser beam is then directed using mirrors to scan specified paths (based on CAD model) to fuse the powder (laser melting). The laser spot produces a small area of very high temperature (the heated zone) which comprises of a heat-affected zone (HOZ) that surrounds a melt pool in SLM. As the laser scans away, the previously heated zone transfers heat to the surrounding and cools down to get fused to the neighboring solidified regions (Figure 2). After the whole desired region in the layer is fused, a new layer of powder is spread (powder layering in Figure 1) and the process is repeated until the whole part is built. The process parameters and influential factors include laser power and scan speed, powder layer height, scan path characteristics such as hatch spacing and scanning strategy, and powder characteristics such as grain size and powder homogeneity.

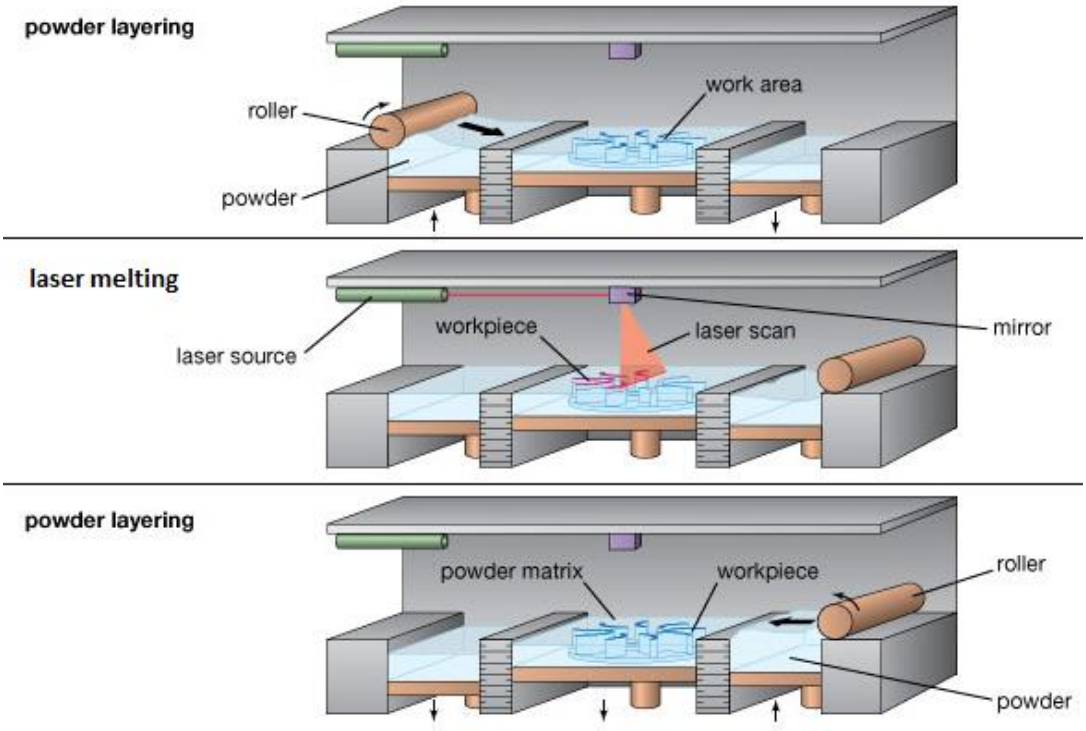

Figure 1- Illustration of L-PBF process [46]

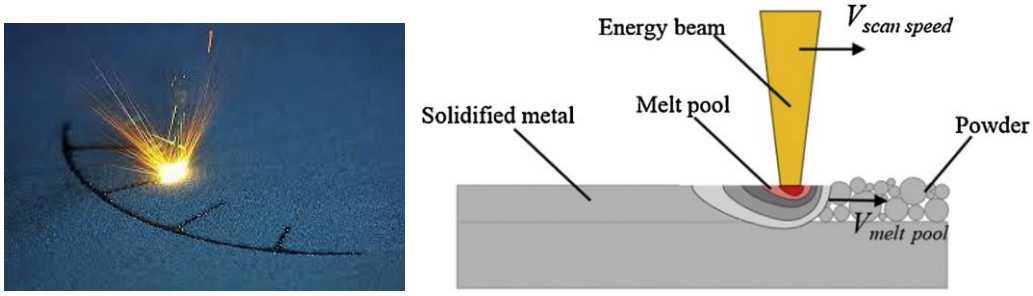

Figure 2- Illustration of laser powder fusion.

2.2 Defects in Metal AM and Defect Formation Mechanism

Defects and flaws in powder-bed AM appear in a variety of forms. A common form of defects is formation of various types of forms in the part (Figure 3 (a)). Porosity can reduce the part density and reduces the structural and mechanical properties such as tensile strength as well as fatigue properties. Other types of defects that may occur in

parts are formation of geometric errors that lead to dimensional inaccuracy as well as lack of dimensional precision (Figure 3 (b)). The part geometry may be unacceptable, or permitted geometric tolerances may not bet met if significant geometric errors occur. Another characteristic of the part that is of importance is the surface finish of the part (see Figure 3 (c)). Rough surfaces that do not meet the finish requirement of the part will need further post processing.

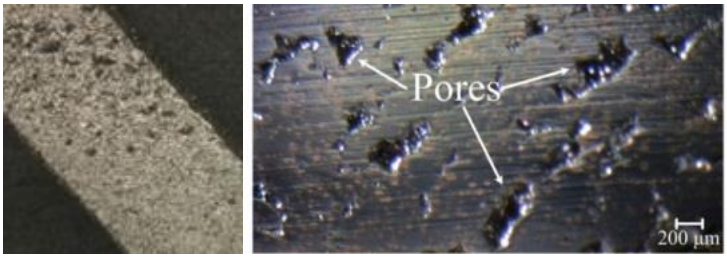

(a)

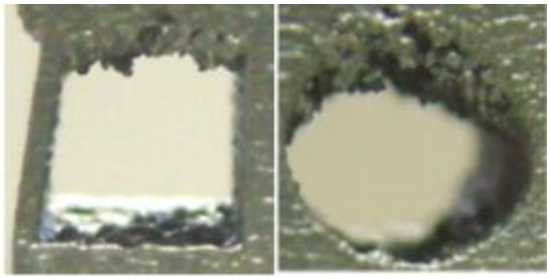

(b)

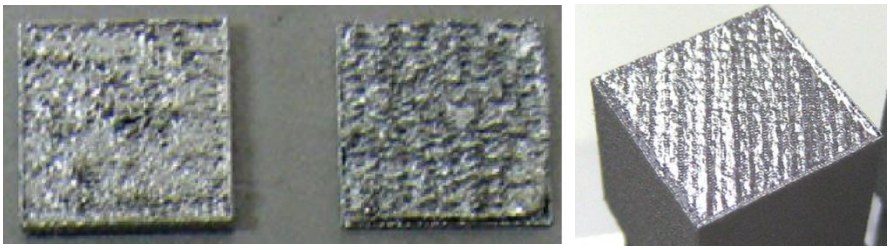

(c)

Figure 3- Examples of various types of defects that occur in metal powder-bed AM. (a) pores (sometimes, in this document, generally referred to as defects), (b) geometric errors, (c) undesirable surface characteristics in terms of surface roughness and quality of fusion [31].

In addition to the defects and errors in parts, some error and flaws related to the process may occur such as fluctuation of laser power and focus, collision between the

coater and the elevated regions (edges) in the part, etc. These flaws may cause defects in parts and result in process stop or malfunction. But these are at the level of process flaws and in this research we are mostly focused on the defects associated with the part itself, both in terms of formation of pores and geometric errors.

The mechanical properties (density, strength, fatigue properties, etc.) are particularly dependent on the quality of the fusion and formation of internal (sub-surface and and surface) defects. The stability of laser powder fusion process which is an important factor on the quality of fusion strongly depends on the net amount of energy received per unit mass of the powder (energy density). The net amount of energy density depends on the input energy density which is defined as [47, 48]:

$$E = \frac{P}{V \cdot h \cdot t}$$

Equation 1

where P is laser power, V is the scan velocity, h is the scan space, and t is layer thickness.

Figure 4 shows SEM images of parts made by L-PBF at three different levels of energy. While sufficient amount of energy density generally leads to complete fusion of the part with no noticeable defect (Figure 4 (a)), lack of sufficient energy leads to incomplete fusion that brings about formation of pores (Figure 4 (b)).

As seen in Figure 5 (a) and (b), insufficient energy leads to formation of pores and voids throughout layer as well as between the hatch paths in form of lack of fusion [49]. These pores are usually characterized with irregular shapes and may be as large as 500 microns (see Figure 6 and Figure 5 (a)). Lack of fusion can also occur between the two layers that are not fused well together due to the insufficient amount of heat (Figure 5 (c)).

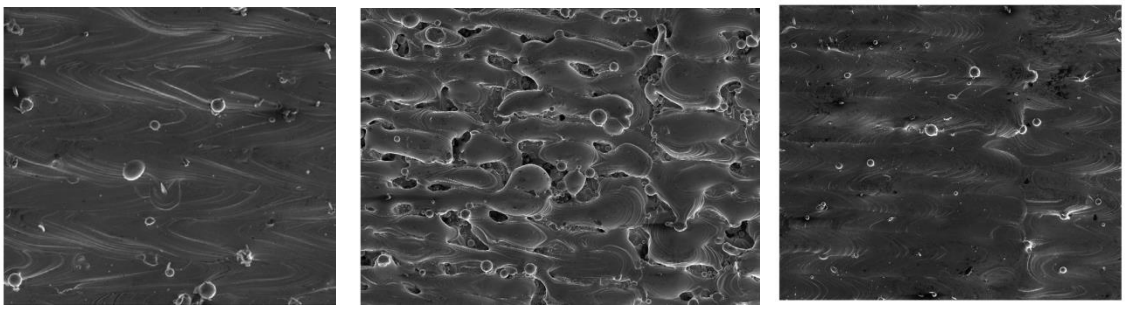

(a) (b) (c)

Figure 4- SEM images of parts made by L-PBF at different levels of energy [48]: (a) sufficient energy, (b) low energy, (c) high energy.

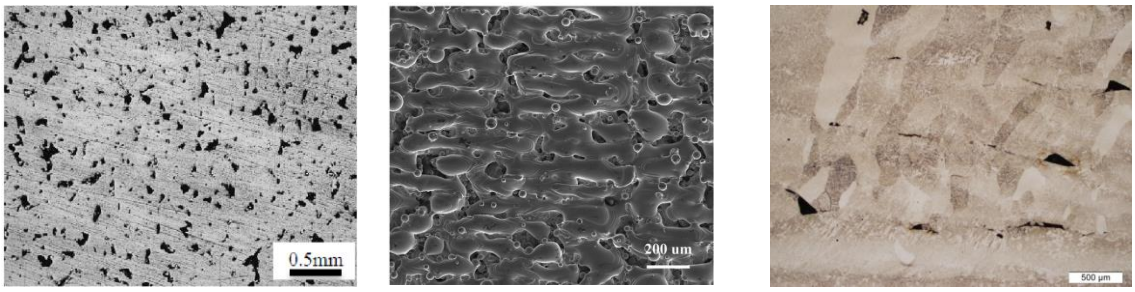

(a) (b) (c)

Figure 5- Porosity due to insufficient energy: (a) and (b) Respectively, microscopic image and SEM image of a part made by L-PBF that encounters lack of fusion in the layer [50], (c) Microscopic image of lack of fusion between layers [51].

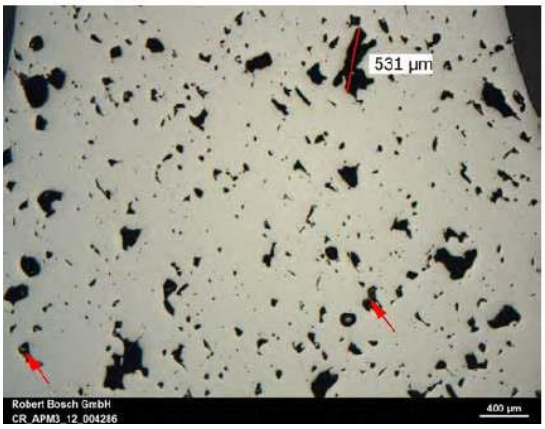

Figure 6- Microscopic image showing pores formed due to insufficient energy.

A large number of studies report that as the energy decreases, the porosity increases and the resultant mechanical properties are deteriorated [32, 52]. This observation matches the intuition that the high level of energy leads to complete fusion that prevents pore formations. However, excessive amount of energy leads to formation of pores as a result of different pore formation mechanism. Although, the SEM image from the surface of a part (Figure 4 (c)) may not show these pores on the surface, excessive energy input, in fact, leads to formation of gas pores and voids (gas porosity) as seen in Figure 7. This type of porosity is not usually visible on the surface of the built layer. It usually is seen in form of subsurface pores that are inspectable when using destructive techniques or CT scanning. Gas porosity is characterized by near spherical shape and is distributed randomly throughout the bulk of the deposited part. They're usually much smaller in size than lack of fusion and pores formed due to insufficient energy. This porosity is believed to arise either from gas entrapment in the melt pool during deposition or from internal porosity present in the metal powder, or both [48, 51, 53].

It is worthwhile to mention that higher level of energy for building parts leads to higher local temperatures, higher temperature gradients, higher thermal stresses, and larger distortions after cooling [12]. These all increase the chances of formation of cracks and defects due to large thermal stresses as well as geometrical distortions and inaccuracies. Additionally, one of the very common defects formed or intensified due to increased energy is formation of larger elevated edges (Figure 11 (c)) that leads to dimensional inaccuracy, interference with uniform powder distribution, as well as contact or collision of the coater with the elevations that can cause damage to the coater or stop the process.

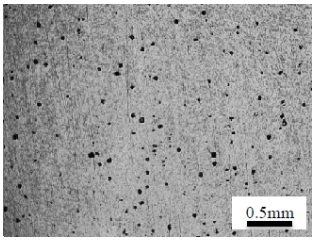

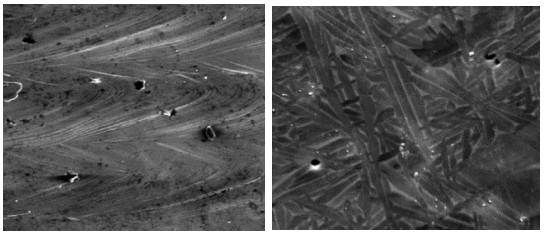

(a) (b)

Figure 7- Porosity due to excessive energy in AM parts: (a) Microscopic image of a cross-section of a built part that show pores [6] (the cross section was obtained by cutting the part), (b) SEM image of parts built with excessive energy that contain small spherical gas pores [48, 51].

Although level of energy is known to be a very influential factor in formation of defects, it is not the only factor causing formation of defects. In fact, even at the same level of input energy, choice of a different combination of process parameters may reduce or decrease defect formation.

In a recent, more extensive study, Gong *et al.* [48] studied the effect of energy as well as two individual process parameters on defect formation in L-PBF through changing laser power and scan speed. They observed that at low values of laser power, as intuitively expected, by increasing the scan speed at the constant laser power, the decreased level of energy led to increase in defect formation and consequently lower density and less desirable mechanical properties (Figure 8 (a)). However, at a higher level of laser powder, as the scan speed decreases beyond some point, the increased level of energy leads to formation of gas porosity that decreases the part density and lowers its mechanical properties (Figure 8 (a)). This continues until the exceedingly high level of energy causes a lot of thermal stresses, distortion, and instabilities that prohibit part fabrication.

This observation suggested that the laser power - scan speed domain can be divided into 3 practical zones, so called Zone I, II, and III and an impractical zone named overheating (OH), as seen in Figure 8 (b) and Figure 9. Zone I being the range where parts with no noticeable pores are created, Zone II being the high-energy zone where small spherical, (usually sub-surface) gas pores are created, and Zone III being low-energy zone where large irregular pores and lack of fusion occur that have large deteriorating effect on the mechanical properties of the part.

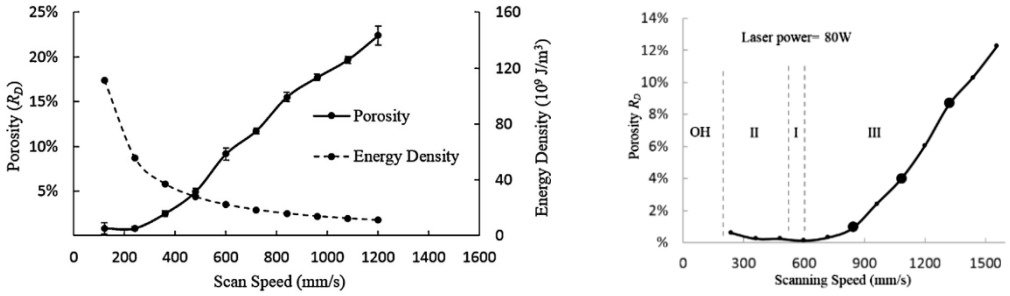

(a) (b)

Figure 8- Variation of porosity (a measure of porosity) with respect to scan speed at constant level of energy. (a) porosity monotonically increasing with decrease in level of energy, (b) a non-monotonic trend for porosity variation with scan speed and introducing the 4 zones of process parameters.

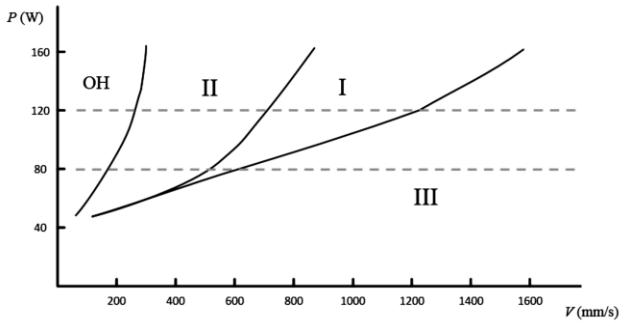

Figure 9- Graph illustrating the 4 zones in the laser power – scan speed space.

To avoid formation of pores as well as undeniable, large geometric distortions due to inappropriate level of energy and process parameters, a desirable nominal set of process parameters are determined. Process parameters such as laser power, scan speed, and hatch spacing are calibrated by usually a large number of trial and errors to avoid process instability and formation of defects. Nominal process parameters are selected by performing many tests on a simple geometry of a specific material to obtain the best possible quality of part made of a given material. Once desirable parameters are chosen, the machine will usually operate at these parameters for a variety of geometries made of the specified material.

In addition to the input energy density determined by process parameters, the rate of heat transfer from the heat-affected zone also plays a role on formation of defects and geometrical errors. Many defects and geometric irregularities are associated with undesirable heat transfer from the heated zone or melt pool. The heat transfer and the resulting fluid flow affect the size and shape of the melt pool, and the cooling rate, and transformation reactions in the melt pool and heat-affected zone. The melt pool shape is responsible for phenomena such as the split of melt pool and formation of droplets. The melt pool geometry also influences the grain growth and the resulting microstructure of the part, consequently affecting the mechanical properties [5, 54-56].

In general, in areas with larger heat input and smaller heat transfer to the surrounding, the melt pool is seen to grow excessively engaging more powder grains. The increased amount of powder causes a larger solidified mass (over-fusion) that leads to elevation in the layer or its edges. The large energy input can also cause balling phenomenon in the melt pool which prevents desirable solidification. On the other hand, larger heat transfer to the surrounding (or smaller energy input) leads to a smaller melt pool and consequently smaller solidified mass, causing lack of fusion, especially between the adjacent scan paths as well as layers [5, 12, 55, 57, 58].

The local geometry of the part and the melt pool surrounding material (powder versus fused solid) and are two influential factors on the local heat transfer from melt pool. Geometry of the part can mainly affect input energy and heat transfer in three ways:

1) The amount of input energy depends on the received laser energy which is a function of laser power, scan speed, and the exposure time. Although in a calibrated process the laser power and scan speed are kept at optimal values, the exposure time may change at points of deceleration and acceleration of laser beam which happen at ends and beginnings of each scan path or more importantly at

acute and sharp corners which are determined by geometry of the part [5, 9, 59]. Examples of defects formed at sharp corners are given in Figure 10.

2) The amount of heat transfer depends on the heat conductivity of the surrounding material. Considering the fact that heat conductivity of metal powders are about three orders of magnitude lower than that of solid metal, how the heated zone is surrounded by powder or fused solid material has a significant impact on the heat transfer. The first path in a layer (usually the boundary contours) as well as the scan paths on the boundaries of a connected region are surrounded by the largest amount of powder compared to the internal scan paths which are adjacent to the previously fused paths. These factors disrupt the heat transfer and cause defects at these regions (see Figure 11). A common defect caused by this disruption is the elevated edges in the parts made by L-PBF [60].
3) Another important example of the area surrounded by large amount of powder is the overhangs where the new paths are scanned over the powder with no substrates (see Figure 12). The first layer of complicated geometries that should be made with no initial substrate is another case considered in this category [5, 12, 55] .

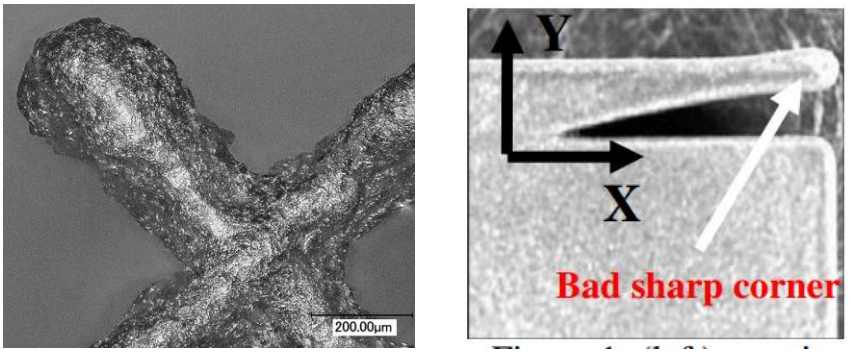

(a) (b)

Figure 10- Nonuniform powder fusion and defects formed at sharp corners: (a) [5] , (b) [9]

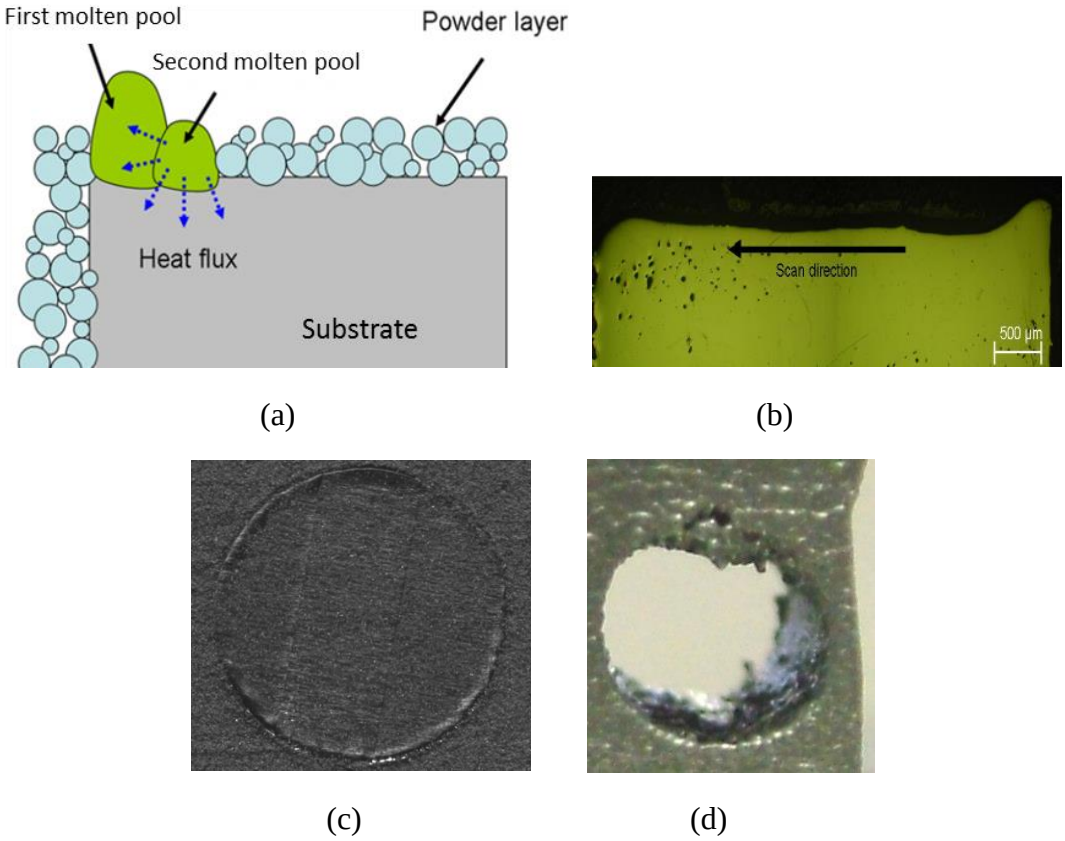

Figure 11- (a) A schematic view of heat transfer from melt pool to its surroundings for first and second scan paths [5], (b) An example of a resulted elevated edge [60], (c) elevated edges at the contour of a circular object [12], (d) a defect caused by disrupted heat transfer at the boundary of the object [9].

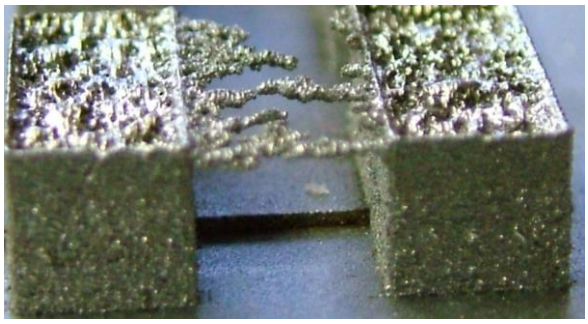

Figure 12- Defect in making a bridge due to overhang [9].

Although nominal parameters are chosen through process calibration, there are a lot of process irregularities and undesirable effects, such as fluctuation of laser power and laser focus, in addition to effects of geometry variations, alter he input energy density and make the process deviate from the nominal conditions leading to formation of defects and geometric errors. Random errors in laser power and laser focus, which change laser intensity and laser spot area, and decelerations and accelerations in scanning speed, also have significant influence on melt pool. Variations in melt pool size, area, and shape, and the amount of resultant fused powder cause formation of pores and lack of fusion (as in cases of insufficient or excessive energy input) as well as undesirable excessive fusion [12, 31, 61].

In addition to parameters that affect the input energy density (laser power, scanning speed, and hatching distance as well as powder layer thickness), other parameters such as powder characteristics, such as powder grain size, voids in powder grains, low-temperature alloys ingredients, may cause formation of defect and pores. Powder non-homogeneities and powder deposition non-uniformities (as due to coater ware), can also affect the melt pool, and the amount and shape of the fused powder that may lead to defect formation.

Another source of defect formation is mass transfer phenomenon e.g. by coater or spatters from melt pool. Process environment e.g. inert gas concentration or the concentration of the remaining oxygen in the chamber affect part quality through oxidation and producing itching regions (see Figure 13). Scanning strategy (see Figure 14) and preheating as well as design of support structure also have determining effect on exciting or preventing formation of defects. The influential factors and parameters on formation of defects have been discussed more detail in [47-51, 53, 61, 62].

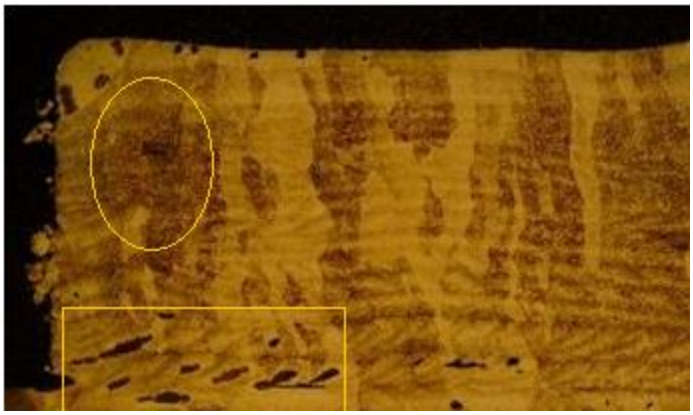

Figure 13- Example image of darkly etching regions formed due to oxidation [51]

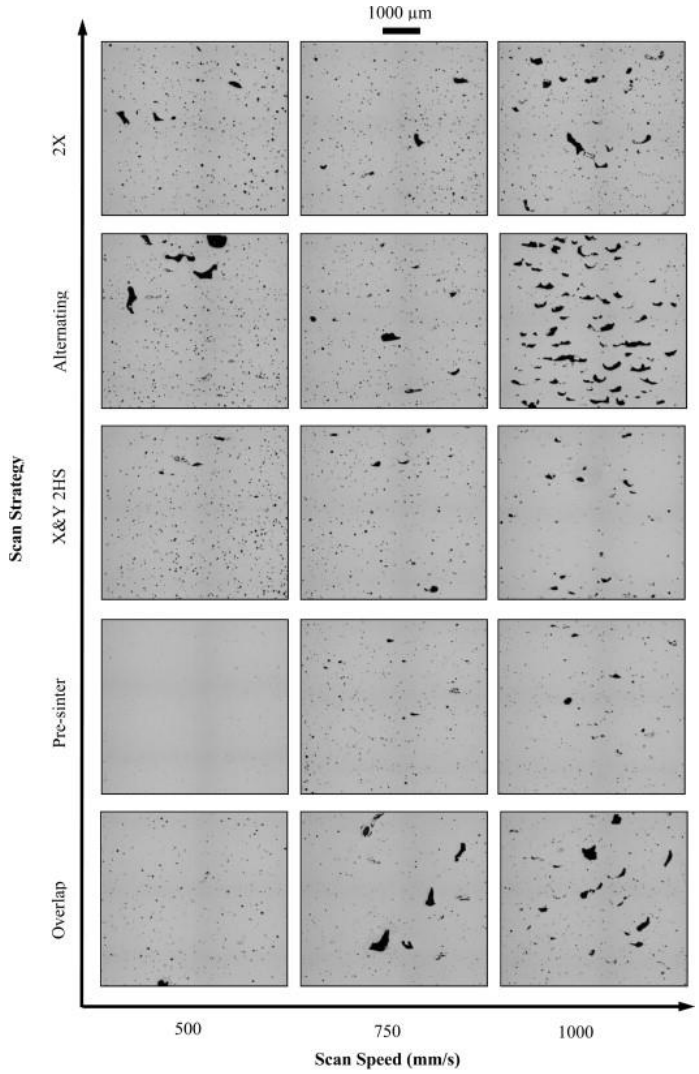

Figure 14- CT scans of porosity in parts made by L-PBF. Images illustrate the effect of scan strategy on formation of pores at different scan speeds. [63]

Material shrinkage after solidification can be regarded as another source of defect formation which affects dimensional accuracy. The exposure to high temperature variations, the resulting expansion and contraction which are an indispensable part of laser powder fusion bring about a high chance of formation of different types of defects such as voids and cracks [5, 12, 31, 61, 64, 65]. The defects formed in a layer also interfere with deposition of a uniform next layer of powder that causes the propagation of defects to next layers. All these defects deteriorate the final product quality and mechanical properties. Any undesirably fused and distorted solidified regions due to the aforementioned defects also cause deviations from the true edges and dimensions, resulting in a relatively low dimensional accuracy and precision. Therefore, to insure fabrication of defect-free parts of desired quality by L-PBF, it is necessary to consider procedures that control the process, and prevent formation of defects and or fix defects in layers during build up.

2.3. Quality Monitoring and Control in AM

Figure 15 shows a flowchart of the current commercial AM machines. As seen, after the whole part is made and post-process, a final quality control is performed. This quality control is mostly through a final visual inspection and is limited only to the exterior of the part. To inspect the internal structure, non-destructive examination such as CT-scanning is required. However, this is a very time-consuming and expensive process and it not performed in practice.

Figure 15- Flowchart of the AM process on the current commercial AM machines.

In order to improve part quality, different build strategies and approaches have been tested and practiced. These include the strategies or techniques that are open-loop actions known to have preventive or corrective effects. Surface remelting, scanning strategies (e.g. changing scan paths orientation or direction in alternate layers), preheating of the platform, as well as design of more appropriate support structures are among the techniques that can help prevent formation of defects or to correct partly the formed superficial defects in the current layer such as surface cracks and pores, and lack of fusion especially between scan lines [55, 58]. These techniques have usually been used regardless of any online observations about irregularities occurring or defects formed and are applied to the entire layer; they are applied based on the knowledge gained from previous observations made at the buildup of parts of similar geometries.

Another open-loop defect preventive action that is more fundamental is control the main source of defect formation which is the net energy density. The net energy density is a function of the input laser power (which is a function of laser power, scan speed, and the hatching space) and the heat conduction from the treated spot. As mentioned earlier, the heat conduction is significantly impacted by the geometry of the part. Therefore, one way to control the net energy density is to vary and adjust the input power, laser power or speed based on variations in geometry according to a previously-found correlation, rather than using constant optimal parameters all throughout the process. For example, use of appropriately-lowered laser power in first contours in each layer, at overhangs, and acute corners can prevent formation of corresponding defects. This technique which is an open-loop control scheme involves determination of process parameters, prior to the build, for each specific geometric feature of the part by experimental calibration [6] or prediction of heat conduction [11].

Although these open-loop approaches have improved the builds, they provide no means to make sure if the part is in fact being built as desired without forming too many

defects and errors. Online monitoring and control of the part or process, however, helps make sure that the process and the part quality are monitored and under the control throughout the build (see Figure 16). Unlike open-loop strategies which do not need any feedback from the build process, online approaches that receive feedback from the part as it is built.

Figure 16- Flowchart of AM process with online quality monitoring and control.

The online quality control approaches can be divided into two categories:

1) Real-time process control that serves as defect preventive actions
2) In-situ quality inspection (or in-situ defect detection) that can be used for both preventive or corrective actions

While there is an extended amount of work done on real-time process control over the past two decades, the amount of work on in-situ quality inspection is very limited and the work is very preliminary. The next two sections extend these two approaches.

2.3.1 Real-Time Process Control

Since the energy density and quality of laser powder fusion process are two very influential factors in defect formation, a fundamental technique to prevent defect formation is to monitor physical aspects of powder fusion process. This approach involves real-time control of physical parameters that are measures of net input energy and quality of powder fusion and/or are known to have direct influence on formation of defects. Monitoring melt pool area is an example of these techniques that has successfully been adopted from laser cladding. Monitoring and controlling physical parameters, such

as melt pool shape and size, or heat-affected zone mean temperature and gradient, have also been practiced [6, 11, 64, 66-69].

The control technique usually involves the control of physical parameters, referred to as process variables, by appropriately adjusting a process parameter, control input, such as laser power or scan speed, based on the received feedback from the measurements of the process variable. The control process parameter was normally chosen as the laser power for simplicity of adjustment, and the process variable was usually a measure of melt pool area, dimensions, or temperature.

The melt pool is usually specified in different ways, which does not necessarily represent the true melt pool. The measured area, dimensions, or temperature of a defined melt pool are usually representatives of these variables for the true melt pool. For example, a photodiode outputs a mean intensity of the area in field of view which covers the heat-affected zone as well as the melt pool; this quantity has been used both as a measure of melt pool temperature [11] and melt pool area [6], justified by the existence of a close correlation. Pyrometer signal has been used as a measure of melt pool temperature [70]. The signals for melt pool dimensions are determined from melt pool imaging by a digital (infrared) camera [9], or an image taken from a visual camera [66].

There are many implementations of melt pool monitoring for laser powder fusion in LPBF as well as laser powder deposition. Hu and Kovacevik, [66], implemented a real-time feedback controller for melt pool area in laser metal deposition by adjusting the laser power; the feedback signal is a measure of melt pool area calculated from an infrared camera image. They accomplished to make a wall of constant thickness which was not achievable without feedback control. Craeghs, et al., [6], used a photodiode and a near-infrared CMOS camera to monitor the melt pool in L-PBF; melt pool length, width and area are measured from CMOS camera. They were able to produce square blocks with much smoother surface with negligible overfusion and pores compared to the case

where no feedback control was used. While the control of melt pool length to width ratio was also considered important to control, only the melt pool area was controlled and the photodiode signal was used as a measure of area for feedback signal due to its faster availability. Laser power was chosen as the control input. It was suggested that use of both laser power and scan speed give more capability of control if several parameters of melt pool are to be controlled.

Kruth et al., [9], also monitored melt pool area in L-PBF, but both photodiode signal and area calculated from CMOS camera were used as process variables separately in two separate control setup. The control input was selected as laser power. The result of real-time process control showed significant improvements for fabrication of a structure with overhang in both control setups compared to constant laser power. They also achieve better precision in making parts with a (square or circular) hole.

Bi et al., [65], integrated a pyrometer to the powder feeding nozzle in laser metal deposition for real-time measurement of melt pool temperature. They studied the effect of geometry on the melt pool temperature where their results showed that the geometry of the parts affects the melt-pool temperature, especially where the heat dissipation is strongly limited. They therefore adopted melt pool temperature as their process variable; the control input was chosen as laser power. A path dependent target value for melt pool temperature was also considered. They showed that with the path-dependent process control, the dimensional accuracy of the deposition can be significantly improved.

Although real-time process parameter control has produced higher quality products compared to the case where they are not used, there are some researches that support the fact that real-time process control has some drawbacks in preventing defect formation even if done perfectly. Some modeling suggests if the power reduction is postponed to the time an increase in melt pool size begins to occur before (as is done in feedback control systems) melt pool size cannot be effectively controlled (in the approach

of free edges) [67]. Additionally melt pool is not always correlated with defect. Also voids smaller than melt pool dimension seem not to have much to do with melt pool. Not any defect formation is captured by the melt pool behavior [11]. Therefor there is a need for in-situ quality inspection that addresses the defects directly. In-situ quality inspection requires a fast and frequent inspection of the part which would only be possible by automatic inspection. Therefore automating the in-situ inspection task is another aspect of the studies in this area.

2.3.2 In-Situ Quality Inspection and Defect Detection in Powder-Bed AM

In-situ quality inspection involves the in-situ detection of defects and errors formed in the part (or possibly some other errors and irregularities in the set-up) rather than the fusion mechanism itself. This can be thought of as a direct quality monitoring where the defects are addressed directly in contrast with monitoring of physical parameters to prevent defects.

Benefits and Advantages over Existing Real-Time Process Control

In-situ defect detection serves in several important ways:

1) Once irregularities and defects are detected, the sources of the detected irregularities that are usually undesirable process parameters or errors in the setup mechanical systems can then be identified and fixed. Based on the known correlations between defect and process parameters (studied in process monitoring researches), once defect are detected in situ, conclusions about the appropriate choice of process parameters can be drawn. For instance, if a specific type of defect such as pore persists occurring, it may be concluded that the laser power should be increased or hatch spacing decreased or a combination of some process parameters adjustment must be done. This is more of a quasi-real-time process control similar to which has been suggested in FDM [71], but has not been seen or implemented in L-PBF.

2) It allows to automatically calibrate process parameter with defect formation without time-consuming manual examinations or through performing destructive tests.

3) The detected defects can be corrected during the build while they're still accessible. Corrective actions can be used such as those strategies (e.g. remelting) that so far have mostly been implemented in an open-loop fashion.

4) If defects are detected early during the process, it allows for ability to make early decisions on stopping the process, discarding the part, continuing the build, or fixing the defects.

5) It provides an assessment of part quality, roughness, internal defects, and dimensional aspects.

6) A true model for the as-built part can be produced for in-situ layerwise information of defects that can be used for simulation, estimation of mechanical properties, evaluation, and demonstration

2.4 Past and Concurrent Work on In-Situ Detection of Defects and Geometry in Metal Powder-Bed AM

Despite a large number of researches on real-time process monitoring, very few works have directly addressed the defects in part by L-PBF [12, 31] in order to provide useful information on part defects for online quality monitoring, assessment, and control. Most research conducted on the study of part defects have been focused on the effect of parameters on defect formation. A lot of work on real-time process monitoring or defect inspection in powder-bed AM are also focused on the inspection and detection of process defects or part defects that are critical to process continuation or quality rather than the part defects that directly determine part quality (such as pores).

For the purpose of real-time (process or defects) inspection, various technologies and sensors have been used or identified useful. Applications of CT scan or acoustics

have been performed to study the defects or for off-line defect detection. Although, some researchers have discussed the capability and research plans for application of acoustics for automated in-situ defect detection [72], CT scanning seem to be feasible merely for offline inspection. Other physical aspects associated with process errors or defects have been used for real-time process monitoring, such as detection of abnormal vibrations of the coater or the machine to detect coater collision with the part elevations [63, 73], and application of impedance to inspect defects [74].

However, there is a larger amount of research performed on thermal monitoring in process monitoring in powder-bed AM both for inspection of the process stability and detection of defects due to the effect of melt pool irregularities on defect formation or different thermal properties of defective areas. Since thermal monitoring has partially proved effective for defect inspection and it also mainly uses (2D) thermal imaging and some basic image processing, this topic will be addressed separately in the Subsection 2.4.1. Application of visible-light imaging for (manual or automated) inspection in powder-bed AM has been addressed in a very limited number of researches as recently as 2010, with the majority of this work conducted concurrently to this research during 2013 to 2016. Visible-light imaging which would then require application of more complicated image processing for automated efficient inspection, is addressed in Subsection 2.4.2.

2.4.1 Thermal Imaging for In-Situ Defect Inspection

Some researchers used the concept of melt pool monitoring to study the correlation between melt pool thermal behaviors to formation of defects. Craeghs et al., [64], used melt pool monitoring to detect only presence of one case of defect. They mapped the melt pool intensity data on the x-y grid of the part and observed that the melt pool irregular behavior corresponds to a defect namely curl-up of the part surface. They used an observed irregularity in the mapping of the melt pool data to detect a defect, but by using prior knowledge about defect from examinations. They did not characterize the

melt pool irregularity that signifies the defects. Nor did they discuss any automated detection of such irregular melt pool behavior.

Clijsters et al., [11], used the mapping of the melt pool data on the x-y grid of the part to investigate the correlation of pore formation and position, and the melt pool data (Figure 17). However, as it was seen in their results, despite some correlation, there are many regions that irregularities are observed but no defects formed, and many regions that defects form where no irregularities signify them. They also tried to verify the correlation by visualizing the defects by CT scanning of the part. According to authors, there are regions of the melt pool variations that are visible on the mappings which do not induce any defects visible on the CT image.

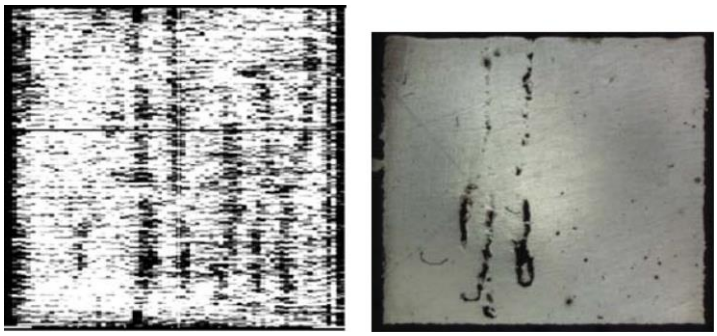

Figure 17- An example of comparison of melt pool mapping (left) with microscopic image of the layer (right) from [6]

Santospirito et al., [72], used theoretical modeling of laser heat source and heat conduction to simulate melt pool temperature for a part having a theoretic 30 micron pore. They observed the temperature decay was abnormally slow close to the pore location. To estimate the defect size, the temperature of the melt pool at the lapse of a certain time was calibrated versus the defect size. However, this work was all numerical and performed on only one simulation. In the same work, authors used ultrasonic to detect a defect (hole) by visual inspection i.e. no automated detection. No result on quantification of the hole was given.

Barua et al., [13], used thermal imaging to detect cracks and porosities in laser metal deposition. They developed a vision system to detect any thermal abnormalities which might signify the presence of a defect. They used an IR camera to obtain images of the deposited track behind the melt pool and approximated the temperature. They studied how a crack or porosity leads to an increase in temperature around the defective region. They generated a 1/64 inch long crack (Figure 18) in the part and observed that an abrupt change in thermal distribution was associated with a crack that could be used to detect presence of the crack. They also drilled 1/800 diameter holes to simulate pores. They observed pores cause concentration of heat around the void. The detection in this work was performed in a reverse order i.e. given a whole (not layerwise) defect, sensor measurements were studied. The technique was not used to detect defects. No information of defect characteristic such as shape, exact location, and size was given. Only two cases of simulated defect were studied (Figure 18). No true defect was addressed. No discussion on the capability of in-situ or layerwise inspection was made.

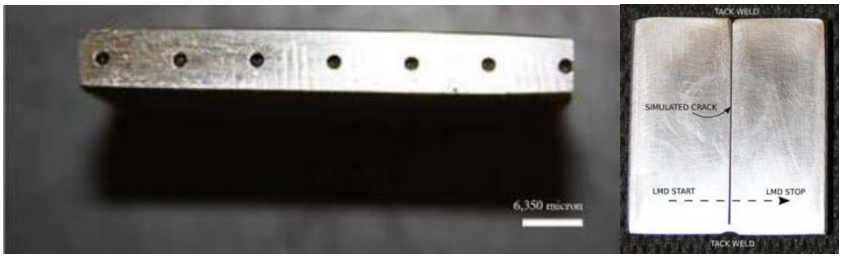

Figure 18- Generated pores and crack [13]

Schwerdtfeger, [75], used IR imaging of the entire of each layer during electron beam powder-bed AM to detect the pores. He compared the IR images after contrast enhancement with visual camera images. The result showed rough correlations for the existent pores between the thermal images and true visible pores in the camera image (Figure 19). However, still significant mismatching of pore locations exists and some defects were not detected or detected as merged. The shapes of detected pores do not

represent the true shapes of pores either. The severity of defect in terms of depth and size is not correlated with the detection results. Additionally, the binary image contains detected objects connected to the boundary that do not correspond to pores. Due to the low-resolution of the imaging, the smallest defects that can be detected are in order of millimeter (1000 microns). It is not studied and known whether or how a higher-resolution thermal imaging would provide a more precise and one-to-one correlation with pores.

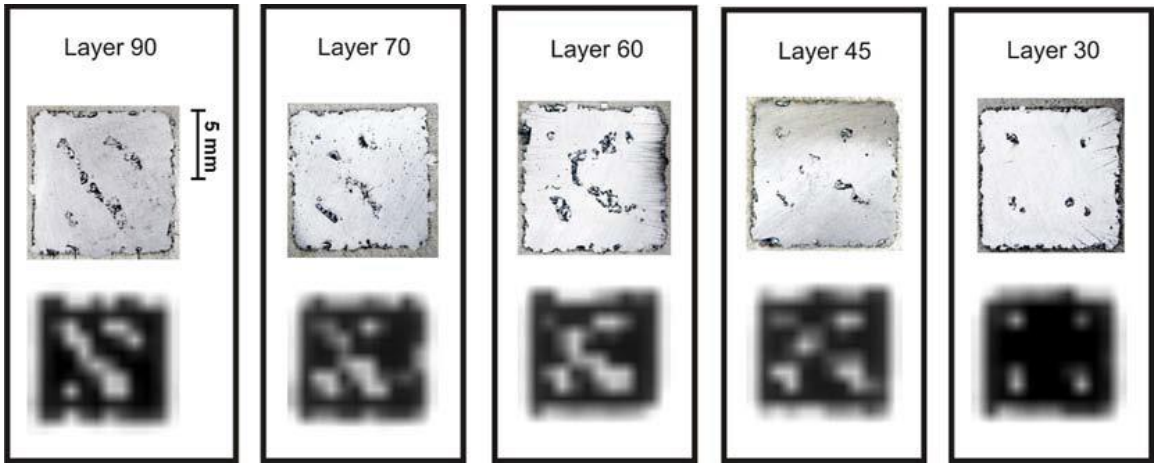

Figure 19- IR imaging for detection of pores [30], top: visual images of layers, bottom: IR imaging results after selected thresholding

2.4.2 Applications of Visible-Light Imaging and Machine Vision in In-Situ Inspection in Metal Powder-Bed AM

Automatic defect detection from 2D measurements (especially visual images) has extensively been used for quality control in various industries such as sheet and surface, weld, ceramic, glass, wood, fruit, and textile. The significant challenge in defect detection is to capture clear images and develop image segmentation algorithms to detect defects accurately enough from the images [18, 20-22, 76].

Online defect detection from 2D images has been used in FDM to detect the two most significant types of defects, i.e. overfill and uderfill. In FDM, the important defects are seen in these two forms (overfill and underfill) which can more straightforwardly be detected by visual images since they correspond with deviations from smooth regular scan paths of the fused deposited material. The results of defect detection can be used in part quality assessment. They can also provide information for defect corrective actions that include (off-line) polishing of the overfills and refilling the underfills. Implementation of a fully online defect correction system in FDM has been suggested but there is no report of its implementation [71, 77-80]. In a recent work, [81, 82], an initial work on design of an image processing software for in-situ detection of the geometry of the built part in FDM was performed that achieved partial success in detection of the built part from the background. Thresholding was used to detect the built object from the background in images captured using a camera imaging from the front view of the machine. Imaging from the build view and detection of the cross section of the build were not attempted.

In-situ defect detection in powder-bed metal AM using imaging and MV is by far a much more challenging task compared to FDM. This is mainly due to the differences associated the material and process characteristics as well as the physical limitations in L-PBF that prevent capturing clear images. Some of the challenges associated with material and process in L-PBF are low contrast between the metal and the formed defects, the very small microscopic size of defects, the difficulty with provision of uniform and efficient illumination with producing no shadows, large variety of shapes, sizes, and forms defects can have, etc. These challenges will be further identified and discussed in CHAPTER IV of this dissertation.

There is a small amount of work that deals with online detection of irregularities and defects in metal powder-bed AM using MV. Although thresholding has been applied

to extract melt pool from local thermal images to measure melt pool area and temperature for feedback control, this basic usage of image processing for extraction of melt pool for other analyses is not considered in the scope of this chapter as the application of MV for defect inspection. The work performed by Schwerdtfeger [75], is one of the few works on processing of thermal images for automated detection of part defects (pore). This work was already discussed in Section 2.4.1. Previous work in automated defect detection from 2D measurements (images), as in [75], is merely limited to simple thresholding. Simple thresholding for many applications of visual inspection usually leads to erroneous results or only provides very rough approximations for certain images of very high contrast.

While there is further research needed to be performed on in-situ defect detection using thermal imaging as a continuation of [75], very limited and mostly all concurrent researches have used visible-light camera images for inspection. These works, however, were mostly focused on examination and inspection of process errors, such as damage coater and critical elevations, rather than part defects (pores) and direct geometry. Very few cases of automated inspection, however of process errors (not part defects), exist.

Craeghs et all., [31], used a visual camera to build a powder deposition monitoring system in L-PBF. They detected the effect of a worn or damaged coater that can be regarded as specific type of process error that can lead to part defects. They detected horizontal stripes in the deposited layer caused by the damaged or worn coater. They analyzed a 1-D signal consisting of the gray values across the image perpendicular to the coater motion direction. They designated excessively large standard deviations for intensity variation to deposition with a damaged coater. They also related the abrupt changes that exceed the limits of intensity variation of an ideally deposited powder to locations of coater wear or damage (Figure 20). The results were used in a powder deposition monitoring system to decide if the coater should be replaced or fixed before

continuation of the build process. Although other factors such as part defects (e.g. elevated edges) can also produce intensity changes in the powder bed, they did not discuss how they would distinguish the coater wear effect from the elevated edge effects.

For their imaging system, they used a camera mounted at an angle to cover the build area in the field of view (see Figure 21) that produces perspective aspects. For accurate quantitative inspection, however, their imaging system would require consideration of perspective effects.

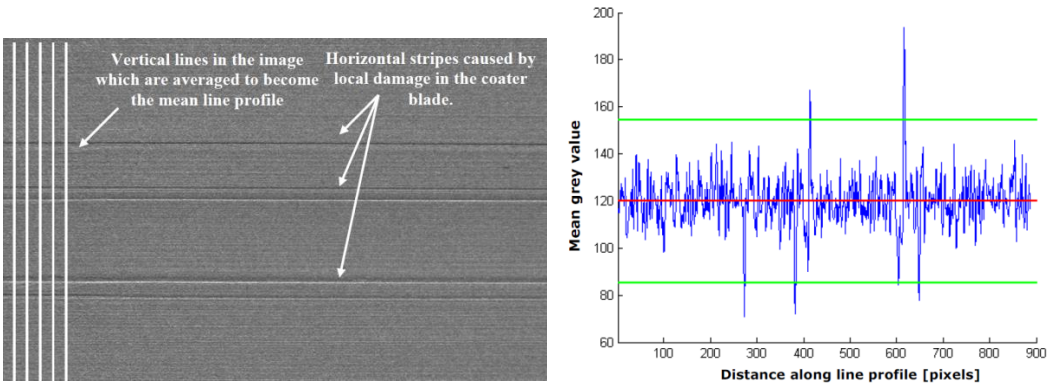

Figure 20- An example image captured from powder deposition and illustration of how abrupt changes correlate to damaged coater [31].

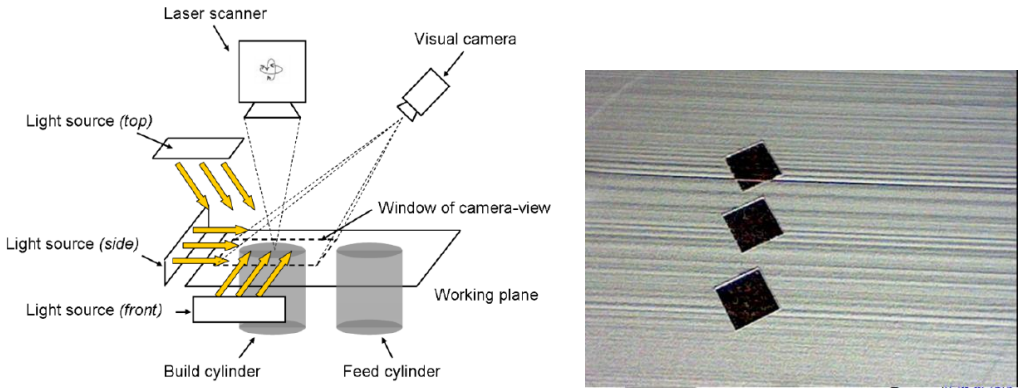

Figure 21- Schematic view of the imaging setup developed in [31] and an example image of the build platform illustrating the perspective effects.

Kleszczynski *et al*., [12], in 2012, used a high-resolution visible-light camera to visually examine process errors in EBM. They studied the effect of support structure, input energy, and powder contamination on formation of elevations at edges and curling effects which they manually observed in high-resolution camera images. No work on automated detection of process errors was performed. No inspection of 2D geometry was performed; nor were defects such as pores addressed.

Their high-resolution images were captured from a camera mounted outside the EBM machine looking through the window. The resulted perspective effects were removed by camera calibration. Produced images were of size 4234×4234 pixels and the achieved pixel size was 24 microns. Images visualized the surface features in terms of texture and roughness, however small features such as pores were not visible.

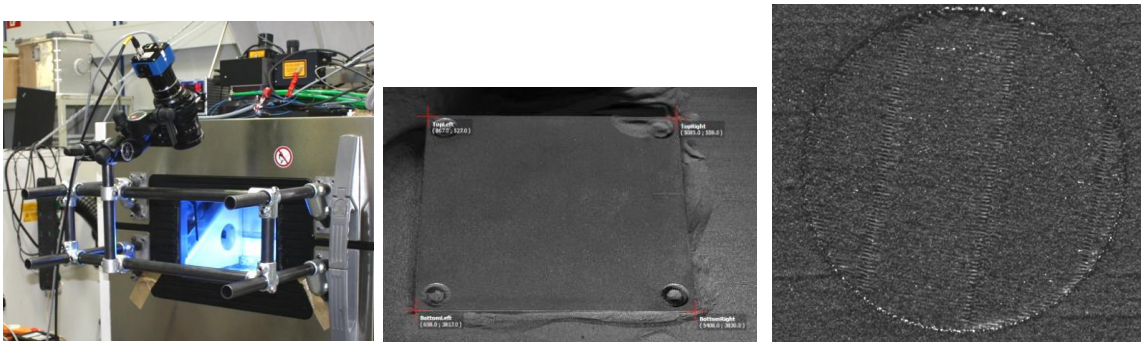

(a) (b) (c)

Figure 22- (a) Illustration of imaging system used in [12] with the camera mounted outside the machine, (b) illustration of perspective effects in images captured from build platform before corrections, (c) an example image of a EBM build after correction of perspective effects and intensity rescaling for better visualization.

Concurrent Research

Concurrent to this PhD research, from the same research group by Kleszczynski in 2013, [32], they used the imaging setup in Figure 22 (a) where the camera was mounted on a tubular fixture connected to the machine. They used two light sources to produce pictures of the build. A 29 megapixel camera was used that produced 6576×4384

pixel images. After camera calibration, they achieved (on part) pixel size of about 24 μm. They captured images after build and after powder deposition. They applied thresholding image of powder deposition to detect elevated regions of the build that stick out of the deposition and may cause problems with the process. They also inspected parts defects (pores) using CT scan and made the general observation that with increased energy, porosity increases. Although the camera images visualized the build and its texture (Figure 24), the images did not show pores despite existence in the part.

Kleszczynski *et al.* performed similar research in 2015, [33], where they used thresholding to detect elevated regions as in [32]. They further analyzed the binary image and measure the elevated region area as a quantitative measure of laser beam melting process stability.

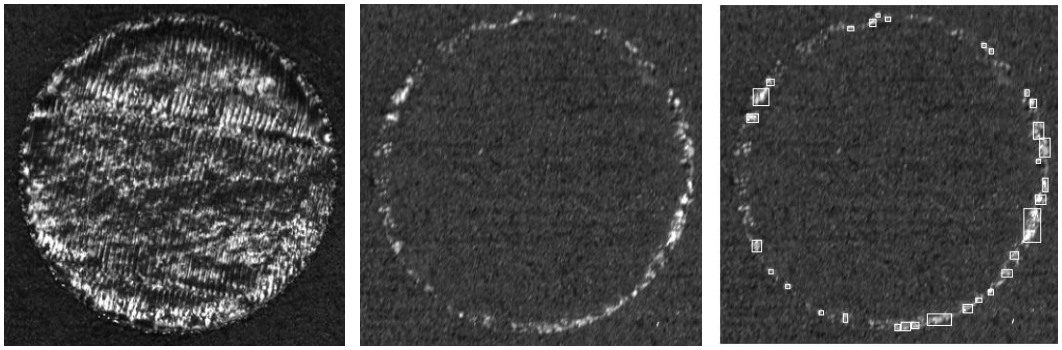

(a) (b) (c)

Figure 23- (a) Camera image (after intensity rescaling) of the build, (b) camera image after powder deposition, (c) result of thresholding of (b) that signify elevated edges.

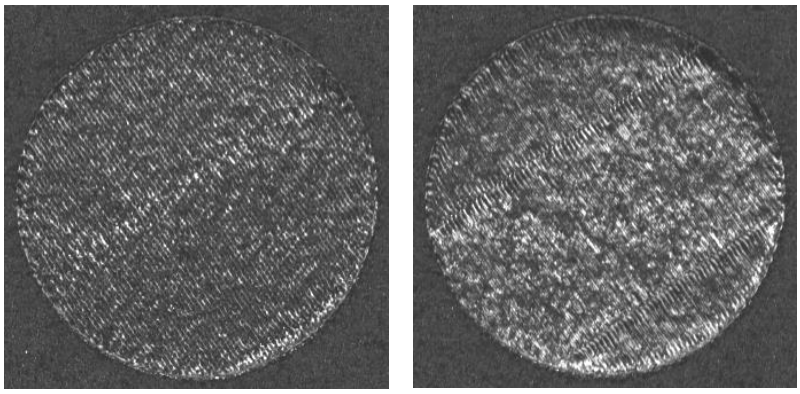

Figure 24- Examples of camera images (after intensity rescaling) from EBM parts from the imaging setup in [32].

In another work in 2013, concurrent to this PhD research, from the same research group, Kleszczynsk *et al.* studied the effect of various process errors on variation of mechanical properties of LBM components [52]. They used same imaging setup (Figure 22 (a)) for visualization of part surface built by different process parameters (see Figure 25). They captured high resolution camera images from which they manually examined the fusion and the weld seam connectivity. They also took microscopic images to visualize the detailed part texture. Figure 26 shows zoomed-in views of camera images in contrast with microscopic images. Both images visualize the surface beams (with different resolutions though). However, as seen, the camera images do not match the microscopic images and they do not show same features.

Although, the camera images visualized surface features, they did not perform any automated detection from camera or direct microscopic images which could be related to two facts: the high level of complexity of detection of an object of interest in these images due to the complicated surface texture, the lack of visibility of individual defects in (camera) images. Instead, in the same work, [52], they applied simple thresholding to micrographs from the finished and cut cross sections of the build to approximately measure porosity. As seen in Figure 27, the photomicrograph from the cut and finished cross section clearly shows pores. However, capturing such images would

require cutting and finishing the part and therefore is not possible for real-time monitoring. Basic thresholding with a constant value has also been applied to similar micrographs by destructive examination of parts by other researches such as in [48, 50, 83].

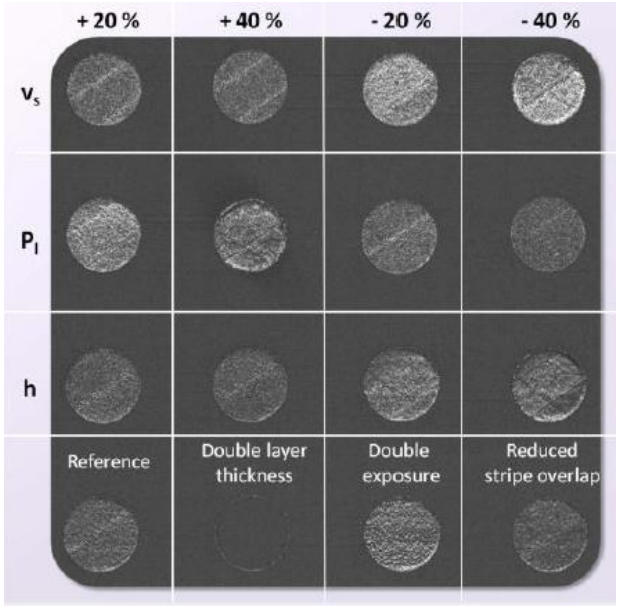

Figure 25- High resolution camera images taken from parts made with different process parameters. Vs is scan velocity, P is laser powder, h is hatch spacing. For more details, see [52].

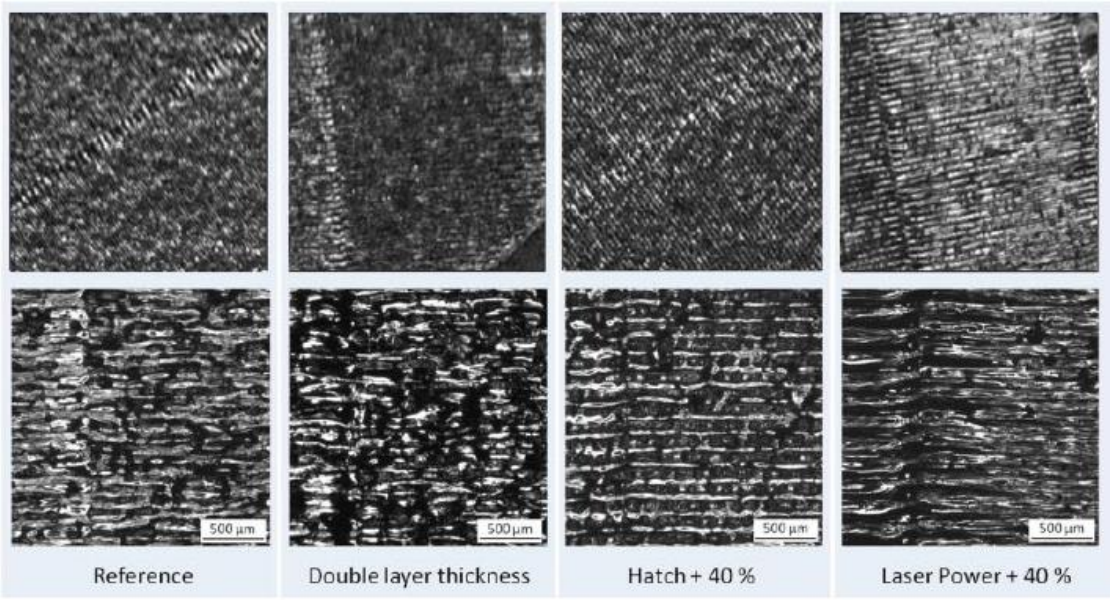

Figure 26- Comparison of selected high resolution (top) images vs. images taken from microscopy (bottom) see [52] for more details.

Figure 27- Photomicrograph from selected test specimens [80].

In 2014, Kleszczynsk *et al*., [84], evaluated the uncertainty in their imaging setup (Figure 22 (a)) imposed to image spatial coordinates due to the vibration of the camera and the variation it causes in camera orientation. They reported their images' pixels size on part between 20µm to 32 µm depending on the field of view. They found that spatial acquisition error can reach a maximum distance of 4.91 pixels (156.1µm on the part).

They regarded this error significant for inspection of LBM parts. They suggested the error could be reduced if camera calibration be performed in each layer during the build.

In another work, (published) in August 2015, Kleszczynsk *et al.*, [85], performed a study on surface roughness which they measured using a contact surface profilometer. They used their high-resolution imaging setup (Figure 22 (a)) merely to document the process and to visualize and manually examine the features associated with part surface and edge smoothness (see Figure 28). However, they did not make any discussion on how visual images can help with any assessment of surface roughness whether manual or automatic. They also stated that observations on smoothness of edges or parts from images were not apparent in every documented image, which they mentioned might be related to inconsistent illumination and reflections of the molten region. Their high resolution imaging setup did not provide the capability of showing defects and therefore they used micrographs (Figure 29) of the cut part to visualize and examine defects (pores and detailed geometric defects). Their imaging setup as mentioned previously achieves a 25 μm/pixel to 35 μm/pixel resolution [52].

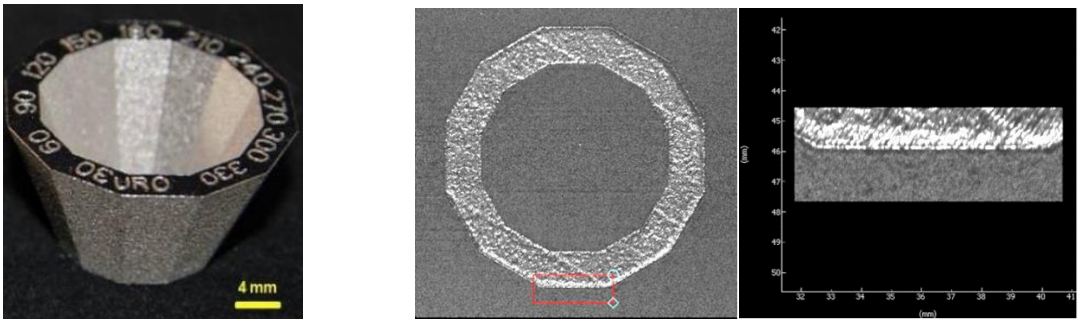

(a) (b)

Figure 28- (a) the geometry made using LBM in [85], (b) a representative image captured from the cross section of the part during build using the high-resolution imaging setup, and a close-up of the marked region in the image.

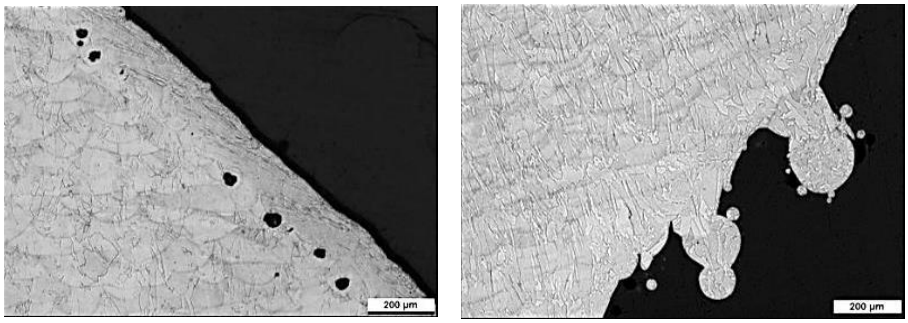

Figure 29- Examples of micrographs captured in [85] to visualize defects.

In another work concurrent to development of the imaging setup in this PhD research, an imaging system was developed by Foster *et al.* [86] in August 2015, with a 29 megapixel camera inside the machine, mounted at an angle from the build platform. The images captured were 7360*4912 pixel and achieved 50 µm/pixel resolution and 15 µm/pixel resolution depending on the utilized camera lens. Figure 30 (a) shows a schematic view of the front view of the machine which showed the location of camera with respect to the build platform. Figure 30 (b) shows an example of a raw image captured by the oblique camera and the resultant perspective effects. Figure 31 shows the result of their study on effect of variation of illumination location on the clearness of images. In Figure 31, each column represents a different illumination setting. The top row shows the original camera image; the middle row shows the zoomed-in views of the marked regions in the top row; and the bottom row shows the specific region (object). No correction of perspective effects has been performed. As seen in the bottom images of Figure 31 the objects and their relative texture are visible but defects (pores) are not visualized.

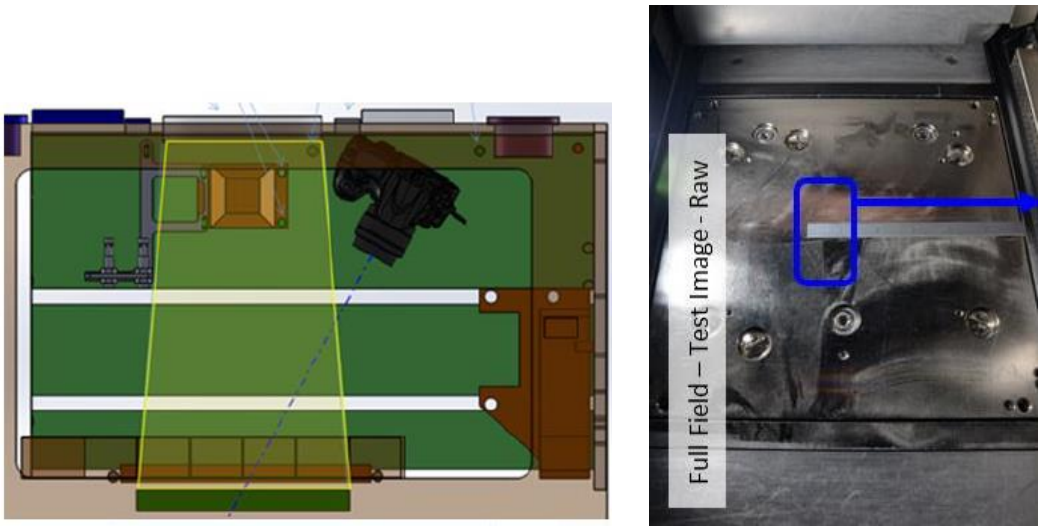

Figure 30- (a) A schematic view of the front view of the machine illustrating the location of camera with respect to the build platform, (b) an example of a raw image captured by the oblique camera and the resultant perspective effect.

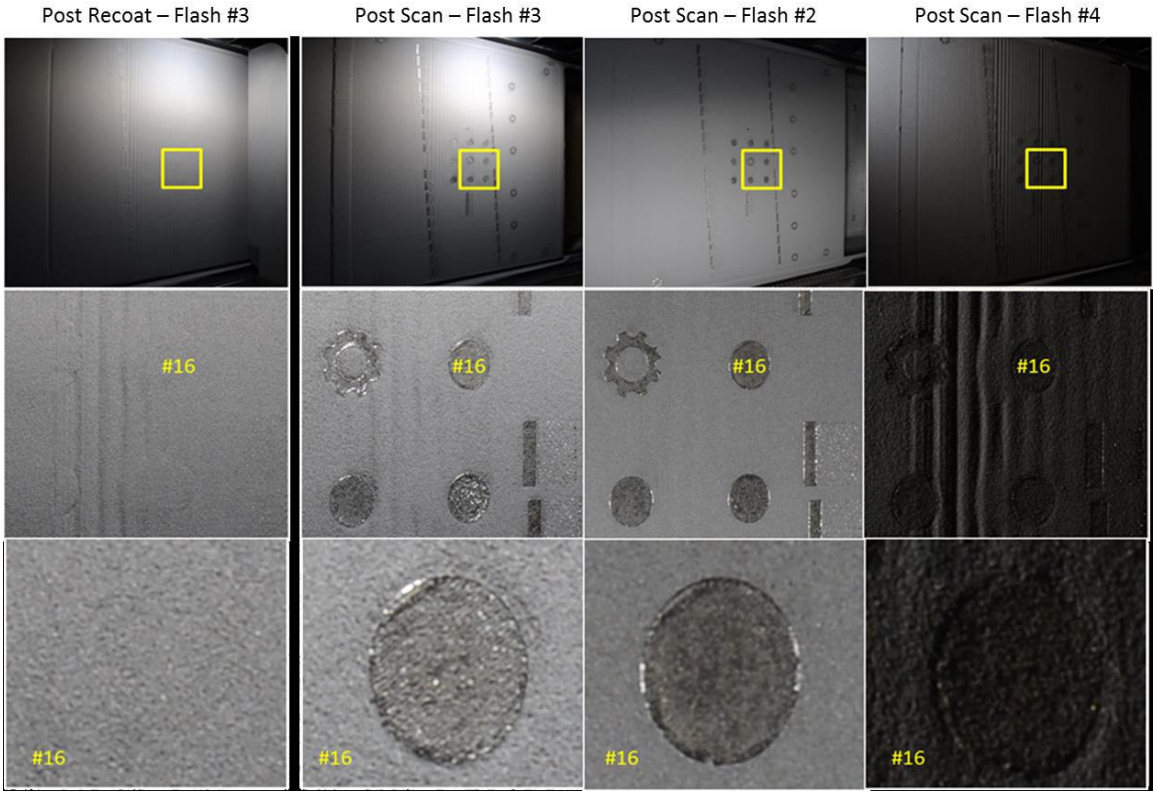

Figure 31- Images captured by imaging setup developed in [86].

In August 2015, Alhwarin *et al*., [87], reported their initial thoughts and an outline for proof-of-concept implementation of a system for post-processing turbine blades during SLM with a drilling robot. In their outline, they suggested using a standard stereo microscope (Figure 32 (a)) to capture images from several layers of the build and use disparity maps to create a depth image of the layer. They suggested applying a constant depth threshold based on layer thickness to the depth image to segment the geometry from the background. They then suggested that this image could be compared with a corresponding layer from CAD model and the discrepancies could be used to design the path for a robotic milling arm.

Figure 32 (a) shows the image of the SLM machine they used for building parts with the stereo microscope mounted on it. Their image resolution was 1392*1040 and covered a field of view of 17mm*16mm leading to a 12.2µm/pixel (on-part) resolution. Figure 32 (b) shows the image captured from the left microscope from a built turbine blade on their machine after powder was removed. No image of the part with the powder was provided. Although their imaging setup provided high-resolution images, no automated image analysis on these images was performed; in fact their suggested layout was all computer simulated and for simulation, they used a virtual RGB-D camera images captured from the CAD model which by no mean represent the actual images and image analysis.

Based on their discussion on thresholding by a constant value related to layer thickness, it seems that they assumed no powder would exist around the fused geometry which by far disagrees the real manufacturing process. The only way to distinguish the fused geometry from the surrounding powder based on depth, is the depth difference due to material shrinkage after fusion. They provided no discussion on whether their actual

stereo imaging system would have the capability to measure depth of one layer thickness or sub-layer-thickness (due to material shrinkage).

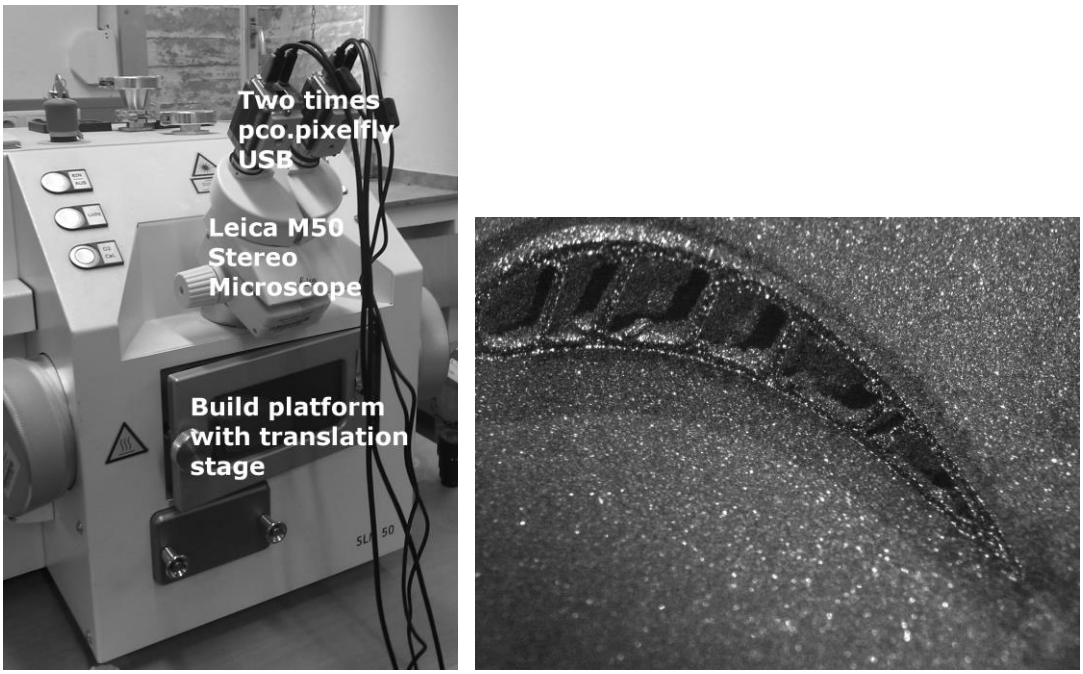

Figure 32- (a) the SLM machine used in [87] with a standard stereo microscope imaging mounted on it, (b) image captured from the left microscope from a built turbine blade on the machine after powder removal.

Due to the novelty and large potentials of AM, the technologies in this field are rapidly developing. This subsection presented the first to the most recent (reported) work on application of visible-light imaging in powder-bed AM. It also included the work that was developed concurrently (2013-2015) to conduction and publication of the results of this PhD research. Based on what was mentioned in this section, the work on application of visible-light imaging for inspection of powder-bed AM is at the very early stages of development. No work on automated inspection of cross-sectional geometry from 2D images has been seen reported so far; no segmentation algorithms with their results for this purpose have been described and evaluated. No visible-light imaging setup has been reported to show pores and microscopic defect parts visibly and no work on automated

detection of pores from (non-destructive and in-situ) visible-light imaging has been performed by other researchers to the time of competition of this PhD research.

In the next subsection, application of MV for automated visual inspection is described in general and principles.

2.5 Terminology and Principles of Machine Vision for Automated Visual Inspection

Machine vision or computer vision is a branch of computer science that deals with processing and analysis of visual images such that desired information can automatically be inferred from the images. Examples of application of computer vision are face recognition, surveillance, motion and human detection, earth observations, robot guidance and navigation, etc. A very important industrial application of computer vision is automated visual inspection (AVI) for non-destructive monitoring and evaluation. Many applications of AVI deal with detection of defects in parts, components, surfaces, structures and products. AVI has extensively been used in inspection of metal sheets, ceramics, textile, agricultural products, medical images, electronic components, printed circuit boards, weld inspection, etc. [88-93]. AVI uses knowledge from computer vision to automatically detect defects from 2D images using image processing algorithms.

Computer vision in general can be divided into two subsets of basic image processing algorithms for the purpose of detection and decision making, and high-level intelligent algorithms that use algorithms in common with data mining, machine learning or artificial intelligence. Image processing also deals with such sorts of image analysis as pre-processing, filtering, compression, fusion, and segmentation of images. Detection of an object from an image is an example of image segmentation that can be used for decision making. High-level computer vision deals with high-level analysis of data usually obtained from lower-level analyses. For this level, algorithms form machine learning are usually utilized to train the machine to understand the image and draw

inferences or conclusions usually based on analyzing data obtained from lower-level processings. Classification or identification is an example of high-level computer vision [17, 76, 94-96].

In AVI applications, machine vision algorithms are mainly used for the purpose of detection and identification of defects or flaws of some sort in part, surface, or a process. The purpose of object (or defect) detection is to locate and detect the pixels associated with the object of interest. Usually the final result of detection can be visualized in terms of representing the boundaries of objects or a binary image where the detected objects are assigned pixel values of 1 (as seen in Figure 33). While there is variety of schemes for automated visual inspection, algorithms used for design of a general machine vision system for defect detection can be divided into three levels of processing:

1) **image processing and image segmentation**,

2) **feature extraction**, and

3) classification or **identification** [97-99].

Each level has detailed specifications and may be divided into several stages that are introduced and described in the following subsections.

2.5.1. Image segmentation

Image segmentation (or sometimes referred to as object detection) in image processing refers to performing analyses on an image containing an object of interest to achieve a final image (or equivalent information) in which the object of interest is located and selected automatically in the image. For the purpose of low-level object segmentation, usually three categories of algorithm development can be considered:

a) Preprocessing: Denoising and image enhancement

b) Thresholding and low-level image segmentation

c) High-level or model-based image segmentation

In preprocessing, (a), the image is denoised using appropriate filters such as Wiener, median, Gaussian, or averaging. The contrast of an image can be increased using intensity (gray level) adjustment. The image will be improved such that it can better be used for visualization or image understanding.

(b) and (c) consist of algorithms and techniques used for the purpose of **image segmentation**. Image segmentation refers to conducting operation or implementing algorithms to convert a given image containing the object of interest into (usually) a binary image such that the object of interest is white (in the foreground of the binary image) and all other regions are black (in the background). Figure 33 shows illustrations of image segmentation (or object detection) examples where in the resulted images the objects of interest are segmented (detected). In detection or image segmentation, an object of interest in the original image is usually referred to as "object" for brevity and the remaining regions are called background (regardless of the intensity value).

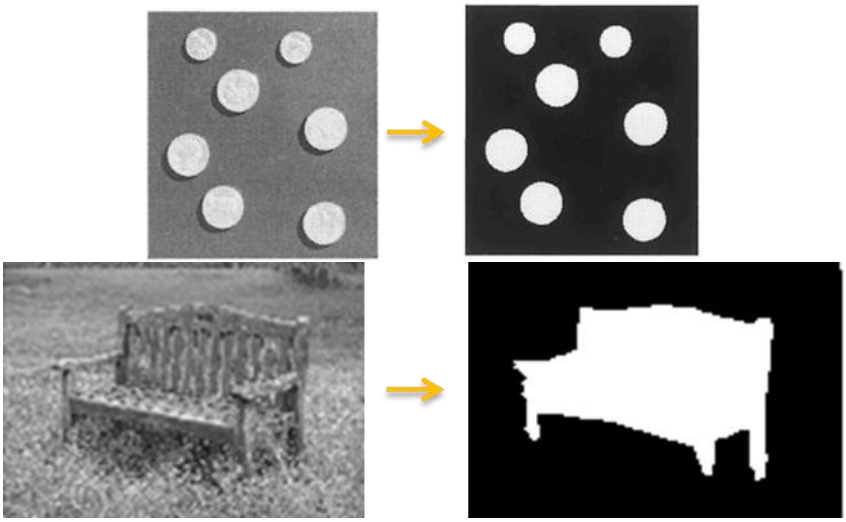

Figure 33- Examples of image segmentation

Although high-level operations such as pixel- or region-based identification can lead to object segmentation, Category (b) for low-level object segmentation consists of low-level image segmentation techniques such as thresholding, edge detection, and some

techniques in background subtraction and morphological operations. These techniques do not require any model or prior specifications of the object to be segmented. This is in contrast with category (c) which consists of model-based segmentation techniques such as Hough transform, pattern matching using correlations, and rule-based segmentation based on a specific characteristic of segmented objects. Using eccentricity value of objects segmented by thresholding to segment lines is such an example of rule-based detection [22, 24-27, 29, 30, 76, 97, 100-116].

Image segmentation techniques based on high-level pixel- or region-based identification fall in the category of intermediate and high-level processing that use intelligent algorithms to identify pixels or regions belonging to object of interest based on extracted discriminators/features.

Unlike human perceptions that segment objects based on synthetics and meanings, machine-based segmentation relies on finding a property or characteristic by which the objects and background are distinguished. This property usually is in form of a specific range of color or intensity, a local property of intensity variations, texture, shapes, etc. Based on these properties, appropriate segmentation algorithms are selected and modified or devised and developed. If such a found property does not have strong discrimination ability, good segmentation results are not usually expected.

2.5.2 Feature Extraction

Sometimes, due to the characters of the image and the object, image segmentation techniques in low-level processing do not yield final accurate detection. Therefore, further analysis is needed to prune or modify the results of low-level processing. This is performed by extraction of specific discriminators (features) from the segmented image and classifying the segmented objects based on these discriminators. This classification can be used for both purposes of identification of true versus false objects as well as classification of different types of (all true) objects as in different types of defects [18, 23,

28, 93, 117-120]. Figure 34 shows an example of object detection using different levels of processing based on object segmentation, feature extraction, and identification.

Alternatively, instead of feature extraction in low-level segmentation results (as in Figure 34), discriminating features can directly be extracted from the original image, for example, based on texture or specific patterns of intensity variations. This is performed by extraction of specific discriminators (features) from the regions or pixels (with their local neighborhood) in the original image and classifying the image regions or pixels based on these discriminators.

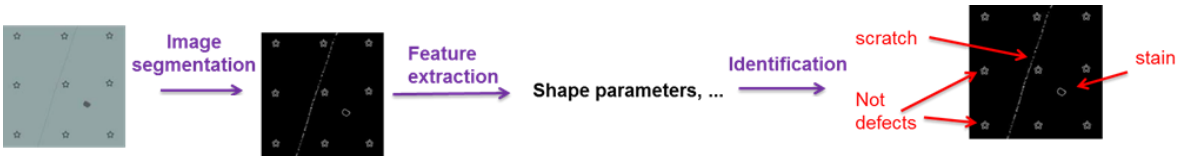

Figure 34- The procedure for detection and identification of defects.

The intermediate level of a MV system, therefore, is feature extraction. In this level, it is required to select several properties that very well distinguish the classes of defects or regions or pixels belonging to defects in a given large database. These features or discriminators should have the following properties:

- have high intraclass correlation and low interclass correlation
- (depending on case) be translation and rotation (or scale) invariant
- have small correlations with each other for best performance
- be as few as possible to be computationally efficient while have sufficient discrimination effect (be selected for principal components)
- can be statistical, geometric, as well as texture features (texture features are extracted based on the intensity of the pixel as well as its local neighborhood in the original image)

Appropriate selection of features should be done based on a comprehensive database containing a large number of objects belonging to all defect classes [99, 121].

The computational load of high-level processing and classification is strongly dependent on the number of features selected in this level. Therefore, it is important to select a few features but of high discrimination effect. To make such a selection of features, techniques for dimensionality reduction such as principal component analysis (PCA) and singular value decomposition (SVD) can be performed [108, 110].

2.5.3. Classification or Identification

High-level processing involves identification or classification of defects based on the features selected in intermediate level. In this level the selected features are used to assign a class to each object, region, or pixel based on similarity of each feature set with that of a class. A comprehensive dataset of object classes with their extracted features is required in order to draw defect models or train a suitable classifier. Defect models can be used in rule-based classifiers, or other sorts of classifiers such as neural network (NN), support vector machine (SVM), k-nearest neighborhood (k-NN), and Euclidean-distance-based classifiers. Probability rules can also be drawn from the database that can be used in statistical classifiers such as Bayesian classifier. Choice of a statistical versus a deterministic classifier depends on the type of data and properties of classes, performance of each classifier, and also availability and size of the database [108, 110, 117, 118, 122].

2.5.4 Remarks on Application of MV in AVI

There is a variety of techniques in computer vision for image segmentation and each technique performs differently. Performance of different techniques depends on the image specifications in terms of true images' characteristics such as resolution, amount of noise, and illumination. The material and defect natural characteristics such as the natural variation of the color, the defect contrast from the background material, and defect size

and form also impact the performance of segmentation techniques. Noisy images with small contrast or unclear borders between the background and objects introduce errors and make segmentation a difficult task.

In many industrial applications of inspection and defect detection in sheets and surfaces, the images of the part or surface to be inspected show a non-uniform variation of intensity and do not have a multi-modal nature. The high level of noise associated with the industrial application or environment, the low contrast between the surface and the inspected defects in the images, and the large variety of defect shapes, sizes, and background textures due to the nature of the application are additional factors that contribute to the difficulty of defect detection in industrial images [108, 110, 123].

Despite many researches on high-level analyses for automatic defect detection and classification, many inspection systems still rely on manual review of defects. Since many defects will be unique to certain products and to certain stages in the product's manufacture, it would be very costly to develop specific defect detection identification systems for each inspection [124]. In other words, most machine vision systems for automated industrial inspection are custom-designed, so they are suitable only for one specific application. Their inherent inflexible and nonversatile structures prevent them from being adapted to other applications, or even adapted to operate on the same application but in a different operating environment [16].

Therefore, for the given task of defect detection in metal AM parts, existent techniques in image processing should be efficiently designed and modified or even new algorithms be developed to efficiently detect defects or fused objects.

2.5 Conclusions from Literature Review and Background

In-situ quality monitoring in L-PBF is an inevitable task for manufacturing high-quality parts. Past work on online quality monitoring was mainly focused on real-time process control based on monitoring physical parameters such as melt pool. Despite

precise process control defects still form in layers. One of the reasons could be the observation that all defects in AM parts are not necessarily associated with irregular melt pool behavior and that not all melt pool irregularities cause defects. On the other hand, automated defect detection provides information about the existence, location, and other characteristics of defects and this knowledge can be used in defect corrective actions, precise 3D quality assessment, and detection of process errors.

Previous defect detection work was very preliminary and did not provide full sufficient information about exact location, shape, and other characteristics of defects. 2D measurements (in form of visible-light images) captured from each layer, if acquired accurately and with sufficient contrast, are a very informative source of information that can be used for automated defect inspection. There is very limited work performed on automated defect detection from 2D images. Among these, either the results are inaccurate and very imprecise or the main purpose of the works is not focused on the detection of defects but rather to inspect process defects (errors) or inspect the simplest form of geometric error i.e. elevated edges. Also, most of these inspections are based on very basic simple image processing such as thresholding. A schematic procedure for development of a MV system for inspection of part defects (pores) and geometric errors, an accurate detection algorithm as well as quantification of performance of the detection algorithms such as precision of detection, percentage of truly detected defects or falsely detected defects are entirely missing in the existing work.

The large limitation of the scope of past work on image-based inspection could be regarded as result of the high level of complexity associated with capturing in-situ, sufficiently clear images as well as development of image segmentation or MV algorithms for analyzing these images for satisfactory results. Developing appropriate segmentation algorithms for detection of defects and geometric fused objects from images of AM layers is a very challenging task.

As was mentioned in Section 2.1.4, Remarks on MV system for AVI, since many defects are unique to certain products, it is very costly to develop specific defect detection and identification systems for each inspection application. The direct quote from [16] is re-stated here to further clarify this point: “Most current machine vision systems for automated industrial inspection are custom-designed, so they are suitable only for one specific application. Their inherent inflexible and nonversatile structures prevent them from being adapted to other applications, or even adapted to operate on the same application but in a different operating environment”. Algorithms from computer vision or other applications cannot be directly applied to a specific inspection purpose. For inspection of each specific type of defect for a specific application in specific operating conditions and using a specific imaging setup, there is a record of development and modification of algorithms to detect defects accurately and precisely. Some algorithms have been tested and identified as ineffective by some researchers and the new algorithms are modifications and expanded versions of the previously developed effective algorithms or are new algorithms. However, for automated detection of defects and geometric objects in powder-bed metal AM, there is no reported prior work and developed algorithms. Therefore, to develop appropriate segmentation algorithms, this research, as the first (seen or reported) MV system for this purpose, would face new challenges and would need to:

1) identify effective algorithms among a variety of existing algorithms, through intuition into the characteristics of the images and performance of different algorithms and mostly by trial and error, or identify similar applications in terms of image and defect characteristics, and identify the most appropriate and relevant algorithms for the similar applications,

2) modify and combine these algorithms and parameterize them by trial and error,

3) find most appropriate algorithms that work best for this application, or even design new algorithms, and finally

6) further modify and evaluate the performance of the final designed algorithms.

CHAPTER III

PROBLEM FORMULATION AND THE AVI FRAMEWORK

In this Chapter, based on the machine vision principles a general framework for a MV system for inspection (detection and identification) of defects and geometric errors in metal powder-bed AM is proposed and described in Section 3.1. Then, a layout of the MV system for detection of the fused geometry as well as assessment (detection or identification) of porosity for the purpose of this dissertation is given and described in Section 3.2. The steps of accomplishing this dissertation research are then explained, and the measures of the quantitative evaluation of these steps are presented in .Sections 3.3 to 3.7. Section 3.8 discusses application of this PhD research work and the implementation of the techniques developed in this thesis to the applications outside of the scope of this thesis in terms of other imaging setups, processes, or material. Section 3.9 presents an overview of the organization of the material presented in Chapters IV to VIII that address the steps of this research as described in Sections 3.3 to 3.7.

3.1 Layout of the Machine Vision System for AVI in Metal Powder-Bed AM

Figure 35 shows a schematic diagram of setup of the in-situ defect inspection system using imaging sensors. This image schematically shows two sensors for producing two image modalities of visible-light images and height maps. Ideally both visible-light images and height maps should be able to provide visual data about the fused geometry and defects. As each layer is built, the optical imagery sensors produce images of the current layer that covers the fused regions as well as the surrounding powder in the layer. If the camera view is not perpendicular to the layer, perspective corrections should be taken. Images of the layer are acquired in the computer and are analyzed for defect

(geometry and defects) inspection. Detected defects are identified with their corresponding locations that can be later used for corrective actions.

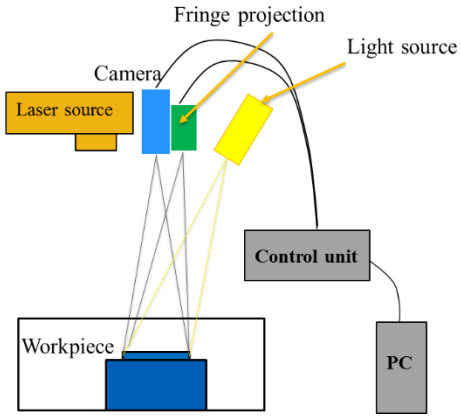

Figure 35- A schematic diagram of setup for in-situ defect inspection system (inclusion of light source is only for illustration, it's not to specify light source location).

The produced images from the powder-bed AM machine contain both powder regions as well as fused regions. To detect defects within fused geometric object, it is helpful to first detect the geometric objects and then limit search for defects within the segmented geometries. Additionally, the results of detection of the fused geometric objects can be used to detect the geometric discrepancies from the target geometry, and consequently detect the geometric errors and dimensional inaccuracies.

Figure 36 shows a proposed outline for the AVI system for inspection of defects and geometric errors. This AVI system accounts for both geometric errors as well as defects. Therefore, two parallel inspection subsystems exist in the combined machine vision system with metrology. Both subsystems have been divided into the three processing levels similar to what was described in Section 2.5. These levels for each subsystem are given in Figure 36. Aspects of both computer vision in defect detection and identification, and metrology in comparison of the objects with target layer model and extraction of synthetic parameters, are involved. Appropriate techniques of both areas can be incorporated when found useful.

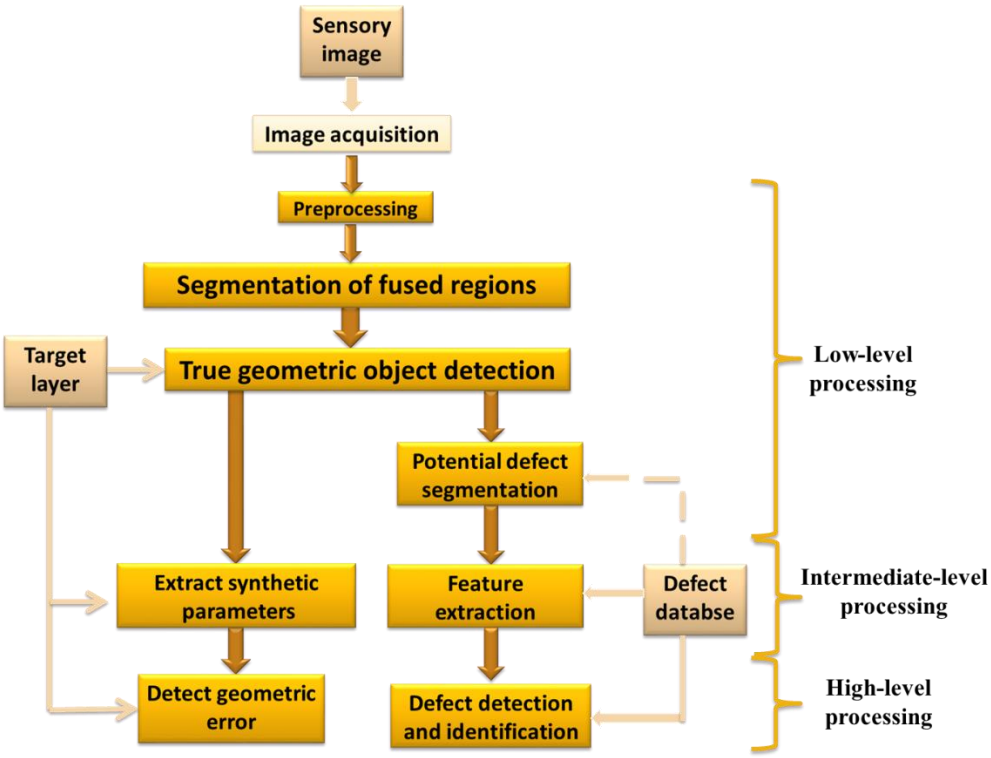

Figure 36 - A schematic diagram of the AVI system including two subsystems of geometric error identification and defect identification.

In contrast with a machine vision system for (surface) defect detection as described in Section2.5, as in [97-99], in the in-situ defect detection system used for powder-bed AM, an additional segmentation step to segment the fused regions is added. Fused regions are in fact regions of interest from which true geometric features versus undesired fused regions are identified. Therefore, in the low-level processing, the fused regions are first segmented from the whole layer. Fused regions that correspond with a valid geometry from the target model are regarded as true geometric objects and those that do not correspond are signified as defects at the very beginning.

True geometric objects, are input to next steps of low-level processing i.e. potential defect segmentation to be searched for defects. Image segmentation techniques are applied to segment the potential defects. From a developed database of defects or defective regions, analyses of different features belonging to different classes (different

types of defects, or defects versus non-defects) should be performed to yield a set of principal discriminating features. These features may be discriminators of segmented defects, defective pixels, or defective regions, depending on the resolution and characteristics of images and objects. These features are extracted from the segmented defects (or defective regions) as a feature vector for each object. The feature vector is then used in high-level processing in a classifier that assigns each object (defect or defective regions) to a class of defect or identifies it as a Not-a-defect or non-defective.

Table 1- Processing levels of the online defect and error detection system and its subsystems

<table>
<tr><td></td><td>Online defect detection subsystem</td><td>Geometric error detection subsystem</td></tr>
<tr><td rowspan="4">Low-level processing</td><td colspan="2">Pre-processing: de-noising and image enhancement</td></tr>
<tr><td colspan="2">Segmentation of fused objects</td></tr>
<tr><td colspan="2">Detection of true geometric objects</td></tr>
<tr><td>Segmentation of defects or defective regions within geometric objects</td><td></td></tr>
<tr><td>Intermediate-level</td><td>Feature extraction of defects or defective regions</td><td>Extraction of synthetic parameters or boundary comparison</td></tr>
<tr><td>High-level</td><td>Identification of defects or defective regions</td><td>Detection of geometric errors and identification of error trends through control chart</td></tr>
</table>

In the geometric error detection subsystem, once true geometric objects are detected, the geometric object should be compared with the target layer (based on the CAD model or known target parameters) which could be done by comparing point-to-

point boundary, or comparison of synthetic parameters of objects. To perform synthetic parameter comparison, synthetic parameters of interest should be extracted from the detected objects. Synthetic parameters include shape parameters such as roundness and angle values, size such as diameter, and positional parameters such as absolute x, y positions or relative positional parameters such as distance between two circle centers. Extracted synthetic parameters should be compared with those of the target layer. To identify a critical geometric error, the detected error should be checked based on allowable errors or acceptable tolerances. Development of control charts for the process is an alternative way for efficient detection of geometric errors that are signified by out-of-control-bounds alerts. Table 1 lists all the steps of these two subsystems in there levels of processing. Figure 37 shows a schematic flowchart of the in-situ detection system for part defects and geometric errors that illustrates the aforementioned steps.

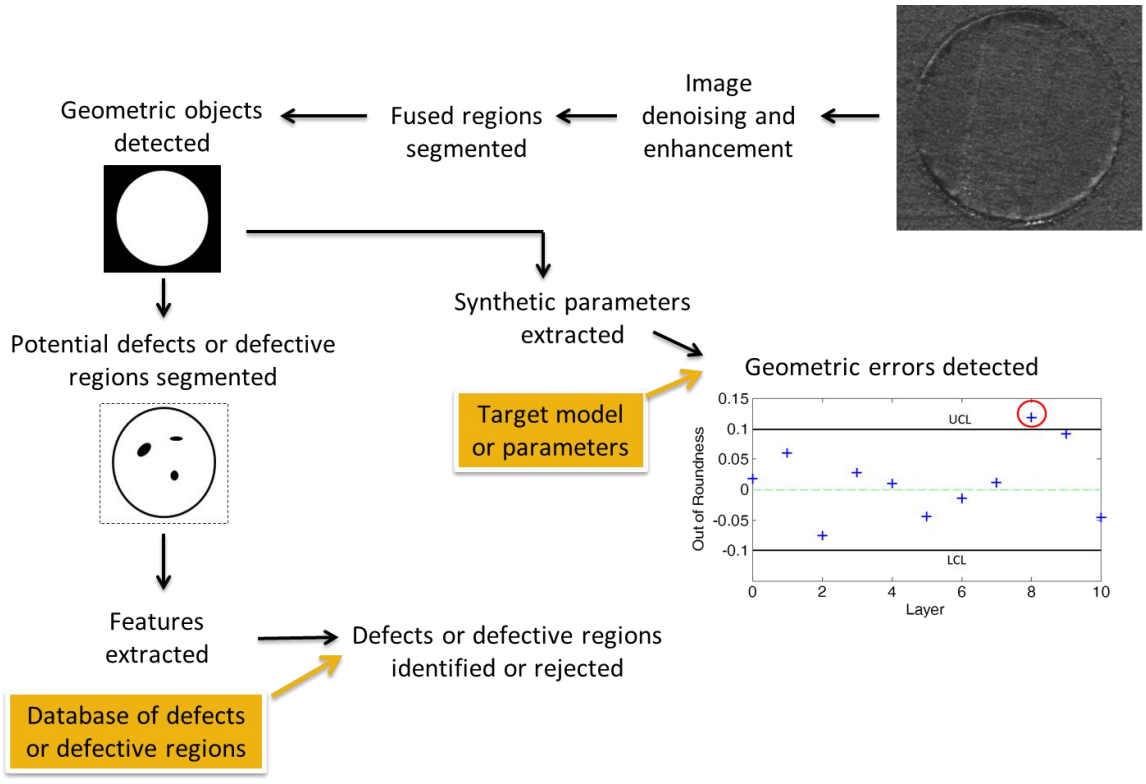

Figure 37- Flowchart of an online AVI system for detection of defects and geometric errors.

3.2 Formulation of the Problem to Be Solved in This Dissertation: The AVI System for Detection of Geometric Objects and Assessment (Detection and Identification) of Porosity from In-Situ, Layerwise Visible-Light Camera Images of Inconel 625 Parts made by Laser Powder-Bed Fusion Process

The AVI system described in the previous section presented a general systematic framework for a visual inspection system for detection of geometric errors (with respect to in-layer tolerances) as well as almost all types of visible part defects for any metal powder-bed AM process and with any 2D imagery input. This dissertation, however, will address detection of fused geometric objects (for the purpose of geometry inspection) and inspection (assessment) of porosity (pores or porous regions) from visible-light camera images of parts made of material Inconel 625in laser powder-bed fusion. For this problem, sufficiently accurate detection of geometric objects from in-situ camera images of parts made of Inconel 625 during laser powder-bed fusion will be performed that can be used for detection of geometric errors by simple comparison with target parameters. Additionally, a reliable assessment of porosity will be given using the detection and identification algorithms. Figure 38 shows the layout for the AVI system and underlying algorithms to be developed in this PhD research. Detailed explanation about what will be performed in this dissertation regarding the steps in Figure 38 will be given in Sections 3.2 to 3.7. Section 3.8 will present a discussion on application of the AVI system addressed and designed in this PhD dissertation to areas outside the scope of this dissertation. Section 3.9 will give an overview with some details of the material and its organization in Chapters IV to VII to address the formulated problem of this thesis and achieve its objectives and tasks as were described in this Chapter.

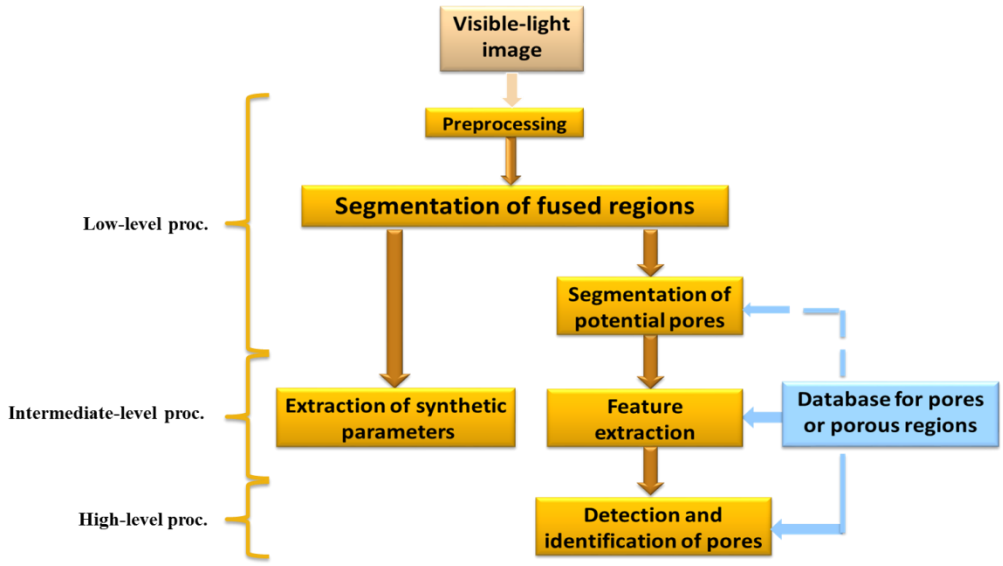

Figure 38- Layout for AVI system for detection and identification of defects (pores) in powder-bed AM (L-PBF) for the purpose of this dissertation.

3.3 Segmentation of Fused Geometric Objects

Images from camera should be acquired, pre-processed and denoised to be ready for application of image segmentation. Image segmentation algorithms then need to be developed to detect fused geometric objects from layer of powder. The segmentation algorithms should yield relatively satisfactory detection. The performance of the segmentation of fused objects is evaluated based on pixel-wise segmentation, point-to-point boundary error, and synthetic parameters. Extraction of synthetic parameter is performed for square objects and can simply be applicable to all polygonal objects, and is generalizable for any parametric object such as square, ellipse, etc.

3.4 Detection and Identification of Pores

In this subsection, different tasks for inspection of pores or porosity from visible-light images for the purpose of this PhD research are described.

a) Segmentation of individual pores:

The first step is pre-processing and image segmentation algorithms that convert the input gray-level image to a binary image where the objects of interest (potential defects) are in foreground (white) in a black background. To achieve defect segmentation, algorithms and techniques from image processing and computer vision are designed and implemented to high resolution visual images to automatically segment and detect potential pores. Considering the low contrast of pores and non-pore regions (background), and non-uniform intensity distribution in the part, development of appropriate segmentation algorithms is a very challenging task. Among existent or developed algorithms, the efficiency of algorithms should be evaluated and the most efficient algorithm will be used for the entire system.

The segmented objects in the binary image do not only include the pores, but also other types of defects as well as non-defective regions. These false segmented objects (false positives) in the result of segmentation of individual pores can be reduced by a further step of identification. To identify pores from non-pores or different types of pores, therefore, it is required to find and select several features such as shape parameters (aspect ratio, roundness, vertices) and size that discriminate the true pores from mistakenly segmented non-pores (false positives or alarms). This identification, in this research, is performed by finding ranges of geometric parameters associated with objects that are pore versus non-pore and imposed to results of detection to remove some of these false positives.

While the result of segmentation of individual pores may be reduced by application of identification directly to the results of segmentation, in this research, an intelligent identification approach is taken and applied to small regions in part layers to distinguish potentially porous versus non-porous regions in builds. As will be seen, this identification is found more robust and accurate, and can also help with pruning false positives in the results of pore segmentations to a large extent.

b) Identification of porous regions:

Feature extraction:

To identify porous regions from non-porous regions, initial analyses may be performed to prepare the image for feature extraction. Features are selected based on the physical intuition into and visual clues from the porous versus non-porous region and are then analyzed statistically. This statistical analysis involves finding the distributions of features for two classes and studying the interclass and interaclass variances.

Identification:

Then identification step should be developed which consists of high-level processing algorithms in machine vision. Identification level receives the set of features or discriminators and outputs a number that shows the identity (porous or non-porous) of the region associated with those features, or outputs the probability of the region being porous. Identification or classification is performed to confirm or reject an inspected object and therefore reduces the false alarms and can also identify different types of pores. While there is a variety of classifiers, Bayesian, as an efficient statistical tool, will be performed in this research. Output of many classifiers such as NN are usually numbers associated with each class (of pore or non-pore) whereas Bayesian will output probabilities of any segmented object to be a pore or non-pore that can then be thresholder to 0 or 1 for each class. The utilized classifier should be trained using an appropriate database to be developed and organized.

3.5 Development and Modification of Imaging Setup

There is not much work reported on visible-light imaging from powder-bed AM. Therefore, there is not much information on approaches and suggestions for selection of appropriate camera characteristics, where (distance and angle) camera be mounted for better imaging, effect of type, number, location, and orientation of light sources, and

procedures to deal with saturation, intense reflections, diffusion, and shadow formation. All these challenges should be addressed for capturing clear images that visualize features of interest clearly and are better suited for image analysis. Providing feedback on and assistance with modification of imaging setup is also performed in this research.

3.6 Development of Image Database of Porosity

To develop database for defect (pore) segmentation, a number of images that visualize pores should be produced. Parts that contain different sorts of pores should be fabricated for example by choosing a range of non-optimal process parameters. Knowledge or reasonable guess should be available for at least several objects in the image whether they correspond to pores or not. For identification step, the database should be sufficient enough to be divided to two subsets of training and testing such that the training includes sufficient number of porous and non-porous regions.

3.7 Measures and Evaluation Metrics

Measures for evaluation of segmentation algorithms:

The precision of segmentation algorithms can be assessed by several means:

1) Pixel-wise segmentation accuracy: How precisely an object has been segmented which can be calculated by the ratio of the pixels of the segmented object to the true area of the object or mathematically:

$$err = 1 - \frac{|F_T|}{|F_o|} \qquad \text{Equation 2}$$

Another criterion that captures the aforementioned three criteria in a single error in pixel-segmentation for task 1 is given by [125] as:

$$err = 1 - \frac{|B_O \cap B_T| + |F_o \cap F_T|}{|B_O| + |F_O|}$$

Equation 3

which is equivalent to complement of "accuracy". B_o and F_o denote the background and foreground (object) area pixels of the manually thresholded image, B_T and F_T denote the background and foreground area pixels in the image that are thresholded using the method to be assessed, and |.| is the number of pixels in the set.

2) Point-to-point boundary error: Distance between correspondent points on each internal and external boundary point. This error can be expressed in terms of root-mean-square (rms) error or maximum error.

Measures for evaluating identification algorithms:

1) Sensitivity (Recall) or true positive rate (TPR) which is percentage of true pores that are segmented (true positives: TP) (or its complement (false negatives rate: FNR))

$$TPR = \frac{TP}{P} = \frac{TP}{TP+FN}$$ Equation 4

2) Specificity or true negative rate (TNR) which is the ratio of truly rejected non-pores. TNR is the compliment of false positive rate (FPR).

$$TNR = \frac{TN}{N} = \frac{TN}{TN+FP}$$ Equation 5

3) Precision which is the ratio of true pores (true positives , TP) to the number of all segmented/ detected objects:

$$precision = \frac{TP}{TP+FP}$$ Equation 6

4) Negative Predictive Value (NPV) which is the ratio of truly rejected items (true negatives, TN) to the number of all rejected items:

$$NPV = \frac{TN}{TN+FN} \quad \text{Equation 7}$$

5) Figure of Merit (F_1), which considers errors with both FPs and FNs and a high value of F_1 represents a low ratio of FPs and FNs to the whole number of true positives. F_1 can be calculated as below:

$$F_1 = 2.\frac{precision.TPR}{precision+TPR} \quad \text{Equation 8}$$

To calculate the above measures, the true identity of considered segmented objects needs to be known which is found by manual observation of the layer or a reasonable intuitive guess.

3.8 Application of the Designed AVI System in This Dissertation to Outside the Scope of This Dissertation

This dissertation will address detection of fused geometric objects and inspection of porosity (pores or porous regions) from visible-light camera images of parts made of material Inconel 625in laser powder-bed fusion. For this problem, in the following chapters, sufficiently accurate detection of geometric objects and porosity from in-situ camera images of parts made of Inconel 625 during laser powder-bed fusion will be performed. While the framework described in Section 3.1 is general and addresses a variety of defects in any powder-bed AM process of any material, the final algorithms developed for detection of geometry and porosity were specifically designed and implemented to camera images that were captured at the imaging setup (camera and

illumination settings) set up at EWI and of parts made from Inconel 625 made by L-PBF process.

In any cases of changes in the imaging setup, such as in camera or illumination, the material, or other process such as EBM, the following considerations can be taken into account.

Application of the Developed Imaging Setup to Other Processes or Materials: In this research, as will be described in Section 4.2, an imaging setup was developed, to visualize porosity, by using a moveable light source mounted at the moving mechanisms of the machine itself. The same imaging setup can be implemented to visualize porosity in layers of builds made from other materials or by other processes such as EBM.

Application to Other Camera and illumination Settings: In case of changing illumination settings or any aspect of imaging setup, the characteristics, quality, or intensity of images would change. In these cases, the intensity of images would change and therefore the current algorithms might need to be parameterized again. For using a different camera, for example of higher resolution, the pixel size or image size might be different. However, it is very reasonably expected that the developed algorithms in this thesis would still be well applicable to similar imaging setups and would only need parameterization or minor adjustments to produce satisfactory results. But, of course, as mentioned earlier, image segmentation algorithms are customized, and for an entirely different imaging setup, the algorithms developed in this work, are not applicable, but the same concept or even same design is reasonably applicable.

Application to Other Materials: In this work, the algorithms for detection of fused geometry and pores were designed and evaluated for material Inconel 625 and the process of laser powder-bed fusion. Different materials would show different color and intensity values in images and therefore, the developed algorithms in their exact current form might not produce accurate results. However, it is expected that the algorithms in

the same form will be applicable and appropriate parameterization and adjustment would produce satisfactory results.

Application to Other Processes such as EBM: Use of EBM with same (or similar) imaging setup may slightly alter the contrast of fused region and powder region or porosity within the part. However, it is highly expected, with similar imaging setup, it the current algorithms for detection of geometry and porosity would be applicable and would lead to satisfactory results, after parameterization, adjustment, or potentially minor modification. In Section 6.1, a set of image processing algorithms will be designed for detection of geometries from images of EBM that were captured with an entirely different imaging setup and for Titanium parts. The analysis proves the efficacy of developing image processing algorithms based on similar concepts for detection of geometric objects for an entirely different imaging setup, material, and process.

3.9 Overview of the Material and its Organization in Chapters IV to VII to Address the Formulated Problem of This Dissertation

Chapter IV addresses the work described in Section 3.5 and describes the system and imaging setup; it provides an overview of the development stages of the imaging setup and the solution to visualizing porosity in camera images by using a moveable illumination setup. Chapter V address the work described in Section 3.6 and describes developing a database for images of porosity to be used for developing machine vision algorithms for assessment of porosity. Chapter VI addresses the work described in Section 3.3 and detection of fused geometric objects; appropriate image processing algorithms are developed to detect the geometric objects from camera images. Chapter VII and VIII address the detection and identification of porosity, as mentioned in Section 3.4 parts (a) and (b). Image processing algorithms are developed in Chapter VII to detect individual pores from camera images and a Bayesian network is developed and

implemented to identify potentially porous regions in Chapter VIII. Finally, Chapter IX gives the conclusions of this research. It discusses in detail the contributions of this research as well as the limitations and provides the scopes of the future work.

CHAPTER IV

SYSTEM SETUP AND MEASUREMENTS

In this chapter, the system and imaging setup will be described. Stages of modification of the imaging setup with the corresponding captured images from the builds will be presented.

4.1. Visual Camera Imaging Setup

Figure 39 shows the image of the SLM machine built at EWI customized such that there would be some room right at the top of the build platform for mounting sensors. Figure 40 shows a close-up of the build chamber with different components. An IPG 600 watt single mode fiber laser was used as lase source. As seen the laser source is mounted with some shift to the left at the top of the build platform. A visible laser pointer was initially and temporarily mounted at the location of the laser to mark the approximate path of the laser to the build. For mounting any sensors or devices, this path should be avoided.

The material used for part fabrication is Inconel 625. The machine operates in inert gas with level of oxygen lower than 500 parts per million (ppm) with the typical oxygen concentration value of 250 ppm. The powder deposition system was designed and set to deposit powder layers of 40 micron thickness.

The visual camera is mounted directly at the top of the build platform looking down perpendicular to the build. Initially a 2 megapixel CCD array camera was used with image size of 1080×1920 pixels. The other important component of the imaging setup in addition to the camera is the illumination (light) source. The location and orientation of the camera and the light source play critical role in the quality of imaging. The best

orientation for the camera is perpendicular to the build to remove the perspective effects and the need for camera calibration that was met in this imaging setup. The camera was mounted conveniently on a stationary fixture connected to the wall of the chamber. It was mounted such that it doesn't block the laser path. It was later understood that the distance of the camera from the build in this setup is not optimal and better image might be captured if the camera be put closer to the build, however, this position was mainly determined for stability and imposed by the physical limitations.

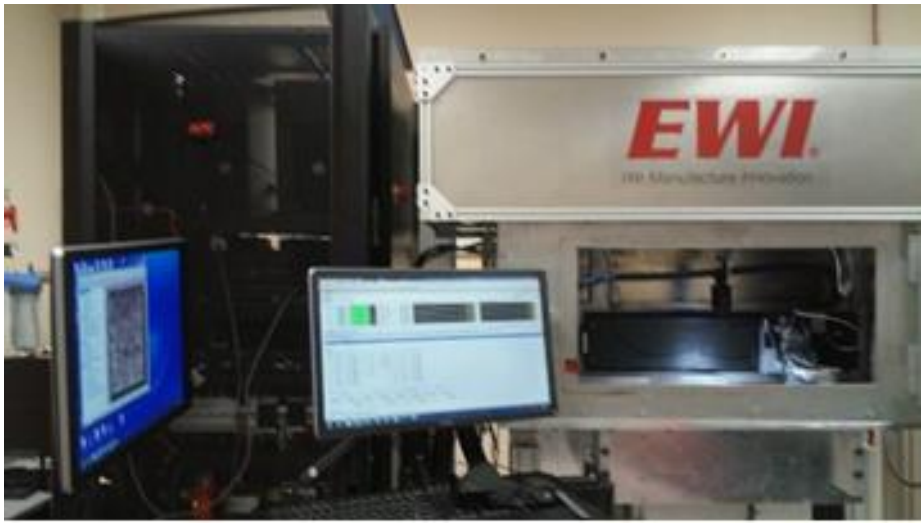

Figure 39- The custom SLM machine built at EWI.

Figure 40 shows the location of the light source that was chosen based on the physical and spatial availabilities of the system. To mount the light source, initially an adjustable, white, high intensity LED spot light, as shown in Figure 40, was mounted at the top of the build platform emanating at an angle. The level of brightness was adjusted until rather clear images of the powder bed could be captured.

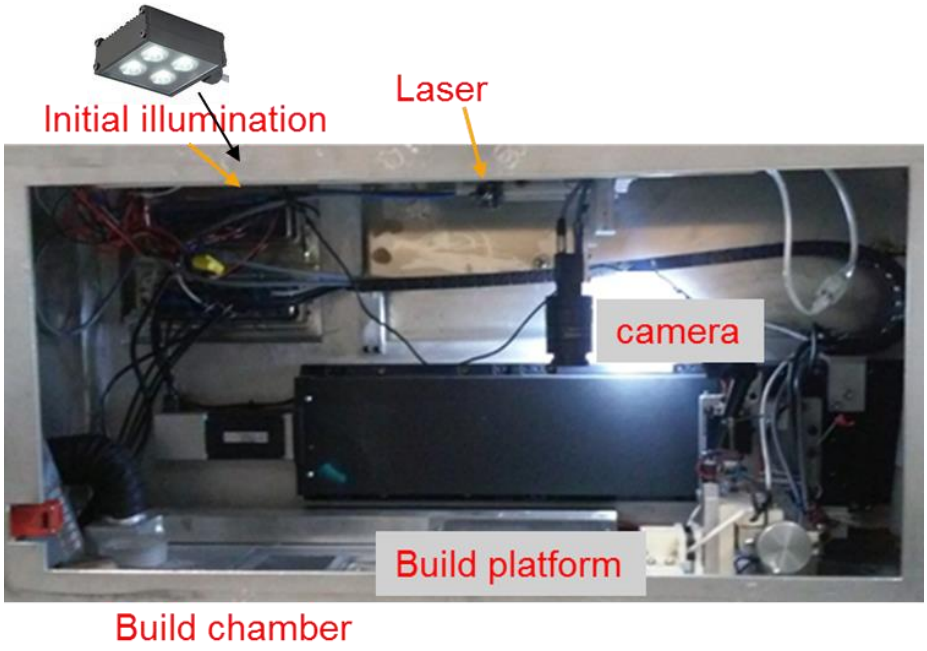

Figure 40- Close-up of the build chamber and its components.

To examine image quality, builds with square cross sections were fabricated for several layers. Images were captured and acquired at leach layer. Figure 41 shows examples of images captured with the current illumination setup. The image shows the fusion beads, fused surface and powder bed texture as well as the clear boundary of the fused object. The images were thought to provide sufficient clarity for segmentation and inspection of fused geometry. Therefore, these images were used for image segmentation initially. The results of this segmentation is presented in CHAPTER V. In that analysis, the bright circle that is the visible laser mark was removed by image processing.

With 1080×1920 pixel image sizes, the on-part pixel size was found as 20 µm. Although the camera resolution is 2 megapixel, the on-part pixel size is better than the resolution achieved by Kleszczynski *et al.* , [12, 32, 84], (24 µ/pixel) where they used a 29 megapixel camera with image size of 4234×4234 pixels. This better resolution (smaller pixel size value) is due to the smaller distance of the camera from the build and the perpendicular view of the camera.

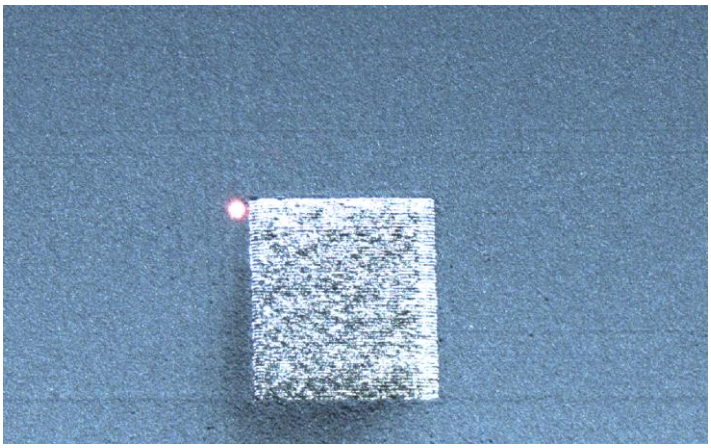

Figure 41- Example of image with the setup using 2 megapixel camera and square LED mounted at an angle from the build.

Despite showing the boundary of the fused geometry and the fusion beads, the captured image does not provide a clear image of the surface characteristics in terms of pores and lack of fusion. In fact, the fused surface contains some dark regions that do not correspond to defects. This is assumed to be due to the formation of shadows and non-uniform illumination. As it is seen from Figure 41, the light source (lighting the picture at an angle from the bottom) causes a non-uniform illumination over the image that leads to brighter regions at the top and darker regions towards the bottom of the image. This has led to creation of some shadows at the bottom part of the fused region as well as within the fused region.

To capture a clearer image of the surface, a higher resolution camera of 8 megapixel was mounted to increase the pixel size. With the selection of the new camera, the image sizes is 2160×4096 pixel and the on-part pixel size was calculated as 6.9 ($\cong$ 7) microns per pixel. The pixel size is much smaller than any previous developed imaging setup using just an 8 megapixel camera that is also in the same order of pixel size of standard microscope images. Given sizes of pores in powder-bed metal AM parts that

includes 20 to 500 microns, with a pixel size of 7 microns, it is possible to visualize pores of interest (e.g. as small as 50 microns) in several number of pixels.

Additionally, it was decided to mount the illumination at the top and perpendicular to the build platform. A ring LED illumination was therefore utilized and mounted around the camera at the camera location. An initial attempt of using this setup to capture images led to low-quality, dark images as in Figure 42. As it is seen, the image appears very dark with lots of badly-illuminated regions.

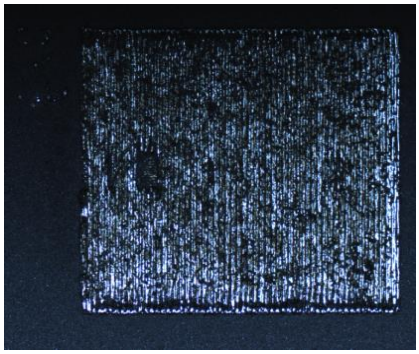

Figure 42- An example of image taken with the setup with 8 megapixel camera and ring illumination mounted around the camera.

Therefore, the white LED spot light was mounted at the previous location as previously shown in Figure 40. Figure 43 shows an example of image with this setup. The previous level of intensity led to too bright images with lots of saturation and producing lots of impulse noise more clearly seen in the powder region.

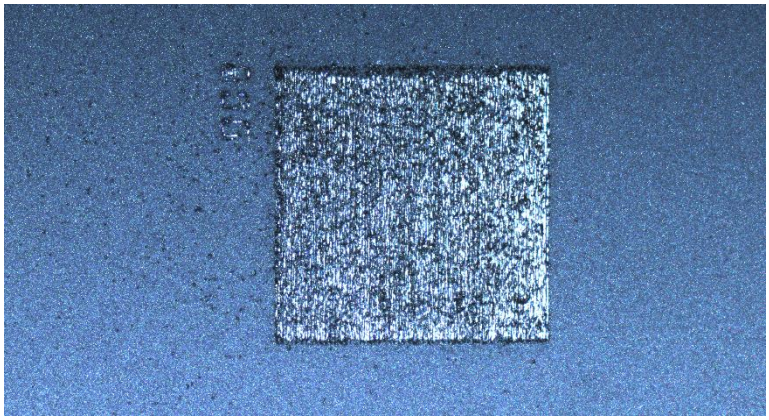

Figure 43- Example of image with the setup using 8 megapixel camera and high-intensity square LED mounted at an angle from the build.

Therefore, the level of intensity of the LED square light was adjusted to remove the effect of saturation and noise, and be more suitable for the current setup. Figure 44 shows an example image captured by this setup. As it is seen, the image does not contain any saturation and noise and shows the fusion seams within the fused region and the powder texture. However, there is still a non-uniform illumination throughout the image that would interfere with precise segmentation. While further work still needed to be performed to visualize the details of fused surface, given that geometry of the fused region seems visible in theses image, the images captured by this setup were used to design, implement, and evaluate image segmentation algorithms for detection of fused geometric objects. The will be covered in CHAPTER V where it will also be shown that the precision of segmentation is rather satisfactory.

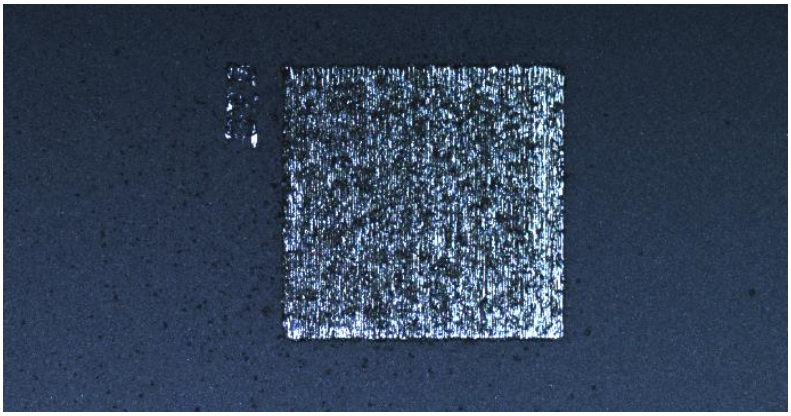

Figure 44- Example of image with the setup using 8 megapixel camera and adjusted level of intensity for square LED mounted at an angle from the build.

4.2 Imaging Setup for Visualizing Porosity

As seen in Figure 44, the powder region again contains some dark regions that do not correspond to pores or lack of fusion. It is similarly assumed that formation of these dark regions is due to the shadows created by non-uniform illumination. This effect was believed to be surpassed by mounting two sources of illumination on opposite sides. However, this still did not provide a clear image of the beads and fused surface texture especially pores. But further attempts to visualize defects and pores suggested a solution to another illumination setup that could more visibly show the details of the fused surface that will be discussed later in this chapter.

While images of the previous setup were found rather satisfactory for inspection of the fused geometry, further clear images need to be captured for inspection of surface and part defects such as pores. To investigate visibility of pores in images, it was required to build parts that are known to contain pores. Therefore, a range of process parameters that are known to produce pores in parts were chosen. A more detailed discussion of selection of process parameters and build of defective (porous) parts will be discussed in CHAPTER V. Microscopic examination and imaging was used to examine and confirm

existence of pores. A standard stereo microscope with a pixel size of 7 microns was used for manual examination and microscopic imaging.

Figure 45 shows three images of the same part captured by the microscope, the imaging setup with the LED spot light mounted at an angle from the build, and the imaging setup with the ring LED mounted perpendicular to the build around the camera. As seen, although the microscopic examination and imaging clearly show existence of pores and the pixel size of the camera and the microscope image are almost the same, the camera images do not visualize these pores.

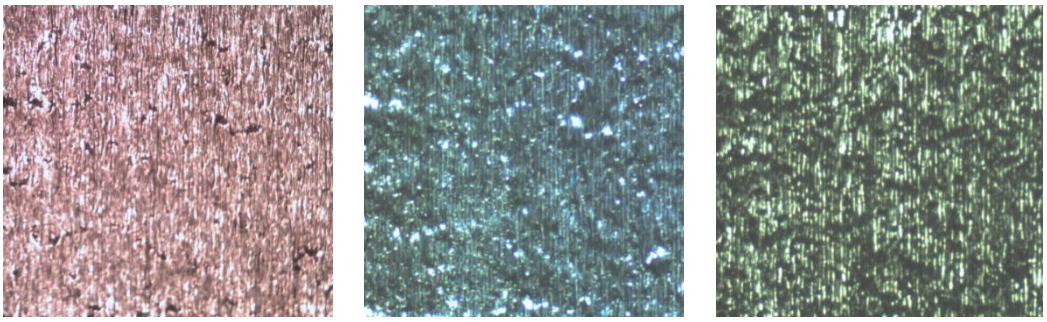

(a) (b) (c)

Figure 45- Images of the same build layer: (a) captured by a standard microscope with the resolution of 7 µm/pixel, (b) captured by visual camera in the imaging setup using the LED spot light at an angle (Figure 40) with the resolution of 7 µm/pixel, (c) captured by visual camera in the imaging setup using the ring LED perpendicular to the build and around the camera with the resolution of 7 µm/pixel.

Capturing images that clearly show the details of fused surface is in fact very challenging as also confronted by other researchers. This is largely due to the highly reflective metallic surface that can simply lead to saturation of some regions while other regions are dark. During adjustment of the imaging setup and illumination in this work, the following factors were identified and found to largely interfere with capturing clear images from the detailed texture and surface characteristic of fused region:

- The high reflectivity of the fused metal surface that vary within the fused region depending on the location, and surface orientation of the weld (fusion) beads.
- non-uniformity of images and non-illuminated regions due to either or both non-asymmetric light sources or non-uniform reflectivity of the metal surface.
- the comparable size of surface elevation with respect to defects that can cause shades over defects even with very good illumination.
- the inability to mount illumination above the build platform and at any distance from the build due to physical limitations (blockage of laser beam and blocking the coater motion)
- the inability of mounting camera above and perpendicular to the build platform and at any distance from the build due to physical limitations (blockage of laser beam and blocking the coater motion)
- the high level of image noise due to process environment,
- the level of dust or molten material smoke that may pollute the camera lens, etc.

In addition to the aforementioned factors that interfere with capturing clear in-situ images from AM part surfaces associated with the process and material, there are the following factors that make analyzing and automatic processing of AM images challenging. Some of these factors have been identified in this research are as follows:

- the low contrast between the metal and the formed defects,
- the large number of possible defect types,
- the very small microscopic size of defects,
- the large variety of shapes, sizes, and forms defects can have,

- the similarity of defects with naturally formed (sometimes non-defective) objects such as darkly etching regions and mass transfer,
- the possibility of defect coverage with powder,
- the low contrast between the powder and the fused powder,
- the formed spatters in the powder region, etc.

The type, location, and orientation of camera and light sources are two of the most influential factors on image quality. The physical limitations of the SLM machine do not allow for mounting light source anywhere. However, to investigate the capability of capturing images that visualize surface small details such as pores, the effect of camera and illumination location was studied on quality of images.

The reason for invisibility of pores from previously captured camera images (see Figure 45) could be that insufficient illumination is reflected from pores into the camera. This could be due to large diffusivity and the non-uniform illumination from an angle, as well as the shades of surface elevations that cover the pores. More uniform illumination should then be considered that can be provided by implementing two or more light sources from different sides to remove that shadows caused by each individual light source. An alternative more effective illumination would be to use a symmetric illumination such as a ring illumination mounted directly at the top of the build with light arrays perpendicular to the build platform.

To provide a uniform, symmetric, and shadow-free illumination such as in microscopes, an adjustable microscope ring light for stereo microscope was used. This is the same ring LED mentioned previously to capture Figure 42 and Figure 45 (c). The ring LED has 2-1/2" (64mm) inside diameter and 4" (100mm) outside diameter. The only place that the ring LED could be mounted, to avoid blockage of the laser beam, was around the camera at the same distance of the camera from the build.

The operating distance of similar microscope lights are in the range of several inches. Therefore, mounting the LED at this distance of about 1 ft. from the part resulted in dark and rather low-quality images and the problem with capturing dark non-illuminated areas within fused region persisted (see Figure 42 and Figure 45 (c)). The fused object showed many regions that were not well-illuminated and many fused regions appeared similar to the powder. This problem was most visibly seen within the fused region that has a relatively rough surface and variations of height that can create shadows and prevent the light to be reflected from the surface uniformly. It was investigated and seen that this problem can be removed if the ring illumination is mounted closer to the build at a distance within 5 cm to 10 cm from the build. By having light reflected from the build surface uniformly and efficiently, the details of the build surface including surface roughness and height variation as well as pores could be visualized.

It was observed as the ring illumination is getting closer to the part surface, the surface gets well illuminated and some surface details show up in the images. As this distance gets smaller from the build, the images get brighter until it seems that images become less clear. To find an optimal distance for light source from the build platform, several parts were fabricated and microscopic images were captured from the parts' surface outside the machine. It was investigated at some distance from the platform, the camera images captured from these parts show strong correspondence with microscopic images and visualized pores as they appear in microscopic images. This distance was marked and arrangements were planned to mount the light source at that distance from the build.

However, mounting the ring illumination at the chosen height would interfere with the laser scanning the build. To mount the ring illumination closer to the build without blocking the laser beam, a ring illumination with a very large inside diameter

would have been needed. On the other hand, a smaller ring illumination centered closely right on the examined area would be ideal for capturing clear well-lit images.

Therefore, it was decided that illumination source would be mounted at a moving fixture so that it stays away as the laser is scanning and moves to the top of the build once the layer is built and is ready to take picture. Given the current mechanism, it was planned that the ring illumination source would be mounted at a fixture connected to the coater and moves away as the coater passes. A fixture with three fixable multi-DoF joints was mounted on the coater (as in Figure 46). The ring LED was mounted on the coater and the fixture was adjusted such that the light would be at the desired distance with the build platform shedding light perpendicular to the platform. The machine was programmed such that after each layer is scanned or deposited using the laser, the coater would get back and stop at the position where the light is at the specified position and the camera would automatically picture from the layer at that stop.

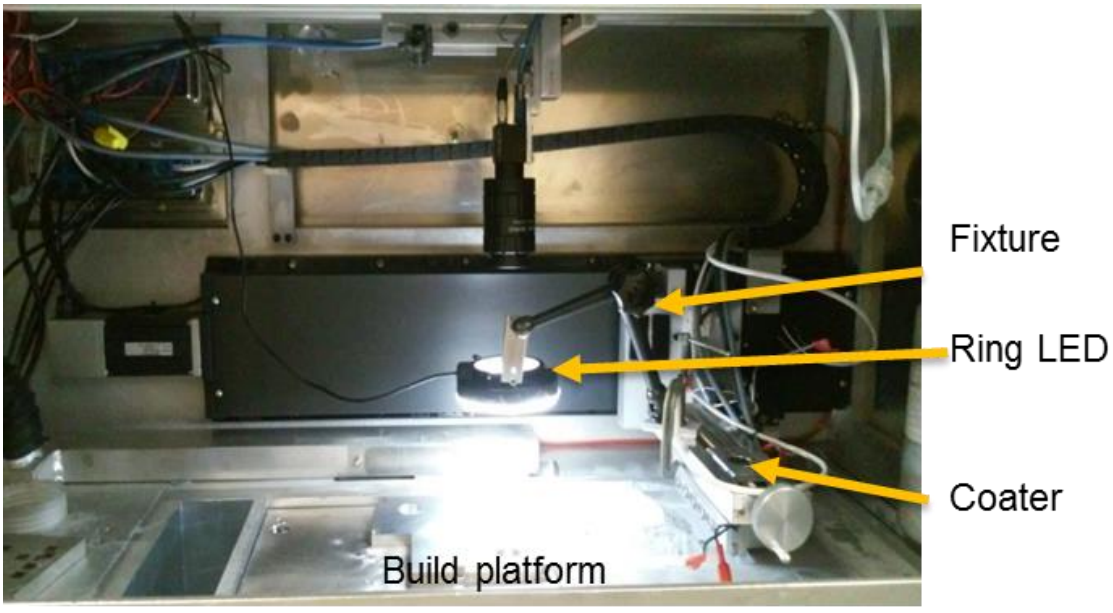

Figure 46- Image of the new imaging setup with movable ring LED mounted at a fixture on the coater at a selected height above the build platform.

Figure 47 (a) shows an example image captured by the new setup. Figure 47 (b) shows the corresponding microscopic image from the part. More examples of these images can be seen in Chapter V (e.g. Figure 54). It can clearly be seen that the two images match well. Additionally the pores are visible in camera images as they appear in microscopic images.

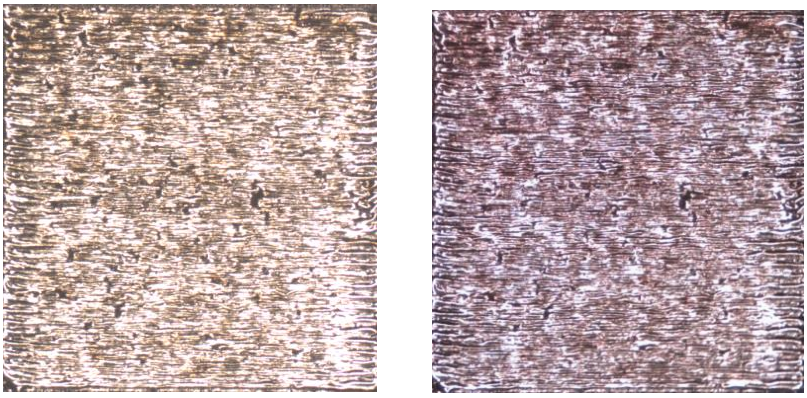

Figure 47- (a) An example image captured from a porous surface by the setup with movable ring LED (Figure 46), (b) corresponding microscopic image of the part.

It was also investigated that mounting the camera closer to the build platform would also improve image quality. For the purpose of this dissertation, since light source had most determinant factor, it was decided that camera would be remained mounted stably and fixed to the chamber wall. It should also be mentioned that this imaging setup is a combination of selected camera settings, use of physical polarizer or filters, illumination settings, and the distance of the illumination source with the build surface. The most influential parameters are the distance of the illumination source and the camera exposure time; camera gain value and application of filters and polarizer have less important effect. These parameters were adjusted in an iterative manner such that the captured camera images look as much similar to microscopic images as possible. The final selected height for illumination source was 65 mm above the build and the camera exposure time at 11 ms.

4.3 Further Discussion of Imaging and Different Aspects for Improving the Clarity of Camera Images

In this section, further discussion on imaging specifications will be given and quality of images will be studied further. Helpful suggestions will also be offered for improving image quality.

The surfae characteristic and the level of porosity seen in camera images match with the microscopic images. However, there were found a few cases of images where some features shown in microscope are not visible in the camera images. Also, sometimes, pores are visible in some cases of camera images that do not exist in the corresponding microscopic images. This section presents the worst cases of mis-match between the camera image and the microscope. Close examination of these cases of images revealed the reasons for occasional dicrepencies between the camera and microscopic images and suggest how camera image can even be further improved. For better organizations, this discussion is categorized in three aspects of camera Field of View (FoV), depth of focus of camera, and the saturation problem.

Effective FoV:

Figure 48 shows three examples parts (one in each row) built with different process paramters. For each part, two example images captured by camera are shown where in each of these two camera images parts are located at different locations in the FoV. Figure 48 (a), (d), and (g) show the microscopic images of these builds.

Figure 48 (b), (e), and (h) are the images tha have been captured when the built part is nearly below the camera, close to the center of the FoV of the camera. However, Figure 48 (c), (f), and (i) were taken when the built part was located closer to the left margins of the FoV. With the illumination centered around the camera, these parts are lit

up from the right side. It is clearly seen that those camera images where the part is below the camera and illumination match the microscopic images very well. However, Figure 48 (c) and (f) show a lot of dark spots that do not correspond to any pore or discoloration in the micrscope image. This observation is more severe in Figure 48 (c). Considering the fact that the part is lit up from the right, it is easy to see that the elevated edge of the part in Figure 48 (c) has created a shadow on the right side of the part. Additonally, surface height variations cause shadow over the part such that low-height regions appear as pores and very small pores appear as large noticeable pores.

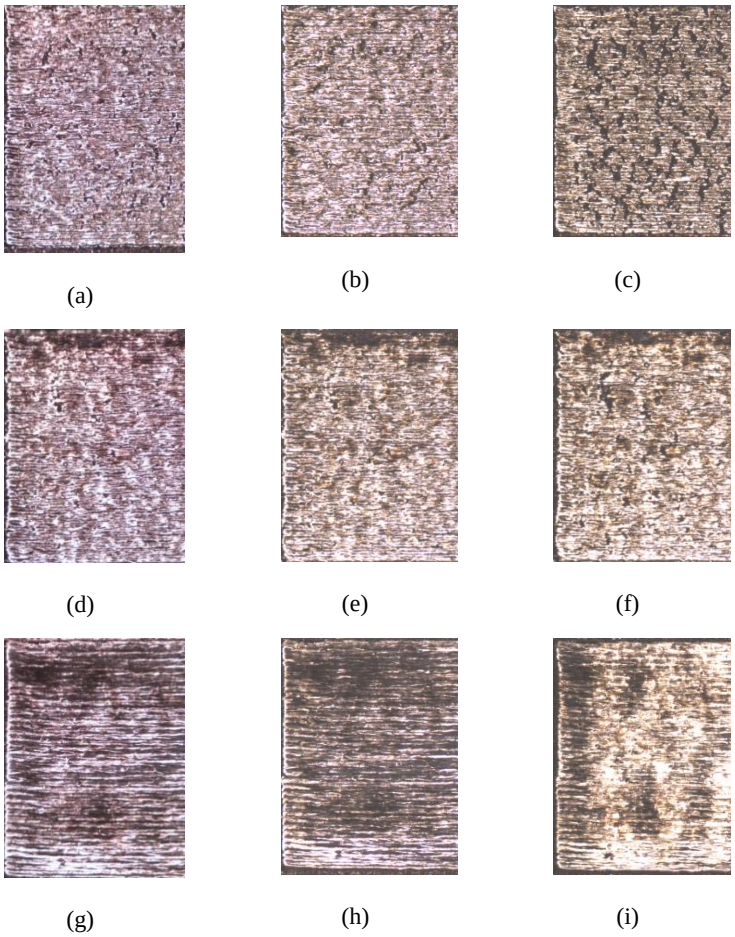

Figure 48- Three example of effect of illumination angle (or build location in FoV) on the camera image. Each row shows a different part (with different process parameters). First column in each row shows the microscopic image correspondent to the same part in that row. Second column shows camera images captured when the part is nearly below the camera. Third column is the camera image captured when the

part is near the left margin of the FoV of the camera. The illumination lights up the part from the right side of the image from above.

In Figure 48 (i) , the elevated edge of the part on the right has created a shadow right after the edge. Additionally, the small region of low-height located at the bottom left part of the surface is seen larger due to the created shadow. Right after the shadow of the elevated edge, very bright regions are seen where large reflection towards the camera has led to saturation. It is easy to see that this large reflection is caused by the smooth relective surface of metal part that is elevated and pointed such that the surface normal of this region points right towards the camera and reflects a large portion of light back to the camera. The opposite is seen at the left portion of this square where the surface normal points towards left and less reflection due to misalignment of surface normal and camera has caused the surface to appear darker (apart from surface discoloration).

The camera FoV that can be captured in images at the current camera disance from the build is 28mm×15mm. It was examined and determined that the FoV that would safely not cause any shadows and image discrepencies is about 15mm×15mm. For the purpose of this research, camnera images were captured from the builds in this FoV, which in this document is referred to as camera effective FoV. Also, it is worthwhile to mention that the microscope FoV for capturing clear (focused) images of these square builds is about 8.5mm×8.5mm.

To prevent formation of shadows at parts located at margins of images and consequently increase the effective FoV of the camera to 28mm×15mm, a larger ring illumination can be used that would provide a more uniform illiumnation thhroughout the camera FoV. Additionally, since with the current ilumination the effeicint camera FoV is smaller than its true FoV, it is possible to mount the camera closer to the build platform without decreasding the efficient FoV. Decreasing the distance between the camers and the build is expected to increase the images clarity.

Another solution to increase the view of the camera is to add a capability of sliding the camera above the platform. This would allow to capture several images that cover a large portion of the build platform.

Depth of Focus of the Camera

Figure 49 shows an example of camera image captured in the camera effective FoV with respect to microscopic image. The camera images looks similar to microscopic mages and features the surface charactersitics of the layer. However, as seen, the camera image suggests there is a pore in the bottom left part of the image. In the microscopic image, this spot corresponds to a darkly etched spot (metal surface discoloration) or a small spot of relatively lower height as a result of height variations and roughness of the surface caused by the correspondent process parameters. By taking images later again using the camera from this part and some others, it was seen that microscope is very sharply focused on the top layer of the build such that the extrusions of the below layers are very blury and rather invisible. However, the camera images clearly show the details of the below layers that had extruded under the top layer. This fact can clearly be seen in Figure 50 (a) in the zoomed-in views of the top parts of an image captured from the same part in Figure 49. Figure 50 (b) presents another example that again clearly shows a sharper camera focus at the top layer could still be achieved.

It was examined and determined that changes of microscope settings such as brightness would have negligible effect on images and surface features are persistently captured in repetitive images of the microscope taken at different settings. The microcope can very clearly and rather simply be focused on the top layer. This may be due to the ability of fine tuning of the lens focus within the microscope's short depth of focus. Setting up the camera, it was attempted to focus the camera on the top layer, however, the coarser focus tuning capability of the available camera within its larger depth of focus

(with respect to microscope) would have made it more difficult to achieve a very sharp focus on the top layer. Additionally, the high sensitivity of images to the focus of the camera within several microns had not been identified at the beginning. But future work can addrees and resolve this issue to a large extent.

Lack of a sharp focus on an image in fact acts like a low-pass filter that removes or blurs the sharp and small ffeatures associated with low-frequency. Therefore, the color value captured by a pixel, is in fact, affected by the color value (light) from both the location corresponding to that pixel and its neighboring regions. This may cause the images to show some spots darker than they truly are, looking like pores, or slightly distort shapes of some pores. It may additionally lead to larger saturation regions in the image as pixels receive light from the neighborhood of their corresponding spacial point and pixels that otherwise would not have been saturated, saturate and are considered as missing data.

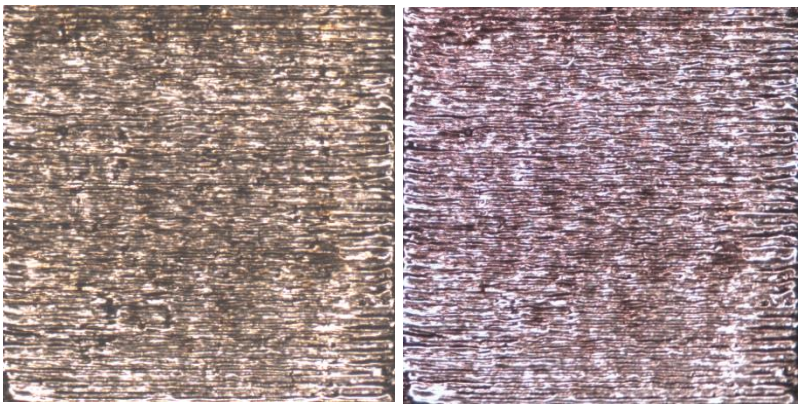

Figure 49- An example of camera image (left) with respect to microscopic image (right) that show comparison of depth of focus and focus sharpness between camera and microscope.

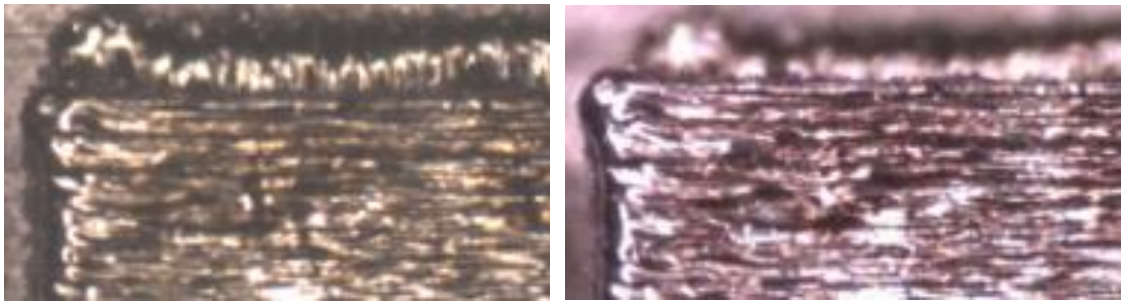

(a)

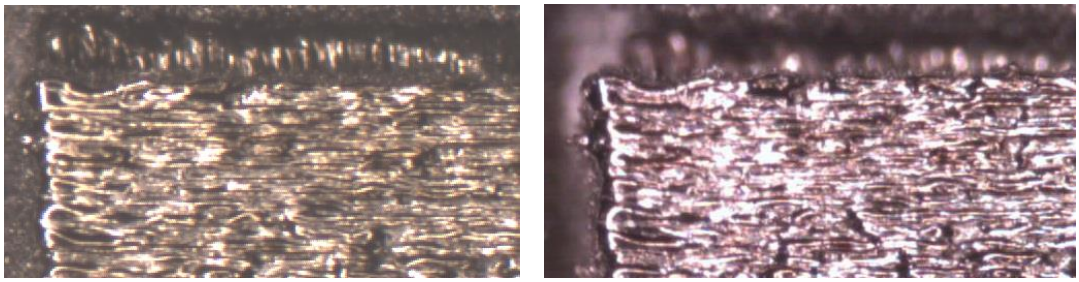

(b)

Figure 50- (a) Zoomed-in views of the top parts of images in Figure 49, (b) Zoomed-in views of the top parts of the images in another examplar build. In each row, the left image is camera image and the right image is the corresponding microscopic image.

Saturation Due to Smoothness and Orientation of Highly Reflective Metallic Surface

Figure 48 (i) clearly shows large saturation regions formed when part surface normal is aligned towards the camera (and illumination source). These saturation regions that cover the beneath surface details are also seen in images of other smooth surfaces when the part is located in the center of FoV (as seen in Figure 51). Although, these regions are mostly caused by smooth surfaces that are unlikely to have defects, these saturtated regions are also seen in images of more rough surfaces but in much smaller sizes and intensity. Figure 52 shows an example of an image of a rough surface that local image saturation has covered some surface features with respect to microscope. The sharp focus of the camera on the top surface reduces the intensity of saturations in microscopic image.

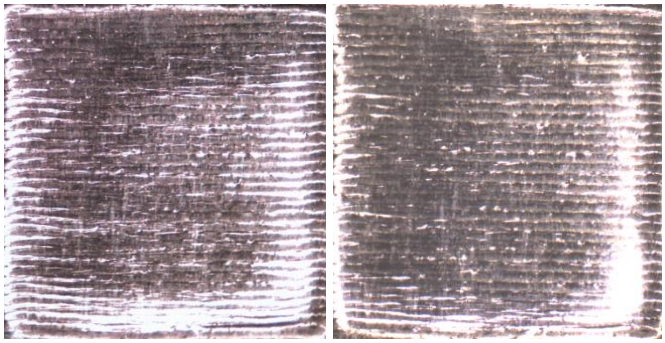

Figure 51- Example of an image taken from a smooth surface that has caused saturation. Left: microscopic image, right: camera image.

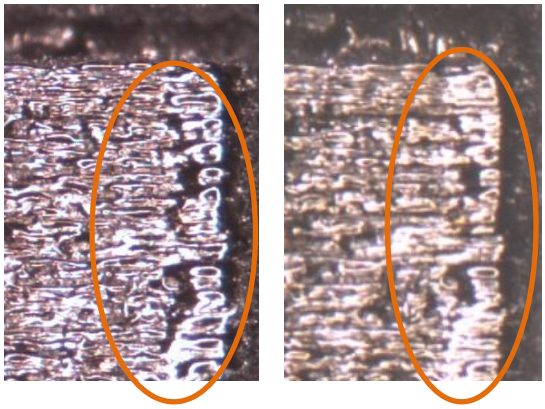

Figure 52- An example of image that local image saturation has covered some surface features with respect to microscope. Left: microscope, right: camera.

As was examined by the study of a large number of images and as seen in most images presented in this report, the majority of surface characteristics and features are captured by camera images (when parts are located in the effective FoV). Therefore, as will be seen in Chapter VIII, it is possible to make inferences about the true surface characteristics from the camera images for the purpose of automated in-situ quality inspection of built layers. It is also possible to provide an assessment of the porosity of the layers from camera images especially if algorithms with very high detection precision are developed. It was also seen that the camera images in most cases show the individual pores of the part surface.

Already, an iterative and careful selection of the imaging settings in terms of distance of the illumination and camera exposure time decreased saturation regions and number of dark shadowed regions that would have led to false alarms. However as a means to increase the clarity and precision of images and to decrease the amount of missing data, it is suggested that several images of each layer is captured at two different camera exposure time or brightness level. At the decreased level of brightness or camera exposure time, the dark regions in the first image become unclear. However, the surface beneath saturated regions becomes visible. Integrating these two images then would provide a clear image that visualizes the features and defects of the entire surface. This can be addressed as extension of this PhD research.

CHAPTER V

DEVELOPMENT OF DEFECT IMAGE DATABASE

In Section 2.2, the effect of process parameters and input energy density on formation of pores and defects was discussed. In this chapter, a series of process parameters are chosen to build a variety of parts (in form of squares). This creates builds with various properties in terms of the layer surface roughness, quality of fusion, and porosity. It is desired to capture (visualize) these properties in the camera images and be able to assess them by analyzing the images. Capturing camera images that visualize the surface variations in the layer including pores was accomplished and discussed in the previous chapter.

To create parts with various characteristics, quality, and defects, process parameters were selected at different levels to cover a range of parameters around the optimal parameters for Inconel 625 material. Table 2 shows a table of available process parameters within the capability of the current system. Laser power and scan speed are varied at increments to provide 35 different pairs of parameters at different levels of energy. Table 3 shows the value of energy for the pairs of process parameters corresponding to Table 2. Figure 53 shows a visualization of the energy level of the 35 pairs of process parameters in Table 2. The stars indicate the location of the pairs in the graph. Process parameter pair number 13 corresponds to the optimal process parameters for build of Inconel 625 parts.

Table 2- Various considered pairs of process parameters with their assigned numbers

Defect Generation by Process Parameters			Scanning Speed (mm/s) (30% inc.)				
			Column 1	Column 2	Column 3	Column 4	Column 5
			384	672	960	1248	1536
Power (w) (15% inc)	Row 1	115.6	31	32	33	34	35
	Row 2	158.95	26	27	28	29	30
	Row 3	202.3	21	22	23	24	25
	Row 4	245.65	16	17	18	19	20
	Row 5	289	11	12	13	14	15
	Row 6	332.35	6	7	8	9	10
	Row 7	370	1	2	3	4	5

Table 3- Energy level of the 35 pairs of process parameters shown in Table 2.

	384	672	960	1248	1536
115.6	301.0417	172.0238	120.4167	92.62821	75.26042
158.95	413.9323	236.5327	165.5729	127.3638	103.4831
202.3	526.8229	301.0417	210.7292	162.0994	131.7057
245.65	639.7135	365.5506	255.8854	196.8349	159.9284
289	752.6042	430.0595	301.0417	231.5705	188.151
332.35	865.4948	494.5685	346.1979	266.3061	216.3737
370	963.5417	550.5952	385.4167	296.4744	240.8854

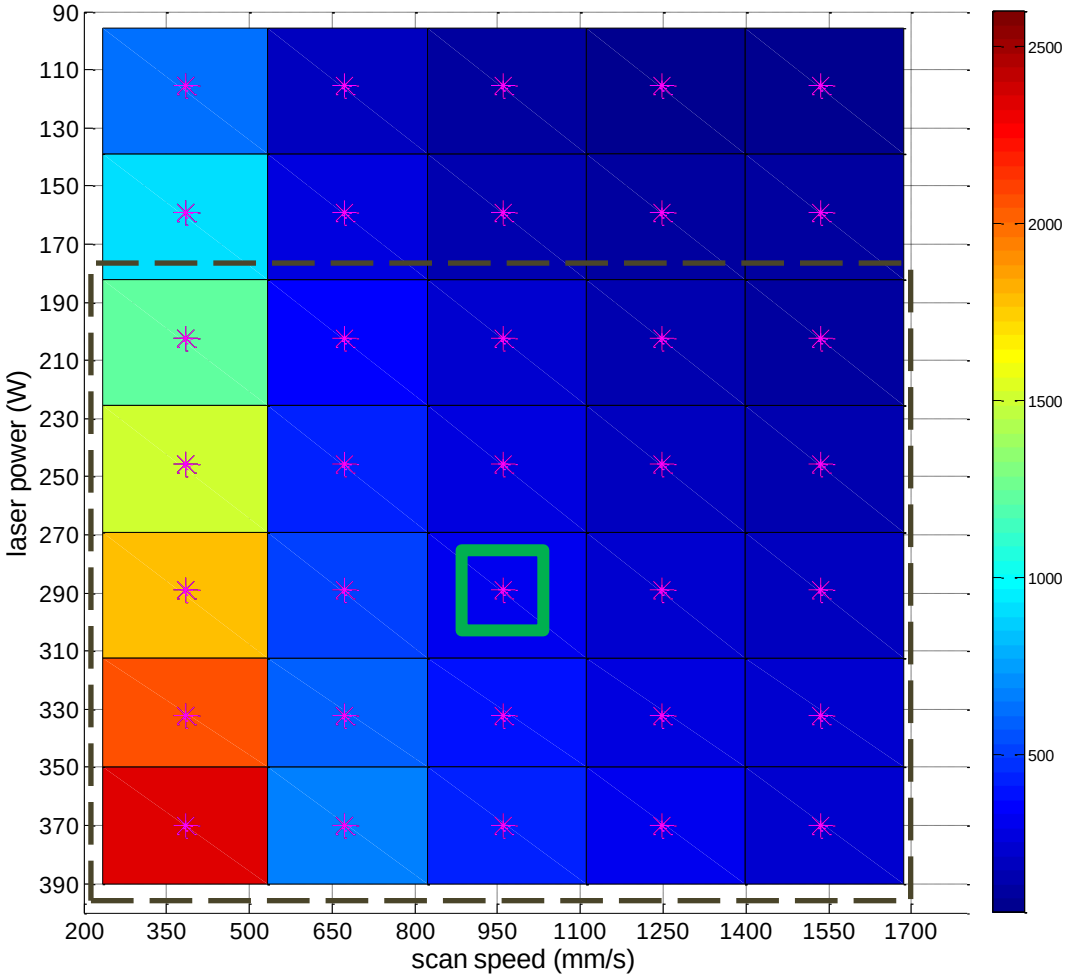

Figure 53- Energy levels of the 35 pairs of process parameters in Table 2. The bottom left of the graph corresponds to process parameter pair number 1, and the upper right corresponds to process parameter pair number 35. The dashed square shows the process parameter pairs used for experiments in this research.

It was investigated and seen that builds with energy level lower than or equal to 25 show very porous surfaces and look similar in camera images. It was also determined that builds with process parameters 1 to 25 capture a sufficiently large variety of surface characteristics; therefore, they were used to produce the builds that range from smooth well-fused to defective surfaces.

After desired imaging setup was adjusted and the process parameters were selected, different blocks were built with each chosen pair of process parameters. The first twenty layers were built with optimal process parameters to stabilize the process, and then a chosen specific pair of non-optimal parameters was applied to 6 layers at the top to

produce layers with different surface characteristics and potentially defects. Images were captured after each layer as the coater pass over the built layer and got back to its starting point. Three sets of builds were fabricated using chosen pairs of parameters.

The surface characteristics and defects of the build parts are clearly seen in the camera images. Figure 54 shows examples of builds at different energy levels. For better insight into the porosity captured by images, corresponding microscopic images are also presented. In Figure 54, the two top pictures present the camera image and the corresponding microscopic image of a build with an enrgy level lower than the optimal process parameters. As seen in the picture, pores have formed in these layers and the layer has a very rough surface. The build in the fourth row of Figure 54 is corrersponding to a build with high energy and as seen it has a very well-fused soomth surface.

Figure 55 shows more examples of microscopic images in comparison with camera images that were captured with blue color setting. Initially a blue color setting was used for capturing images. Later on, red color was used to capture images since it provided better visual aid to compare individual pores in camera image with microscopic images. However, the blue color setting provided better visual contrast between the pores and the surface that seems to serve somewhat better with automatic pore detection. Figure 55 also shows part in order of asecending level of energy from a very porous surface to a smooth surface.

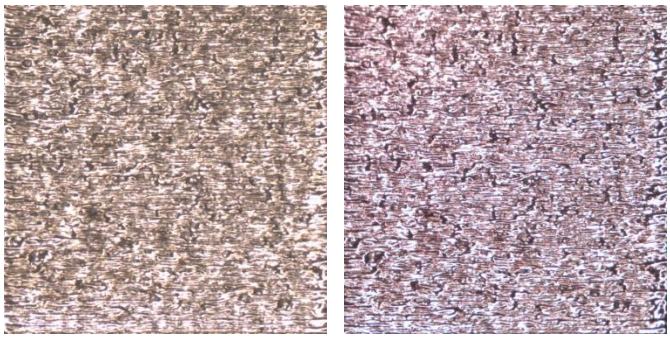

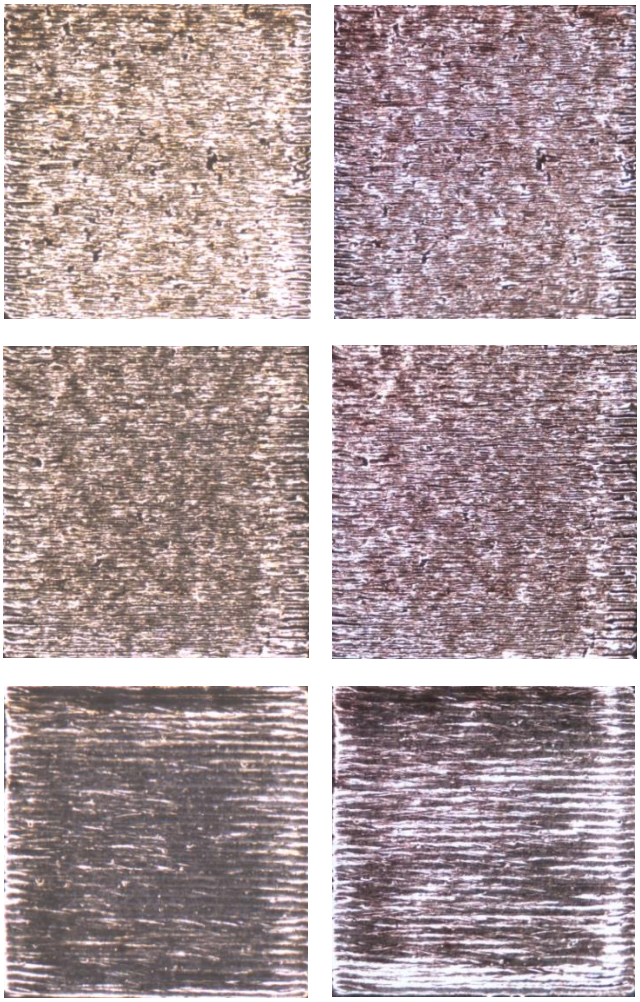

Figure 54- Images captured from high-resolution camera at the new setting in comparison with microscopic images. Each row shows a build with different process parameters. The left image in each row is the camera image and the right image is the corresponding microscopic image.

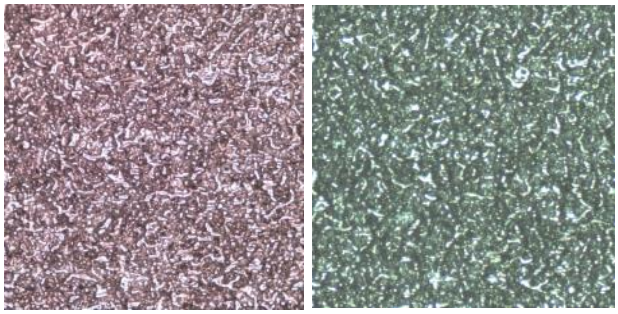

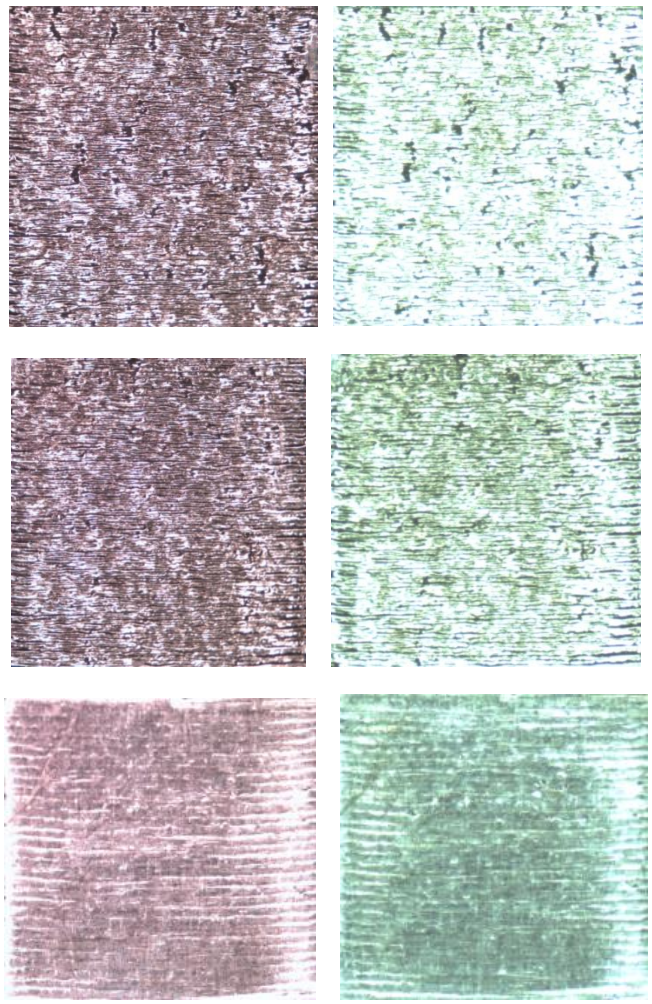

Figure 55- More examples of microscopic images in comparison with camera images that were captured with blue color setting.

Builds with their corresponding camera images were visually studied to identify layers in terms of build quality. Perfect powder fusion would lead to smooth part surfaces without any visible porosity. Studying the layer surface charcteristics reveals that there is also a correlation between the level of enrgy and the visible surface roughness and porosity of the layer. As the energy drops further below the optimal level of energy, the surface gets rougher which also corresponds with an imperfect fusion, and pores tend to appear in the layer.

Figure 56 shows six more examples of builds with different process parameters. Figure 56 (c) represents a build with optimal process parameters equivalent to the parameter pair numbered as 13 in Table 2. Figure 56 (a) to (b) are examples of builds made with energy higher than that of the optimal layer and Figure 56 (d) to (f) are examples of builds made with energy lower than that of the optimal layer. The figures show the general trend of the following observations.

The following observations were made from the experiments that also agree with the physical expectations: At high energy, the build surfaces are very smooth and have no visible pores. As the energy decreases, sill below the energy level of the optimal process parameters, the surface tends to show slight height variations that signify a rougher surface. Within this range of energy, there is usually no visible pore on the surface. Around the energy level of the optimal parameters, the surface shows a relatively rough surface but no visible pores are formed. As the energy goes lower and much below the optimal parameters', the layers become very rough, lack of fusion is formed between the scan paths, especially close to the part boundaries, and pores start to appear on the layer. At this stage, laser scan paths are still distinguishable. Once the energy gets too low, the powder fusion is not performed uniformly throughout the surface; lack of powder fusion in the layer generates large pores and the scan paths are too difficult or no longer visible or identifiable. Examples of builds with their corresponding process parameters are shown in Figure 57 that supports the above observations.

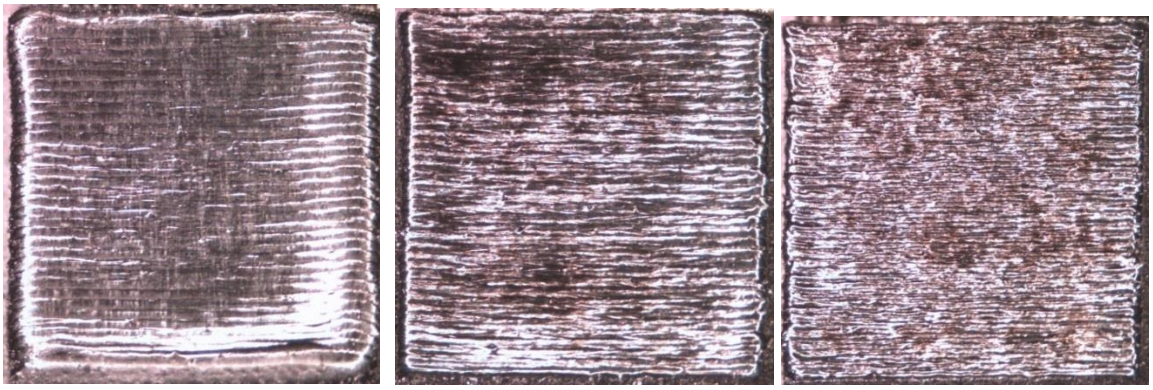

(a) (b) (c)

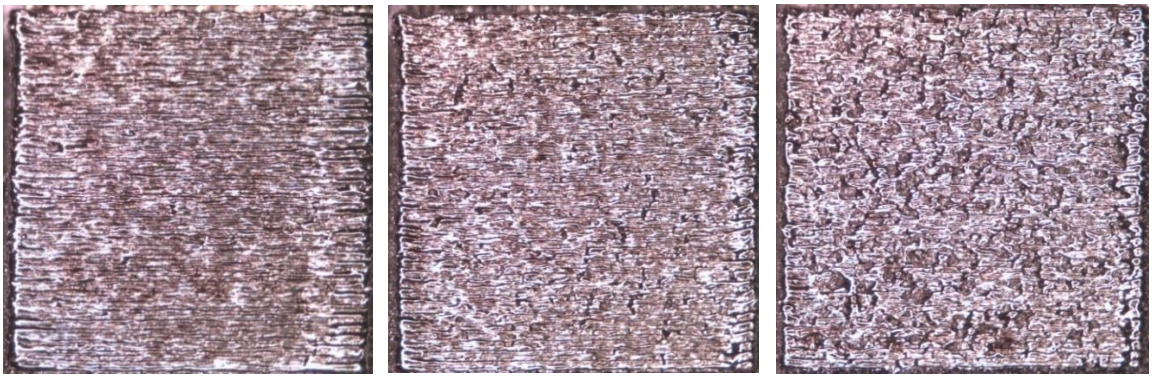

(d) (e) (f)

Figure 56- Microscopic images of different builds at various energy levels: (a) the build with process parameters numbered as 1 (numberings are based on Table 2), (b) the build with process parameters numbered as 12, (c) the build with process parameters numbered as 13, (d) the build with process parameters numbered as 9, (e) the build with process parameters numbered as 15, (f) the build with process parameters numbered as 25.

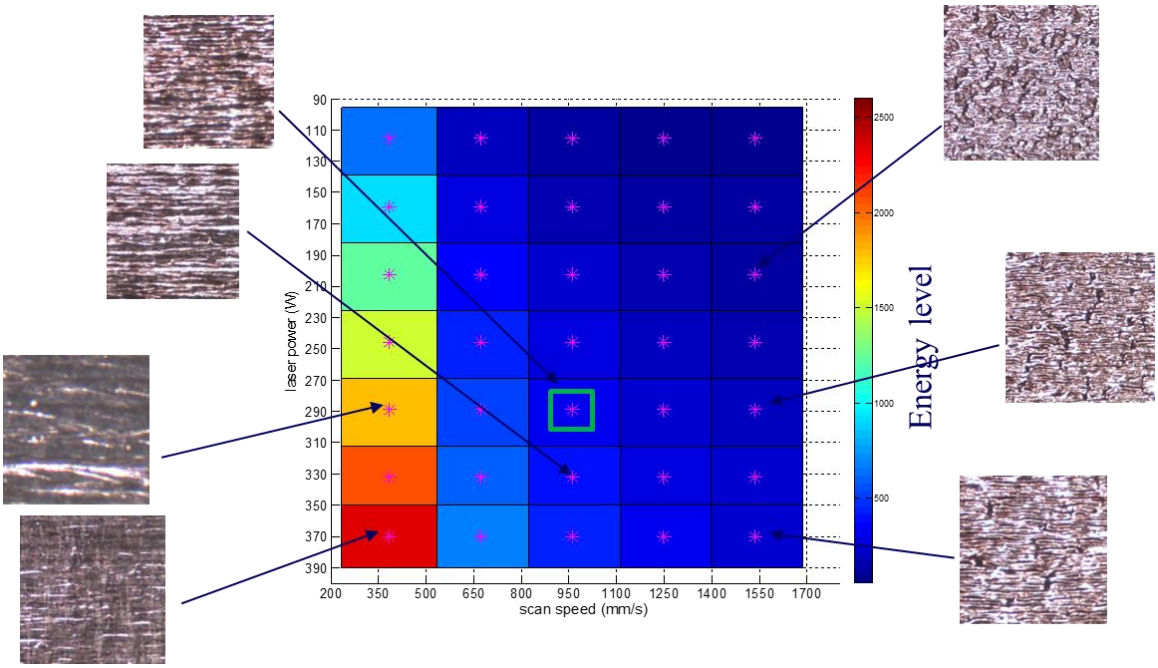

Figure 57- Examples of builds associated with different process parameters.

It was also observed at very high energy builds, the boundaries of the fused layer show visible deviations from the desired geometry. Additionally, the elevated edge problem is very significant at high energy level. However, at the level of energy close to the optimal parameters, the boundaries of the fused geometry show less error compared to the desired geometry, and the problem with elevated edges is surpassed. This observation matched the literature and can easily be explained by the following fact. At high energy, molten pool grows larger and a large amount of powder including the powder surrounding the laser spot is fused into the solid, and, therefore, the fused material does not exactly match the laser path. This factor is even more dominant and visible at the boundary of the object (for example, the first contour) where the laser spot is surrounded by powder in the top layer as well as the layer beneath that. Less conductivity of the neighboring powder contributes into even further growth of the melt pool at the boundary of the object when it is scanned. The formation of highly elevated edges at high energy builds can similarly be explained with the large size of the melt pool

at the boundary. Optimal process parameters are chosen high enough to produce a complete fusion with ideally no porosity and lack of fusion but not too high to lead to dimensional inaccuracy and formation of high elevated edges.

Based on what was mentioned, three cases of surfaces are possible: smooth surfaces with no visible pores associated with high energy, around optimal process parameters with relatively smooth surface and no visible pores, and rough surfaces containing pores and lack of fusion associated with low energy. Although, the trend of quality of fusion and formation of pores has a strong correlation with level of energy, it was in fact observed that at the same level of energy, a specific change of process parameters led a porous surface with a visibly rougher surface. Additionally, there were cases that at the specific set of parameters, reduction of energy led to a smoother surface. The aforementioned observation agreed with the observations made by Starr et al. [48, 50] for Ti6-Al4 and the three zones they suggested.

It was then decided to visually examine surfaces built at each pair of process parameters for the three series of builds and identify the layers (with their corresponding process parameters) that pores are visibly formed from layers without any visible pore. It was also attempted to divide the layers without any pores (non-porous layers) to two types of surfaces based on the visible smoothness and characteristics of the surface. Figure 58 shows the results of these observations and identifications based on that. The produced chart shows strong agreement with Figure 59 by Starr et al [48]. Note that constant energy levels in laser power – scan speed space are radial straight lines all passing through the origin.

Decision on identifying porous versus non-porous layers was relatively easy and reliable by observations from camera images as well as the stereo microscopic view of the surface. It was therefore very certain to decide visibly porous layers that belong to Zone III (see Figure 59). However, decision on the level of smoothness was not obvious

or reliable. In fact, based on [48, 50], Zone II distinguishes from Zone I based on the usually sub-surface, very small, spherical pores that can be examined using destructive examinations, CT scanning, etc. Therefore, decision based on Zone I and II was mainly made based on closer similarity of surface characteristics and quality of fusion to high-energy fusion or optimal energy. Wherever decision could not be made, no identification was made (i.e. pairs of process parameters that are not marked or are marked differently based on the chart guide). For two cases at the boundary of Zone III with no marks, decision on existence of surface pores could not be made for certain.

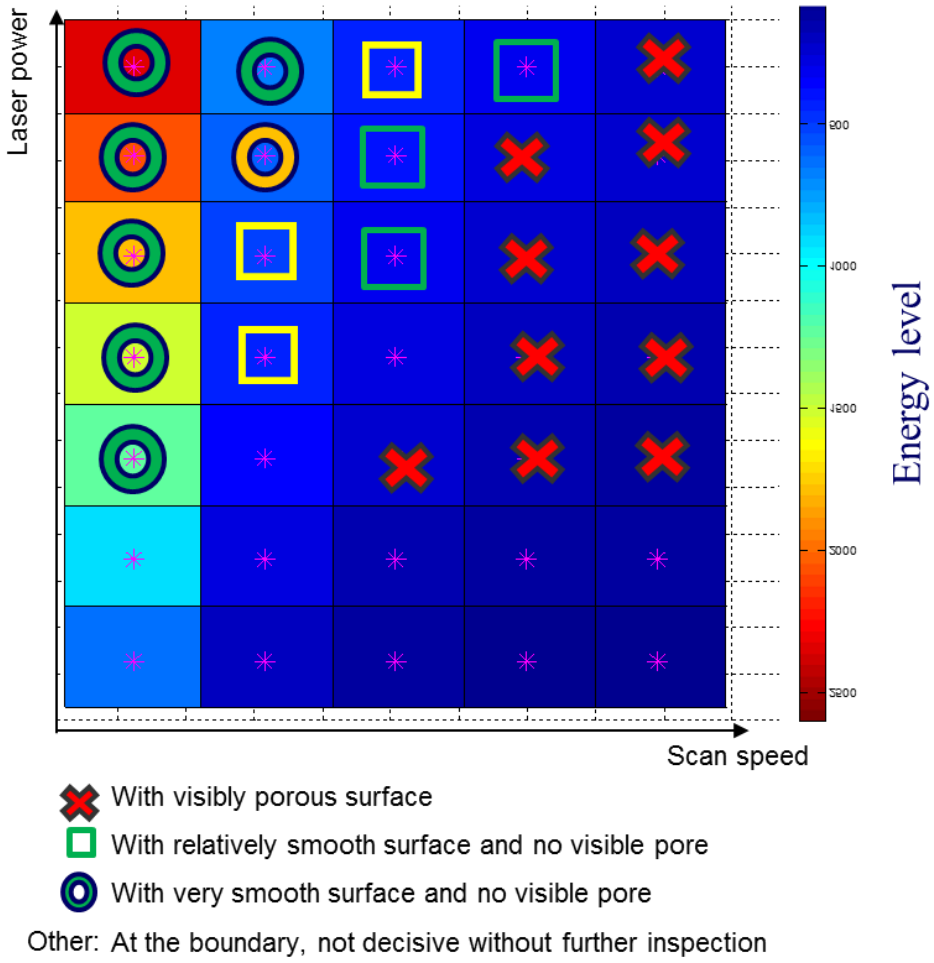

Figure 58- Visual identification of porous surfaces versus non-porous surfaces and marking their corresponding process parameters.

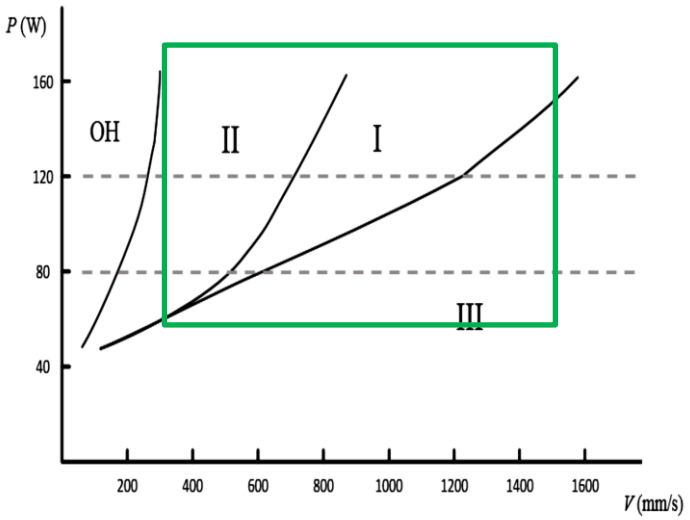

Figure 59- Illustration of three feasible zones of builds in process parameter space based on part properties from [48]. The marked square represents the region that relatively matches with the chart in Figure 58.

In addition to the fact that Zone I and II did not show any surface pores as suggested by Starr et al, the layers with visible pores on the surface, in fact, showed a very similar morphology to the pores formed in Zone III as studied in [50]. This suggests that the pores that we observed in camera images on the surface of each layer in the porous region, in fact, remain in the part as pores after deposition of next layers. Figure 60 (a) and (b) shows an example microscopic image of a porous layer from our setup as well as a microscopic image of the (polished) cross section of a part corresponding to Zone III after destructive testing, made by Starr et al. [50]. Figure 60 (c) shows a microscopic image after destructive testing of porosity formed in Zone II, [50], to present a measure to see the similarity of morphology of pores in Figure 60 (a) and (b).

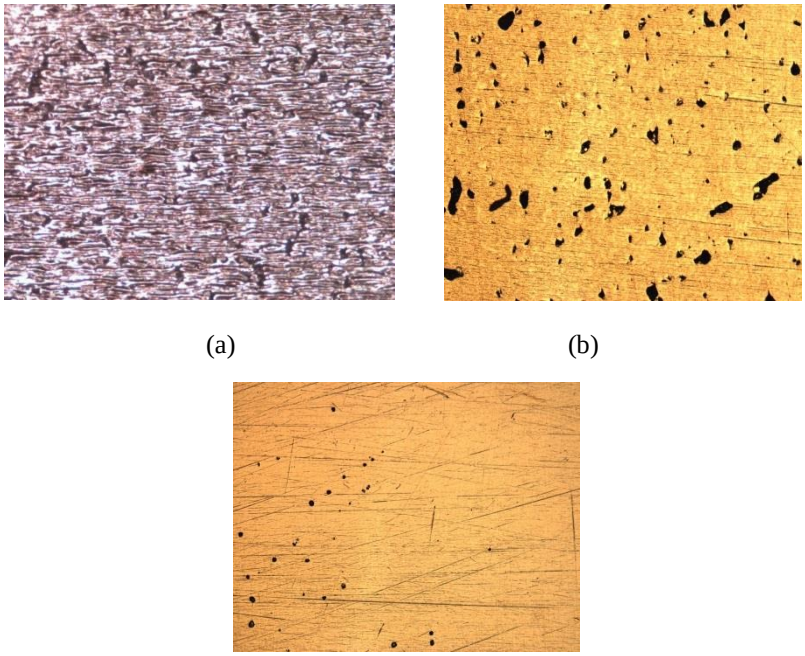

(a) (b)

(c)

Figure 60- Microscopic images of (a) from the surface of a porous layer corresponding to Zone III, (b) (cut and polished) cross section of a part built with Zone III parameters [50], (c) cross section of a part built with Zone II parameters [50].

As it was seen in this chapter, it is possible to visually examine surface characteristics, quality of fusion, and formed porosity in camera images from each build layer for a variety of build parts. However, this examination so far was performed manually. For in-situ inspection of part quality and defects to be feasible, this examination should be performed automatically. After creating a dataset of images that visualize a variety of build surfaces with different characterstics and levels of porosity, it is now possible to automatically detect pores or assess part quality. The dataset of images described in this chapter will be used for detection of pores and identification of porosity which are the topics of CHAPTERs VII and VIII. To perform and evaluate the detection of fused geometries, however, the earlier created database as described in Section 4.1 (see Figure 44) will be used.

CHAPTER VI

DETECTION OF FUSED OBJECTS

As mentioned in Chapter III, the images of the layers in L-PBF contain the objects within the layer of powder. To search for any defect of the part, the fused regions should be detected from the visual image by image segmentation. Additionally, the result of segmentation of fused regions can be used for detection of geometric objects and consequently the study of dimensional accuracy as previously mentioned in Chapter III. In the following sections, a series of image processing techniques will be designed and implemented to detect fused objects from the layer. For this purpose a set of image processing algorithms will be used; explanation and performance of these algorithms can be found in [106, 110, 116, 126-131].

It was mentioned in Chapter II, that some researchers including Kleszczynski *et al.* [12], captured images from AM layers that showed the fused object from the layer of powder. They used their camera images for detection of elevated regions that may cause coater collision. While the imaging setup at EWI was being developed, it was worthwhile to investigate the possibility of inspection of the geometry from these types of images. Section 6.1 presents results of analyses of an image adopted from [12] for inspection of geometry. These attempts provided insight into characteristic of images that have impact on accuracy of image segmentation algorithms.

As the work on development of the imaging setup was progressed, different sets of images were produced. Each set was examined to determine whether fused objects can be detected with sufficient accuracy. This chapter presents results of analyses of two sets of these images. The first set includes the set of images that the example image in Figure 41 was captured. The first set of images, covered in Section 6.2, was analyzed to identify

the image characteristics that interfere with accurate fused object detection. Section 6.3 covers the second set of images, including Figure 44, that were meant to be used for inspection of geometry as was mentioned earlier in Chapter III. For this set of images, images were analyzed thoroughly and image processing algorithms were developed for detection of fused objects and the performance was evaluated.

6.1 Example of a Noisy Low-Contrast Image

Figure 61 shows an image of a layer built with L-PBF, adopted from [12], as an example image. It is desired to segment the fused regions as shown in the figure from the powder layer. As it is seen the image is noisy and shows very little contrast between the powder region and the fused regions. Additionally, there are some non-uniformities in the powder region due to the non-uniformity in illumination. Also there are several dark marks in form of lines formed in the powder region due to the coater wear. All these factors make segmentation of the fused objects very difficult. Appropriate segmentation techniques should be developed for this image to compensate for low-contrast, noise, non-uniformities, and undesirable marks and to segment fused objects from the powder with satisfactory precision. The segmentation techniques developed for this type of image may not be applicable to other images especially those produced by the camera images from our setup. However, this image is presented as an example of design and implementation of segmentation of fused objects from camera images and the difficulties that may be encountered. It also provides insight into the characteristic of the image that have impact over the efficiency of image segmentation. Also, once segmentation techniques are developed for this image, similar techniques with modification can offer potential techniques for images in our setup as well as other camera settings and setups.

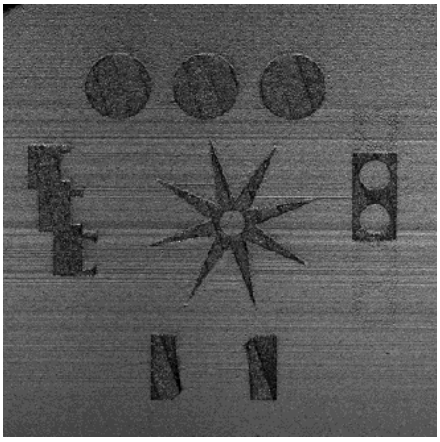

Figure 61- An image of a layer made with laser powder-bed AM [12]

As mentioned earlier, the variation of intensity and non-uniformity of the regions in Figure 61 makes segmentation a difficult task. Wiener filter was applied to the image to remove the noise. Initially some of the basic techniques such as Otsu thresholding and edge detection were applied to the image. Despite selection of most efficient noise removal filter size, these algorithms did not lead to efficient segmentation of fused objects, as seen in Figure 62. Canny edge detection, in the automatic manner produced completely erroneous results. When the parameters of Canny were manually selected after more than ten trials and errors for this specific image, the segmented boundary showed much better agreement with the true boundary. However, these parameters were only obtainable manually and not automatically. Still in the result, there are also some edges that do not correspond to the true objects. Additionally, many portions of the object boundaries have not been detected at all. Applying boundary tracking operations did not lead to detection of the whole boundaries either. Additionally, this manual trail-and-error selection of Canny parameters is very specific to the image.

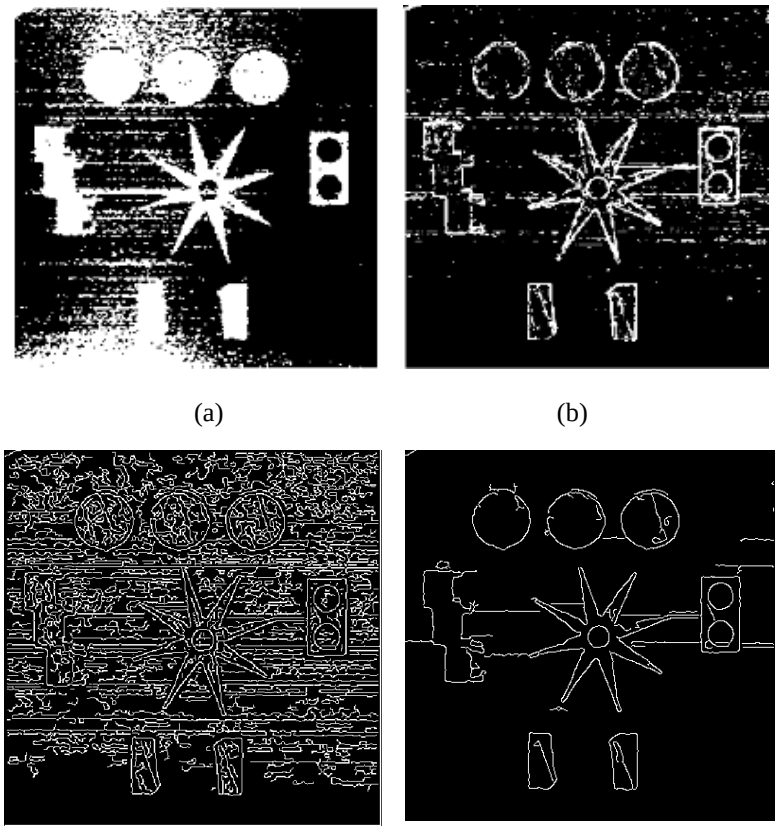

(a) (b)

(c) (d)

Figure 62- Results of attempting some of the image segmentation techniques applied to Figure 61 for detection of fused objects. (a) Optimal Otsu thresholding, (b) local thresholding by local standard deviation, (c) Canny edge detection, (d) Canny edge detection with manually selected parameters after about 10 trials.

Among the techniques attempted, the following technique provided relatively better results and is described briefly. After noise removal by Wiener, the histogram of the image (shown in Figure 63) showed a rather bimodal behavior that suggests thresholding can be used to separate these modes. Histogram of an image shows the number of pixels (vertical axis) of a specific intensity versus the intensity range, [0-255] or [0-1], in horizontal axis. Applying thresholding nearly segments the objects, but leaving lots of internal and external noise (Figure 64 (a)). After clearing the border to remove the border noise, the morphological operation of "opening by reconstruction", [106, 129] is used to remove the external noise while maintaining the original shape of segmented objects (Figure 64 (b)). Internal noise is removed by closing (Figure 64 (c))

to yield the final image. Figure 64 (d) shows the final result superimposed with the original image.

This algorithm was designed only for this specific image and the parameters were manually chosen to improve results specifically for this image. As it is seen in Figure 64 (d), some of the objects and some parts of the boundary have been segmented well, however, there are several very large local errors between the detected boundary and the true boundary of the fused object. The error between the two was measured as large as 2 mm.

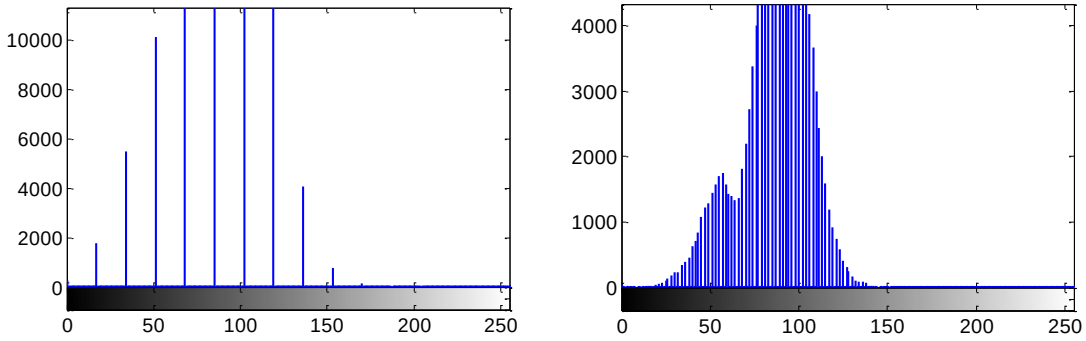

Figure 63- Histogram of the original image (left), histogram after Wiener filtering (right).

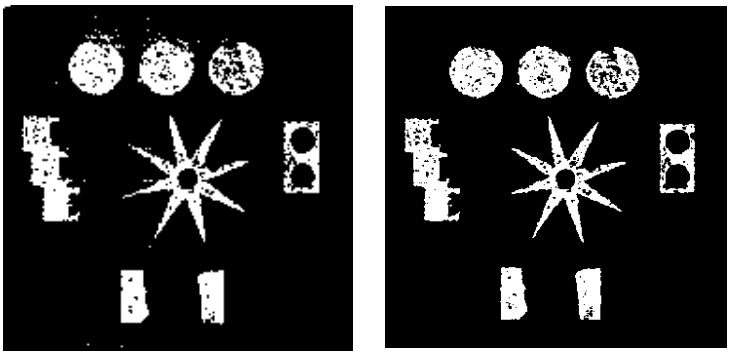

(a) (b)

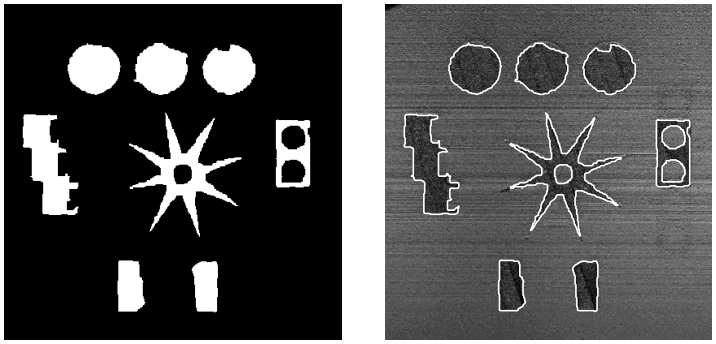

(c) (d)

Figure 64- a) Result of thresholding by histogram study, b) after clearing the border items and applying opening by reconstruction, c) after closing, d) superimposing with the original image.

6.2 Camera Images of the Build Layer by the Camera Setup at EWI- Dataset before Modification

The image analyzed in Section 6.1 showed an example of an image of a layer during the build of a part made of Nickel alloy captured through a specific camera and illumination setup. Development of segmentation algorithms were attempted to show that in order to detect fused objects accurately, cleared images with better resolution would be needed.

In this section, it will be attempted to detect fused objects from camera images captured at the imaging setup in this work. As mentioned earlier algorithms developed for a specific image, imaging setup, and material are not applicable to the camera images from the parts made of Inconel 625 from the setup at EWI due to different level of noise, illumination, camera resolutions (or image pixel size), and materials.

To develop appropriate segmentation algorithms, true images were captured at our setup from the powder layer at each layer during the build of a block. Figure 65 shows an example image taken from the powder bed during this build. This image belongs to the set of image captured with a 2 megapixel camera, and the while, high intensity LED spot light mounted in the top of the machine at an angle from the build. As

seen, the characteristics of this image are different from those of Figure 61. Image segmentation algorithms should be developed to segment the fused object (in this case, the square) from the powder layer.

The size of the square is 10 mm ×10 mm and the resolution of the whole image is 1080×1920 pixel. The on-part pixel size was measured as 20 microns and the number of pixels along the side of the square is 50 pixels.

It was investigated that the coloring information does not offer notoceable improvement in segmentation. Therefore, segmentation algorithms are developed based on intensity and the color image is converted to gray scale. However, as will be seen the color information will be used for segmentation of the laser spot and removing it from the results of segmentation of the square.

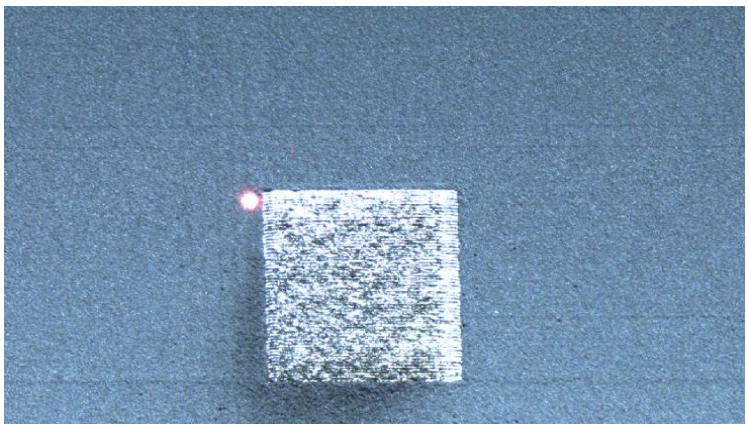

Figure 65- Image of the powder layer during build of a block- setup at EWI

To improve the efficiency of image segmentation, a noise removal filter is applied. Based on the characteristic of the noise in the image which appears as white dots and occasionally black dots (i.e. similar to salt and pepper noise), median filter is one of the most efficient noise removal filter for this type of noise [132, 133]. A median filter of size 3×3 seems to be satisfactory for removing the noise and not affecting the segmentation results. The result of median noise removal filter is seen in Figure 66.

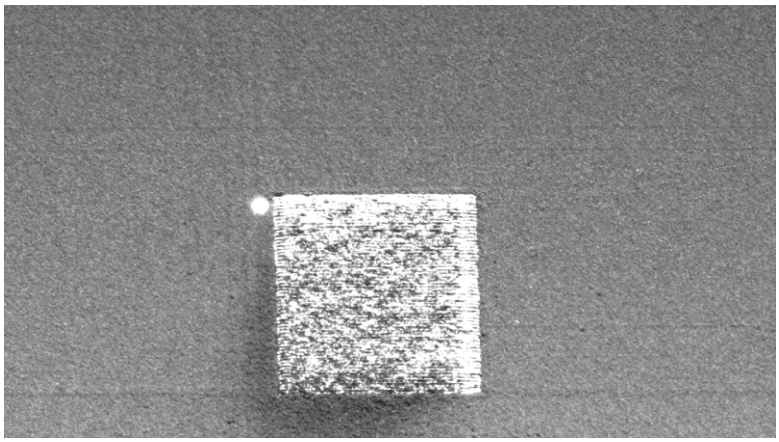

Figure 66- Result of converting Figure 65 to gray scale and applying a 3×3 median filter.

From Figure 66, it is seen that the intensity of the fused region in general is higher than the powder region. This characteristic suggests use of thresholding. It is desired to find the best threshold value that can segment the square well enough without too many miss-segmentations. The histogram of the original image is shown in Figure 67 (a). To find appropriate thresholds, based on the technique proposed in [134], the histogram of the powder region is examined in contrast with the histogram of the whole image, as shown in Figure 67 (b). For this, several regions including only powder were cropped from the main image to obtain the histogram of the powder region. The normalized histogram of the whole image is plotted in contrast with that of image of powder region. The normalized histogram is the histogram values divided by the number of pixels of the image that can also be regarded as probability of existence of an intensity value in the image.

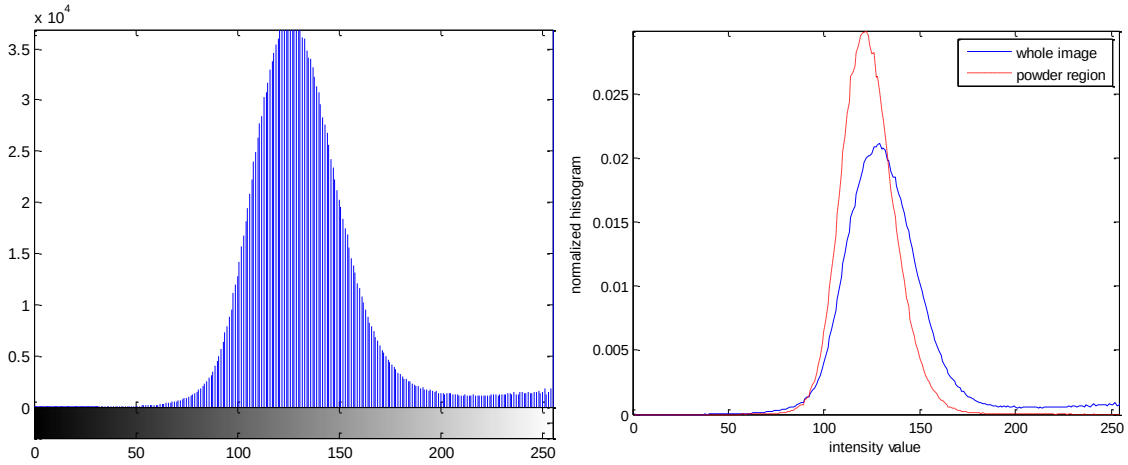

(a) (b)

Figure 67- (a) Histogram of Figure 66, (b) normalized histogram of the whole image in contrast with that of image of powder regions

As seen in Figure 67 (b), the powder region histogram extends in the range of 30 to almost 200. Therefore, these values are selected for thresholding of Figure 66. The result of thresholding is seen in Figure 68. As seen, the square has been segmented efficiently with few miss-segmented dots in the powder regions as well as the miss-segmented laser spot. The square itself is not segmented solid which was expected since the fused regions do not show uniform intensity variations and has overlap with the intensity range of the powder region as seen in Figure 67. Therefore, further image processing operations should be performed to segment the whole solid square and remove the miss-segmentations. It should be mentioned, that selection of these thresholds was also verified by manually adjusting the thresholds and observing that the consequent thresholding leads to degrading the final results (towards segmenting the solid square). The size of the median filter was also optimized by observing the fact that increasing the size would cause many small regions of the fused region to be filtered and not to be segmented in the result of thresholding.

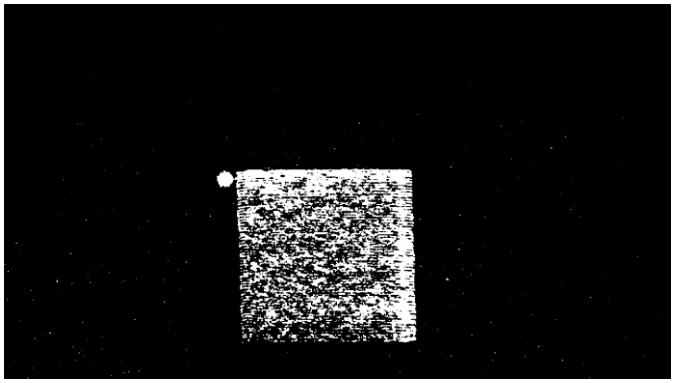

Figure 68- Result of bi-level thresholding of Figure 66.

As seen in Figure 68, the density of segmented regions is higher in the fused region. This characteristic can be used to segment the square in a solid way and remove the isolated noisy dots. To use the density characteristic, a correlation with a neighborhood mask can be implemented. However, since the laser spot is in the neighborhood of the fused object, the neighborhood mask would include the laser spot in the solid square. To resolve this problem, two ways are suggested. Changing the imaging setup such that the laser setup is not captured in the image or segmenting the laser spot using image processing. Given the current data from EWI setup, we would choose to segment the laser spot using image processing. The next sets of data after the adjustment of imaging setup, however, will not have the issue of laser spot.

To segment the laser spot, the best technique is to use the color information as the laser spot is characterized better by the red boundary as seen in Figure 65. The steps of segmentation of the laser spot are shown in Figure 69.

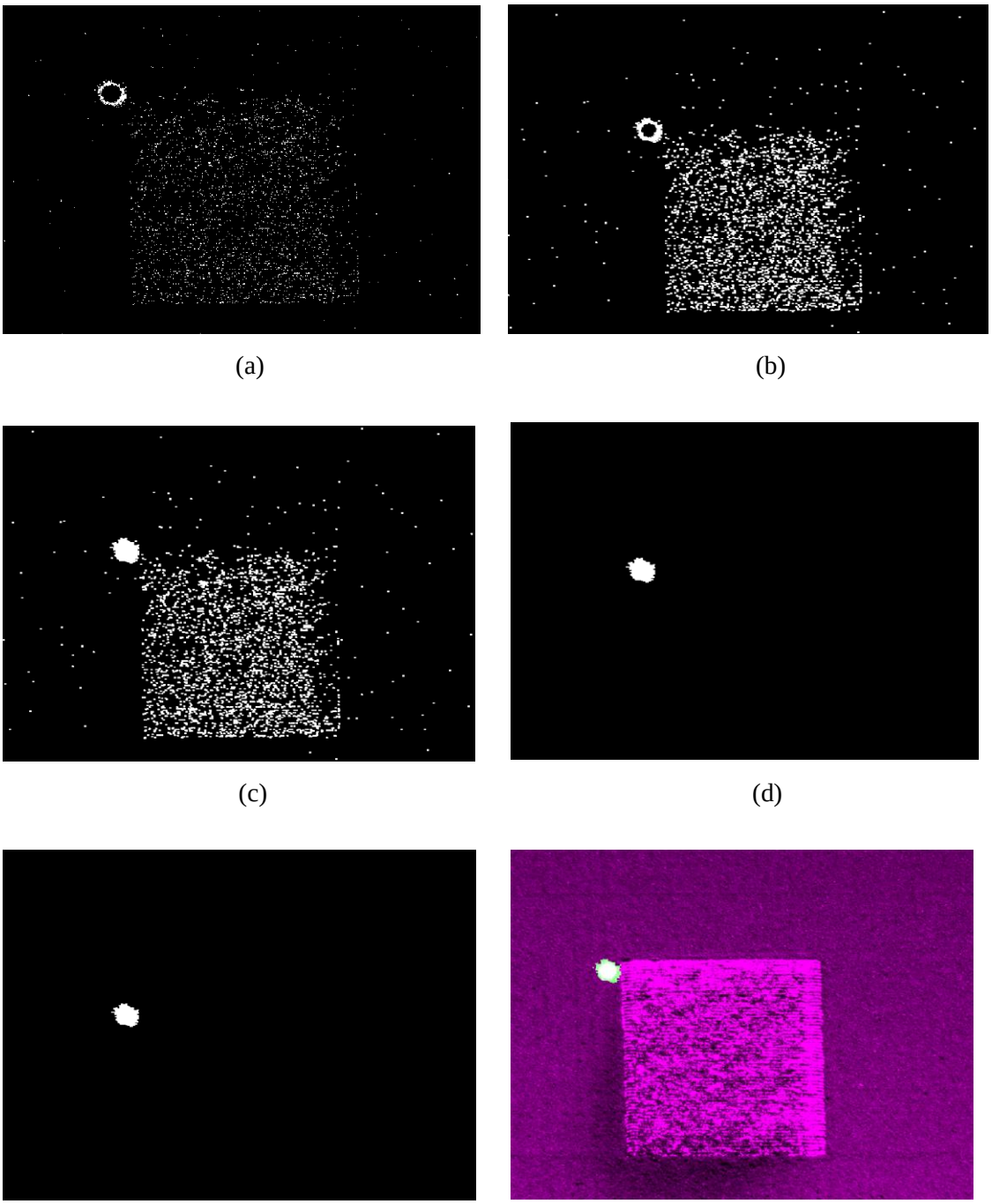

Figure 69- Different steps to remove the laser spot: (a) thresholding of dominantly red regions, (b) dilation of the results to make sure about the connectivity of the laser spot boundary, (d) morphological filling of the enclosed regions to fill in the laser spot, (d) selection of the largest object, (e) results after erosion to restore the size of the segmented laser spot, (f) superimposing the result on the original image.

Figure 69 (a) shows the result of thresholding of the regions that are dominated by red color. These regions were selected by three thresholds of red larger than 180 and green and blue components smaller than 250. These thresholds were selected to best capture the boundary without too many miss-segmentations. Figure 69 (b) is the result of Figure 69 (a) after applying a dilation [106, 116, 130] by a mask of ones of size 3×5 to ensure the connectivity of the boundary of the laser. Figure 69 (c) is the result of implementing a filling operation to fill the holes in enclosed regions. Filing yields turning the laser spot into a big solid object that is the largest object in the image. By keeping the largest object in the image and removing the smaller objects, Figure 69 (d) is obtained. Figure 69 (e) is obtained after implementing erosion by the same mask to restore the original size of the segmented laser spot before dilation. Subtraction of Figure 69 (e) from Figure 68 removed the laser sport from the segmentation results, as shown in Figure 70.

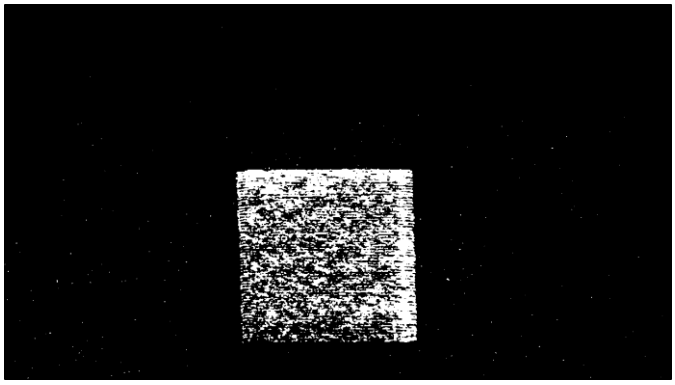

Figure 70- Result of thresholding to segment the square after removal of the laser spot

As it was seen in Figure 69 (a), the segmented boundary of the laser spot is enclosed and therefore there was no need for dilation, however, the algorithm must perform desirably for all the images. After implementing the algorithm to four images of the design subset, the need for dilation and erosion was identified and the algorithms

were appropriately designed and parameters were chosen. The algorithm was then implemented to the test subset of 14 more images and it was proved to perform effectively.

The factors that make segmentation of the fused object a very difficult task is the rather non-uniform smoothness in laser powder fusion within the fused solid object. Segmentation of more of the fused region is achieved at the cost of segmenting more of the powder region. The rather non-uniform illumination on the image is the other factor that causes brighter regions in the top right corner of the square and darker regions (a shadow) in the lower left corner of the image. The dark region in the powder at the bottom left of the square necessitates selection of a smaller lower threshold that consequently leads to some dark regions within the square not be segmented. The aforementioned illumination problem was addressed in the next setup at EWI and relatively a more uniform illumination was achieved. This new set of data will be addressed in the next section.

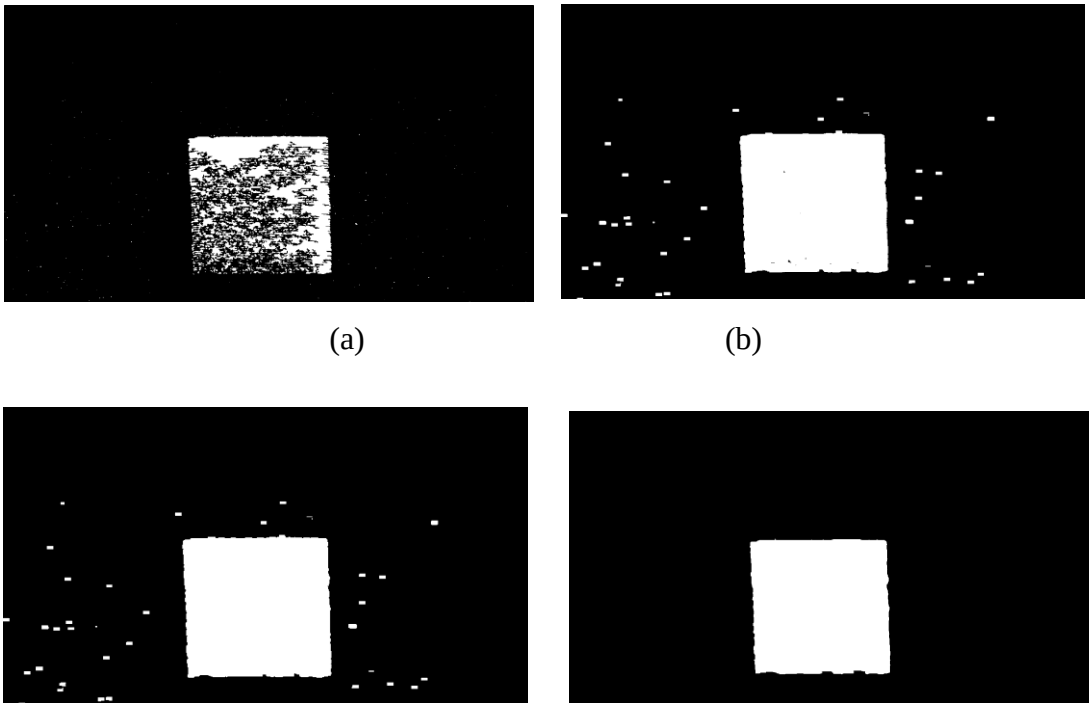

(a) (b)

(c) (d)

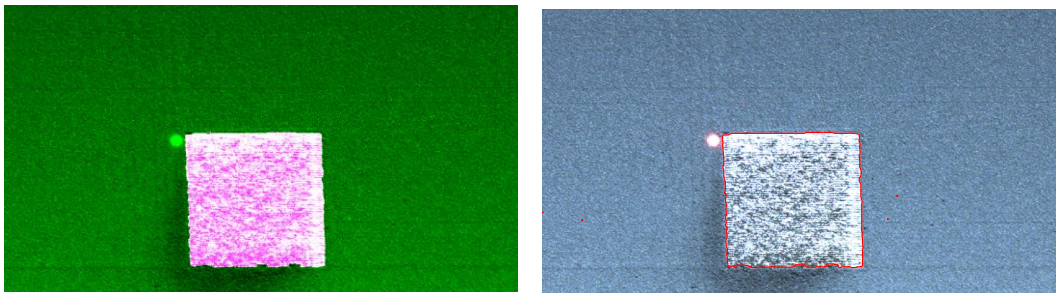

(e) (f)

Figure 71- Segmentation of the solid square: (a) Result of implementing “fill” operation to Figure 70, (b) after implementing the correlation by the top-neighborhood mask and applying the neighborhood threshold, (c) after filing operation, (d) after applying the erosion by the complement of the top-neighborhood mask to restore the size.

Figure 70 shows the square as distributed dots but not a solid object. Additionally the background (powder regions) contains a number of dots but at sparser distribution. To segment the square as a solid object, the characteristic of more dense distribution of segmented objects was used. First the “fill” operation was used to cover the internal parts that were not segmented and make it look more solid (as seen in Figure 71 (a)). Note that “fill” operation was only used in this section as a trial algorithm. Later, in Section 6.3, to design the final segmentation algorithm, “fill” will not be used to increase the generality of the algorithm to hollow objects. The “fill” operation could simply be replaced with a closing operation with a certain-sized mask that would not then have affected the internal geometric holes of sizes larger than the mask used for closing.

Next, the regions of large local distribution of white dots should be detected. Correlation of the image by a neighborhood mask of all 1’s could reveal the density of dots. Then by setting a threshold for the density only the regions of larger density can be segmented. However, since in some regions of the fused object, the dots are spars, the size of the neighborhood mask should be chosen relatively large which results in a large

expansion in the object. However, as seen, the top part of the fused object is segmented in a more solid way, and it is the lower part of the fused object that is sparser due to the non-uniform scanning or illumination from the fused region. As a result a neighborhood mask of size 25×25 was selected where the top half of the mask is all ones, and the bottom half is zero, as below:

$$top\ neighborhood\ mask = \begin{bmatrix} 13\ rows\ of\ all\ 1's \\ 12\ rows\ of\ all\ 0's \end{bmatrix}_{25\times25}$$

Equation 9

This selection of mask was seen to produce better results. The result of correlation of Figure 71 (a) with this mask and selection of a threshold value of 5, yields Figure 71 (b). The boundaries of the solid object are segmented efficiently, and the internal holes are then covered by a filling operation as seen in Figure 71 (c). To remove results of expansion, erosion by the complement of the neighborhood mask is performed. The complement mask is shown in Equation 10. The noisy dots are removed by opening, eliminating single small objects. The result of these operations is seen in Figure 71 (d). As seen in Figure 71 (e) and (d), the square is segmented very efficiently.

$$bottom\ neighborhood\ mask = \begin{bmatrix} 13\ rows\ of\ all\ 0's \\ 12\ rows\ of\ all\ 1's \end{bmatrix}_{25\times25}$$

Equation 10

The series of these algorithms and appropriate masks and parameters were designed based on a set of 4 design images. The segmentation algorithms were then implemented to 10 images in the test subset and the efficiency of the algorithm was confirmed in segmentation of the fused object. Figure 72 shows the result of implementing the designed segmentation algorithms to some of these test images. In all the images, the maxim distance from the true boundary of the fused square and the

segmented square was measured as 9 pixels which is less than 200 microns i.e. a maximum error of 0.2 mm in segmentation, given the pixel size of 20 microns. It is well expected by increasing the image precision (decreasing pixel size), higher segmentation precision will be achieved with these segmentation techniques. Therefore, the next set of images captured by the modified imaging setup, as in Figure 44, that is considered in the next section, Section 6.3. In addition to increasing the pixel size, it was seen that illumination can be adjusted to increase the lighting uniformity throughout the image.

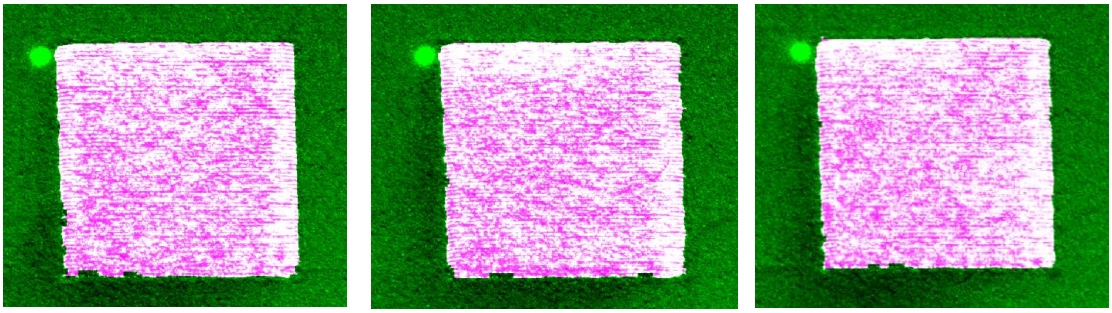

Figure 72- Results of implementing the designed segmentation algorithms to several of the test images.

6.3 Camera Images of the Build Layer by the Camera Setup at EWI- Dataset after Modification

After providing feedback on the existence of the laser spot in the images, camera resolution, and the illumination, the imaging setup at EWI was modified as mentioned in Section 4.1, to provide better resolution and remove the bright spot. Figure 73 shows an example of an image captured at the modified setup. This section presents the design procedure and final results of algorithms for geometry segmentation applied to these sets of images. This section comes in two subsections. The first subsection (6.3.1) presents an initial analysis of the image intensity and characteristics, and algorithms that might potentially lead to satisfactory results. Subsection 6.3.2 presents the final algorithms of geometry segmentation for these images that were designed based on the knowledge

inferred from the analyses in Subsection 6.3.1. The algorithms designed in this subsection (6.3.2) lead to satisfactory segmentation of the fused object. Examples of results of implementation of these algorithms to square objects and several arbitrary objects will also be given. These algorithms are then evaluated in Section 6.4.

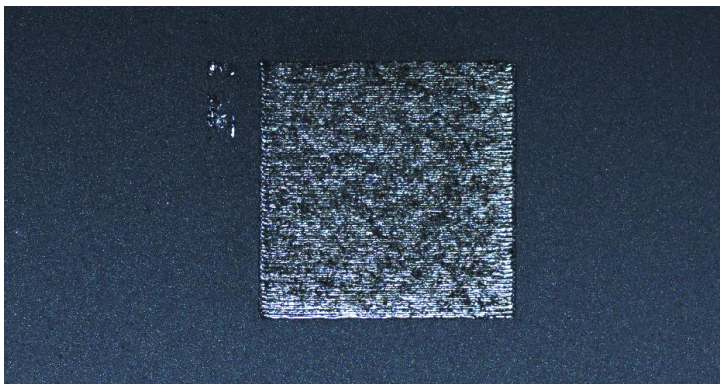

Figure 73- Example of an image captured from the build at the setup after modifying camera and illumination.

6.3.1 Initial Analysis and Algorithm Trials

The size of the new camera images are 2160×4096 pixels. The image pixel size is about 6.9 microns and the 10 mm side of the fused square of is captured by about 1455 pixels. It is desired in these images to segment the fused square objects. The small fused regions at the top left corner of the square were produced as an attempt to label and distinguish different layers. Therefore, despite being segmented in algorithms, they are not the objective of the segmentation and they are not used in design and assessment of the algorithms. This decision is also justified by the fact that some parts of the numbering region are only 1 scanning-width wide which is not fused precisely and that some parts are within the expected detection tolerance, which will be discussed later in the section.

It was determined, by examining the images, that the color information of the image does not provide any additional benefit for segmentation over intensity information. Therefore images are converted to gray scale images (Figure 74 (a)) and the

analyses are performed to gray images. As seen in Figure 73 and Figure 74 (a), the image contains sparsely distributed impulse (salt and pepper) noise which is better visible in the powder region. Therefore noise removal filters are implemented to the image in the pre-processing stage to remove the effect of noise as much as possible without noticeable impact on the important image information. A median filter of size 7×7 is applied to all images before image analysis. In other words, in in-situ inspection, after image of each layer is acquired, the image is converted to gray scale and the median filter is applied. Figure 74 (b) shows the result of implementing these operations to Figure 74 (a).

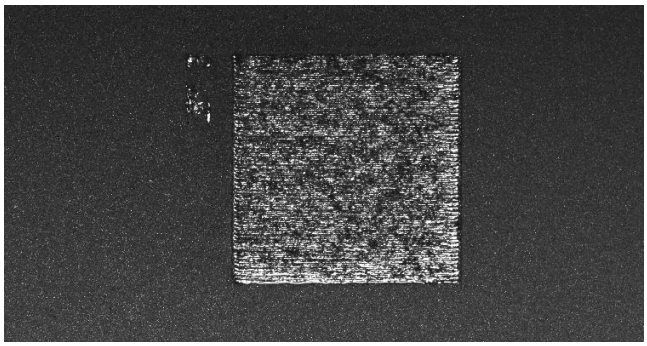

(a)

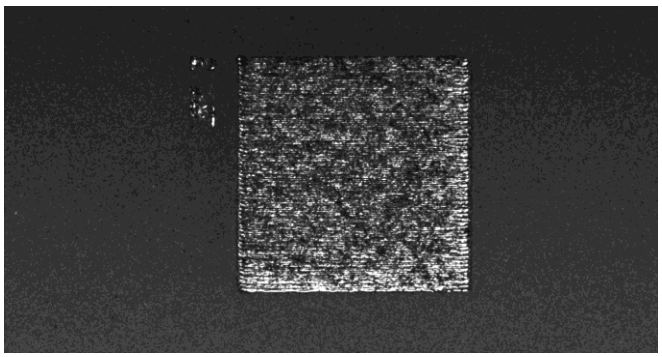

(b)

Figure 74- (a) Result of conversion of Figure 73 to gray-scale image (white noisy dots in the image should be removed to avoid their interference with segmentation results), (b) Result of conversion to gray image and applying a median filter of size 7×7 to Figure 73.

Common existing image segmentation techniques include various methods of thresholding (including global and locally adaptive methods), edge detection,

morphological operations, pattern matching, region growing, etc. [106-108, 110, 112, 114, 116, 135-137]. Each technique is more appropriate for specific characteristics of images and objects of interest. By examining the captured camera images from the AM build layers, it was investigated and determined that none of these algorithms by itself can lead to satisfactory results. Figure 75 shows examples of common image segmentation techniques such as optimal Otsu thresholding and edge detection to the image in Figure 74 (b). However, since fused regions are generally specified by several bright concentrated spots, pixel-level segmentation based on thresholding is considered helpful as a stage in the design of the final algorithm.

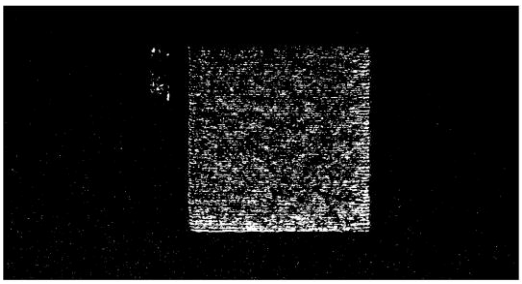

(a)

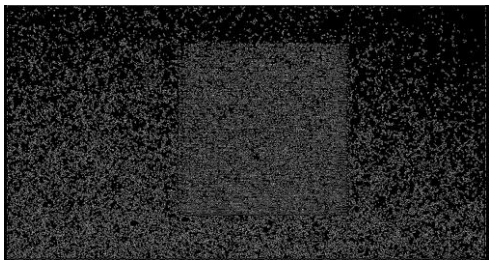

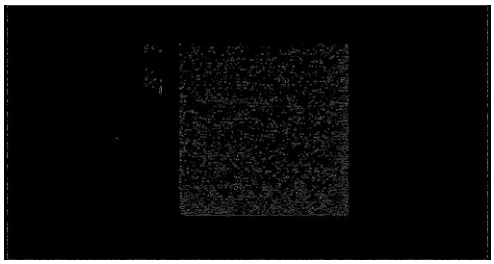

(b) (c)

Figure 75- Results of implementation of several representative common image segmentation techniques to image in Figure 74 (b): (a) Optimal Otsu thresholding, (b) Canny edge detection (automatic), (c) Canny edge detection with manually selected parameters.

To use thresholding, the histogram of the image is studied. However, as seen in Figure 76, the histogram of the whole image only has one mode and does not illustrate the range of gray values belonging to the fused region and powder region. Therefore, to find appropriate thresholds, instead of the common study of the histogram of the whole

image, the histograms of the powder region and fused region are extracted and compared as suggested in [134]. For this purpose, the regions only encompassing powder regions, and the regions only encompassing fused regions are extracted manually and used for histogram analysis of each region individually. Figure 76 (a) shows the histogram of the powder and fused regions versus that of the original image (containing the fused object). Figure 76 (b) shows the normalized histogram and probability distributions of the powder region versus the fused region.

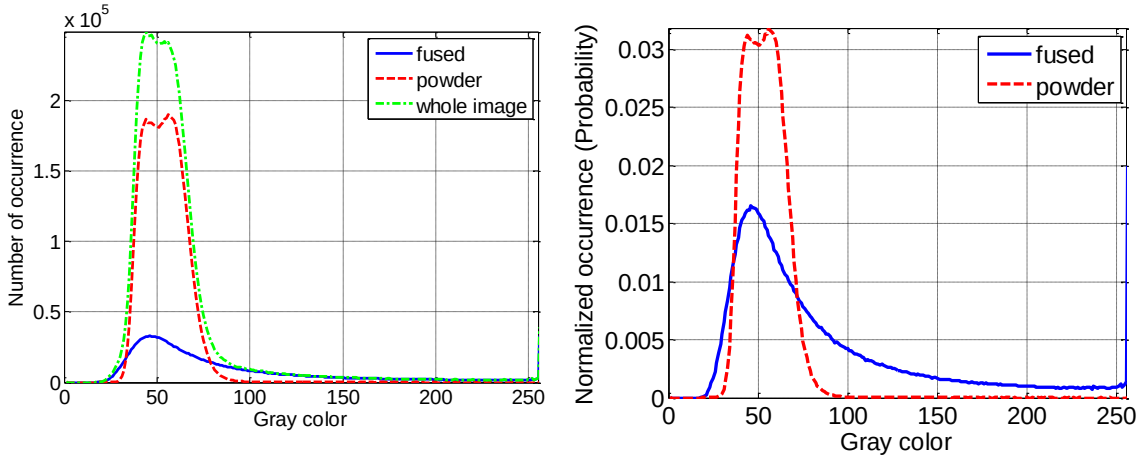

(a) (b)

Figure 76- Histograms and normalized histograms of the fused region versus the powder region and versus the whole image.

As seen in Figure 76 (b), the histogram of the powder region almost reaches 0 at the lower end of 20 and at upper end of 125, and this range almost covers the entire powder region range. Therefore these two values are selected as thresholds that would eliminate almost the entire powder region (about 99.999% of background pixels). These two values are marked in Figure 77 by two vertical green lines. Therefore these two values are selected as thresholds that would eliminate almost the entire powder region.

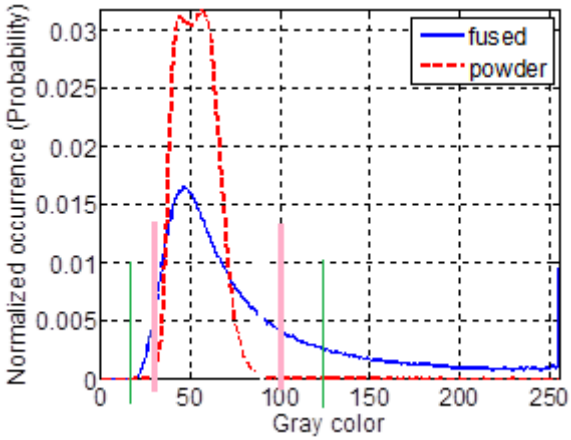

Figure 77- The two pairs of thresholds selected at the wider and narrower band of histogram of the fused powder.

The result of thresholding of Figure 74 (b) by these threshold values, 20 and 125, is given in Figure 78. As expected, there are very few small miss-segmentations in the powder region, however, the fused region is also not segmented as a solid object and instead consists of densely distributed segmented small regions. Choosing thresholds at the narrower band of powder region intensity range (such as 30 and 100) allows the fused region to be segmented more densely, however, this will be achieved at the cost of large regions of powder being segmented and leading to large errors as will be seen in Figure 81. This pair of thresholds that removes a narrower band of the fused region is shown in Figure 77 as two pink vertical lines along with the pair of thresholds that was already used for obtaining Figure 78 that removes a wider band of the powder region.

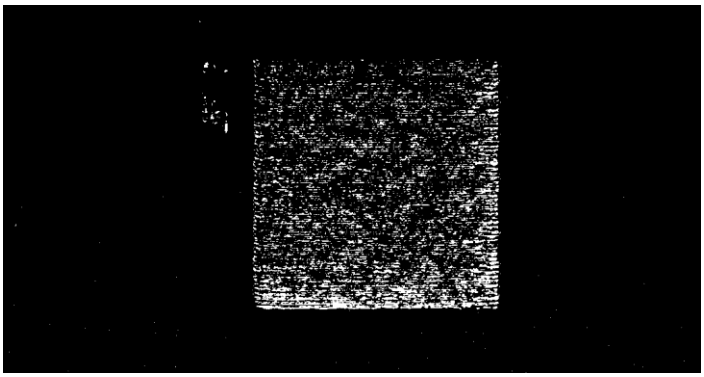

Figure 78- Result of thresholding Figure 74 (b) by the thresholds selected by histogram comparison, i.e. 20 and 125.

Similar to the image set in the previous section, areas corresponding to the fused regions are associated with larger concentration of segmented dots in the thresholded image. Therefore, a cross correlation with a mask whose sizes determines the size of the neighborhood of an examined pixel can help with finding the density of the segmented dots within that neighborhood of the pixel.

Although the final results for this specific image are not affected very much, the neighborhood mask for the new set of images is chosen as a bottom neighborhood mask where the bottom half is ones. This selection is made to match the reasoning that for the upper part of the square which is segmented sparsely, a region is in the fused object if its close bottom neighborhood satisfies the density threshold. It will be seen that this choice will be helpful in final segmentation results for all the images in this set. Therefore, the neighborhood mask is chosen of size 75 (due to larger image resolution) and selected as:

$$bottom\ neighborhood\ mask = \begin{bmatrix} 37\ rows\ of\ all\ 0's \\ 38\ rows\ of\ all\ 1's \end{bmatrix}_{75\times 75}$$

Equation 11

The threshold density is chosen as 15. To remove the effect of expansion due to cross-correlation, similar to Section 6.2, erosion is performed. The erosion mask that led to rather satisfactory results was found to be the complement mask of the cross-

correlation mask given in Equation 11, that is presented in Equation 12. The results of correlation of Figure 78 by the above mask, erosion by the complement mask, shown in Equation 12, and the final segmentation are given in Figure 79. The deviation of the segmented boundary from the true fused object is due to the larger density threshold and size of chosen mask to capture the more sparsely distributed regions within the fused object. These deviations can even get more severe in other cases of images (see Figure 80).

$$top\ neighborhood\ mask = \begin{bmatrix} 37\ rows\ of\ all\ 1's \\ 38\ rows\ of\ all\ 0's \end{bmatrix}_{75\times75}$$

Equation 12

(a)

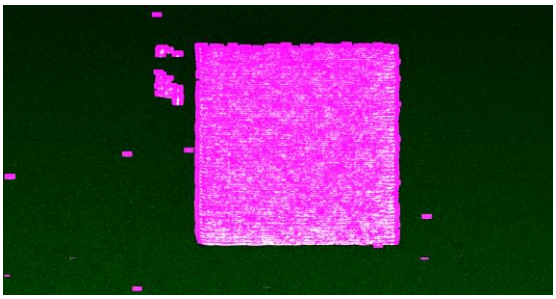

(b)

(c)

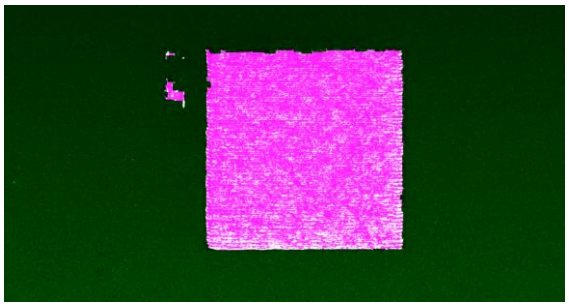

(d)

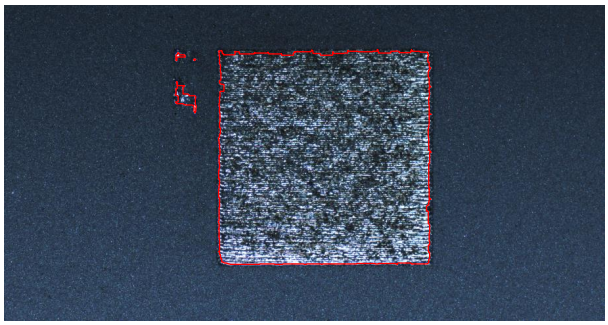

(e)

Figure 79- Segmentation of fused region: (a) and (b) correlation by bottom neighborhood mask respectively: binary image by itself and overlapped on the original image (Figure 73), (c) and (d) erosion by the complement mask, respectively: binary image by itself and the overlapped with the original image, (e) overlap of the boundary of the segmentation results with the original image.

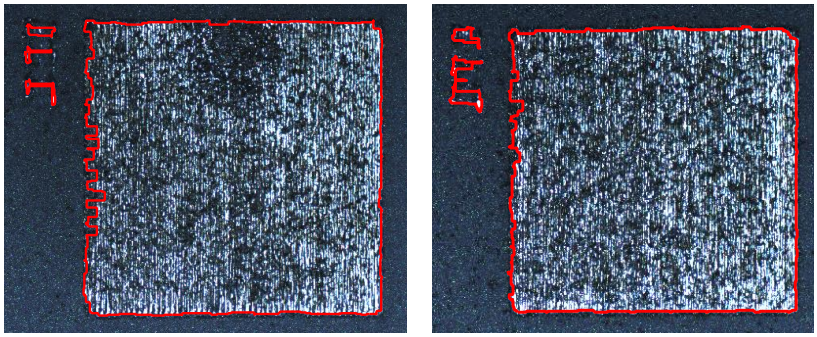

Figure 80- Examples of application of segmentation of fused regions based on applying one set of thresholds at the far extents of the fused region histogram, i.e. 20 and 125.

However, if the distribution of these segmentations could be increased by choosing a narrower band of thresholds in histogram and consequently smaller mask, the fused object boundary would have been segmented with a smaller error. Figure 81 shows the result of choosing thresholds that would increase the density of the segmentations in the fused region. For this example, these thresholds were chosen as 30 and 100. But as seen, this leads to more miss-segmentations in the powder region. Although 0.01% of background pixels are eliminated by this selection of thresholds, the few remaining mis-segmented regions of the background lead to large errors for segmentation of the square.

This is due to the fact that the choice of the neighborhood mask can cause the nearby segmented powder regions to be merged with the solid fused object. Although these miss-segmentations are very small, they lead to a large error in the final results (Figure 81 (b) and (c)).

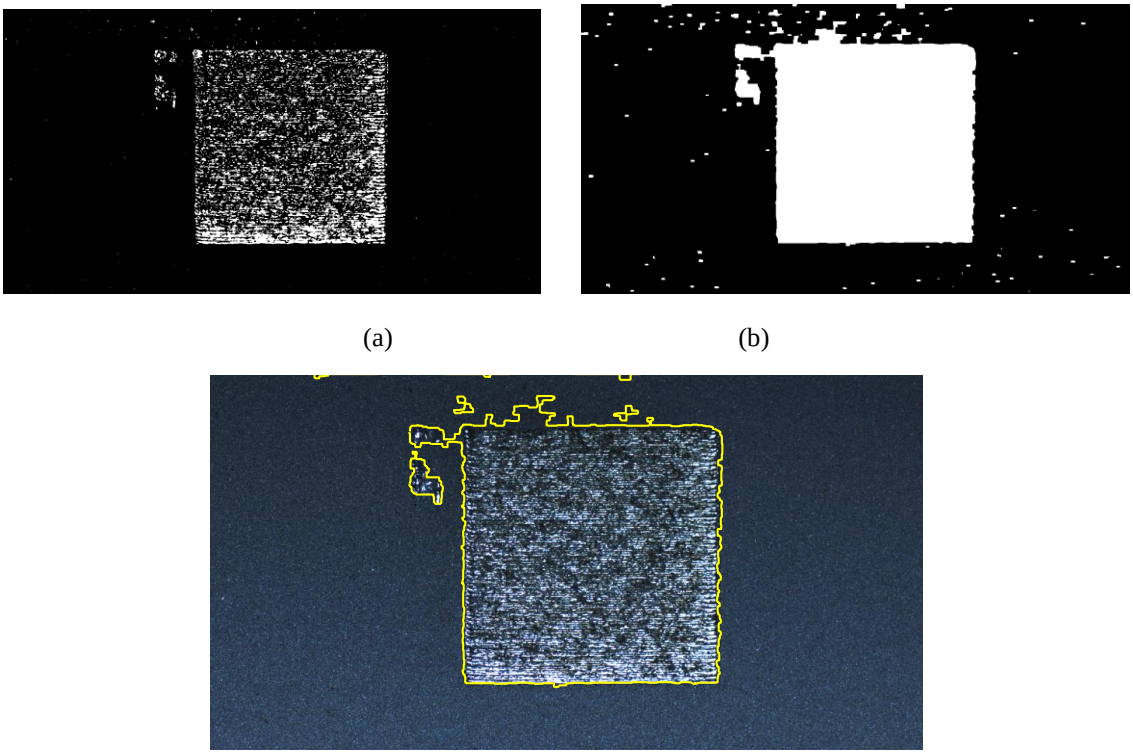

(a) (b)

(c)

Figure 81- (a) Result of thresholding of by a different threshold (by narrow threshold bands of the powder region to segment more of the fused region (30 and 100)), (b) and (c) the resulted errors in final segmentation.

It was seen that a denser segmentation in the fused region is obtained at the cost of more miss-segmentations in the powder region that cause larger error in the final result. However, if an approximated region for the powder and fused object could be estimated and the powder region would have been removed, the miss-segmentations in the powder region would have been avoided leading to the ability to choose larger band of thresholds. This idea is implemented in the following subsection and it is seen that the results will improve the precision of segmentation of the fused objects for all the images

in this set regardless of the defects occurring close to the boundary. The algorithms in the next subsection, at an intermediate stage, provide an over-approximation of the fused region that allows for part defect inspection to be performed within the part. Knowing this estimation will allow defect detection to be performed within this region and increases the chance of every defect being inspected. Defect detection will be addressed in Chapter VII.

6.3.2 Image Segmentation Algorithms for Detection of the Fused Geometric Objects from Camera Images

This section presents the finally designed image segmentation algorithm for detection of the fused geometric object from the powder bed in the set of camera images that were selected for the purpose of geometry inspection. This set of camera images, as mentioned earlier, were captured with a 8.8 megapixel camera and a while LED spot light mounted in the ceiling of the build chamber lighting the build platform from an angle (Figure 40). Examples of these images were shown in Figure 44 or Figure 73.

The algorithm described in this section contains of two stages: 1) Obtaining an over-approximation of the fused region using a set of threshold values at the far extents of the powder histogram to almost remove entire the background, and then use appropriate cross-correlation to get an over-approximation of the fused region, and then extracting this over-approximation from the original gray-scale image. 2) Implementing a second set of threshold to the new gray-scale image containing over-approximated fused region such that to get dense segmentation within the fused region and then implementing appropriate cross-correlation and erosion to segment the object closely to the boundary. The steps of the algorithm are represented in the flowchart given in Figure 82 and will be explained in detailed in the following of this subsection.

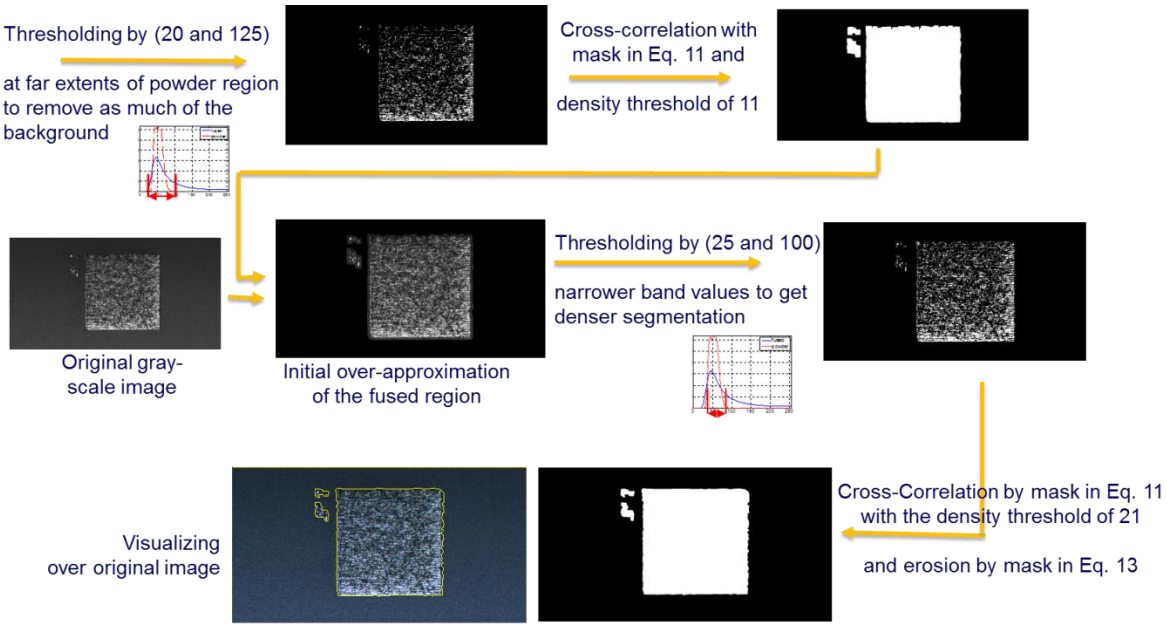

Figure 82- The flowchart representing the stages of the algorithm, designed and described in this subsection, for segmentation of the fused geometric object from camera images meant for inspection of geometry.

The following procedure allows segmentation of an approximate region closely covering all fused regions. This will allow a broader intensity range to be chosen for thresholding the fused region. It will also allow for search of defects within this region to make sure all defects are examined.

Consider again the gray scale image of Figure 73 and applying a median filter of size 7×7 and applying the thresholds at the far extents of the histogram of the powder region (20 and 125) to yield Figure 83. The selection of 7 for filter size was made to remove as many white dots in the powder region as possible and to avoid an unnecessarily large filter.

Applying a neighborhood mask of ones of a relatively large size of 75×75 pixels, Equation 11, and setting a relatively low density threshold of 11 allows for segmentation of regions with low density that would encompass all the fused regions and provides an over-approximation. Segmented objects of areas of lower than the mask size (75×75) are removed to avoid segmentation of the regions encompassing a single small region of

white dots in the powder region that were not removed by median filter. Figure 84 shows the result of these operations. The figure clearly shows that all fused regions are covered in the segmented regions.

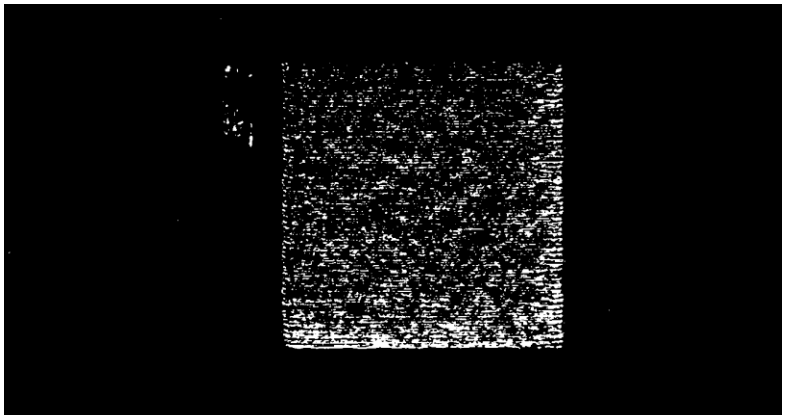

Figure 83- Result of median filtering and thresholding applied to the gray scale image of Figure 73.

(a)

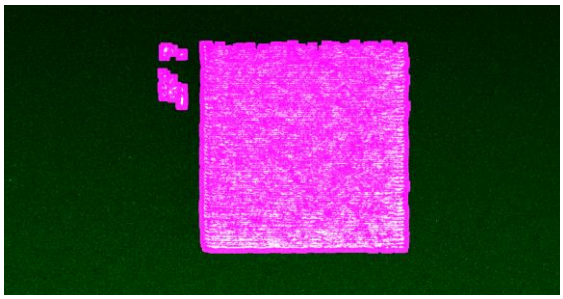

(b)

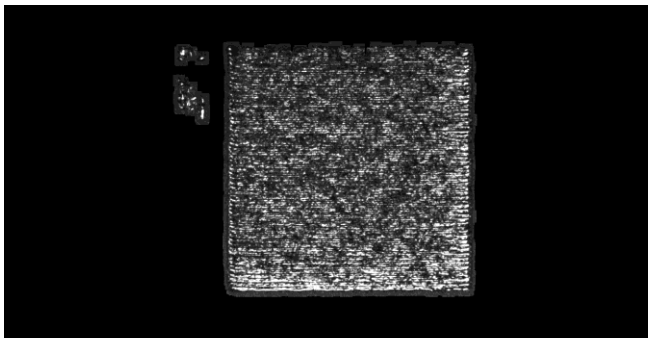

(c)

Figure 84- Result of segmentation of regions encompassing all fused regions: (a) binary image, (b) binary image plotted on the original image, (c) the gray scale image encompassing the fused.

After the encompassing region is segmented, the corresponding regions are extracted from the gray image after implementation of a median filter of size 5×5 (see Figure 84 (c)). The smaller selection of filter size is to maintain more segmentation of the fused regions. This selection is now possible because the segmented white dots in powder region now lie in the black regions that are already removed. Figure 84 (c) also allows the intensity range for thresholding be selected wider so as to lead to more of the fused region being segmented. The thresholds can be selected from Figure 76 now not necessarily at the extents, but close enough to the extents would be sufficient. These thresholds are selected as 25 and 100. After thresholding within the segmented, Figure 85 will be achieved which shows larger concentration compared to Figure 78 and with no miss-segmentations in the powder region.

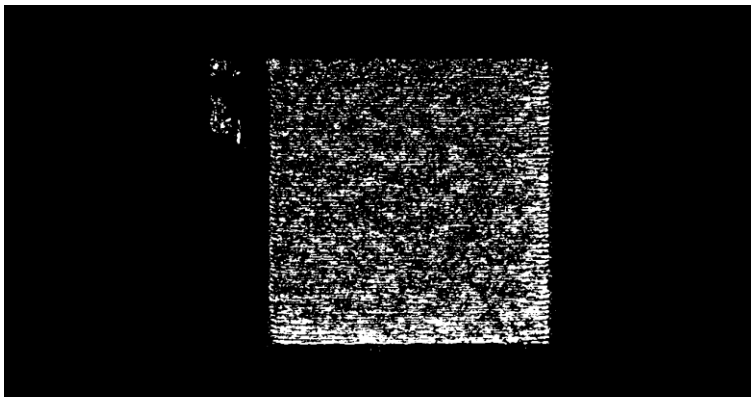

Figure 85- Thresholding of segmented regions in Figure 84 (c) by the new set of thrseholds of 25 and 100 (a wider band of segmentation).

Now from Figure 85, the regions associated with large density of segmented dots, should be selected as a solid object. Since the concentration is larger the density threshold is larger, and therefore was selected as 21. The neighborhood mask for cross

correlation operation to segment regions with high density was chosen as the bottom neighborhood mask of size 75×75, given previously in Equation 11. To remove the expansion and segment the boundary precisely, erosion should be performed as in Subsection 3.6.1. However, since the density threshold was chosen larger, this expansion was found to be much smaller and an erosion mask of as smaller size would be more appropriate and would lead to more precise boundary segmentation and smaller errors. The appropriate erosion mask was found to be a top neighborhood mask of size 45×45, shown in Equation 13. The result of these operations applied to Figure 85 is shown in Figure 86.

$$top\ neighborhood\ mask = \begin{bmatrix} 22\ rows\ of\ all\ 1's \\ 23\ rows\ of\ all\ 0's \end{bmatrix}_{45\times45}$$

Equation 13

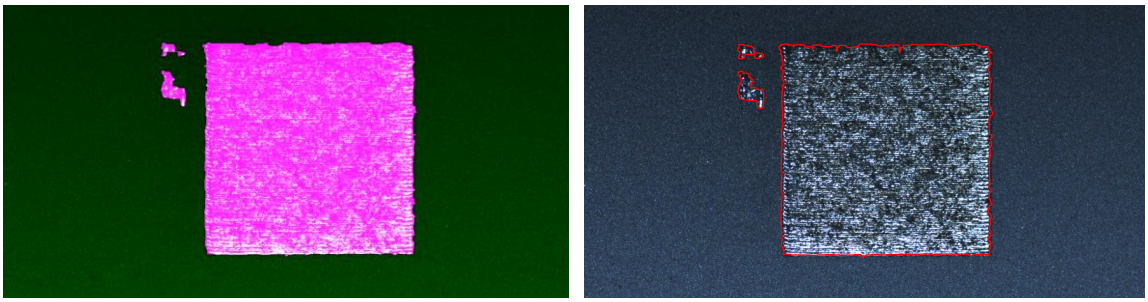

Figure 86- Result of segmentation of fused objects using an initial approximation.

The parameters of the new algorithms (in this subsection) were selected for a design set of 7 images to minimize the maximum error for each image (implementation). The non-uniformity of the fused region and the small dark regions in the powder which exactly have the intensity of the fused region (see Figure 93) make minimization of the error very challenging. Discussion of image characteristics and the estimated achievable

precision is given in next section, 6.4. It was realized that an average error of about 10 to 15 pixels can be achieved for design set images and is very satisfactory.

Figure 87 shows the result of segmentation technique applied to two example images in the design set. As seen, the fused regions are segmented with very high precision, and in most parts the error is less than 5 pixels. The maximum error was measured at the worst place where the boundary of the segmented fused region had the farthest distance from the true boundary. The maximum error for each of these images is less than 27 pixels. In most implementations, the main objective is to segment the fused square. The segmentation of the numbering attempts at the top left corner is not considered in the main objective of segmentation of fused regions because parts of these regions are just 1 scan width wide (0.09 mm) which only consists of 13 pixels that can easily be confused with the dark spots in the powder region. In fact, obtaining better segmentation of small dark fused regions are sometimes achieved at the cost of increasing the error for segmenting more of the powder regions Discussion of the expected minimum error is given later in this section.

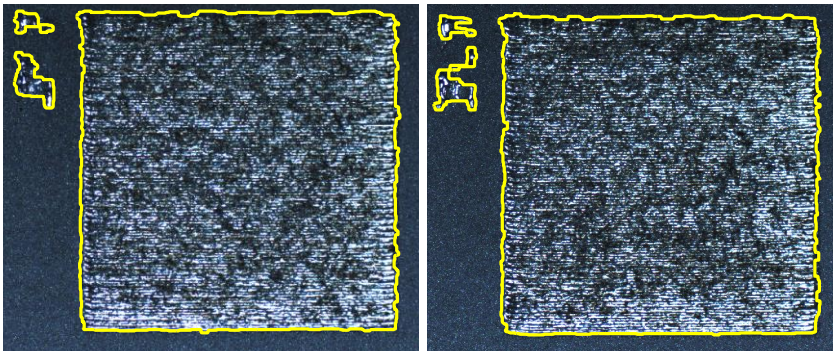

Figure 87- Implementation of the algorithm to three of the design images.

The segmentation technique was implemented to 43 more images of different layers (43 test images) and it was examined that the algorithm performs efficiently for segmentation of the fused regions. The implementation results for several of these layers

are given in Figure 88. As seen, the segmentation boundary very closely follows the boundary of the true fused region (although being rather non-smooth due to the variation of the true boundary itself and also the precision of the segmentation). The precision of the segmentation will be evaluated in the next section where it will be seen that the error between the two boundaries in almost %95 of the boundary is less than 20 pixels with the root-mean-square of 11.6 pixels.

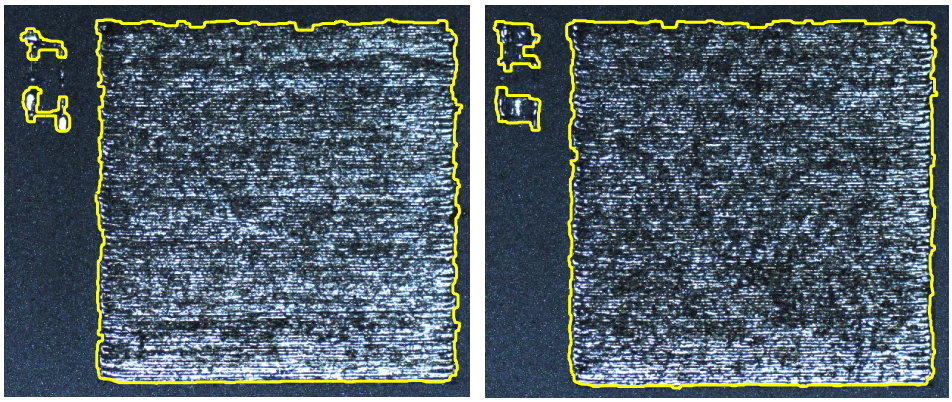

Figure 88- Examples of the result of the implementation of the segmentation algorithm implemented to the test images.

6.3.3 Application of the Algorithm to Other geometries

The algorithms designed in this section, are based on identifying pixels in the image that satisfy several specifications that were tested using the designed morphological operations. These specifications are mainly that the window containing each of these examined pixels and their neighboring pixels satisfies the density of the segmented dots based on two sets of thresholds and that the intensity values and distributions are such that the selected parameters would lead the algorithm to correctly identify the pixels belonging to the fused object. Therefore, the performance of the algorithm would majorly depend on the intensity values and distributions of pixels

belonging to the fused and powder regions. This distribution follows a statistical trend and therefore, the performance of the algorithm can be evaluated by implementing the algorithm to a large number of images to see whether the extracted statistical relation in fact holds for all images. This is going to be performed in Section 6.5.

However, in the designed algorithms, there is no assumption of geometry or shape characteristics and therefore, it is fully expected, that these algorithms would produce satisfactory results for any other geometry. To verify this reasoning, however, several other geometries including several hollow geometries as well as curved geometries were tested. Figure 89 and Figure 90 show several examples of these images and the implementation results. As seen, the detected boundary very closely matches the boundary of the true object. To evaluate the accuracy of the segmentation, the poin-to-point boundary error was calculated between the true, manually-segmented object with the algorithm-segmented object (see Subsection 6.5.2 for more explanation). The maximum point-to-point boundary errors for the images in Figure 89 were calculated as 14 pixels and 20 pixels respectively, and it was calculated as 17 pixels for Figure 90. Figure 90 (d) shows the point-to-point boundary error calculated radially throughout the circumference of the circular geometry versus angle.

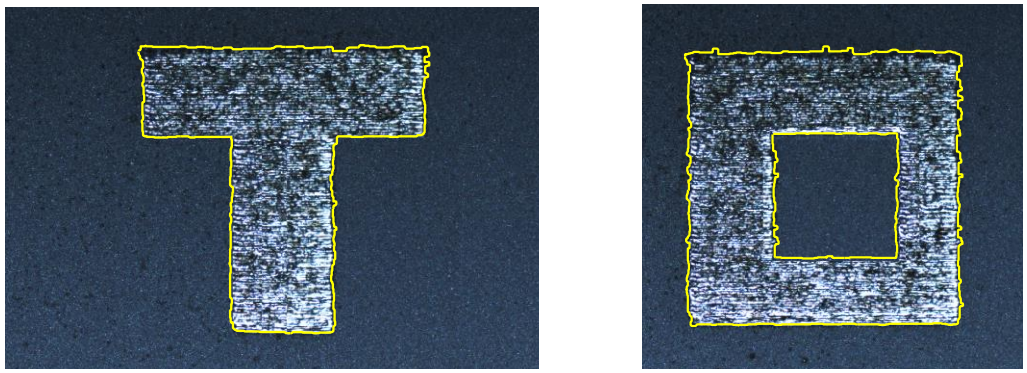

(a) (b)

Figure 89- Examples of results of implementation of the developed algorithm to segmentation of the fused objects of geometries other than square object, (a) a T- cross-sectional object, (b) a hollow object.

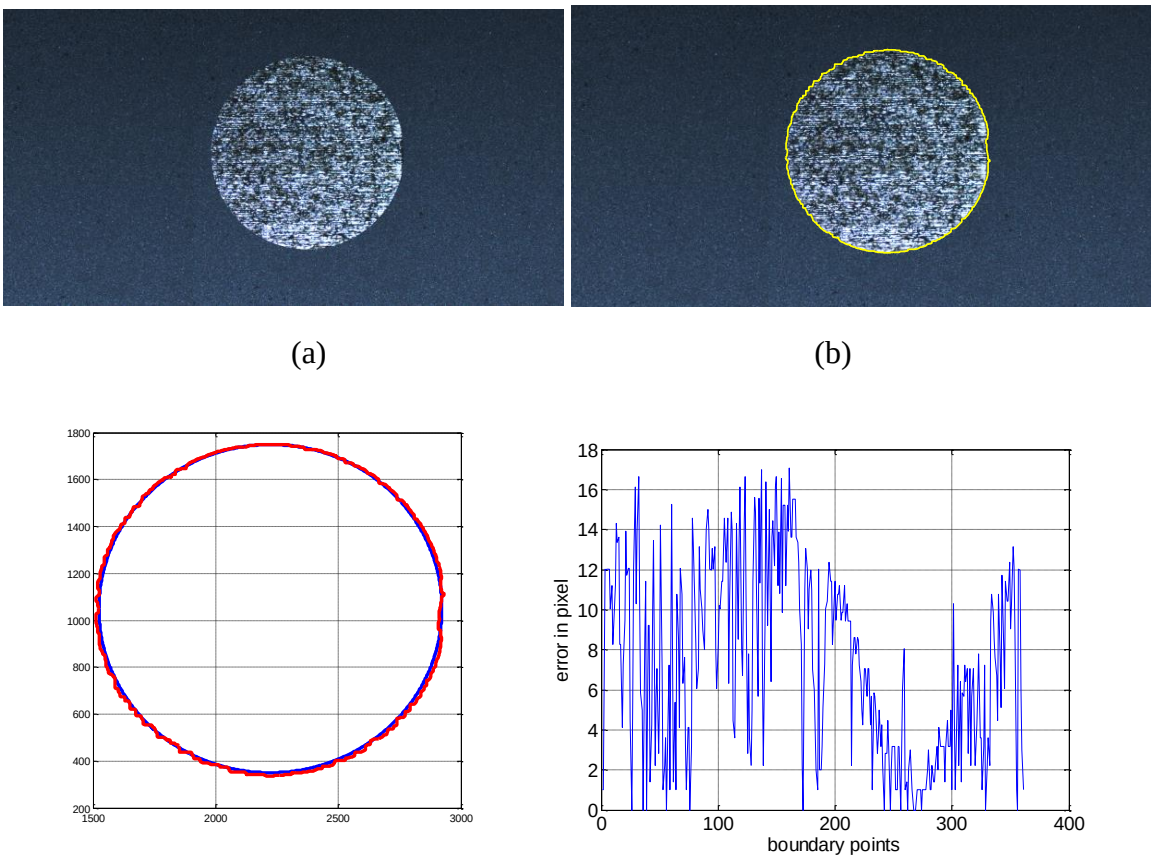

Figure 90- Application of the developed image processing algorithms for a circle: (a) the image of the cross section of the part in powder layer, (b) the result of segmentation of the circular cross section using the developed algorithm (shown by solid, yellow line), (c) the comparison of the true circle, true cross section, (blue) with the segmented geometric object (red), (d) the point-to-point boundary error calculated radially throughout the circumference versus all angles.

6.4 Assessment of Imaging Characteristics and an Achievable Segmentation Precision

Figure 91 shows an example of an image captured from the part using the current build and imaging setup. The figure also shows zoomed-in views of parts of the powder region and fused region individually. As it is seen, the scanned fused regions do not reflect a uniform bright illumination throughout the fused region (as seen in Figure 91 (c)

and Figure 92) and therefore the fused region is not captured as an entirely uniform bright region and shows several dark regions. Also, as seen from Figure 91 (b) and Figure 92, the powder region does not consist of uniform relatively blue illumination and contain several dark dots and non-uniformities. The formation of these dark dots is due to the splash of molten material from the melt pool over the powder region. These dark spots have exactly the same intensity as the dark parts of the fused regions within the solid object. The non-uniformity of the fused region and the existence of these small dark regions in the powder which exactly have the intensity of the fused region interfere with achieving high segmentation precision.

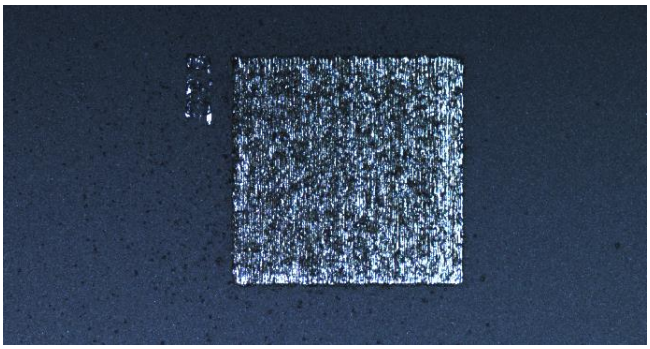

(a)

(b)

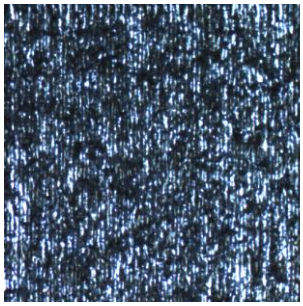

(c)

Figure 91- (a) original image, (b) the dark spots in powder region, (c) non-uniformity within fused region due to non-optimal scanning and non-uniform illumination.

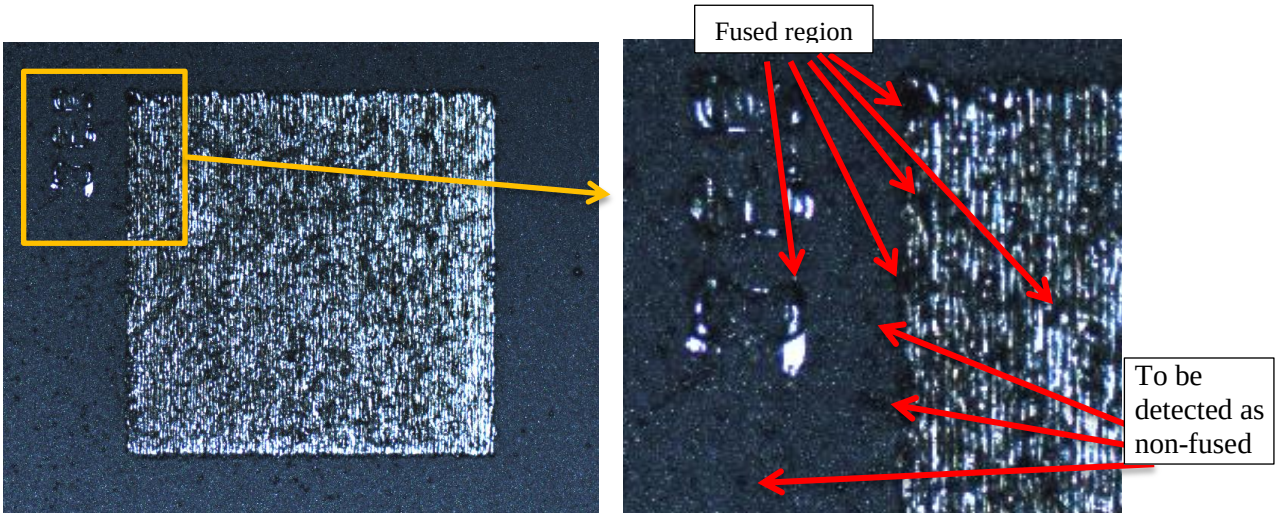

Figure 92- Illustration of the small dark regions in the powder which exactly have the intensity of the fused region that interfere with segmentation of the fused region and its boundary.

Examining the characteristics of the camera images at the current setup, it is either rather impossible or too difficult to develop segmentation algorithms that can guarantee an error less than 21 pixels for at least %90 of images as illustrated in Figure 93. Figure 93 shows four cropped regions of size 21×21 pixel from the powder region and fused region. It is very clear from these images that the intensity and intensity variation information in a 21×21 pixel window cannot distinguish fused regions from the powder region. Also, implementation of color transformation did not achieve a noticeable effect. Therefore, it is reasonable to expect intensity-based algorithms are not able to achieve a segmentation error of less than 21 pixels or even 30 pixels in some other images of the set. For about 5% of the images, due to the non-uniform and sparse intensity distribution of the fused region and the large noisy spots in the background (as seen in Figure 92), it is even too difficult to develop segmentation algorithms with the error guaranteed to be less than 60 pixels. The values of 21 pixels and 60 pixels, for the current camera setup, correspond to 147 and 415 microns respectively.

(a) (b) (c) (d)

Figure 93- Illustration of intensity distribution of the fused and powder regions (21×21 pixels regions): (a) a selection from a general (bright) region of the fused object (b) a selection from a general region of the powder, (c) a selection from a non-well-illuminated (dark) region of the fused object, (d) a selection from a dark spot or a non-well-illuminated region of the powder.

Based on the intensity distribution of the current images, it is reasonably concluded that development of intensity-based algorithms (either in terms of values or local variations or patterns) would not yield an error less than 415 microns.

However, it should also be mentioned that this error is based on a local worst-case deviation between the detected boundary and the true boundary. For many applications, a relatively large local point-to-point error does not pose an error to the design specification of a manufactured object. As will be seen in Section 6.5, the pixel-wise precision, the overall boundary detection precision in terms of root-mean-square, and also the precision for detection of the synthetic parameters are much higher and the results of these detections are very confident. Further discussion of the precisions of the algorithms will be given in the next section, 6.5.

Despite the unnoticeable effect of current segmentation error on inspection of geometry in terms of geometric synthetic parameters, the segmentation precision error can still be further reduced by further modification of the camera and imaging setup. This can be achieved by decreasing the pixel size by increasing the camera resolution, and/or decreasing the imaging distance. Removing the problems with the intensity distribution and illumination (as seen in Figure 91) is an alternative solution. These ways to fix this

problem include: 1) adjusting the illumination to decrease the sparseness and non-uniformity of intensity distribution within the fused region, and 2) removal of the cause of formation of rather large dark regions in the powder region that exactly have the same intensity values of the fused region. An example of this modification can be seen in the final set of images with moveable ring LED.

An alternative method to intensity-based (and low-level) algorithms for segmentation of fused regions is to use feature-based intelligent segmentation algorithms. For this purpose, several mathematical features should be found and selected that can distinguish sub-regions (such as those in Figure 93) belonging to fused and powder regions. This might increase segmentation precision, however, it would be achieved at a large computational load. For example, for a precision of 21 pixels, more than 20,000 implementations of the feature-based classifier would be required with a classifier with very high accuracy. And to achieve a precision of about 11 pixels, more than 70,000 implementations would be required in the main form of the classifier. This would significantly increase the computational load and still despite the high computational load, the precision of the classifier would rarely be high enough to achieve 100% classification performance for such similar textures of powder and fused region (see Figure 93).

6.5 Evaluation of the Performance and Precision of the Segmentation Algorithms of Fused Geometric Objects

After the algorithms perform desirably for the design images, they should be implemented to the enough number of test images to verify the performance. The segmentation technique was implemented to 43 more images of different layers (43 test images) and it was determined that the algorithm performs efficiently for segmentation of the fused regions. The implementation results for several examples of test images were given in Figure 88. The errors in boundary segmentation in each image are quantified

using two measures in this research, the root-mean-square (averaged L2 norm) of the error for the boundary points and the maximum point-to-point error in each layer (image).

6.5.1 Pixel-Wise Segmentation Error

Although the boundary is rather non-smooth (as seen in Figure 88), due to variation of intensity at the boundary, the pixel-wise segmentation precision is very large for all the images. Large pixel-wise segmentation precision means that a very small portion of the interested object or background (powder region) has been mis-segmented. Figure 94 and Figure 95 show two examples of the algorithm's result of segmentation of the fused object compared with the true fused object. As seen, the squares have been segmented with high precision and with very small pixel-wise segmentation error. A very efficient way to assess the segmentation precision of algorithms in image processing is to calculate the pixel-wise segmentation error by a criterion given in [125], i.e. Equation 3, represented again as below:

$$\mathrm{err} = 1 - \frac{|B_O \cap B_T| + |F_o \cap F_T|}{|B_O| + |F_O|}$$

Equation 14

B_o and F_o denote the background and foreground (object) area pixels of the manually thresholded image, B_T and F_T denote the background and foreground area pixels in the image that are segmented using the method to be assessed, and |.| is the number of pixels in the set. The above criterion takes into account the errors due to both cases of pixels of the object not being segmented and pixels of background being falsely segmented.

The pixel-wise error based on the above formula was calculated as 0.0050 for the image in Figure 94, and as 0.0061 for the image in Figure 95. The maximum pixel-wise

error for all the 50 images was calculated as 0.0070 which attests a very precise pixel-wise segmentation.

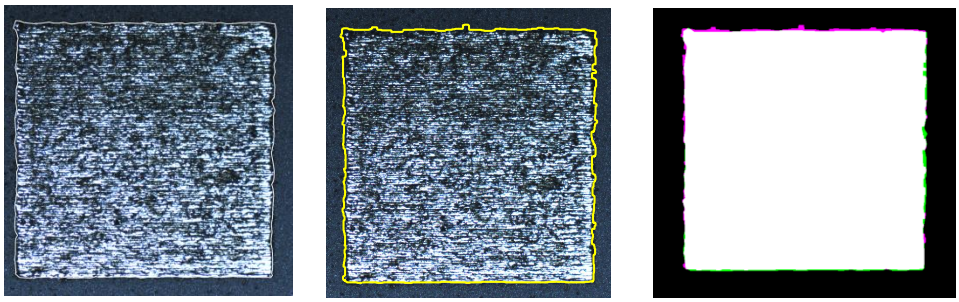

(a) (b) (c)

Figure 94- An example of a fused object. (a) The original image with the fused object segmented manually, regarded as the true fused object (the error of the manual segmentation of the square object is assumed to be negligible), (b) the result of algorithm in segmenting the fused object, (c) overlap of the result of segmentation algorithm with the true fused object; white regions belong to both, the green regions only belong to the true fused object, the pink regions only belong to the algorithm segmentation result.

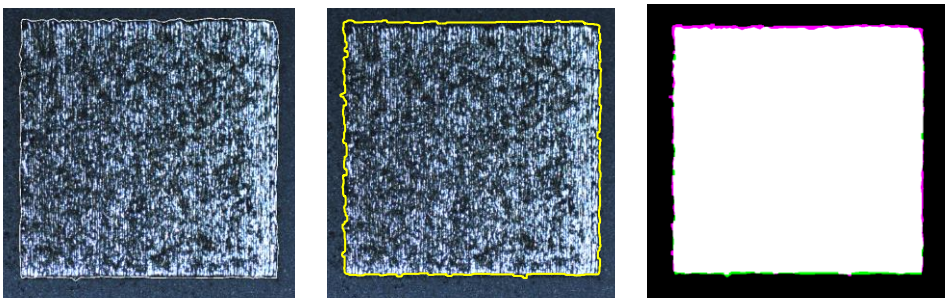

(a) (b) (c)

Figure 95- Second example of a fused object. (a) The original image with the fused object segmented manually, regarded as the true fused object (the error of the manual segmentation of the square object is assumed to be negligible), (b) the result of algorithm in segmenting the fused object, (c) overlap of the result of segmentation algorithm with the true fused object; white regions belong to both, the green regions only belong to the true fused object, the pink regions only belong to the algorithm segmentation result.

6.5.2 Point-To-Point Segmentation Error

Although the pixel-wise segmentation error is a very widely-used, efficient measure for assessing image segmentation algorithms in computer vision, for applications of inspection of dimensional accuracies in manufacturing, it is also important to inspect the boundaries and features of the manufactured object. Therefore, the inspection algorithm should be able to detect these features with acceptable precision. To calculate the point-to-point error, the corresponding boundary points were found. For this purpose, the vertices of the true square and the segmented square were found and radially matched from the center of the area, and the squares were then divided to four quadrants. The distance between all the corresponding points on each side of the square was then calculated by tracking the boundary starting from an arbitrary point on the boundary. Figure 96 (a) shows the boundaries of the true square (white) and the segmented square (pink) for the example image in Figure 94. The cross marks show the vertices of each square in the corresponding color. The star mark shows the start point on the boundary to track the boundary clockwise and calculate point-to-point error. Figure 96 (b) shows the (absolute of) calculated point-to-point error between these two squares.

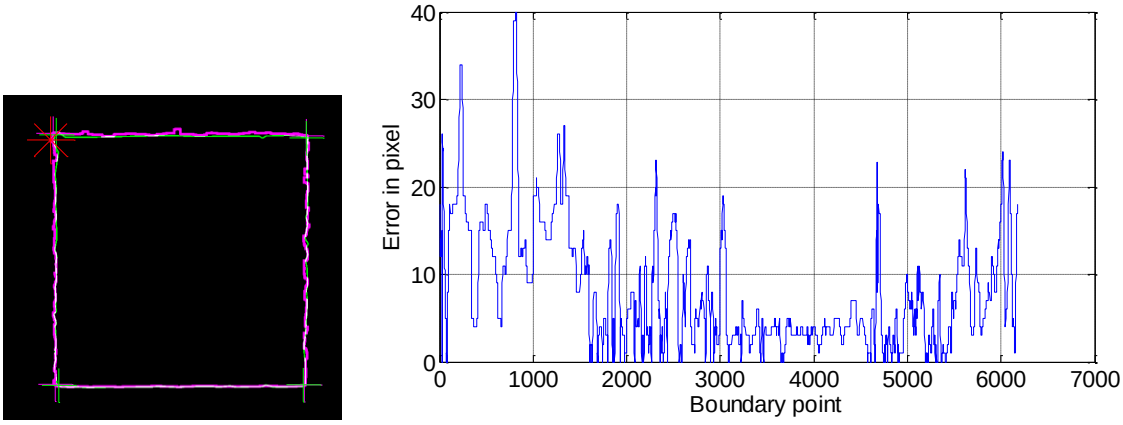

(a) (b)

Figure 96- Calculation of the point-to-point error between the boundaries of the true square (the white line) and the segmented square (the pink line) in example image in Figure 94. See description in the text.

As it seen and calculated from Figure 96, for only 4% of the boundary the point-to-point error is greater than 20 pixels, and only in very small local regions the point-to-point error reaches over 30 pixels with the maximum error of 40 pixels. The root-mean-square error for this image is 10.6 pixels which is relatively a small amount.

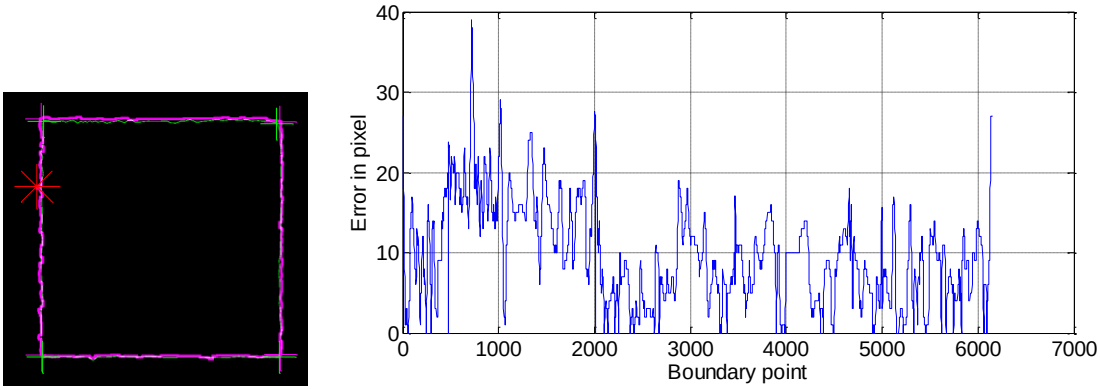

(a) (b)

Figure 97- Calculation of the point-to-point error between the boundaries of the true square (the green line) and the segmented square (the pink line) in example image in Figure 95. See description in the text.

Figure 97 shows the boundaries of the segmented and true squares for example image in Figure 95. Similarly the vertices are shown with cross marks, and the start point for tracking the boundary clockwise is shown by a red star mark. Figure 97 (b) shows the calculated point-to-point error. As seen and calculated, in only 5% of the boundary, the point-to-point error is greater than 20 pixels, and only in a very small local region the point-to-point error reaches over 30 pixels with the maximum error of less than 40 pixels. The root-mean-square error for this image is 11.6 pixels which shows a relatively good segmentation precision.

Figure 98 shows another example of the image segmentation results and its corresponding segmentation errors. The pixel-wise segmentation error for this image is 0.0048 and the root-mean-square of the point-top-point error is 10.3 pixels. Similarly, for this image only a low percentage of 3.6% of the boundary points have a point-to-point error larger than 20 pixels, and the maximum error is less than 40 pixels.

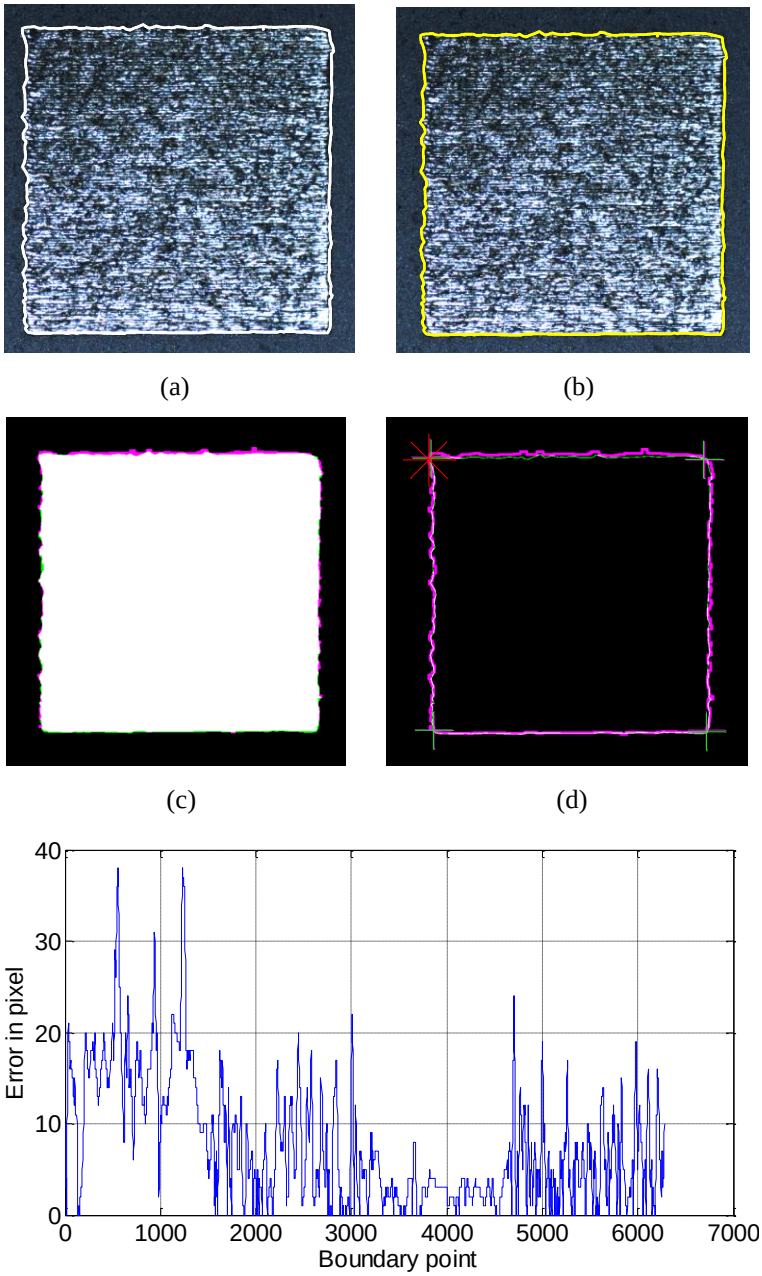

Figure 98- Another example of the result of segmentation of the fused object and illustration of the corresponding pixel-wise segmentation error and point-to-point error. (a) True square, (b) Segmentation result, (c) True square and segmentation results plotted on the same figure (the green regions belong to the true square, the pink regions belong to the segmented square, and the white regions belong to both.), (d) The boundaries of true square (green) and segmented square (pink) plotted again each other (see description in text), (e) Point-to-point error.

The point-to-point error was calculated for the boundary points in all 50 images. For all images, the error between the two boundaries in more than 90% of the boundary is less than 20 pixels. The maximum root-mean-square error for all the images was calculated smaller than 13 pixels (the laser scan width). For all images, the maximum point-to-point errors correspond to only very small local regions at the boundary that are mis-segmented due to the existence of white dots or small dark spots in the powder neighboring the fused region as well as the dark spots within the fused objects close to the boundary (as previously shown in Figure 92).

The maximum point-to-point error was calculated for all the images and, except for two cases, the maximum error is lower than (or, only for one image, equal to) 40 pixels. Figure 99 illustrates one of these cases along with segmentation and boundary error. The pixels-wise segmentation errors for these two cases are as low as 0.0063 and 0.0045 respectively. Additionally, more than 94% of the boundaries of each of these images show a point-to-point error smaller than 20 pixels, and the root-mean-square errors are as low as 12.8 and 11 pixels respectively.

However, two local small regions of maximum point-to-point errors of about 60 pixels occur in each image. By zooming into the regions of maximum error, it is seen that this mis-segmentation is due to the non-smooth fusion marks within the fused objects close to the boundary due to lack of sufficient reflecting illumination from these regions as well as small amounts of powder particles covering the fused region. It is seen that these fused regions look very similar to the powder region and it is even difficult for a human eye to distinguish between the two. The largest value of maximum point-to-point errors for all the images was measured as 62 pixels (Figure 88 (e)) which would be 428 microns or 0.43 mm. Except for the aforementioned two cases, the segmentation boundary (for all test images) very closely follows the boundary of the true fused region

(as shown in Figure 88, 20, 21, and 24) and the worst-case maximum point-to-point error is 40 pixels which for the current pixel size is about 280 microns (0.28 mm).

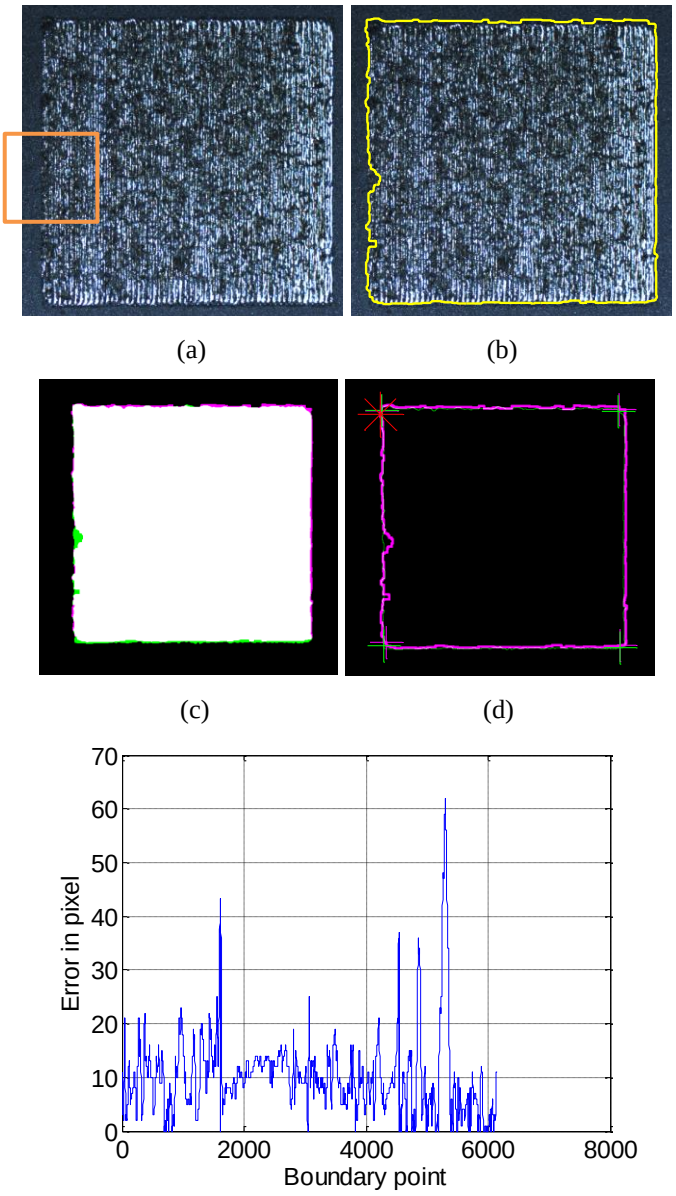

Figure 99- Original image and segmentation results for the image one of the two cases that lead to maximum local point-to-point error of over 40. (a) Original image, the red square shows the region of maximum point-to-point error. Description of other parts is the same as in Figure 98.

Figure 100 shows the distribution of the maximum local point-to-point error (in pixel and micron) in each implementation of the algorithm (each image) for 50 images. The maximum measurement error for most images is less than 40 pixels (280 microns) and only two images, as mentioned earlier, out of 50 images show a maximum error of larger than 40 pixels.

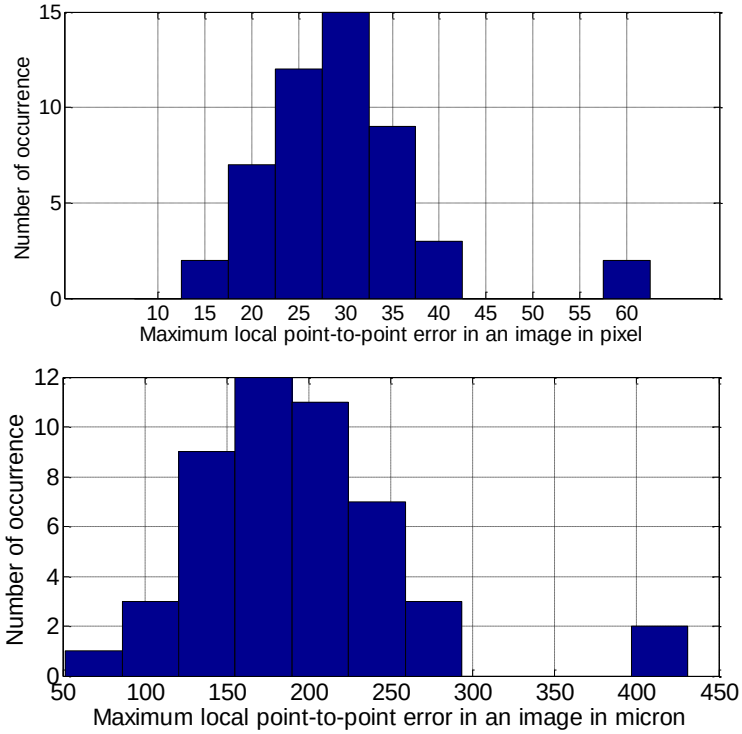

Figure 100- Distributions of maximum of local point-to-point error in each image for 50 images in terms of pixel and micron.

The maximum local point-to-point error of the algorithm for this imaging setup is, therefore, estimated around 62 pixels which for the current pixel size of 6.9 micron is less than 430 microns (0.43 mm). Additionally, with the probability of 96%, the maximum point-to-point error is smaller than 40 pixels and correspondingly less than 300 microns (= 43 pixels) or 0.3 mm. Therefore, for applications that occurrence of a local point-to-point error of up to 0.3 mm with the likelihood of 5% is acceptable, the developed inspection system (consisting of the current hardware and detection algorithms) is

satisfactory. This is in addition to the fact that the maximum root-mean-square error is as small as 11.6 pixels (smaller than the scan width) and for more than 90% of the boundary points the error is smaller than 20 pixels.

It is also important to note that for many applications, however, the tolerance limitations are over the synthetic parameters such as spacings and sizes. A moderately large point-to-point error at a single small location does not introduce a noticeable error into the values of synthetic parameters. Therefore, this inspection system also works for those applications that have tolerances on the synthetic parameters. Study of the errors of the developed inspection system for determination of synthetic parameters is given in next section, Section 6.6.

6.6 Calculation of Synthetic Parameters using Model-Based Image Processing Algorithms

In many applications of part geometric inspection, the tolerances and geometric specification are imposed over synthetic parameters of part features such as sizes, angles, roundness, diameter, spacings between features, etc. Therefore, extraction of the synthetic parameters in these applications should be performed automatically to enable the in-situ geometric inspection of the metal AM parts. There are several ways in metrology and mathematics to extract different synthetic parameters including maximum inscribed shape, minimum subscribed shape, and least-square error for parametric curves and shapes. Each of these techniques can be implemented to the boundary of the fused object that was segmented using previously designed image processing algorithms. However, image processing and computer science provides several very useful model-based mathematical tools that can efficiently extract curves and shapes with parametric model from the images containing the curves and object boundaries.

In this section, a model-bade image processing algorithm, called Hough transform, is used to extract the synthetic parameters of the fused object in the images captured during the build of the block. The synthetic parameters in this build case are the characteristic associated with the square sides, angles, location, and size. Once the sides of the square are known, any other synthetic parameter can be calculated by simple mathematical operations. To apply Hough transform, the boundary points of the fused object as detected in the previous sections is extracted by image processing algorithms and a binary image containing these boundary points is generated. Hough transform is applied to each binary image to extract lines associated with sides of the fused object and extract the fused object which is in form of a polygon (i.e. square).

The problem with Hough transform is that it is very sensitive to the points that do not exactly lie on the parametric curve. If boundary points do not exactly lie on a line, either no line is detected or only those portions of line are detected that exactly lie on the same line. Detecting only few line segments prohibits every point on the boundary from contributing to the extraction of the line and therefore only those that exactly lie on the line determine the extracted line. To resolve this problem, the existent solution is to increase the increments (bin size) of the curve parameters in Hough transform until the lines can be detected. But it was investigated that, for this application, this solution would significantly decrease the precision of each extracted line parameter. Additionally, this solution does not resolve the problem with very wavy detected lines as in Figure 101.

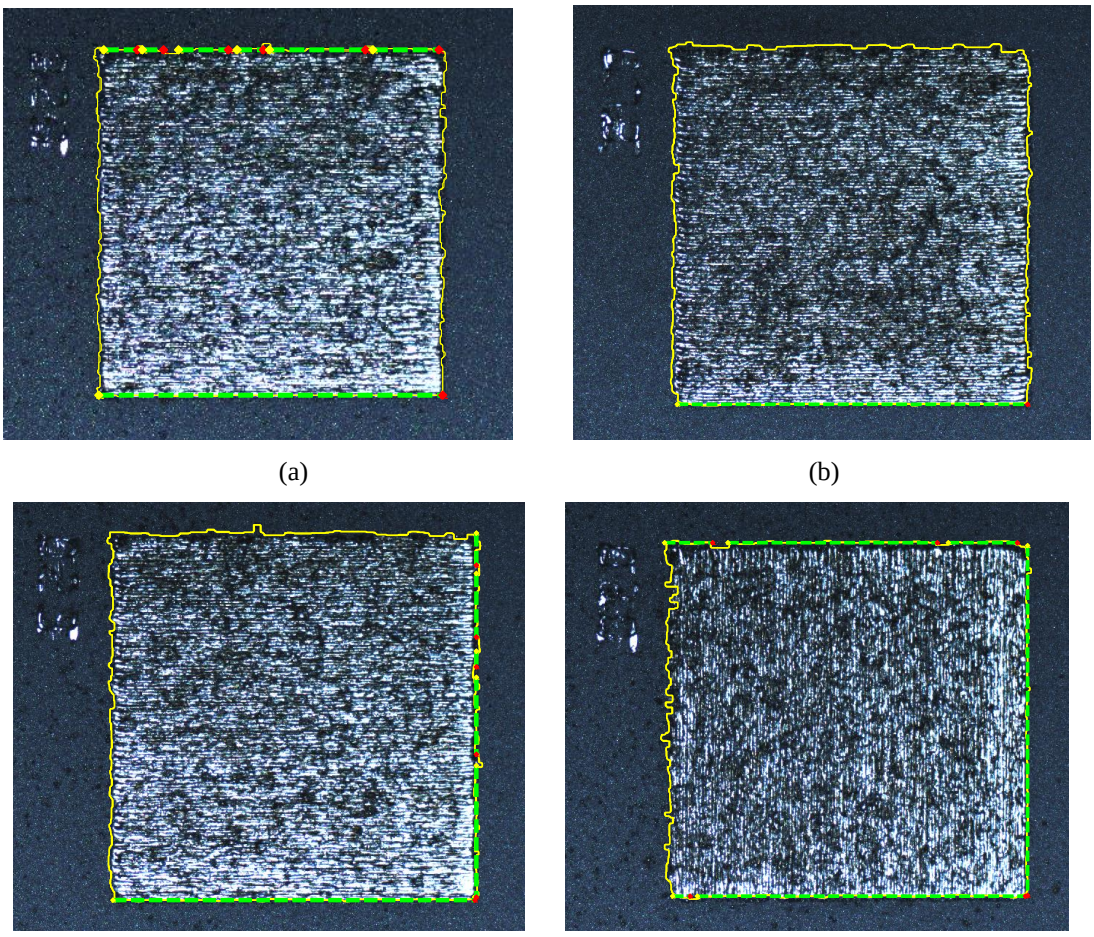

(a) (b)

(c) (d)

Figure 101- Examples of failure of Hough transform to detect the sides of the fused object from the detected boundary. The yellow solid line shows the detected boundary, the green dashed lines show the detected lined by Hough, and the (yellow and red) points show the beginning and end of each detected line. (a) No line segment from the lateral sides are detected by Hough, (b) and (c) The bottom line is only detected by Hough, (d) No line segment from the left side is detected by Hough.

Figure 101 (a) to (c) shows four examples of images where Hough transform is not able to detect line segments from every side of the boundary. In Figure 101 (a), although the lateral sides of the object have been segmented precisely and close to the true boundary, no line segment within these sides of the object has been detected. Figure 101 (b) shows another image where line segments were detected from the sides. In Figure 101 (b) only the bottom side of the square is detected. Similar to part (a), despite the highly precise segmentation in some regions of the boundary, no line segments have been

extracted from those regions. In some other examples where a few lines are segmented, many portions of the boundary have not been extracted and therefore do not contribute to the result of the Hough.

One reason of the deficiency of Hough results for this application is that even the true fused objects are not a perfect square due to the lack of precision in metal powder fusion process. Similarly, in Figure 101 (c) only one side of the square is detected. Figure 101 (d) clearly illustrates the reason why Hough transform, even with increased parameter increment (bin size), cannot detect lines on the left square side. In addition to the wavy nature of the true fused object, as it was seen in the previous sections, the resulted point-to-point boundary segmentation error of the algorithm can reach to 40 pixels. The oscillating point-to-point boundary error creates a further wavy detected boundary line that is hard to fit in a line model. To capture this waviness by increasing the parameters increment, a significantly increased increment (bin size) would be required that produces erroneous results.

However, from the study of point-to-point boundary, it was seen that more than 90% of the detected boundary points lie within a 20 pixel-wide band on each side of the true boundary. Therefore, the true boundary lies within the detected line by some distance. To capture the boundary deviations in the line extraction, in this work a new solution is proposed. The segmented boundary of the fused object is thickened using morphological dilation operation to cover the whole band that the true boundary point most likely lies in. From the discussion of the point-to-point error, a dilation mask of 41 pixels (20 pixels on each side) pixels seems useful; however, it was investigated that even a mask of 11 pixels would detect enough line segments in all sides of the fused object that can lead to accurate extraction of synthetic parameters. A mask size of 15, however, seemed to result in extraction of enough line segments that it seems to cover about 90%

of each side of the boundary, allowing for more number of points contributing to the extraction of synthetic parameters (see Figure 102 and Figure 103).

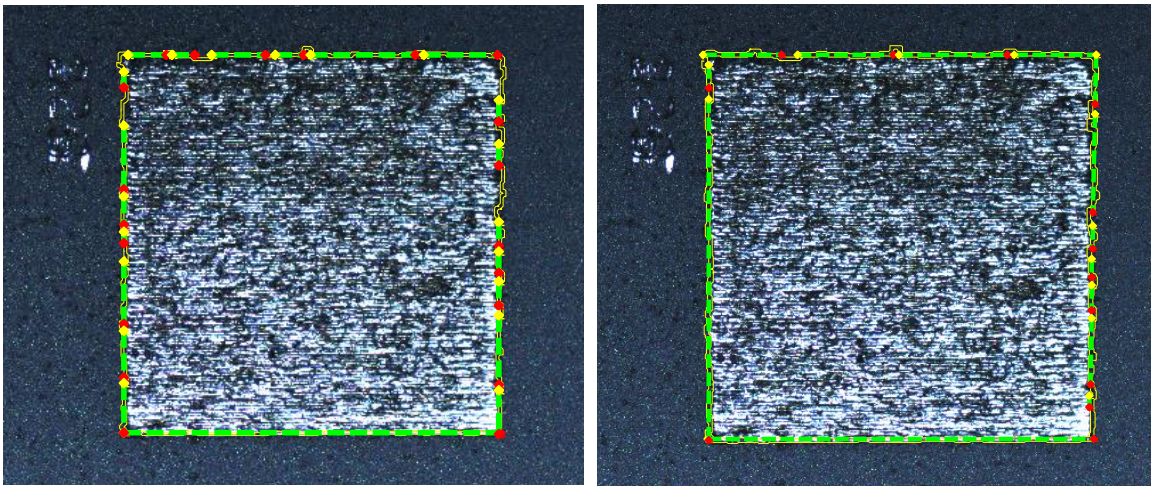

(a) (b)

Figure 102- Example of results of application of Hough to extract sides of the fused object in Figure 101 (a): (a) dilation with mask size of 11, (b) dilation with mask size of 15. The two adjacent yellow lines show the band of variation of the boundary captured by dilation (an 11-pixel-wide and a 15-pixel-wide band for corresponding images).

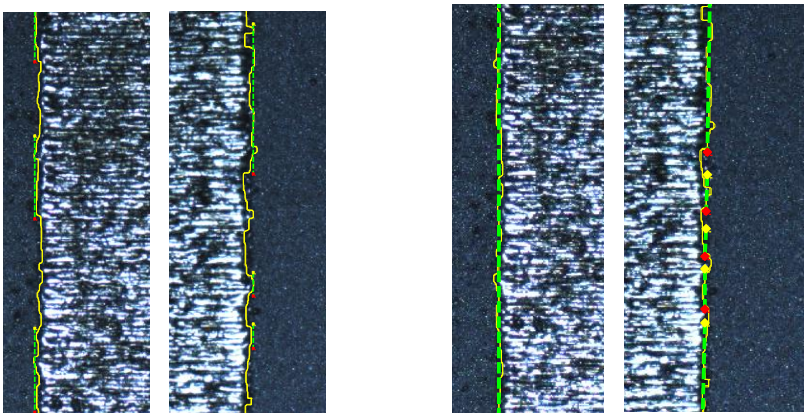

(a) (b)

Figure 103- Zoomed-in views of some sections of Figure 102 for result of dilation with mask sizes of (a) 11 pixels, (b) 15 pixels. No line segment was detected without dilation on these sides. Mask size of 15 pixels leads to detection of lines covering about 90% of the boundary points.

Therefore, dilation with a mask size of 15 pixels was applied to the boundary in each image and then Hough transform was applied. Figure 104 shows the results for

application of Hough transform after boundary dilation to Figure 101 (c) to (d). (The result for Figure 101 (a) was given earlier in Figure 102 (b)). Figure 105 shows a large view of result of application of Hough without dilation and with dilation with a mask of 15. In the image in the figure, although the segmented boundary closely follows the true boundary, the Hough without dilation cannot detect the line segments of the sides of the fused square due to the natural variation of the fused object. Figure 104 illustrates how capturing the band of variation allows Hough transform to detect line segments within this band.

The operations of dilation with mask of 15 pixels and Hough transform were applied to all the 50 images. The results showed that line segments within each side of the fused object are detected with high precision that almost cover 90% of the boundary for all the images. These line segments can now serve well to precisely extract the true line associated with each side of the polygonal fused object.

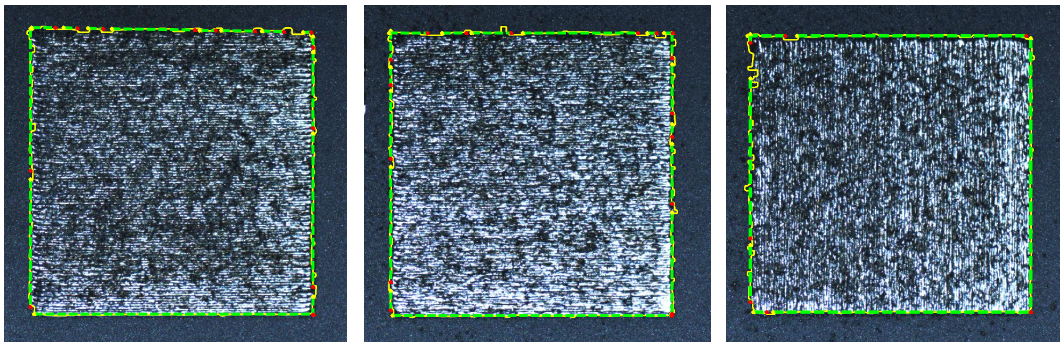

(a) (b) (c)

Figure 104- Results of application of Hough transform after dilation with mask size of 15 pixels applied to the images in Figure 101.

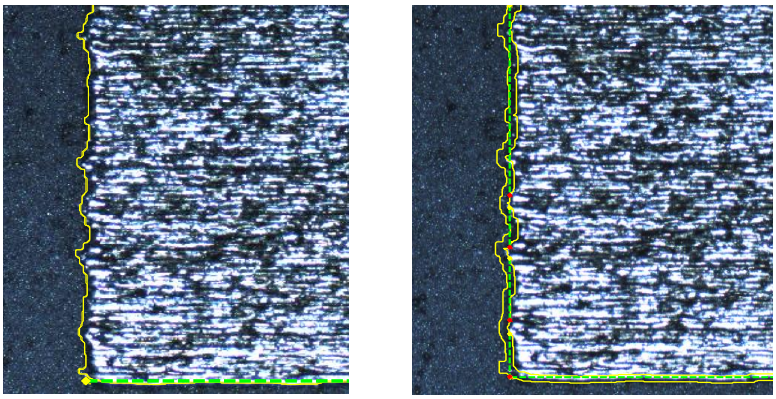

(a) (b)

Figure 105- Large view of results of application of Hough transform: (a) without dilation; despite the precise boundary segmentation, the lateral line is not detected by Hough, (b) with dilation of mask size 15 (the two yellow lines show the 15-pixel-wide band to capture variation of the boundary that was considered by dilation).

After the line segments on each side of the fused object are detected, the line parameter as calculated by Hough transform can be used to extract mathematical models for four lines corresponding to four sides of the fused object. Finding the intersections of these lines provide the locations for the vertices of the fused object. It is clearly seen that the developed inspection algorithms allows for precise detection of fused objects and their geometric and dimensional specifications and parameters. The developed system therefore provides a high-precision inspection system for in-situ control of dimensional accuracy that was verified for polygonal shapes in this section.

CHAPTER VII

DETECTION OF PORES

7.1 Automated Inspection of In-Situ Camera Images

After the imaging setup enables to capture in-situ images from each layer that visualize detailed surface features and pores, automatic analysis of these images for part quality inspection can be performed. Three purposes can be suggested that the camera images visualizing the surface details as well as pores can be used for.

The first purpose is to study defects (pores) or porosity directly which can be done in two ways. The first way is to detect each pore individually by developing appropriate image processing algorithms. This is a complicated task because of the high level of intensity variation in the layer surface that can simply be confused with pores. But this information, if obtained, can specify individual pores and their approximate location and size. Information about number of pores and their approximate sizes also allows to directly estimate the porosity in each layer and consequently enables to calculate the level of porosity in the whole part and the density of the part and to make an assessment of correspondent structural behavior. The second way is to find and extract a measure of porosity from the layer. In other words, instead of directly detecting pores, a set of features from the surface that have statistical correlation with the porosity of the layer are found and used as a measure of porosity or are calibrated versus the level of porosity of the layer. This measure could be an indicator that the examined surface is porous (or likely to be porous) or contains no pore. It could also indicate a more precise (quantitative or multi-class qualitative) level of porosity and helps to estimate the porosity.

The second purpose is to extract a measure of some physical characteristic of interest (other than pore) from the surface. For example finding and extracting a feature

or quantity from the surface texture that shows strong correlation with some physical characteristic such as the quality of fusion, level of energy, or the physical roughness. Such a quantity can serve as a measure of that physical characteristic by appropriate calibration. Estimation of porosity using features, explained earlier, can be regarded as a special case of this.

The third purpose is to use the measure of surface roughness or quality of fusion or porosity or extract another measure and calibrate this measure with respect to the process parameters (or the build energy) for a variety of process parameters. This calibration will allow to automatically identify layers that are built with characteristics that are associated with undesired (non-optimal) process parameters that tend to create defects and pores in the layer. Therefore, this information can serve as feedback about process parameters and help maintain the process parameters close to the optimal ones.

In this dissertation, the first purpose is addressed. It is desired to study the pores in the layers. One approach is detection of individual pores that is the topic of this chapter. The second approach is identification of a porous (or defective) layer. The result of identification of porous layers can help with identifying defective layers, can also help with pruning and improving the results of detection of individual pores; it can also serve as feedback for process control or decision. The approach for identification of porous layers based on features from surface, also presents the benchmark approach for extraction of a measure for any physical surface characteristics such as quality of fusion and surface roughness. Identification of porous layers is the topic of CHAPTER VIII.

7.2 Detection of Individual Pores

To detect pores individually in an automatic manner, appropriate image processing algorithms should be developed. The devloped algorithms would have some level of performance in terms of percision or accuracy that could be satisfactory or

insufficient for a given application or a specific build. The development and the performance of algoritms would strongly depend on the characteristics and clarity of images, the visibility, contrast, and discriminability of pores compared to the background and non-defective regions, the level of noise, etc.

By observing camera and microscopic images of different layers, is seen that the part surfaces have some discolored regions that appear brown on the surface (see Figure 106). These brown regions have formed due to oxidation with the small amounts of Oxygen in the chamber or the gas bubbles in the powder grains [51]. The level of oxygen in the chamber was always mainttained lower than 500 ppm and mainly at 250 ppm. This oxidation level could significantly be reduced if the build was performed at lower oxygen concentrations such as 100 ppm which is completely feasible on commercial machines. These brown regions, also called darkly etching regions, in images, look like pores in the layers and, unless closely observed, they can sometimes easily be mistaken with pores by visual observation of the images with human eye. Therefore, in processing of the images, they also intefere with segmentation of pores and appear as false alarms.

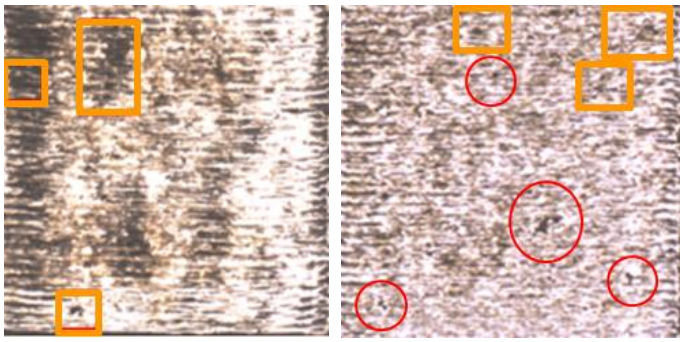

Figure 106- Two example camera images that show a smooth pore-less layer (left) and a porous layer (right). Squares mark examples of darkly-etched regions that are of the same color as pores and sometimes have same characteristic of pores after segmentation, and circles mark examples of true pores.

For defect detection, image segmentation algoritms are developed with the objective of detection of pores in layers from images. However, due to the large variety of layer charactersitics, and surface appearances, and different looks of pores, and darkly

etching regions, development of an algorihtm to detect individual pores wihout segmentig surface discolorations and darkly etching spots is very challenging and complicated. Therefore, the image segmentation algorithms that are developed to detect pores consequently detect some of the darkly-etching regions as well. After segmentation of pores and darkly-etching regions, the characteristics of the segmented objects can be used to remove many of these false detections. Additionally, it will be seen that smoother surfaces tend to have more and larger darkly-etching regions compared to rougher surfaces (see Figure 106). This could be explained by that high level of energy and increased melt pool temperature on a smooth surface increases the oxidation.

On the other hand, as was mentioned earlier, by examining images, it is seen, that layers that are created with lower energy are likely to have pores that are categorized in Zone III. Earlier in Chapter V, the layers and their corresponding process parameters that create pores on the layer were manually identified and mactch Zone III as introduced in [48]. These pores, in this Zone, form on the surface and tend to remain in the part. Layers and their corresponding parameters with no visible pores on the surface were also manually identified that matched Zone I and II. This observation suggests that automatic identification of layers that likely have pores (Zone III) from layers that have very low chances of having pores (Zones I and II) would then help to more confidently decide if the segmentd objects in the image are pores or darkly etchinng spots. This identification will be performed successfully and will be discussed in CHAPTER VIII. The results of automatic identification can then be used in conjunction with automatic detection of pores so that the pore detection algorithm will be designed for and appllied only to porous layers so as to increase the precision.

In the following, approprite image procesing algorithms will be developed to detect pores using inetnsity-based algorithms. Images of layers from all Zones are considered in this section, and geometric features will then be used to identify and

remove many of FPs in non-porous layers using a rule-based identification. Then, the image processing algorithms will be designed and optimized only for images of layers in Zone III. This set of algorithms use the result of Bayesian identification for identifiying porous layers in Zone III (that will be addressed in Chapter VIII). Finally, the algorithms will be evaluated.

Figure 107 shows an example image of a porous layer. As it is seen, there are many darkly-etching spots that have the same color as pores and even sometimes it is difficult for human eye to distinguish between the two. Pores and these dark spots can very clearly be distinguished by directly looking through microscope with both eyes that can detect depth. Microscopic images also in general show relatively good discrimination between pores and these dark spots. However, due to the reasons mentioned in Section 4.2, camera images do not show the level of clarity of microscopic images.

To detect pores, the main objective of design, at this stage, is to make an appropriate assessment of porosity in the layers. This purpose also entails that as many true pores as possible be detected with fewest possible number of FPs. It will also be taken into consideration that pores larger than equivalent diameter of 100 microns (15 pixels) be segmented. With this objective, some smaller pores such as those of 80 microns (~11 pixels) are also detected. However, pores as small as 20 to 50 microns in this imaging setup are only seen in 3 to 7 pixels and are not very clearly distinguishable from surface discolorations and noise. Designing parameters that would detect the majority of pores as small as 50 microns would usually lead to a large number of false detections. Therefore, if number of segmented darkly-etching regions can be reduced with a choice of parameters that would lead to not segmenting small pores that are not usually detrimental, these parameters would be considered more desired. Further discussion on algorithm design specifications and evaluation is given in Section 7.3.

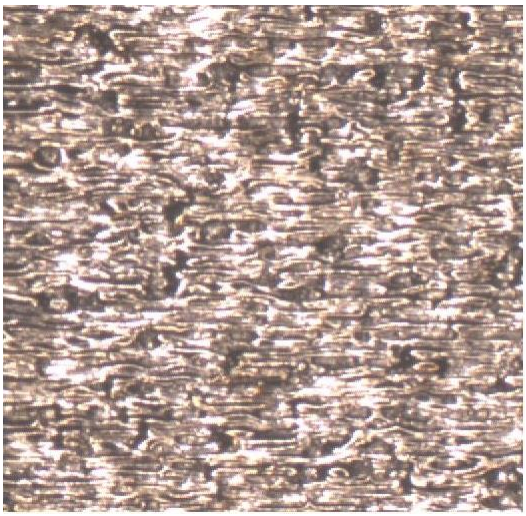

Figure 107- Example image of a porous layer

To start designing segmentation algorithms, we would start with thresholding and would study how pores would appear by different threshold values. A Wiener filter of size 5 was first applied to remove the effect of noise and smoothen the image. Noise removal filter significantly helps with removal of a large number of small false detections. Figure 108 show results of thresholding with four different thresholds. A high threshold segments most and larger portions of pores, but it also segments large regions of darkly-etched spots. A low threshold segments fewer darkly-etching spots; however, it doesn't segment all areas of a pore and does not detect some of the small pores at all.

To get a better insight into the intensity values that pores take compared to not-pore areas, the majority of pores were manually segmented in the camera image and were isolated in a separate image (see Figure 109). The histogram of these pores is shown in Figure 110 in comparison with the histogram of the image excluding the pores. Figure 110 clearly shows that the intensity of pores range from about 0.26 to 0.58, and this range of intensity is clearly included in the range of intensity of the regions with negligible pores. This large overlap of intensity poses a challenge against efficient segmentation of pores using intensity-based algorithms alone.

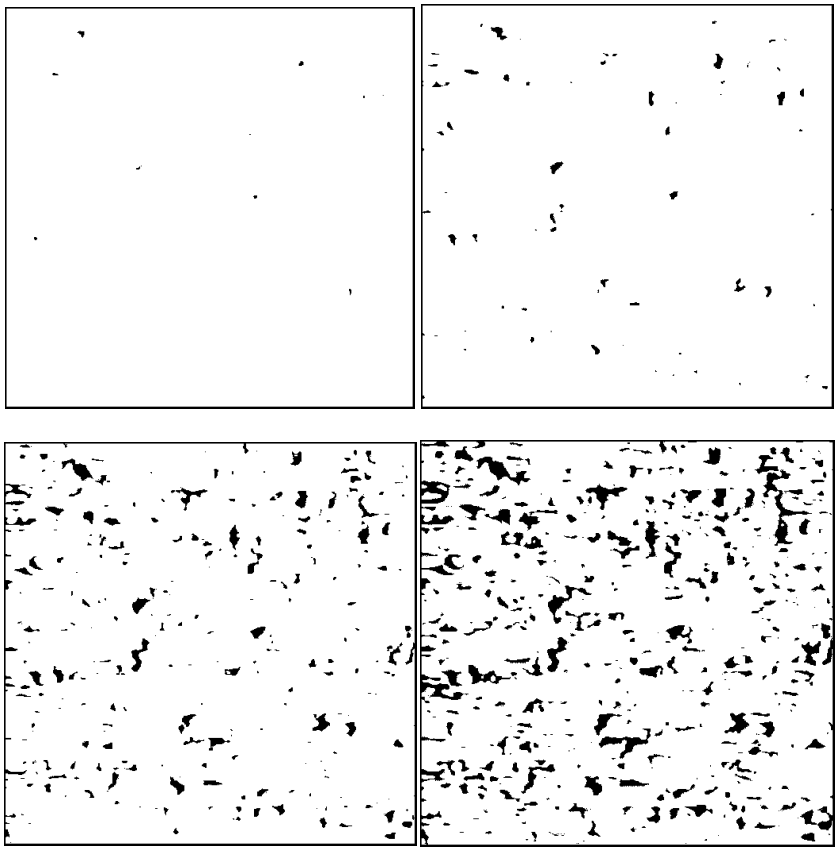

Figure 108- Result of thresholding of wiener-filtered gray-scale image of Figure 107 with different thresholds. The thresholds are: (a) 0.32, (b) 0.35, (c) 0.4, (d) 0.43.

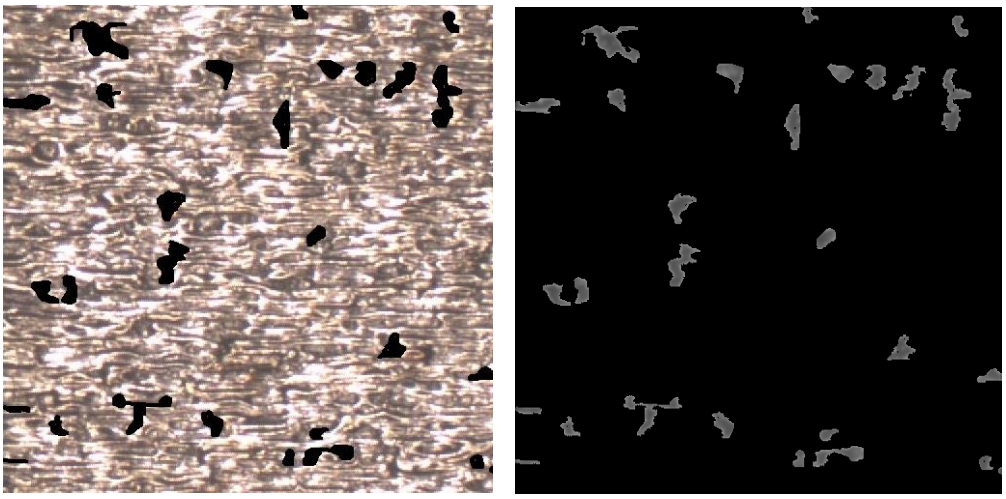

Figure 109- Pores manually segmented from the camera image and isolated in the new image for examining the intensity distribution of pores.

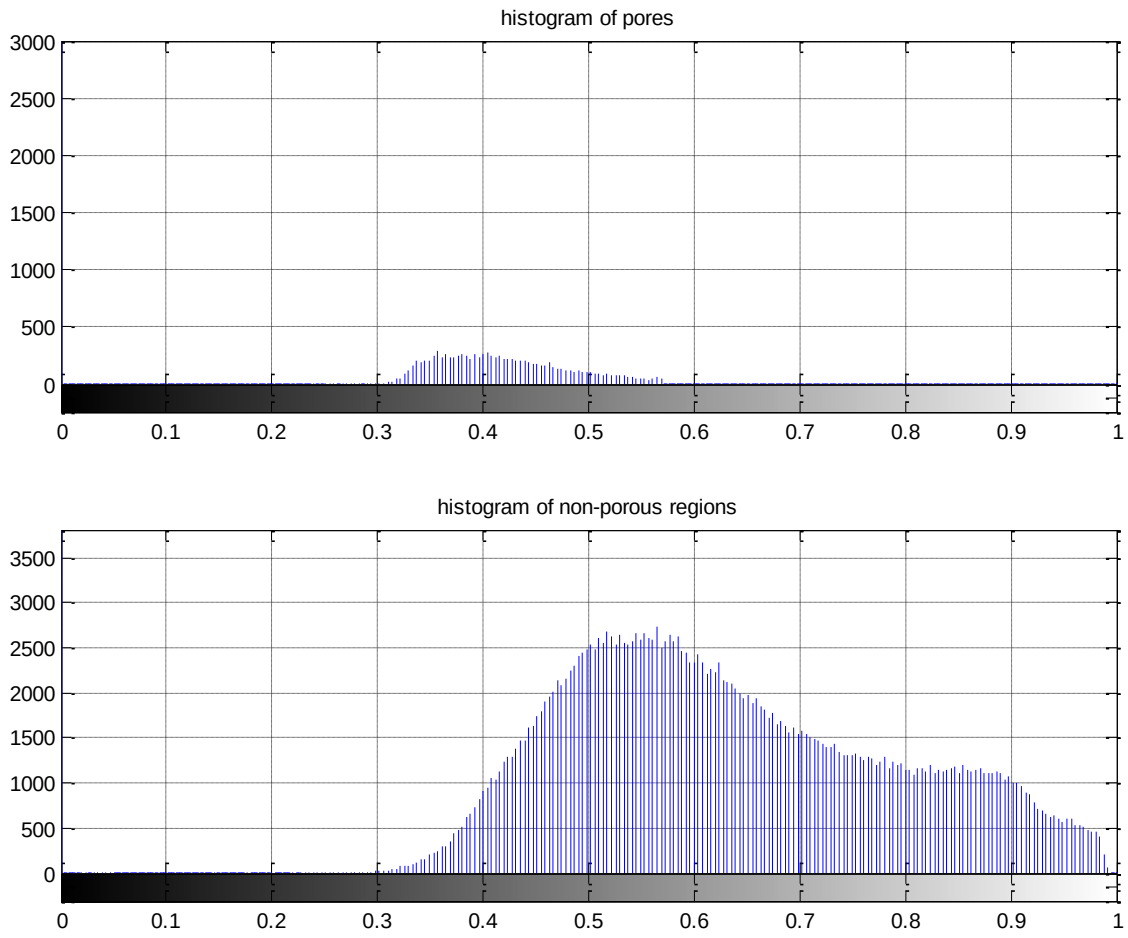

Figure 110- Histograms of pores segmented from camera image in comparison with histogram of regions that contain no pore.

By looking closely at images in Figure 108 and the intensity ranges of pores in Figure 109, it is seen that a low threshold can then be used to detect locations of pores, and a high threshold gives a better estimate of pores shape and size. In other words, the image with a low threshold not too low to segment noisy spots can locate or mark defects and the image with a higher threshold shows the full shape of defects at the markers. This context can be implemented using an image processing algorithm called reconstruction [106, 130, 131]. Therefore, the image with a low threshold of 0.35 after, removal of objects of area smaller than 5 pixels that constitute noise (Figure 111 (a)), was

used as a marker to signify locations of pores. An image with a higher threshold of 0.4, Figure 111 (b), was used as a mask in the (morphological) reconstruction operation.

Figure 111 (c) shows the result of implementing reconstruction. As it is seen, visually, almost all pores have been detected, but the image segments several darkly-etching regions as well as pores. It is possible to remove the number of these false segmentations by increasing the threshold, however at the cost of missing to detect some of the pores. Additionally, although almost all pores are detected, in some cases, the exact shape has not been detected. It is also possible to increase the higher threshold to segment the shapes closely, however, it would be obtained at the cost of further growing the false segmented objects. Therefore, a better balance between increasing false positives (FP) and detecting closer shapes and areas of pores would be to select segmentation parameters that give the area of all the segmentation results close to the area of real visible pores (as seen in Figure 109 (a)), which will be discussed later in this section.

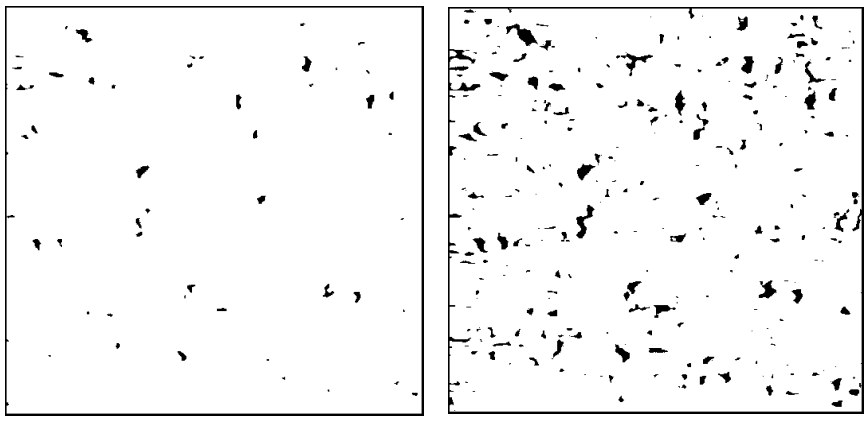

(a) (b)

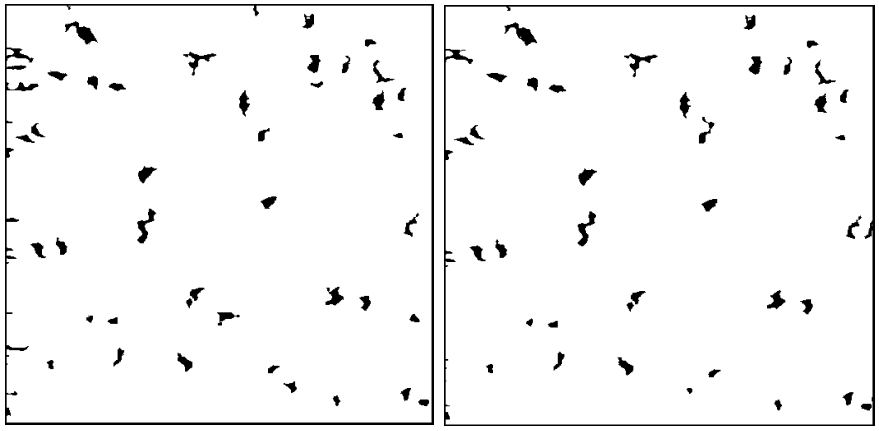

(c) (d)

Figure 111- Application of reconstruction to segment pores from the camera image: (a) marker, (b) mask, (c) result of reconstruction, (d) removal of long, horizontal, narrow objects.

Due to the large intensity overlap between pores and darkly etching regions, it is not possible to eliminate these false positives (FP) using only intensity information. Removal of these FPs only using intensity information, would only be possible by removal of a large number of true pores. To remove some of these false segmentations, characteristics other than intensity should be used, such as geometric characteristics. However, both pores and darkly etching regions get a variety of shapes and forms that do not visibly discriminate from each other and cannot be found intuitively. It will later be seen in this section, however, that the parameters of the algorithm will be optimized to make a better estimate of the area of the true pores which is a better measure than individual pores in terms of FPs or FNs.

By closely looking at the segmented objects, it can be seen, however, that some of these darkly-etching regions correspond with some markings parallel to and at the boundary of laser scan paths that are not lack of fusion. It was mentioned earlier that surfaces built with lower energy and consequently rougher surface, the darkly-etching regions grow smaller and appear less often (see Figure 106). This can be explained by

reduction in melt pool area and temperature that consequently leads to reduced surface temperature. Reduced surface temperatures as well as the surface roughness resist against large and easy oxidation of the surface. For these layers, therefore, it was seen that the majority of the segmented objects are true pores and the total area is comparable with the area of true pores as seen in microscopic image.

As the energy of the build of the layer increases, these markings become larger and have higher contrast (see Figure 112). Therefore, they appear in the segmentation result of reconstruction. Figure 113 (a) shows the example of the porous layer (Zone III) in Figure 112 (b) that is of higher energy compared to the one in Figure 107 along the result of reconstruction shown in Figure 113 (b). As seen, the segmented markings due to laser scans and oxidation are larger and more in number.

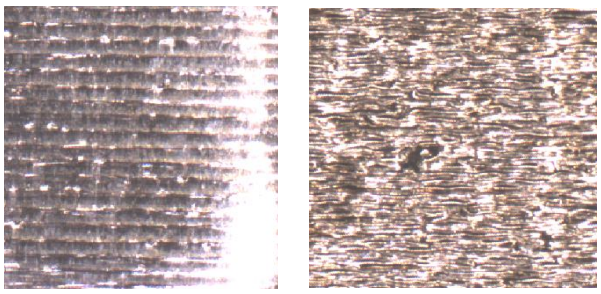

(a) (b)

Figure 112- Example images of (a) a smooth surface (Zone II), and (b) a porous surface (Zone III). It is clearly seen that Zone II surface shows larger darkly etching regions due to higher energy and temperature.

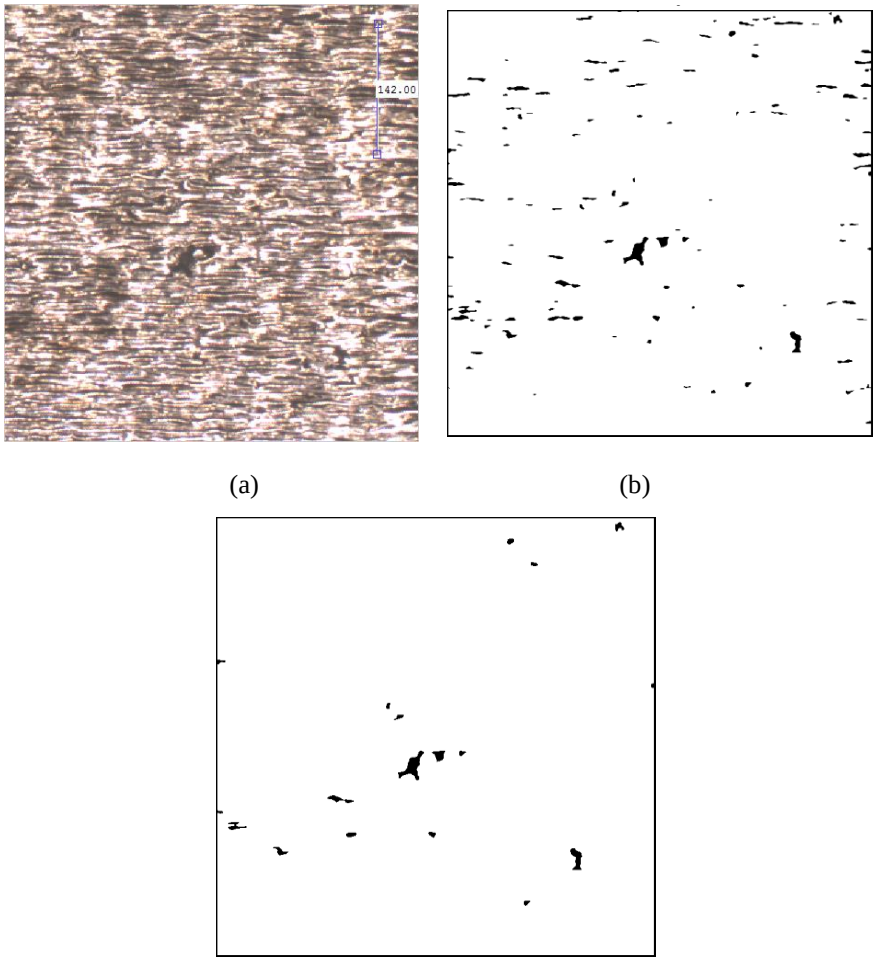

Figure 113- (a) Example of the porous layer (Zone III), (b) segmentation result of reconstruction, (c) result after implementing rule-based identification on geometric features.

These markings are associated with laser scanning that are characterized with long, horizontal, narrow objects. Study of the orientation and the eccentricity of the segmented objects in these example images (see Figure 114 and Figure 115) and several others revealed that the objects with eccentricity over 0.9 and orientation between $\pm 15^{o}$ and a thickness smaller than 10 pixels are a good representative of these scan markings and can remove the majority of FPs without removal of fewer thick horizontal lack of fusion.

Additionally, objects smaller than equivalent diameter of 50 microns were also removed due to less significance and higher chances of being noisy spots (see Section 7.3for discussion). Implementing these constraints eliminated almost all darkly etching regions corresponding to narrow scan path markings. Results of these implementations to Figure 107and Figure 113 are seen in Figure 111 (d) Figure 113 (c). The results show segmented all pores larger than 50 microns, after removal of the majority of the markings of laser scanning and darkly-etching regions.

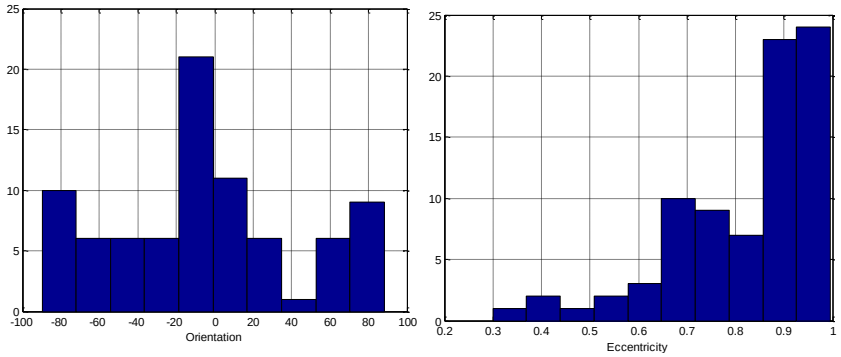

(a) (b)

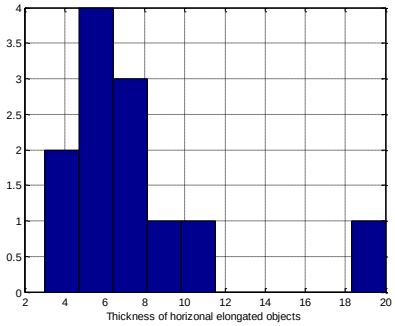

(c)

Figure 114- Histogram of the geometric features of the segmented objects in Figure 111 that majorly consist of true pores: (a) orientation, (b) eccentricity, (c) thickness of long horizontal objects.

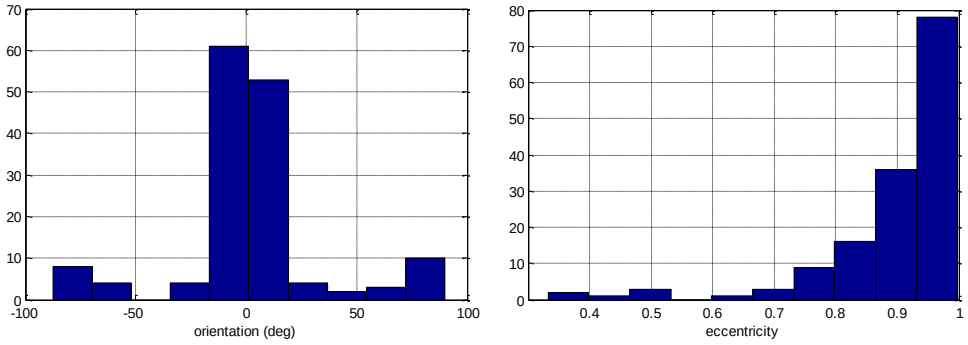

(a) (b)

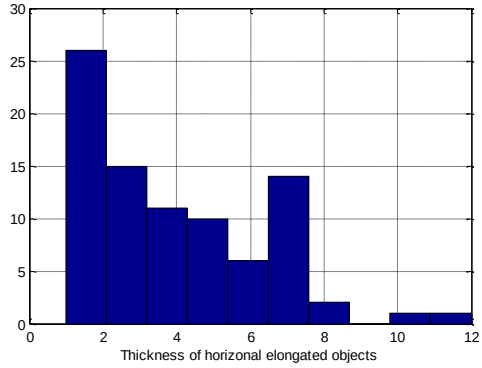

(c)

Figure 115- Histogram of the geometric features of the segmented objects in Figure 111 that majorly consist of long horizontal scan markings: (a) orientation, (b) eccentricity, (c) thickness of the long horizontal objects.

Figure 116 shows the segmentation results for the high-energy example in Figure 112 where reconstruction led to irregularly large region of darkly-etching region with several horizontal scan markings (Figure 116 (c)). Applying same geometric-based feature removal of long horizontal lines due to laser scan marking removed the majority of these FPs (Figure 116 (h)). There are still three segmented FPs. It will be seen in next chapter that Bayesian identification can successfully identify porous layers from non-porous layers and would serve to remove any FPs in layers corresponding to Zone I and II.

To remove the FPs from all images i.e. high-energy layers as well as low-energy porous layers, the pore segmentation algorithm has to be adjusted such that they produce better result for all types of images together. This, as was mentioned earlier, lowers the pore detection precision for porous layers compared to the case where the algorithms are only designed for non-porous layers, as was addressed in previous subsection.

Further work can be performed to remove more of these false segmentations. One of the approaches that can further improve the segmentation results is complementing the results with high-level intelligent identification algorithms. A more precise and thorough segmentation approach that would potentially remove false segmentations is possible by application of feature-based detection. This approach would require several highly discriminating features of segmented objects should be identified and used to train and implement an intelligent classifier.

To eliminate the aforementioned false segmentations in these layers, an approach based on intelligent identification is taken in this dissertation that can also provide other useful information. In order to prevent false detection of pores in layers that do not have pores, it is possible to identify these layers from the layers that have or are likely to have pores (Zone III). To identify these layers, it is possible to find discriminators associated with non-porous regions and identify them from porous regions. This would be possible using application of classification algorithms to identify the texture associated with porous regions from non-porous regions. Classification of porous versus non-porous regions is the topic of next chapter.

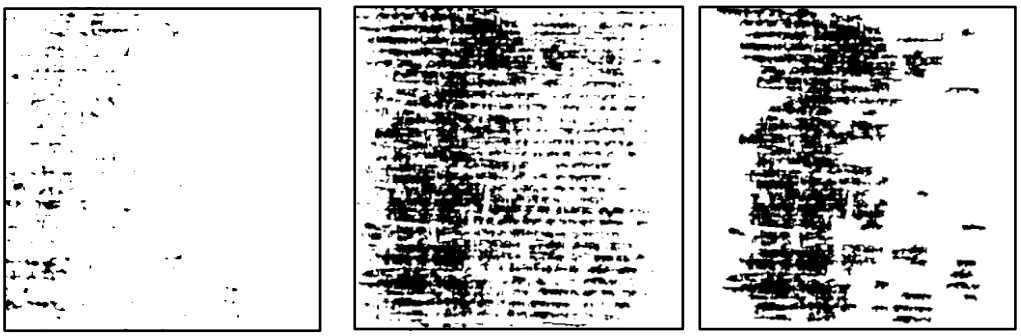

(a) (b) (c)

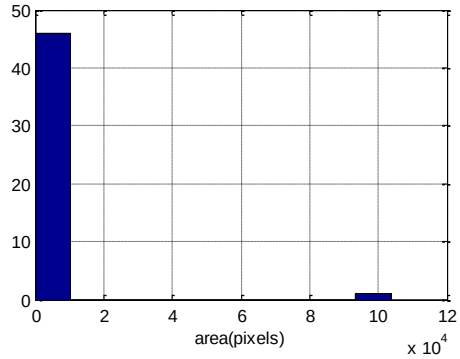

(d)

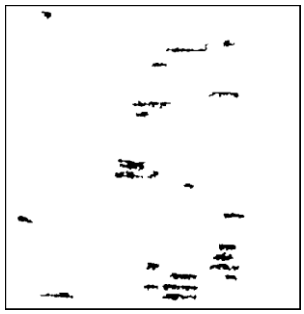

(e)

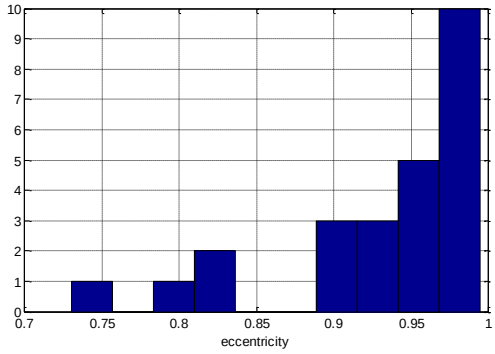

(f)

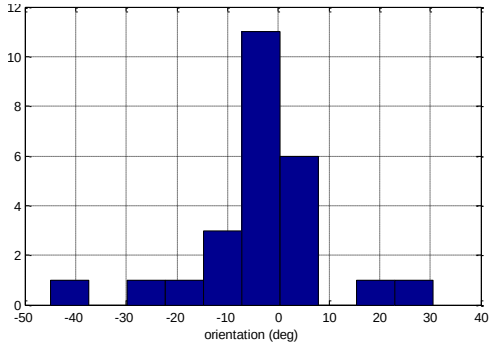

(g)

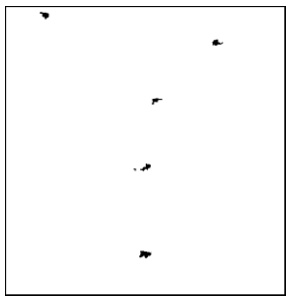

(h)

Figure 116- Results of application of pore detection algorithm to Figure 112 (a): (a) and (b) result of thresholding of wiener-filtered gray-scale image of Figure 112 (a) with thresholds: (a) 0.35, (b) 0.41; (c) reconstructing of image in part (b) as a mask and image in part (a) as a marker; (d) the distribution and histogram of the area of the segmented objects in Figure 116 (c); (e) image after removal of objects with

an area larger than 100 pixels and smaller than 50 micron equivalent diameter ; (f) and (g) the distribution and histogram of the eccentricity and orientation of the objects in Figure 116 (e); (h) the image after removal of horizontal objects (within $\pm 15^0$ from horizontal line and with eccentricity larger than 0.9 and thickness smaller than 10 pixels).

After, FPs are removed, it is possible to increase the match between the shape of the segmented objects and pores (e.g. in Figure 107); a new mask can be produced with a higher threshold, and the result after removal of FPs can be used as a new marker in a second reconstruction operation. This operation would lead to better match between the shape of segmented and true poress, however it would also lead to the growth of false segmentations (see Figure 117 (a)). Alternatively, it is possible to use a region-growing algorithm to the results of the reconstruction after removal of some of the FPs to make the geometry grow closer to the true shape of the pores with high parameters of similarity. The used region-growing algorithm considers the mean of the so-far grown region and the similarity parameter indicates how close the new pixel value is to the mean of the current grown region. The results of reconstruction and region-growing using the characteristic of the grown region seem similar and exchangeable. To determine what parameters give best true porosity estimate, the measure of area is the most appropriate criterion for selecting parameters (see Section 7.3).

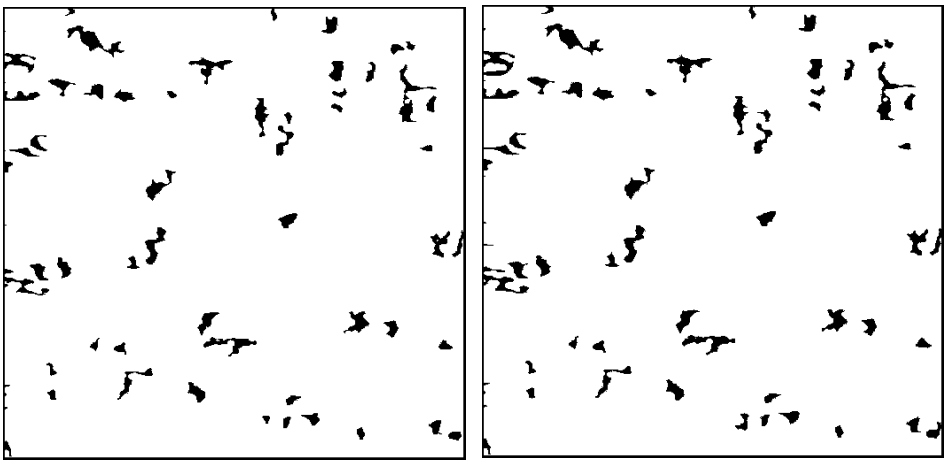

(a) (b)

Figure 117- (a) application of reconstruction using a mask made by a higher threshold (0.42), (b) application of region-growing with the similarity parameter of 0.06.

Figure 118 shows the corresponding microscopic image of Figure 107. A region-growing algorithm was implemented to the microscopic image and the parameter was manually adjusted, specific to the examined image, to provide a good estimate of the porosity seen by eye. The area of the detected porosity was measured as 9230 pixels. It should be noted that, since the matching was performed visually, a series of parameters seemed to produce good results and within this series it was found that a maximum relative error of about 16% exists in the estimation of area of pores using region-growing applied to microscopic images. For the pore segmentation algorithm of the camera, the parameter of the similarity algorithm for the region-growing was adjusted such that the area of the detected pores in the camera image matches the area of the detected pores from microscope.

Figure 119 shows the result of error between the area of detected pores in camera with respect to that of microscope for various selection of the mask parameter in reconstruction operation. This experiment was repeated for two more example images and finally, a parameter of 0.41 was selected for the reconstruction operation to produce

least error for test images. Similarly, a region-growing algorithm of similarity parameter of 0.06 was found to produce similar results for region-growing algorithm applied to camera images (Figure 120). For each case of microscopic image, the region-growing algorithm was adjusted specific to that image, and if needed, rule-based identification based on geometric features was performed to remove FPs.

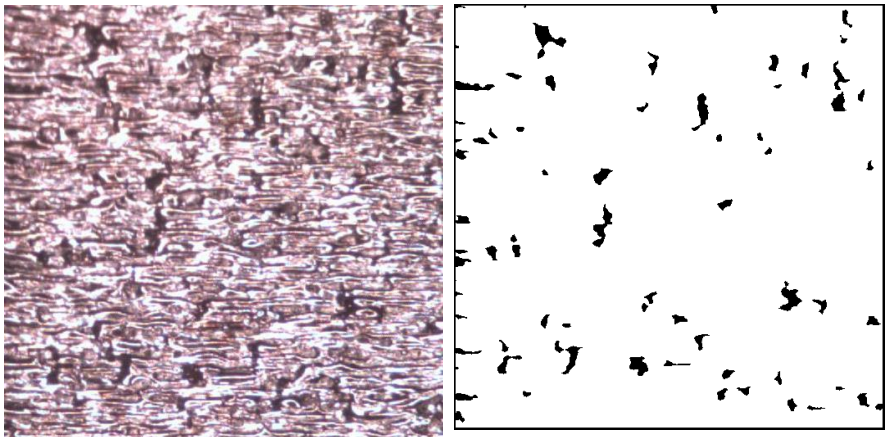

Figure 118- Microscopic image of a layer in Zone III corresponding to the camera image in Figure 107 with the results of pore segmentation using region-growing after manual parameter optimization.

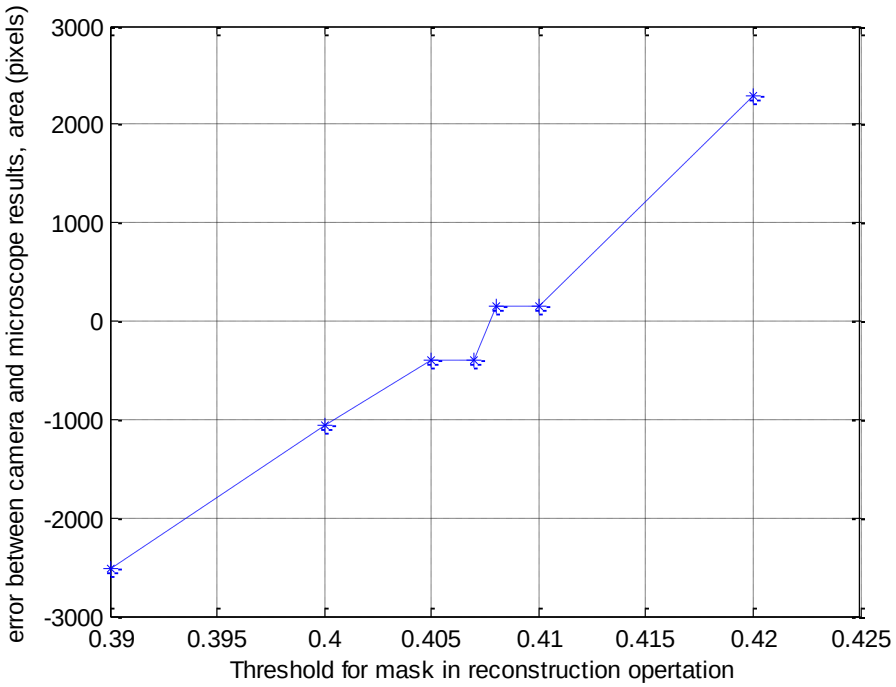

Figure 119- Result of error between the area of detected pores in camera with respect to that of microscope for various selection of the mask parameter in reconstruction operation.

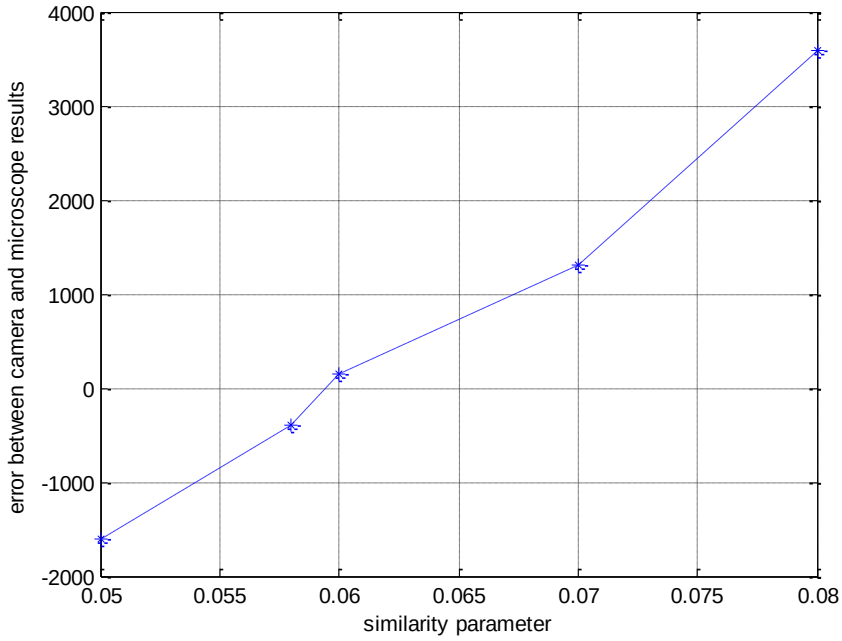

Figure 120- Result of error between the area of detected pores in camera with respect to that of microscope for various selection of the similarity parameter in region-growing operation.

The final pore segmentation algorithm, using reconstruction and rule-based identification based on geometric features, was used to segment pores from other images of different layers and builds. Figure 121 shows examples of these images. By close visual examination of segmentation results for various images it can be seen that almost all pores larger than 100 microns are segmented in addition to many of the smaller pores.

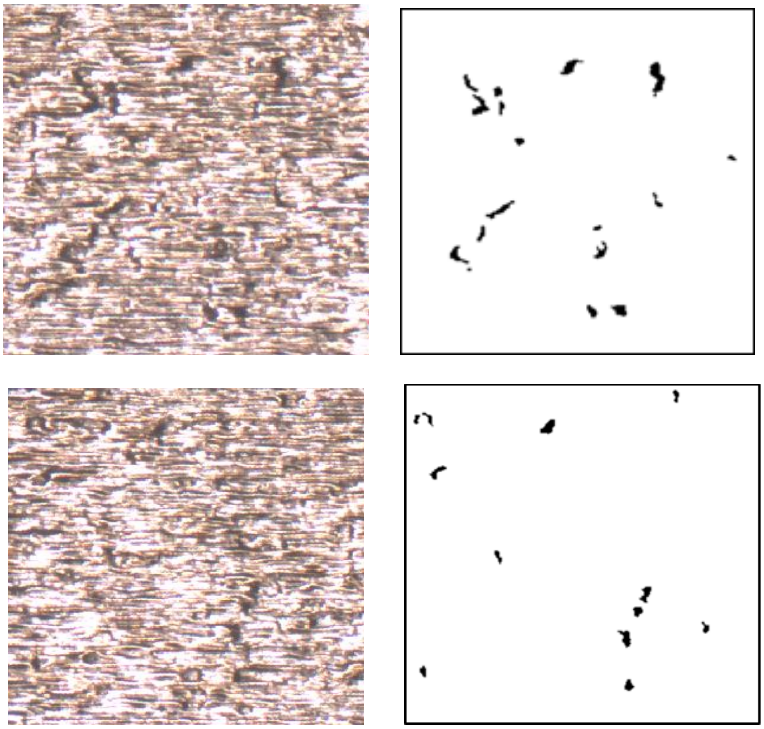

Figure 121- Examples of application of the segmentation algorithm to other layers. Each row shows an individual layer with the original image on the left and the segmentation results on the right.

As seen, visually, pores can be detected; however, there are false segmentations. Due to the large number of data and number of pores, it is not possible to examine each individual detected object. Therefore, it was decided to randomly select 10 images of 2mm × 2mm regions of different porous layers and make an estimate of error of detection of pores. The corresponding microscopic images were found and region-growing

algorithm was implemented to microscopic images. For each individual image, the parameters were adjusted such that pores are detected and fewest darkly-etching regions are segmented. This is to provide an estimated database of the true pores. Figure 122 to Figure 124 show several examples of these implementations.

After an estimation of true pores was available, the designed pore segmentation algorithm was implemented to the camera images and the area of detected pores was calculated and compared with microscopic ones for all the ten randomly selected images. Figure 125 shows the result of this comparison. Figure 126 shows the percentage of relative error between the detected pores from camera images and the true pores from microscope. The mean-root-square of this error is 15%. 70% of tested cases have an error smaller than 15% and the maximum of these errors is 27%.

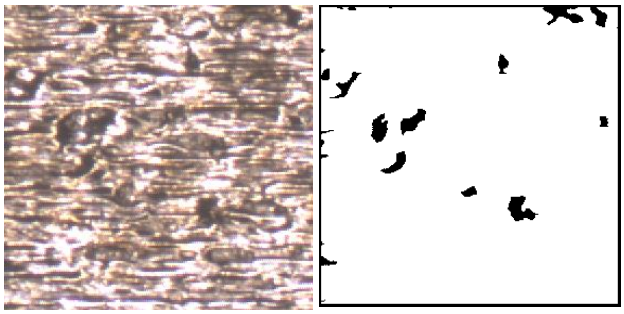

(a) (b)

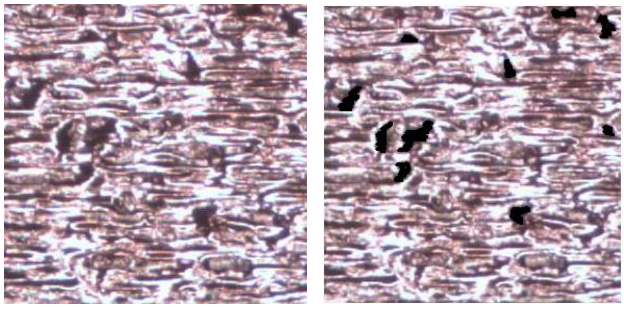

(c) (d)

Figure 122- Comparison of pore detection in camera image with the true pores detected from microscopic image: (a) camera image, (b) result of pore segmentation with reconstruction, (c) microscopic image, (d) pores detected from microscopic image using manually adjusted region-growing.

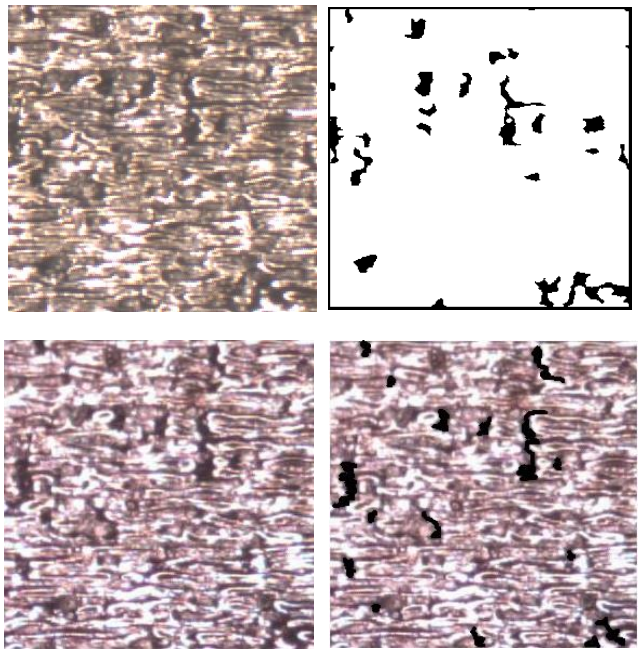

Figure 123- Comparison of pore detection in camera image with the true pores detected from microscopic image. See description of Figure 122.

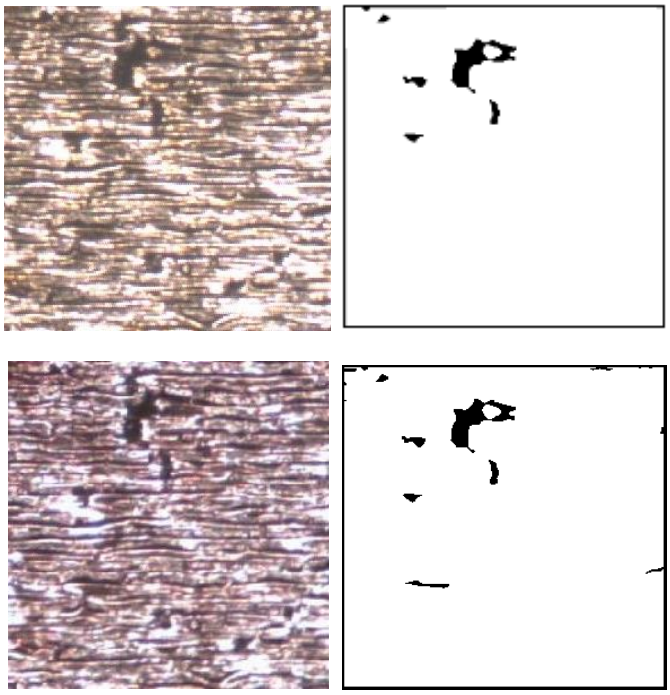

Figure 124- Comparison of pore detection in camera image with the true pores detected from microscopic image. See description of Figure 122.

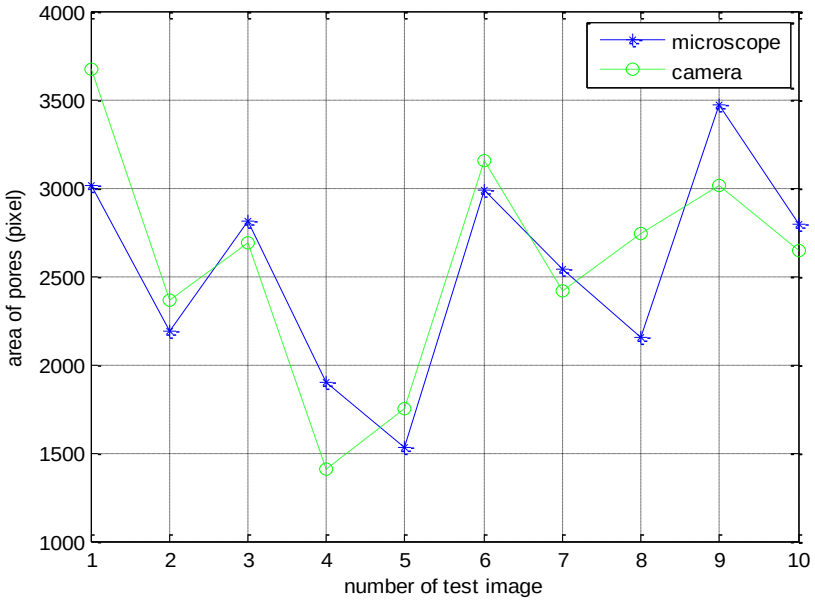

Figure 125- Comparison between the area of segmented pores from camera image and microscope image calculated for 10 randomly selected images.

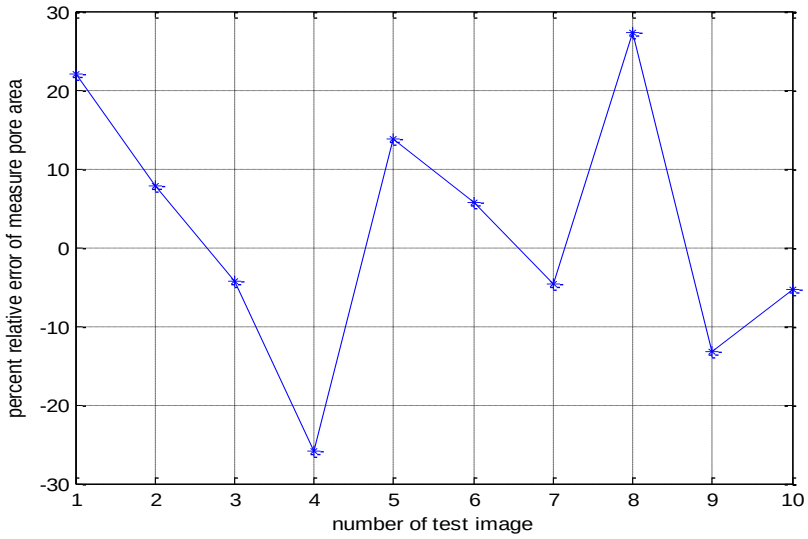

Figure 126- Percentage relative error between the area of segmented pores from camera image and microscope image calculated for 10 randomly selected images.

7.3 Discussion on Image Characteristics and Algorithm Design and Evaluation for Detection of Pores

To design algorithms systematically, it is needed to evaluate the performance of the algorithms, and select parameters that would lead to best or an acceptable performance in terms of the requirements of the application. In many applications, existence of pores smaller than a certain size is not of importance. This accepted certain size almost always is larger than 20 microns and in many cases larger than 50 microns since it is widely studied and determined that pores of size smaller than 20 microns do not have any effect on the structural properties of the material [51]. Pores smaller than 50 microns would also have very small effect on the density of the material and the level of porosity of a material is usually affected by much larger pores [48, 50]. Given the fact the volume of a pore of size 50 microns is $1/27^{th}$ (less than 4%) of the volume of a pore of size 150 microns, it can be seen that detection of large pores are almost 30 times more important than detection of small pores in terms of measure of porosity (or density). Additionally, it is known that the even at the same level of porosity, large pores would affect the structural and material properties more than small pores. Therefore, it can easily be concluded that detection of larger pores are even more than 30 times more important than small pores.

It then seems very reasonable that, for many applications where a close estimation of porosity is needed, if selection of some parameters for an algorithm would result in detection of a large non-pore item at the cost of detection of several very small pores, that selection would not be appropriate. This suggests that the area of the segmented pores is more important than the number of false negatives containing very small pores or number of FPs including very small brown regions. This is why in this research it was decided to match the porosity area rather than the exact shape of pores at the cost of introducing larger areas of falsely segmented objects. And area was used as a

measure for designing and evaluating the algorithms. However, if the application requires making sure that there are no pores of a specific size range or geometric feature-based identification is used, the algorithm should be designed in order to detect pores shapes exactly or consider minimizing level of FNs (False Negatives) for pores of that specific size range rather than decreasing FPs (False Positives).

Earlier, as specifications for this project, it was mentioned that detection of pores of sizes larger than 80 microns (11 pixels) was of interest. At the best level of the imaging setup developed at EWI and given the characteristics of current images in terms of level of noise, and appearance of darkly-etching regions similar to pores, it is even, sometimes, too difficult for human eyes to distinguish small pores from discolorations. For objects that are distinguishable by human, design of appropriate algorithms to detect pores more confidently, would require much more clear images and larger pixel size. Note that, to remove the effect of noise or appearance of small non-pore dots from the image, a wiener filter of size 5 pixels was used which means that objects of size about 5-10 pixels would be faded, distorted and almost become non-distinguishable.

A very common measure for evaluating segmentation precision in computer vision is the visual similarity between objects of interest (surface porosity or lack of fusion), and the segmentation results. This is a very common and widely-used approach in computer vision for (quantitative) evaluation of segmentation algorithms especially for images of high noisy regions and a large number of objects to be segmented [100, 107, 125, 136, 138, 139]. The latter approach was used in this thesis to design and tune the region-growing algorithm to make a close estimation of the area of porosity in the layer.

To evaluate precision of segmentation in camera images, the measure of area was used to be compared against a more precise detection (i.e. manually-monitored segmentation of pores in microscopic images). Generally, to evaluate the algorithms automatically, the algorithm results should be compared against another automatic

algorithm that has already been evaluated and proved to be accurate for the same application and same (or similar) images. Since, no prior algorithm for automatic detection of pores in camera images of metal powder-bed AM layers exists in literature, the automatic evaluation of the algorithm is not possible. Therefore, an alternative statistical approach was taken. Since each individual image is 4000*2000 pixels and each porous layer might contain more than 100 objects that are pores or look like pores, it is difficult to manually examine the original large images. It was investigated that images of sizes smaller than about 2mm×2mm (~ 285×285 pixels) are possible to visually and manually examine while inspecting every object in the image. Therefore, 10 sub-images of size 285×285 pixels were randomly selected and their corresponding microscopic images were manually examined for designing region-growing to detect pores with fewest FPs. After all objects in the original images were identified, they were compared with the results of detection algorithm. The comparison led to a root-mean-square segmentation error of 15% (see Figure 126) and FNR of 0% for pores larger than 100 microns equivalent diameter and 0 FPs for objects larger than 100 microns equivalent diameter.

CHAPTER VIII

IDENTIFICATION OF POROUS REGIONS

As mentioned earlier in Section 7.1, instead of directly detecting pores, it is possible to find a set of features from the surface that have statistical correlation with the porosity of the layer and use them as a measure of porosity. This measure could be an indicator that the examined surface is porous (or likely to be porous) or contains no pore. It could also indicate a more precise (quantitative or qualitative) level of porosity and helps to estimate the porosity.

Additionally, it was seen in Section 7.2 that identification approach allows to identify porous from non-porous regions or layers before application of segmentation algorithms for detection of individual pores. This allows to customize the pore segmentation algoprithm only for porous layers (Zone III), and therefore, significantly increases the precision of pore segmentation, and reduces the FPs.

Figure 127 shows an example image of a smooth, non-porous layer versus a porous layer. It is seen that the smooth surface is associated with smooth variation of intensity and a porous surface is associated with sharp and abrupt variation. Therefore, a feature associated with the spatial variation of intensity would be able to discriminate these surfaces.

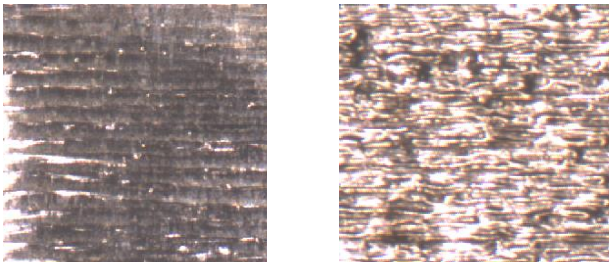

(a) (b)

Figure 127- Example images of (a) a smooth surface, and (b) a porous surface.

After choosing appropriate discriminating features, a classifier should be chosen and trained. There are a variety of choices of classifiers such as neural network, support vector machine, k-mean clustering, and statistical classifiers such as Bayesian. For this work, a Bayesian network is chosen as a reliable statistical inference system. Bayesian inference is described briefly in the next section.

8.1 Description of Bayesian Classifier

Bayesian classifier is a probabilistic classifier that in addition to deterministic classification, can provide statistical information including the probabilities of an object belonging to each class. Statistical classifiers such as Bayesian classifier provide very reliable results on the probability of occurrence of each class given the observed features using likelihood and a priori probability that are obtained from statistical analyses of a large number of data [140-143].

Bayesian inference has been used in a variety of applications including uncertainty quantification, decision-making, and automated medical diagnosis [144-146]. Bayesian inference can be used for classification of objects and determines the probability that an object belongs to a class C_i given that the object has features *F, i.e.* $P(C_i|F)$. The Bayes rule which is the base of Bayesian classifier can be reformulated as below:

$$P(C_i|F) = \frac{P(F|C_i).P(C_i)}{P(F)}, \quad i = 1, \dots, N$$

Equation 15

where N is the number of all possible classes, F is an m-element feature vector $(f_1, f_2, \dots, f_m)$ extracted from an object, and $P(F)$ is the probability of occurrence of the

features F. $P(C_i)$ is the a-priori probability of occurrence of a class C_i and $P(F|C_i)$ is the likelihood which is the conditional probability of occurrence of feature F given a class C_i.

To implement the Bayesian classifier, a-priori probabilities and likelihood should be developed by statistical analyses of a large and comprehensive database of images of layers including porous as well as non-porous layers. Single-element discrete event probabilities such as probability of occurrence of defect i, i.e., $P(C_i)$ can simply be calculated by ratio of occurrence of C_i to all the occurrences in a normal machine operation.

The likelihood that consists of joint conditional probabilities, assuming the independent features assumption, can be written as below:

$$P(F|C_i) = P(f_1, f_2, \dots, f_m|C_i) = P(f_1|C_i)P(f_2|C_i) \dots P(f_m|C_i) = \prod_{j=1}^{m} P(f_j|C_i)$$

Equation 16

Individual conditional probabilities for a given class C_i , i.e. $P(f_j|C_i)$, can be found by 1-D histogram study of feature f_j for objects in a known class C_i. To calculate 1-D histogram analysis, the following factors hold:

1) The precision of the probability distribution function depends on the size of the chosen bins (boxes) within the valid range of feature range in each dimension.
2) The sizes of each dimension of the bin may be chosen differently.
3) If the size of bin is chosen too large, the precision of the probability is too low, and if chosen too small, some bins may not be occupied resulting in a non-smooth broken probability distribution function.
4) For multi-dimensional data, the possibility of a bin remaining empty will be very large. Therefore, the size of the required database will be increased exponentially to the dimensionality of feature space.

To avoid complexity of calculation of a histogram, an alternative widely-used approach is to assume a given probability distribution and calculate the parameters of the distribution from the data. Normal distribution, Equation 17, is an appropriate choice for modeling unknown distributions. The two parameters μ and σ represent the mean and standard deviation of the distribution, respectively. The normal distribution is useful because of the central limit theorem. In its most general form, under some conditions (which include finite variance), central limit theorem states that averages of random variables independently drawn from independent distributions converge to the normal distribution, that is, become normally distributed when the number of random variables is sufficiently large [147].

$$f(x \mid \mu, \sigma^2) = \frac{1}{\sqrt{2\sigma^2\pi}}\, e^{-\frac{(x-\mu)^2}{2\sigma^2}}$$

Equation 17

In most cases, the assumption of independent features leads to satisfactory results, however, If the assumption of the independent observations does not hold, or in other words $P(f_j|C_i, f_k) = P(f_j|C_i)$ for $k \neq j$ does not meet and performance of the resultant Bayesian classifier is not satisfactory, multi-dimensional probability surface fit or histogram study of a large dataset needs to be done to calculate $P(F|C_i)$, which is more cumbersome and is usually avoided.

To calculate joint probability $P(F)$ through multiplication rule based on observations independence assumption, probability of occurrence of each feature, $P(f_j)$, needs to be calculated. If it is not easy to calculate directly, it can more conveniently be calculated by summation of independent subsets of feature space of f_j as below:

$$P(f_j) = P(f_j \cap C_1) + P(f_j \cap C_2) + \cdots + P(f_j \cap C_N) =$$
$$= P(f_j|C_1)P(C_1) + P(f_j|C_2)P(C_2) + \cdots + P(f_j|C_N)P(C_N) \quad j = 1, \ldots, m$$

Equation 18

If the assumption of independent observations does not hold and joint probability of occurrence of feature set, i.e., $P(F)$, is not easy to calculate directly either, it can similarly be calculated by summation of subsets of feature space of *F* and can be written in terms of likelihoods as below:

$$P(F) = P(F \cap C_1) + P(F \cap C_2) + \cdots + P(F \cap C_N)$$
$$= P(F|C_1)P(C_1) + P(F|C_2)P(C_2) + \cdots + P(F|C_N)P(C_N)$$

Equation 19

Once all the a-priori probabilities and likelihoods are calculated based on a train subset of data, the Bayesian classifier can be used for classification, evaluation, or modification or re-selection of the features.

8.2 Feature Extraction

Figure 128 shows two examples of images of the 5.5 mm × 5.5 mm of layers of parts made with high energy and low energy. As mentioned earlier, a layer made with sufficient energy is characterized with smoother variation of intensity and a surface that is porous is characterized with a surface or texture that includes sharper and abrupt and more irregular variation of intensity. Although some measures associated with intensity variations can be extracted directly from the color image or 255-level gray scale image, it is possible to extract these variations, however, from a binary image that captures the local intensity variations and is suitable for further analysis. Adaptive local thresholding by itself can be a segmentation technique and also an operation that captures local intensity variation of the image and visualizes it in a binary format. Therefore, to reduce

the dimensionality of the image, Sauvola adaptive thresholding [148], as an effective local thresholding technique, is applied to the image.

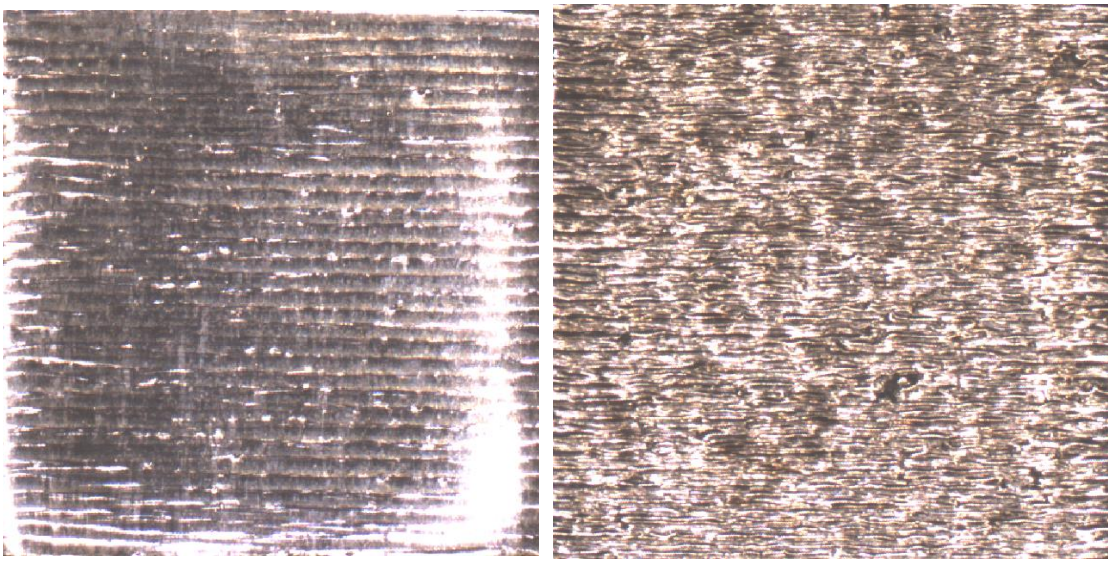

(a) (b)

Figure 128- Example images of (a) a smooth, non-porous surface, and (b) a porous surface.

Figure 129 shows results of application of local thresholding to images in Figure 128 after selection of appropriate parameters. As seen, the texture and appearance of the segmentation results for each case are entirely different throughout the image. Therefore, theoretically, it is possible to extract features from these images and be able to identify them. However, this is for image of a large portion of the layer. However, it is more informative and useful to be able to identify smaller areas of a layer of the part which provides information about the local quality or porosity of each small portion of a layer of the part. Therefore, it was examined if smaller portions of the layer can also discriminate the texture of a porous (Zone III) versus non-porous layers (Zone I and II).

Figure 130 shows two smaller portions of the layer surface of size 201 ×201 pixels (1.5 mm × 1.5 mm). They correspond to cropped portions of images in Figure 129. It is seen that within this window, it is still possible for human eye to distinguish and

identify a non-porous layer from a porous layer. The next step would then be to extract some features that would enable the machine to distinguish between these two surfaces. When appropriate features are selected and a classification algorithm such as NN or Bayesian is trained they can be used to identify the regions. Once the inspected portion of a surface has been identified as porous, the pore detection algorithm, designed in the previous chapter, can be implemented to the image of the surface and used to confidently detect all the pores that are larger than 100 microns. Reduction of FPs in the pore detection algorithm, as mentioned earlier, can then be achieved.

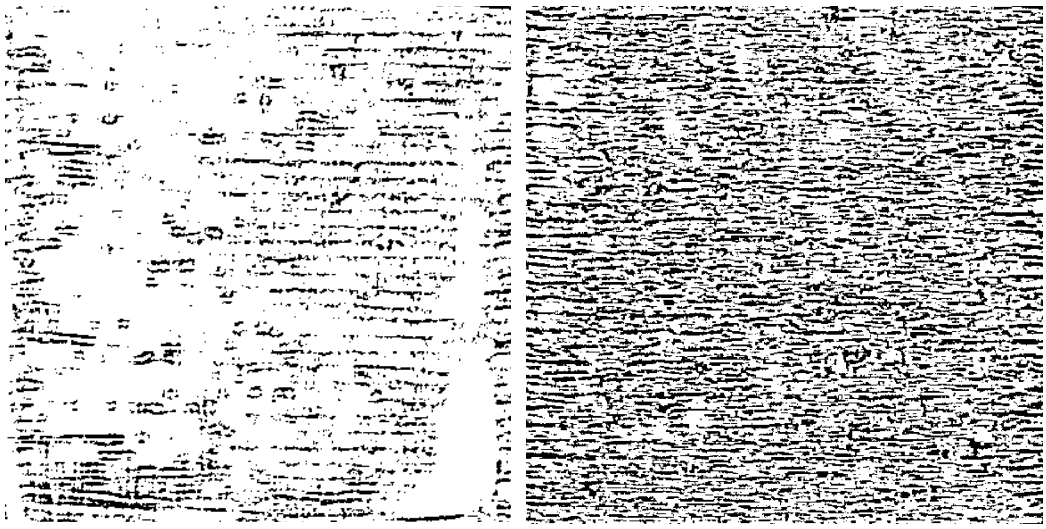

Figure 129- Application of local thresholding to images in Figure 128.

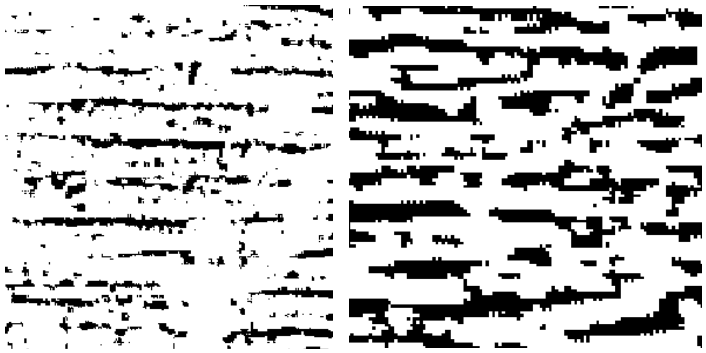

Figure 130- Zoomed-in views of small cropped portions of the two images in Figure 129.

Finding appropriate features that can discriminate these surfaces, however, can be very complicated. Intuition into the texture characteristics and how a human can distinguish between the two textures can initially be used to find these discriminating features that can be formulated into a form computer can understand and easily compute and use.

It was mentioned earlier that the darkly etching regions in high energy, smooth surfaces appear larger. This suggests that the segmented white regions in the images of high-energy layers after applying local thresholding appear larger (i.e. the black spots would be smaller). It was also mentioned that the intensity variation in smooth, non-porous surfaces is generally smoother than intensity variation of porous surfaces which are generally rougher. Therefore, it suggests that areas of different local intensity and of sudden intensity variations, represented by black spots in local thresholding results, may appear more sparsely than in porous layers. In other words, the black objects in the results of local thresholding may be in general smaller and sparser for non-porous surfaces rather than porous surfaces. Figure 129 and Figure 130 support this idea. Therefore, one feature can be chosen as area of all the black regions.

Figure 131 shows more examples of results of local thresholding for two high-energy, smooth layers (Zone II) versus two low-energy, porous layers (Zone III). As it is seen, the black regions in results of local thresholding of surfaces in Zone I are much smaller than those in Zone III. The black areas of all 201*201 pixel regions of layers belonging to Zone II and Zone III were calculated and assuming normal distributions, their distributions parameters were calculated. Figure 132 shows the probability distribution function (pdf) of the black areas in local thresholding results for all camera images belonging to Zone II (high-energy, non-porous) vesus Zone III (porous) layers. HE represents the high-energy (Zone II) and LE represents low-energy (Zone III). As

seen, the distributions clearly support that area is a strongly discriminating factor between these two zones and therefore, would be able to classify them with high accuracy.

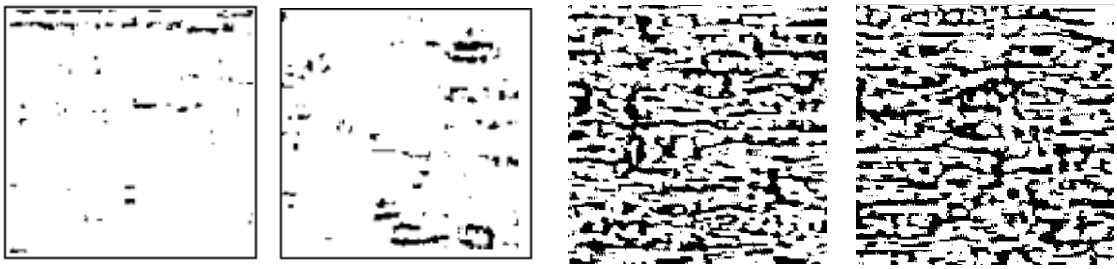

(a) (b) (c) (d)

Figure 131- Results of local thresholding applied to (a) and (b) two examples of high-energy, smooth surfaces (zone II), (c) and (d) low-energy, porous layers (Zone III).

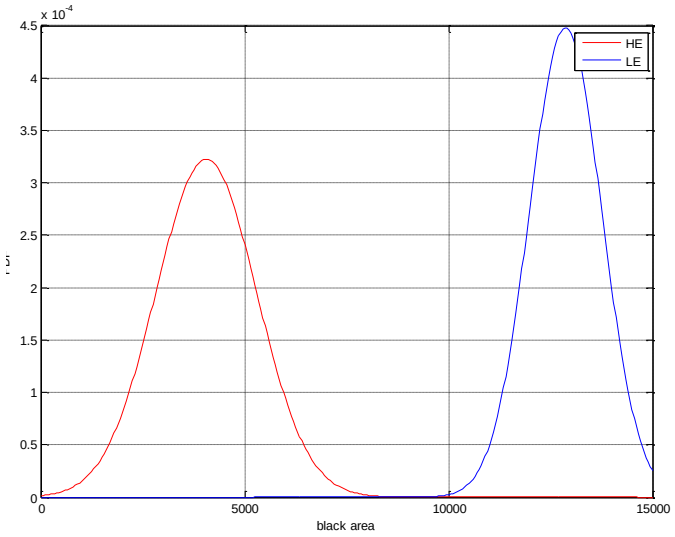

Figure 132- The probability distribution of the black areas in local thresholding results for all camera images of Zone II (high-energy, non-porous: HE) and Zone III (low-energy, porous: LE) layers.

Therefore, to examine the ability of the discriminating capability of this feature (area) used in a Bayesian classifier, this features would be used as the first attempt of the classification of porous versus non-porous regions. Figure 132 shows the pdf of area for a layer subregion given it belongs to a layer in Zone II or Zone III. By definition, this pdf can serve as the likelihood of the feature area given class Zone II or class Zone III i.e. $P(f_1 = \text{area}|C_i = Zone\ I)$ and $P(\text{area}|Zone\ II)$. However, since likelihoods are

calculated in the training step, the corresponding pdf's extracted from the set of training samples, would serve as the likelihoods to be used in classification. For this example, 70% of data belonging to Zone II and III were used for training and calculating the likelihoods, and 30% was used for evaluating the performance. It was seen that the Bayesian classifier with only area as feature, would be able to identify porous (Zone III) from high-energy, non-porous (Zone II) with a TPR (sensitivity) of 100% and a TNR (specificity) of about 98%. In other words, all porous regions were identified as porous, but 2% of high-energy, non-porous regions were identified as non-porous. This level of performance was expected from the pdf's of the area for two different classes that almost showed no overlap.

Figure 133 shows illustration of the results for classification of Zone III (low energy, LE) versus Zone II (high energy, HE). The red line in Figure 133 (a) shows the target value for $P(HE|area)$ which should be 1 for HE regions and 0 for LE (Zone III) regions. The blue "+" signs show the output of the Bayesian network i.e. $P(HE|area)$ for each of the images. As seen, the output of Bayesian closely follows the target value. To binarize the final output in form of a binary decision, porous or non-porous, a threshold should be selected to classify the output. This threshold is usually selected to minimize the number of FPs or FNs or make a compromise between the two. It is sometimes simply selected as 0.5. Given the results in Figure 133 (a), a threshold value between 0.4 to 0.6 would be appropriate to give best results. Therefore, the threshold was selected as 0.5. Figure 133 (b) shows the error associated with the results of the binary decision, i.e. the result of binary decision subtracted from the target value. Therefore, an error of +1 designates a FP (for identification of porous layers) and -1 designates FN (i.e. a porous layer identified as non-porous).

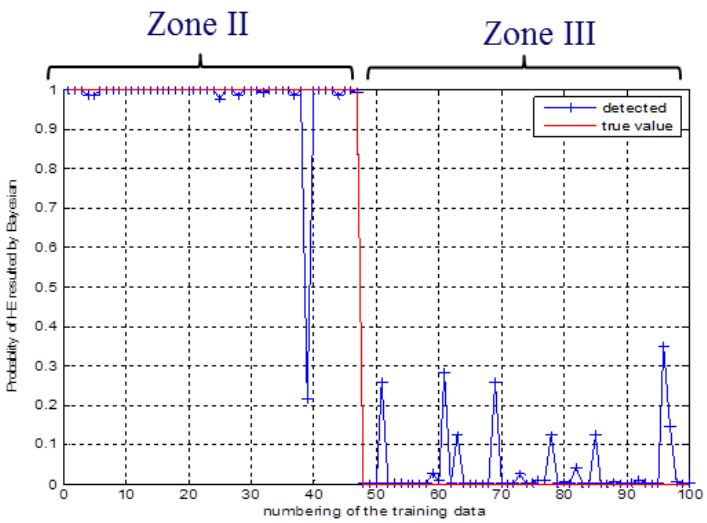

(a)

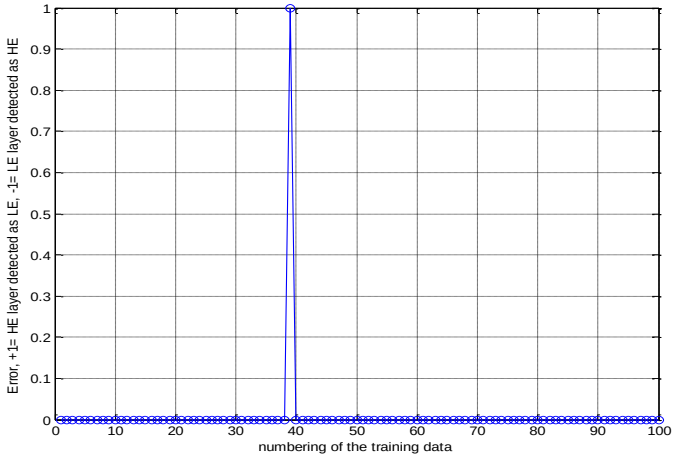

(b)

Figure 133- Result of using Bayesian network to identify Zone III (LE) versus Zone II (HE) using area as the only feature: (a) output of Bayesian, (b) Bayesian output after binarizing.

Although area provides a good classification performance for the classification of zone II and Zone III, the performance for classifying porous layers (Zone III) from all non-porous layers (both Zone II and I) is very poor. Figure 134 shows the pdf's for porous (Zone III) and non-porous (Zone II and I combined). As it is seen, by adding region corresponding to Zone I, the pdf will show a strong overlap between the porous

regions and non-porous regions such that almost the entire range (3σ, σ = standard deviation) of area for Zone III is also covered within $3\,\sigma$ of non-porous regions. This clearly suggests that Bayesian based on area alone will not be able to correctly identify between porous and non-porous for all regions with areas lying within this range.

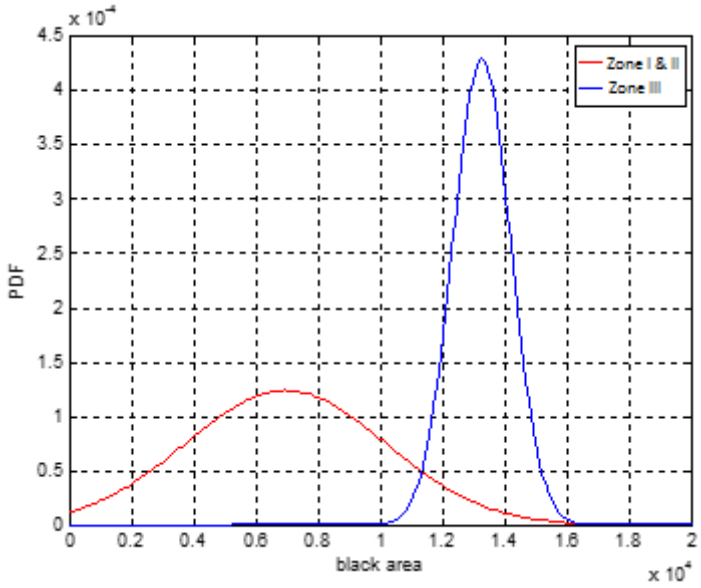

Figure 134- Pdf's of area for porous (Zone III) and non-porous (Zone II and I combined).

Figure 135 shows the result of Bayesian network for identification of Zone III versus Zone II and I. Figure 135 (b) shows the error associated with the results of the binary decision. Similar as before, an error of +1 designates a FN (a porous identified as non-porous) and -1 designates FP (i.e. a non-porous layer identified as porous). As it is seen, although the majority of porous layers are identified as porous, many of the layers belonging to Zone I are misclassified as porous. To select the value of thresholds, the threshold was picked such that the $|TPR| + |TNR|$ gets maximized (see Figure 136). A threshold of 0.6 was found to be the best choice using this measure. Using this threshold, a performance of sensitivity of 94% and specificity of 42% was achieved. In terms of

precision and negative predictive value (NPV), the performance was obtained as precision of 60% and NPV of 88%.

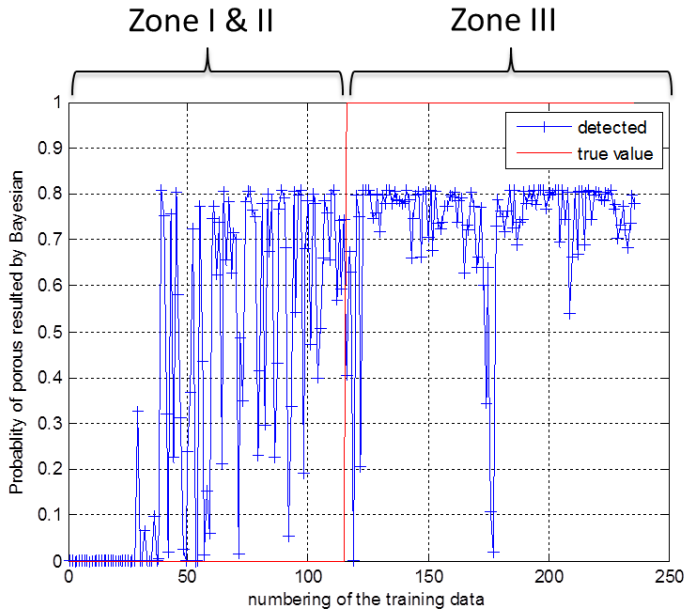

(a)

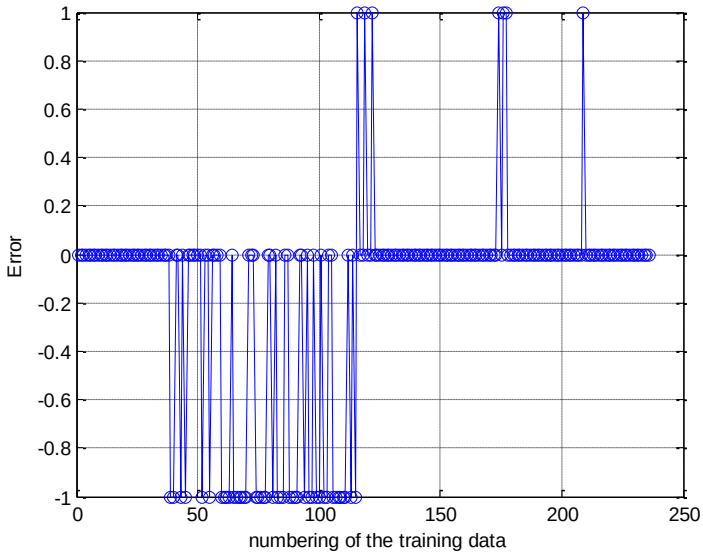

(b)

Figure 135- Result of Bayesian network to identify Zone III versus Zone II and I using area as the only feature: (a) output of Bayesian, (b) Bayesian output after binarizing using optimal threshold of 0.6.

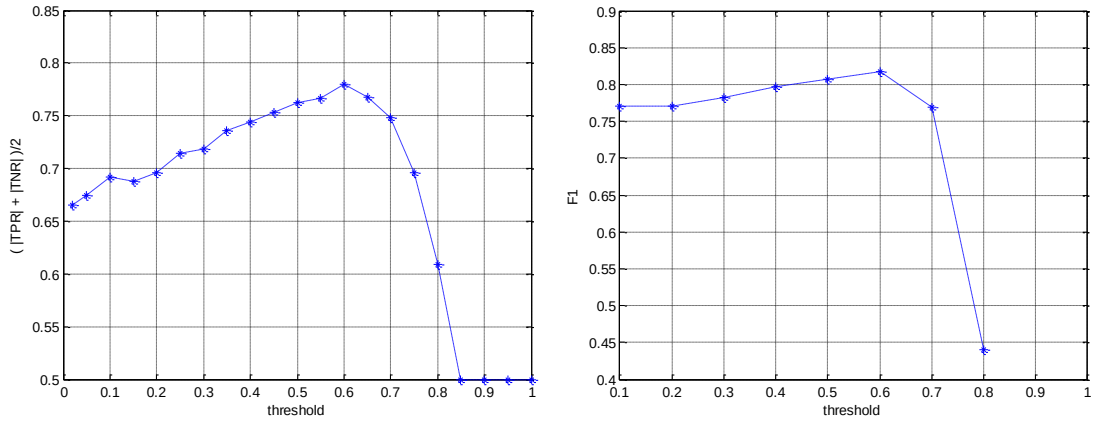

Figure 136- Performance of Bayesian network, using area as the only feature, for various values of thresholds: (a) average of $|TPR| + |TNR|$, (b) Figure of Merit (F1).

Figure 137 shows the pdf for area of the three zones separately. As seen, the pdf of area for Zone I has a strong overlap with pdf of Zone III. Therefore, it is needed to find a feature that discriminate Zone I from Zone III.

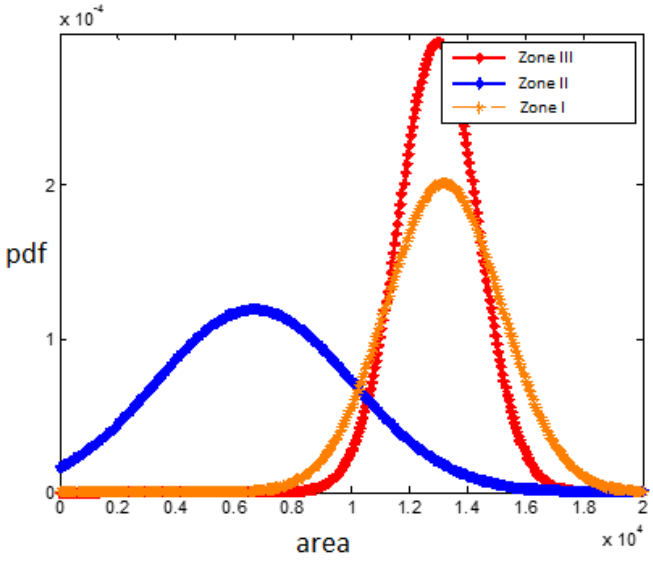

Figure 137- Pdf's of area for porous (Zone III) versus non-porous, Zone II and Zone I individually.

Given the earlier discussion on the distribution of darkly etching region with respect to energy, it was seen that the brown darkly etching region appear along the horizontal marks associated with laser scan. Therefore, it was postulated that regions belonging to Zone I would show a more repetitively occurring, segmented horizontal markings and a feature that counts the number of intensity changes perpendicular to the scan path would be a representative of this characteristics. A mathematical feature corresponding to the number of changes of intensity value along the vertical central line after removal of objects smaller than 5 pixels was extracted from regions belonging to the three zones.

Figure 138 shows the pdf of this feature for all the three zones individually. As seen, the pdf of this feature for Zone I and Zone III show a relatively shifted mode that suggests that results may be improved by including this feature. Figure 139 shows the output of Bayesian network to identify porous (Zone III) versus non-porous (Zone II and I) using number of intensity changes as a feature in addition to area. A threshold of 0.6 was found to achieve best performance reducing $|FPR| + |FNR|$, or maximizing $|TPR| + |TNR|$, or similarly Figure of Merit (F_1) can be used (See Figure 140). After binarizing the results, using the two features of area and number of changes of intensity in Bayesian network, a classification performance of 91% sensitivity and 58% specificity was achieved. In terms of precision and negative predictive value (NPV), the performance was obtained as precision of 67% and NPV of 88%.

By further examination, it was seen that this high number of FPs (low specificity) are actually associated with regions in Zone I that are mistakenly identified as porous. Therefore, although including the number of variation of intensity slightly improved the TNR (specificity), features that further distinguish between Zone I and Zone III are needed to reduce the number of FPs.

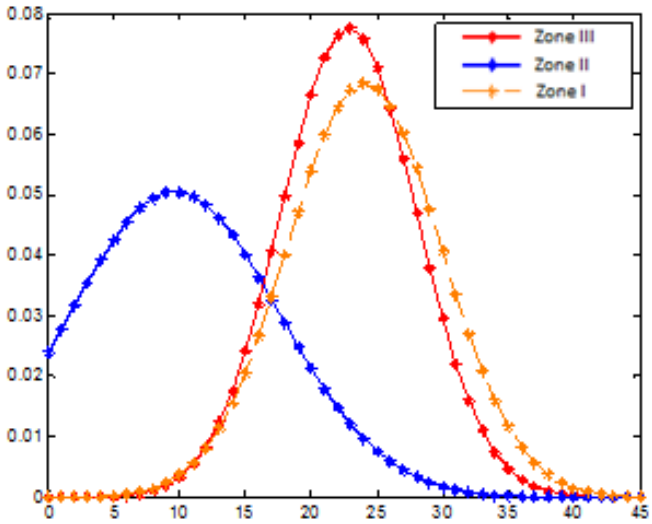

Figure 138- Pdf's of number of intensity changes for Zone III (porous) versus Zone II and Zone I individually.

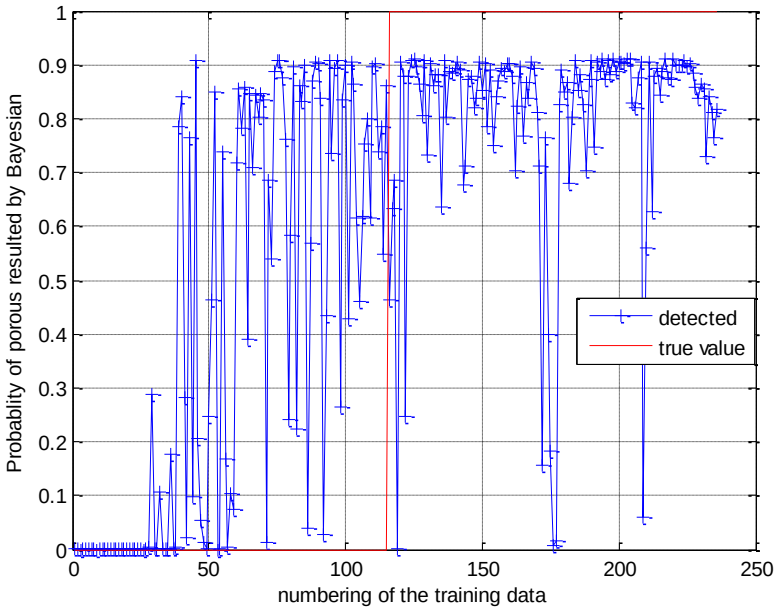

Figure 139- Output of Bayesian network to identify Zone III versus Zone II and I using two features of area and number of intensity changes. True value of 1 represents Zone III, true value of 0 represents Zones I & II.

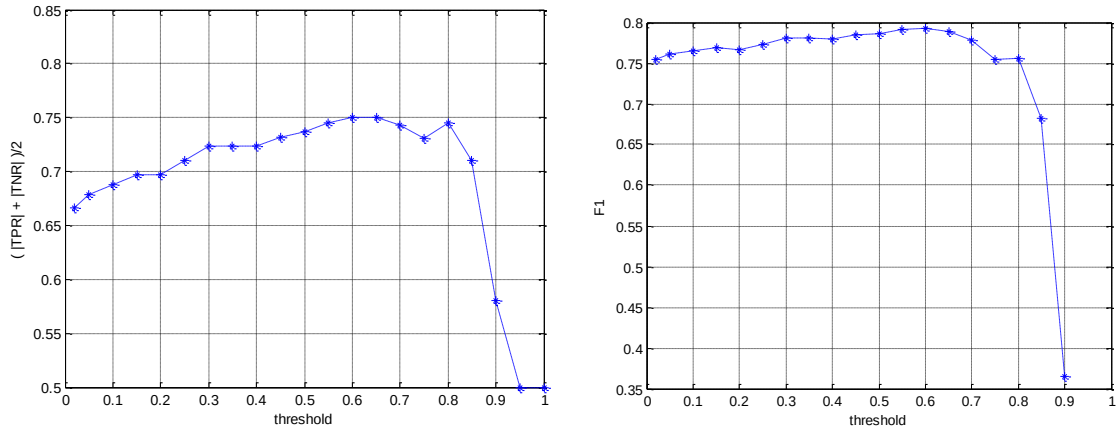

Figure 140- Performance of Bayesian network, using two features of area and number of intensity changes, for various values of thresholds: (a) average of $|TPR| + |TNR|$, (b) Figure of Merit (F1).

As was mentioned earlier, in layers of high-energy builds, the darkly-etching regions appear large and therefore the black regions after local thresholding are small, the smoothness of the surface also makes the black regions after local thresholding be very sparse. However, as the level of energy from high energy (Zone II) decreases to optimal layers, the darkly etching regions grow smaller and the surface smoothness decreases. This causes the black regions after local thresholding to no longer be small and sparse, and in fact, they capture the intensity variations along the scan paths between two adjacent paths. Figure 141 shows the results of local thresholding for more examples of (only) non-porous layers, as the level of energy starts from highest in Zone II (Figure 141 (a)) and decreases close to optimal parameters and lowest in Zone I (Figure 141 (b)), but not entering Zone III. The mentioned observation can be clearly seen in these images.

Figure 142 on the other hand shows three examples of applying local thresholding to sub-regions belonging to porous layers (Zone III). It can now be seen why the two features area and intensity changes count not distinguish the pattern associated with Zone III from Zone I. Therefore, it is required to find features that better discriminate Zone III from Zone I.

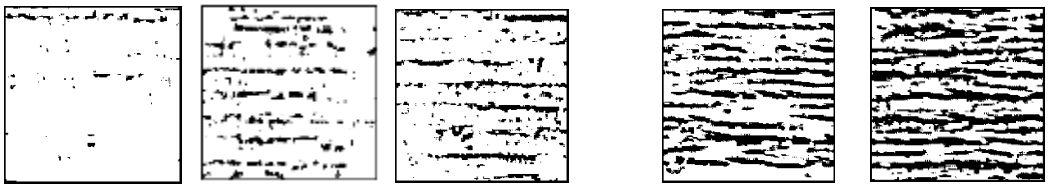

(a) (b)

Figure 141- Results of local thresholding for several examples of (only) non-porous layers: (a) Zone II, (b) Zone I.

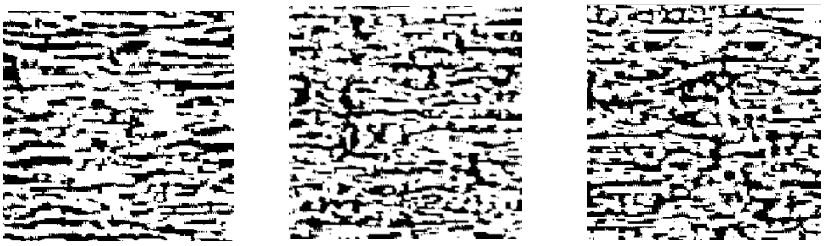

Figure 142- Results of local thresholding for several examples of porous layers, Zone III.

By looking closely into the local thresholding results of Zone I layers, it is seen, since the surface is still fused well and does not contain elevations due to high roughness and porosity, these black regions form exactly along and following the lines between two adjacent scan paths. They look more regularly shaped in form of parallel horizontal lines across the image, while for porous layers, these patterns look much more irregular. Therefore, it seems possible that these characteristics can be captured by some mathematically-formulated features. While it may be possible to capture this behavior in spatial domain, the regularity and harmony of these patterns seem to be representable more clearly and by a smaller number of features in frequency domain.

Several sample images from different zones (especially Zone I and III) were converted to frequency domain. Due to the irregular and non-ideal shapes of the frequency distributions of the images, it was found difficult to identify the features known to certainly discriminate the frequency distributions of images belonging to different zones. Therefore, it was decided to study two cases of an ideal regular pattern compared to a distorted pattern.

To test this hypothesis and more intuitively find and select the appropriate features, two sample patterns were generated as shown in Figure 143. The left image shows a regular pattern to represent the Zone I images and the right image is a disrupted and deformed irregular form of the left pattern to represent Zone III images. The spacing between the horizontal lines was chosen as 13 pixels which is equal to the laser scan width or hatch spacing distance (90 microns). These images were converted to frequency domain using fast Fourier transform (fft). However, to remove the D.C value of the signal, the fft was applied to the image where the mean value was subtracted. Note that the D.C value of the image (or mean of the image) represents the area of the white (or black) regions in the image and this feature has already been captured by the feature area considered previously.

Figure 144 shows the fft of these images in the x-y plane where the color represents the z value of each component. The x-y plane represents the two frequencies in x and y directions and the z value represents the amplitude of the fft component at the frequency specified by x and y values.

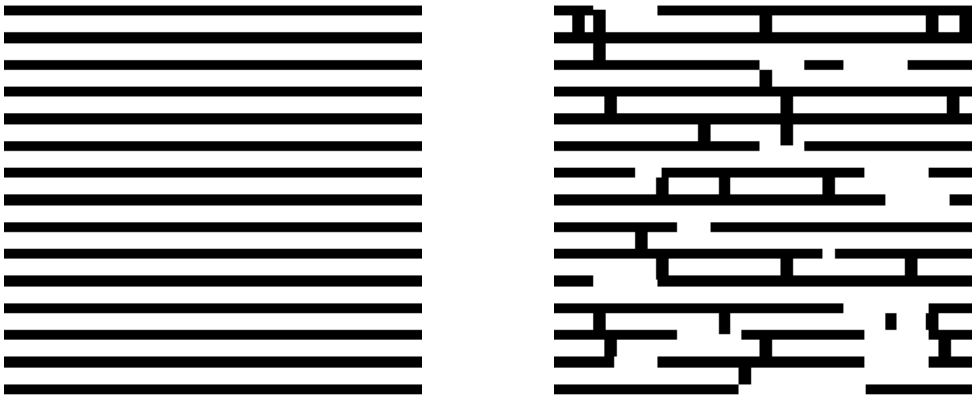

Figure 143- Two patterns generated to simulate regions belonging to Zone I (left) for non-porous versus Zone III (right) for porous layers.

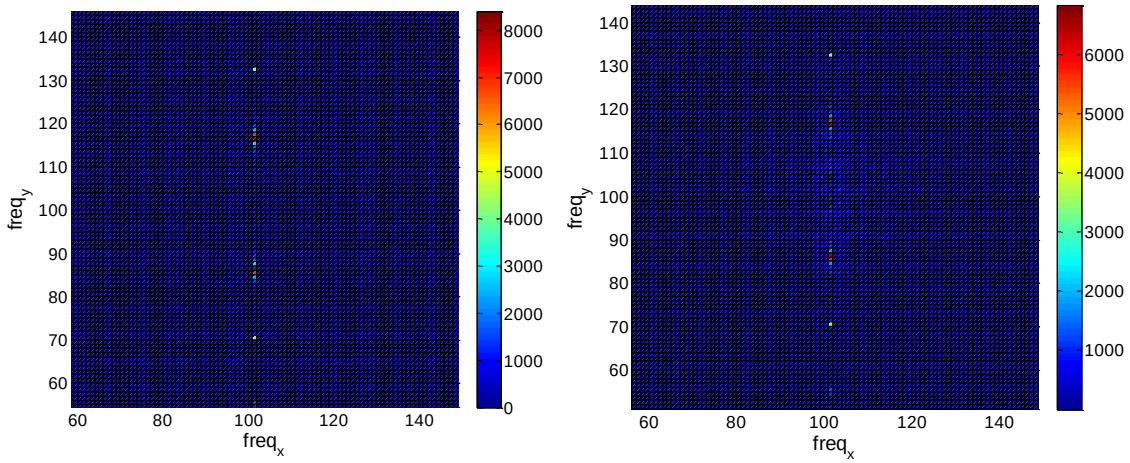

Figure 144- fft of images in Figure 143 in the x-y frequency plane while the color represents the z value of each component, i.e. amplitude at that frequency pair.

Equation 20 shows the discrete Fourier transform of a 2D digital signal $f[m,n]$ for $m = 1{:}M$ and $n = 1{:}N$. $F[k,l]$ are the frequency transform of $f[m,n]$ and are the coefficients of each harmonic component at frequency $\frac{k}{M}m$ along x direction and $\frac{l}{N}n$ along y direction. k and l are simply the count numbers of each frequency component along x and y directions. The amplitude of this harmonic component is the absolute value of $F[k,l]$ which in general are complex numbers. M and N are the total number of discrete data along x and y direction which equal the number of fft frequencies in x and y directions respectively. Therefore, for our case, M and N are equal to 201 which are the number of pixel values in each direction. For $k = l = 0$, the frequency 0 would be obtained which represents the mean value or D.C. component of the signal. If M and N are odd, the remainder of the frequencies and their corresponding factors are symmetric around 0.

$$F[k,l] = \frac{1}{MN}\sum_{m=0}^{M-1}\sum_{n=0}^{N-1} f[m,n]e^{-j2\pi\left(\frac{k}{M}m+\frac{l}{N}n\right)}$$

Equation 20

Since the image size is 201 × 201 pixels for our thresholding image results, for Figure 144, there would be 201 frequency components in each x and y directions. These 201 frequencies consist of frequency 0 corresponding to the D.C. value of the signal which is 0 for our image as mentioned earlier, and 100 symmetric frequency components around 0. The frequency counts in the fft plots have been shifted by 101 to center the fft and only include positive frequency counts that is 0 to 201. Therefore, frequency 101 represents 0 frequency component, D.C. value. Also, the x and y directions in original images, i.e. Figure 142 or similarly Figure 141, are horizontal toward right and vertical downwards, respectively, where the origin is considered at the top left corner.

To better study the behavior of the images in frequency domain, the y-z views and x-z views of the fft of Figure 143 (a) are shown in Figure 145. As seen in Figure 145 (b) the projection of the x-z view of the fft of the image has a sharply distributed spike around frequency 101 and resembles the fft of a 1D square wave (see Figure 146) and this is in agreement with the fact that the image along x direction resembles a 1D constant signal. Also, the y-z view of fft as seen in Figure 145 (a) resembles the fft of a 1D constant-value function (see Figure 146) which the 2D image looks like along y direction. In Figure 145 (a), the 0 frequency value is 0 and there is one large spike at frequency 116 symmetrically around center frequency 101. This spike occurs at the original frequency of 15 (116-101) which shows the first major harmony of the image along y direction. Looking into the spatial behavior of the image, the image is periodic with spatial period of 13 pixels which would be equivalent to frequency $\frac{201}{13} = 15$ where 201 is the image size.

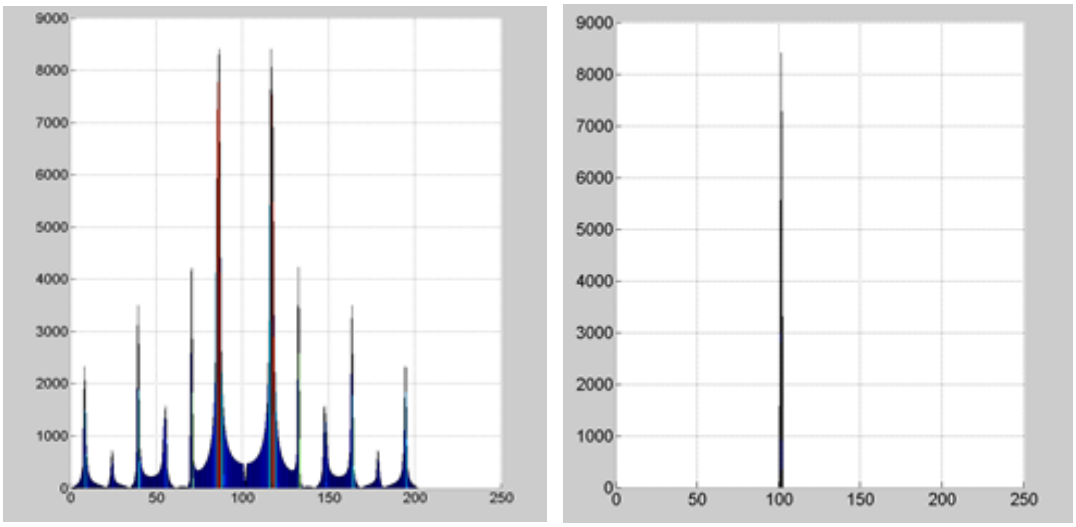

(a) (b)

Figure 145- fft of Figure 143 (a): (a) the y-z view, (b) x-z view.

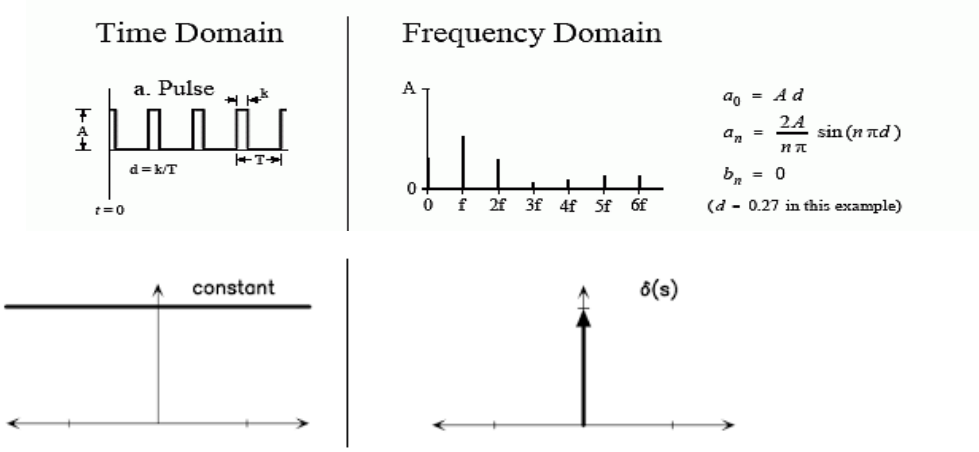

Figure 146- fft of 1D signals corresponding to a square wave and a constant value. Square wave represents the variation of the 2D image (Figure 143 (a)) along y direction and the constant function represents the variation of the 2D image along x direction.

It is now desired to identify the differences in frequency domain between the two images in Figure 143. Figure 147 and Figure 148 show the fft of both images in Figure 143 in y-z and x-z view, respectively, next to each other. The major differences between the fft of the regular pattern and distorted pattern can easily be seen in y-z and x-z views of the fft. The regular image has an ideal periodic change in y direction at a frequency of

15 which manifests itself as a large spike at that frequency in y-z view. However, as the image deviates from this ideal periodic motion along y direction, the amplitude of this spike, which still occurs at frequency 15, gets smaller and the frequency components get distributed less sharply around that value.

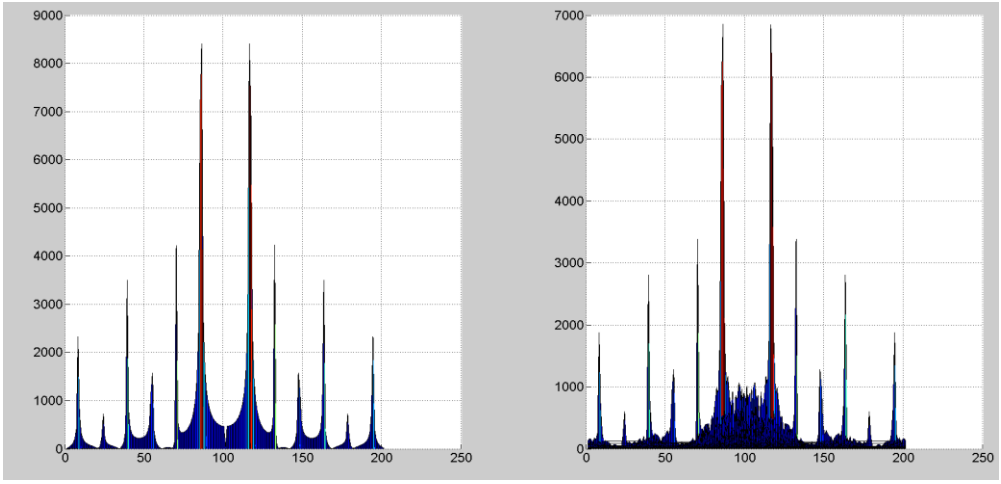

Figure 147- fft of the two images in Figure 143 in y-z view. Left fft corresponds to left image in Figure 143 and similarly for the right image and fft.

Similar behavior can clearly be seen in the x-z view of the fft. As the image gets distorted from a constant value along x direction, the fft shape deviates from a large spike and therefore, the amplitude decreases and the fft gets distributed and less sharp, or mathematically the variance of the amplitude distribution around the peak spike increases significantly.

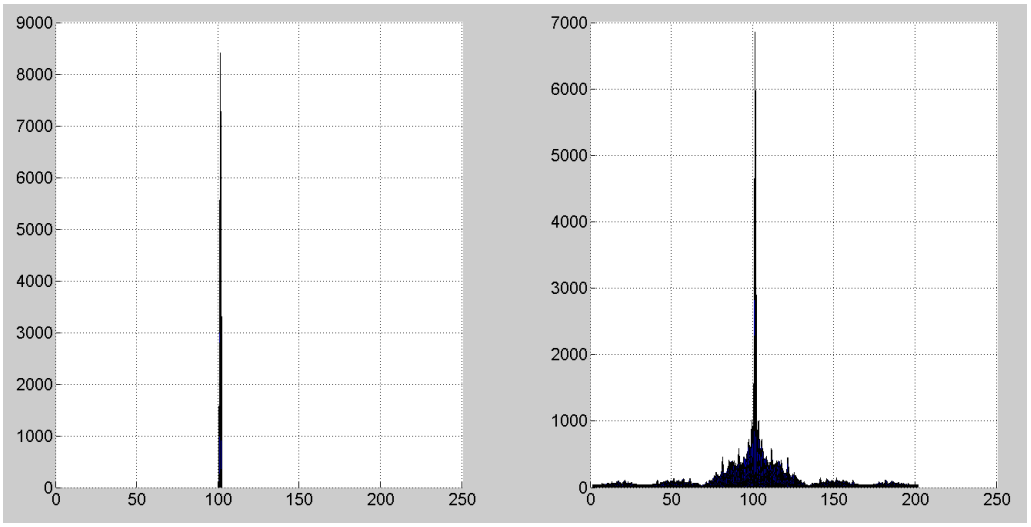

Figure 148- fft of the two images in Figure 143 in x-z view.

Figure 149 (a) to (d) show four cases of 1D signals in each row on left with their corresponding Fourier transform on the right. (a) and (b) present two regular harmonic signals without distortion, and (b) and (c) present those two signals have been distorted or in other word some level of irregularity has been added which are marked in blue. As seen in the right side, in the corresponding fft, the values of spikes have been reduced and the fft components have been more flatly distributed around that spike. This observation supports the observation made from the 2D signal and suggests that this behavior would constantly be seen between regular patterns associated with Zone I and irregular patterns associated with Zone III.

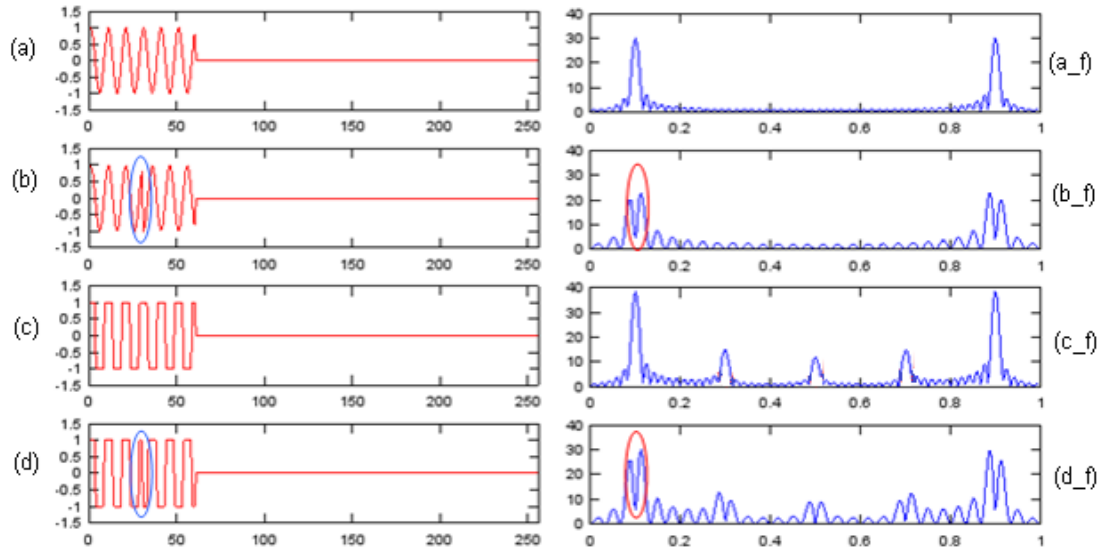

Figure 149- Four cases of 1D signals in each row on left with their corresponding Fourier transform on the right. "_f" denotes the fft of the corresponding signal.

Now this observation needs to be verified for the true images for Zone I and Zone III. Figure 150 shows two example images of Zone I and III after applying local thresholding. From these images, it can clearly be seen that Zone I shows more regular and periodic pattern whereas Zone III image looks irregular and a distorted version of an image belonging to Zone I. Figure 151 and Figure 152 show the fft of images in Figure 150 next to each other in yz and xz views respectively. As seen in Figure 151, similar observations in Figure 147 can be made here. First of all, both frequency distributions in Figure 151 have a spike (also the maximum amplitude of the fft) at the frequency 15 which corresponds to spatial period of 13 pixels. Therefore, the previous observation from original color camera images from the layers that these horizontal brown regions in images form along the scan path between two adjacent paths is confirmed. With further investigation, it was seen that the maximum amplitude of the fft for results of local thresholding of all the examined camera images captured from layers of all parts belonging to Zone III and Zone I occur at frequency 15.

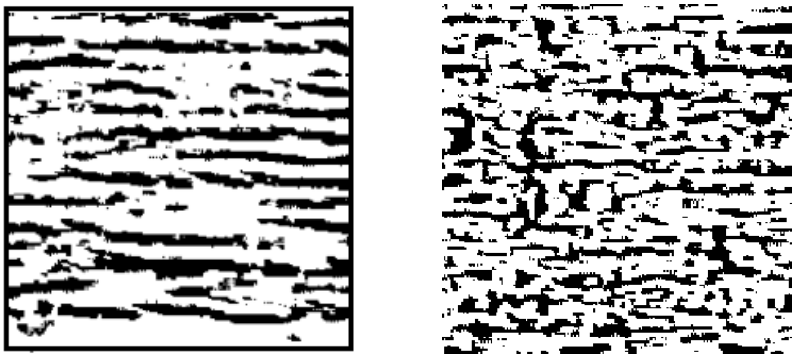

Figure 150- Two sample images of Zone I (left) and Zone III (right) after applying local thresholding.

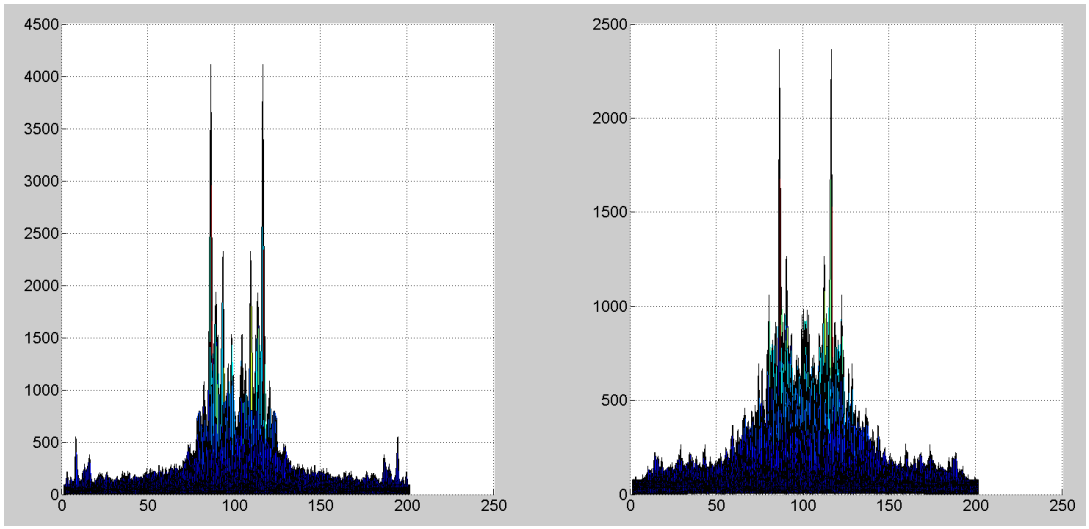

Figure 151- fft of images in Figure 150 next to each other in yz view.

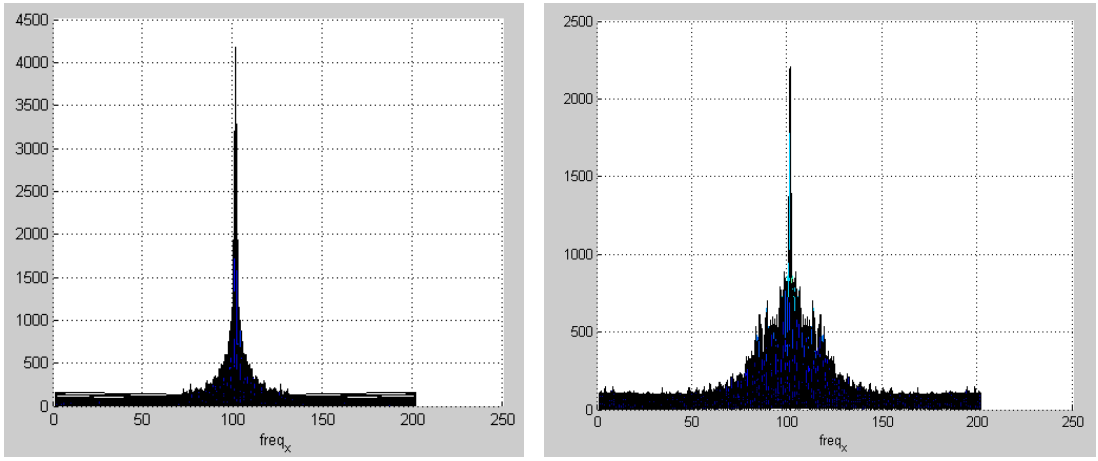

Figure 152- fft of images in Figure 150 next to each other in xz view.

The second observation is that Zone III patterns show smaller amplitude at the spike and the amplitudes get distributed around the spike frequency as held for Figure 147. The same observation can be seen in the xz view of the fft (Figure 152) which matches observations from Figure 148. These observations were visually confirmed from several other image samples from Zones I and III.

After these physical features are identified to show discriminating ability between two different patterns, to extract the features, it is now required to mathematically formulate these observed features and be able to assign a number to them. Based on what was mentioned, the amplitude at the spike frequencies in y-z view (which is same as x-z view) will be a good measure of deviation from a regular pattern. Therefore, the maximum amplitude of the fft projected on yz plane (named $f_{max_{yz}}$) was selected as a feature. A second feature defined as the normalized maximum amplitude in y-z domain was used which was calculated as below:

$$f_{max_{normalized}} = \frac{f_{max_{yz}}}{\|max_k F[k, 101 + l]\|}$$

Equation 21

where $\|\ \ \|$ denotes the norm of the vector or array.

Additionally, it was observed that the frequency components around spikes get more widely distributed which can mathematically be represented as variance of these values, or to show the wide distribution as well as the variation, it can be represented as the second moment of the frequency distribution around the spike within the entire domain or a neighborhood interval centered as 0 frequency (equivalent to 101 in the fft plots). This neighborhood interval was selected as ± 50 in frequency around 0 frequency which interval includes spike frequencies (i.e. 15 and 0 for yz and xz respectively). In other words, three features were calculated as below:

$$M_{y_{entire\ domain}} = \sum_{l=-100}^{+100} max_k F[k, 101 + l] \times l^2 \quad \text{Equation 22}$$

$$M_y = \sum_{l=-50}^{+50} max_k F[k, 101 + l] \times l^2 \quad \text{Equation 23}$$

$$M_x = \sum_{k=-50}^{+50} max_l F[101 + k, l] \times k^2 \quad \text{Equation 24}$$

Through the above equations, features can now be calculated from the results of local thresholding applied to each 201×201 pixel subregion of images of the layers including high-energy, smooth, non-porous layers (Zone II), the less smooth, close-to-optimal, non-porous layers (Zone I), and low-energy, porous layers (Zone III).

Now, to study how the new features would serve to better classify porous layers (Zone III) from non-porous layer (Zone I and II), the probability distribution function (pdf) of each feature for images belonging to a different Zones can be calculated; they are shown in Figure 153. The pdf of the two previous features namely area and number of intensity changes are shown in Figure 154 for better comparison. As it was seen earlier, area were able to discriminate Zone III from Zone II with very good accuracy. However, it was not able to discriminate Zone III versus Zone I. Number of intensity changes did not noticeably improve results. Figure 154 supports this results. As seen, the area pdf for Zone III and Zone II almost form two separate pdfs with small percentage of overlap, however, the pdf for Zone I almost corresponds to the pdf of Zone III and also has a very large overlap with it. These characteristics deprive area of the ability to distinguish these classes from each other. Similar observations can be seen for the pdf of number of intensity changes (in Figure 154).

Therefore, to effectively classify Zone I from Zone III, the appropriate features should show more distinguished distributions and with smaller percentage of overlap between the pdf corresponding to the two Zones III and I. As can be seen from Figure 153, the pdf's belonging to these two Zones do not correspond to each other and also

show a smaller overlap for the feature range. These characteristics are much more visible in the pdf of the first feature, i.e. amplitude at the spike in y-z view. This means that this feature should provide much higher discrimination between the two Zones. In cases of features that have overlaps for two classes, the more features that have some level of discriminability between the two classes (i.e. not entirely overlapping pdf's), will usually provide better classification results. Therefore, for this work, to select the most influential features, a series of tests will be performed that will be given later in this Chapter.

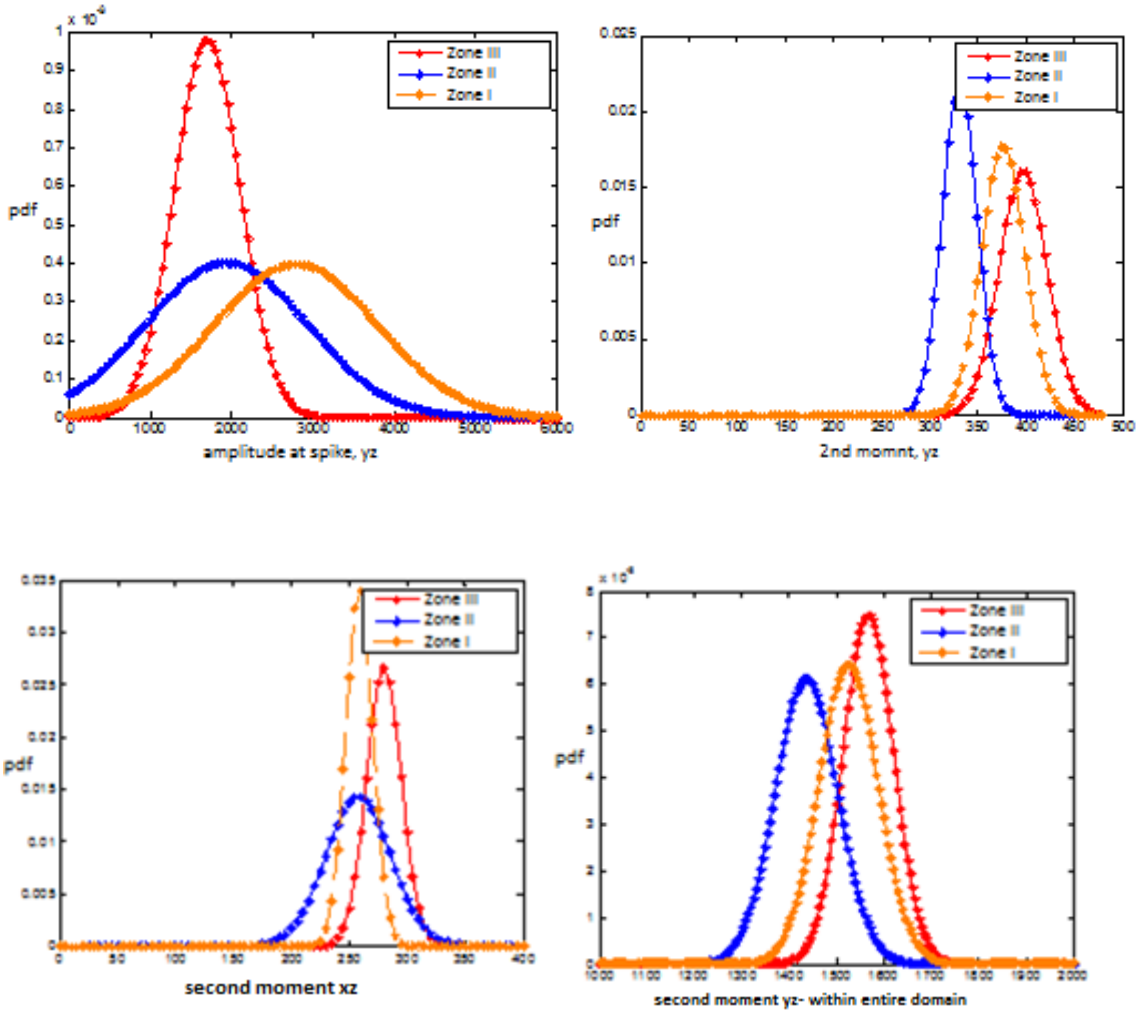

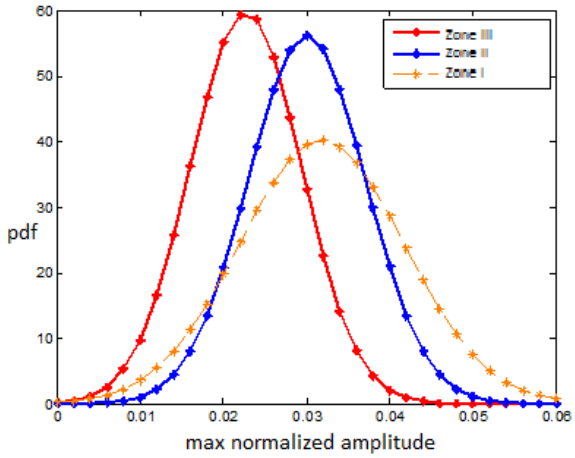

Figure 153- pdf of each of the 5 frequency features for regions belonging to the three different Zones.

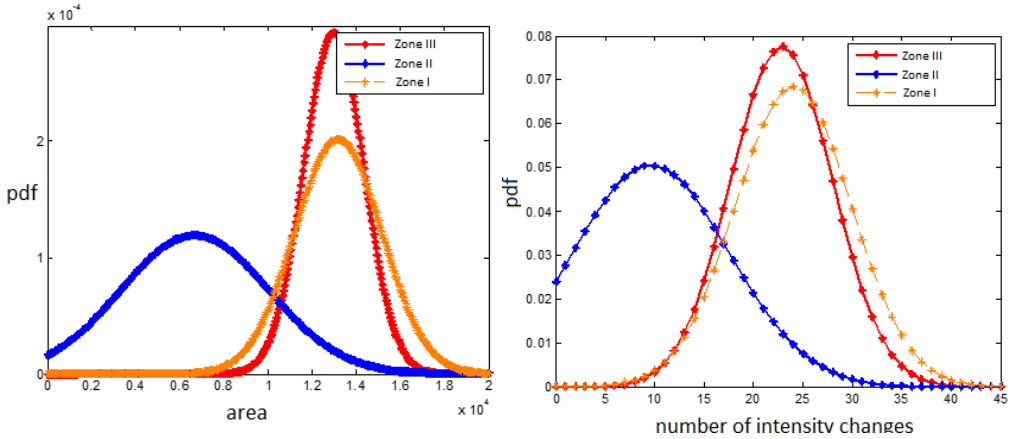

Figure 154- pdf of the two features, area and number of intensity changes, represented here for comparison.

8.3 Identification of Porous versus Non-Porous Layers using Bayesian

Now that the candidate features with discriminating ability have been selected, to perform classification, the Bayes rule should be implemented, i.e.:

$$P(C_i|F) = \frac{P(F|C_i).P(C_i)}{P(F)}, \quad i = 1,2 \text{ for porous and non} - \text{porous}$$

Equation 25

where there are two classes of porous (Zone III) and non-porous (Zone I and III), and F includes the 7 candidate features (2 from spatial domain and 5 from frequency domain). For Bayesian implementations, the likelihood for all the features, i.e. $P(F|C_i)$, should be calculated. Here we use the commonly-used independency assumption and calculate this joint likelihood as a summation of the individual conditional probabilities as follows:

$$P(F|C_i) = P(f_1, f_2, \dots, f_m|C_i) = P(f_1|C_i)P(f_2|C_i) \dots P(f_m|C_i) = \prod_{j=1}^{m} P(f_j|C_i)$$

Equation 26

where m is the number of the features among these 7 candidate features that are to be used in classification. Each individual conditional probability is the pdf corresponding to that class i.e. porous (Zone III) and non-porous (Zone I and II combined).

To calculate the likelihoods, a set of samples called training set would be used that serve for developing the Bayesian to be ready to be implemented. Then, the trained Bayesian network can be performed to new samples from so-called test set to evaluate the performance of the Bayesian classification. From the database of images, we had an entire of 336 samples of regions that were for certain identified to belong to a Zone out of the three Zones covering all the three Zones from the highest level of energy to the lowest energy in the experiments (see Chapter V). Out of these 336 samples, 70% (236 samples) were randomly selected as train set and 100 samples were used as test set for testing the performance and evaluation.

After, the training set was selected, the non-conditional probabilities of the two classes (porous and non-porous) and all the 14 conditional probabilities (for 7 features and two classes) were calculated as mentioned earlier in this Chapter, from the data in the training set. The calculated pdf's, as ones shown in Figure 153 and Figure 154, would be used as likelihoods to calculate the joint probability (likelihood) in the Bayesian network through Equation 26.

To select best features, 8 different appropriate combinations of the 7 features were selected to be considered to choose the best combination out of. For each of these 8 combinations, the conditional probabilities of the features corresponding to that combination were used to calculate the joint probability i.e. the likelihood. After the parameters of the Bayesian were calculated, the Bayesian was implemented to classify the training dataset. The two evaluation measures, sensitivity or True Positive Rate (TPR), and specificity or True Negative Rate (TNR) were calculated for each combination. Table 4 shows the results of these experiments. The 7 features in order of usage in the Table correspond to the vector [area, number of intensity changes, second moment in y-z view within 100 frequency range, second moment in y-z view within entire frequency range, second moment in y-z view within 100 frequency range, amplitude at spike frequency, normalized maximum frequency]. The binary vector features in the Table designates which features have been used for that Bayesian analysis, 1 for the corresponding feature being used and 0 for not being used.

In each case of feature combinations, the optimal threshold was found to maximize Figure of Merit. From the results, it can be seen that the combination of features [area, second moment in y-z view within 100 frequency range, second moment in y-z view within entire frequency range, second moment in y-z view within 100 frequency range, amplitude at spike frequency], yields best maximum of Figure of Merit (F_1) and performance for the training set of data. Figure 155 shows the variation of Figure of Merit versus threshold for the final selection of features. It is seen that a Figure of Merit of 0.86 (or 86%) can be achieved with the threshold of 0.5, which is higher than other combinations. This value of Figure of Merit ($F_1 = 0.86$) is significantly higher than the ones for the first three cases in Table 4 where the two features of area and number of intensity changes were only used ($F_1 \sim 0.73$).

It is expected and seen that this optimal combination of features, the highlighted row in Table 4, leads to the best performance of the Bayesian overall. This set of features was then used for the Bayesian classification where it achieved the maximum overall performance as seen in Table 4.

After the Bayesian is ready to be performed, it can be tested and evaluated by implementing to the test data. Table 4 also shows the performance of the classifier for the test data. As it is seen, as was expected, the selected set of features led to the best performance which is sensitivity of 89%, specificity of 82%, precision of 83%, and NPV of 89%, with overall Figure of Merit of 86%. This is satisfactory results for identification of porous layers and is among good results for identification in industrial inspection.

Table 4- Results and performance of Bayesian identification for different combination of features and for selection of optimal threshold (* shows two cases of non-optimal thresholds for the finally selected set of features).

features in Bayesian	sensitivity (train)	specificity (train)	sensitivity (test)	specificity (test)	sensitivity (overall)	specificity (overall)	Precision	NPV	F1	optimal threshold
[1 0 0 0 0 0 0]	94.0	42.0	92.7	48.9	93.6	44.1	60.6	88.0	0.7372	0.6
[0 1 0 0 0 0 0]	86.8	49.6	78.2	42.2	84.2	47.4	62.1	79.8	0.7236	0.5
[1 1 0 0 0 0 0]	91.7	58.3	89.1	53.3	90.9	56.8	67.6	88.1	0.7786	0.6
[1 0 1 1 0 1 0]	87.6	76.5	87.3	75.6	87.5	76.2	78.0	86.7	0.8253	0.5
[1 0 1 1 0 0 0]	91.7	72.2	89.1	68.9	90.9	71.2	75.8	90.2	0.8301	0.5
[1 0 1 1 1 1 1]	87.6	80.0	85.5	80.0	87.0	80.0	80.6	87.2	0.8397	0.5
[1 1 1 1 1 1 1]	89.3	78.3	85.5	80.0	88.1	78.8	79.6	88.5	0.8415	0.5
[1 0 1 1 0 1 0]	86.1	84.3	86.7	83.6	86.3	84.1	83.9	86.5	0.8499	0.8
[1 0 1 0 1 1 0]	87.6	83.5	85.5	84.4	87.0	83.8	83.4	87.6	0.8547	0.7
[1 0 1 1 1 1 0]	89.3	82.6	88.7	81.9	89.1	82.4	83.0	89.0	0.8603	0.5
[1 0 1 1 1 1 0]	92.9	73.0	91.1	72.8	92.4	72.9	76.6	91.5	0.8396	0.1 *
[1 0 1 1 1 1 0]	89.3	76.5	88.3	77.8	89.0	76.9	78.3	88.3	0.8345	0.3 *

Figure 156 and Figure 157 show the performance of Bayesian, using the final optimal features, for various values of threshold. As it is seen, there is almost always a trade-off between the sensitivity and specificity, or precision and NPV. It is possible to achieve a high value of sensitivity (TPR) of 93% with threshold of 0.1 but at the cost of a lower TNR of 73%. In this study, Figure of Merit was used as a criterion for selection of

optimal features and threshold. For applications where there is a more emphasis on some specific measure of performance, that measure can be used for optimizing the classification.

Table 4 shows various values of precision and NPV for various values of thresholds. Also, Figure 157 show various values of precision and NPV for various combination of features. Precision, in fact, indicates the probability of that a region identified as porous is truly porous, and NPV indicates the probability of that a region identified as non-porous is truly non-porous. These probability values can serve in developing a new Bayesian framework to fuse the results from two different Bayesian networks. For example, it is possible to select a Bayesian network with a high precision and for the rejected regions in this Bayesian network, use a new Bayesian network to further and more reliably identify the true identity of the regions. In other words, it is possible to select two Bayesian networks by using two different sets of features or two different thresholds with different performances, and use a new Bayesian framework to fuse the results for better performance. In this thesis, the obtained performance was found satisfactory, and this suggested approach can be considered as the extension of this PhD research.

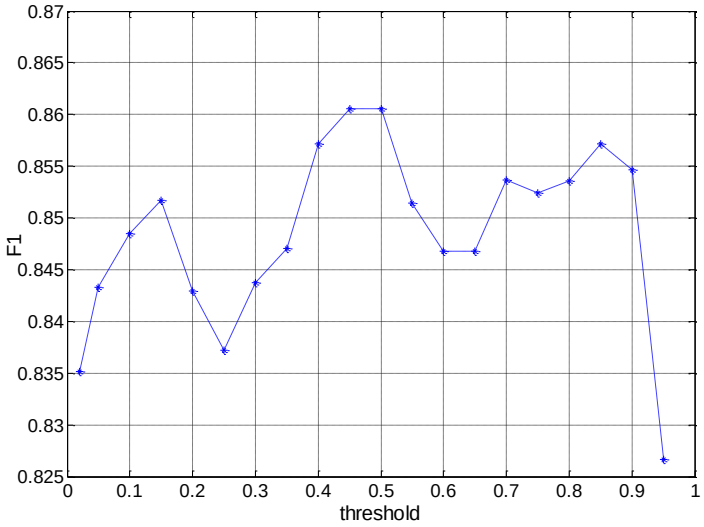

Figure 155- Performance of Bayesian, using the final optimal features, in terms of Figure of Merit, for various values of threshold.

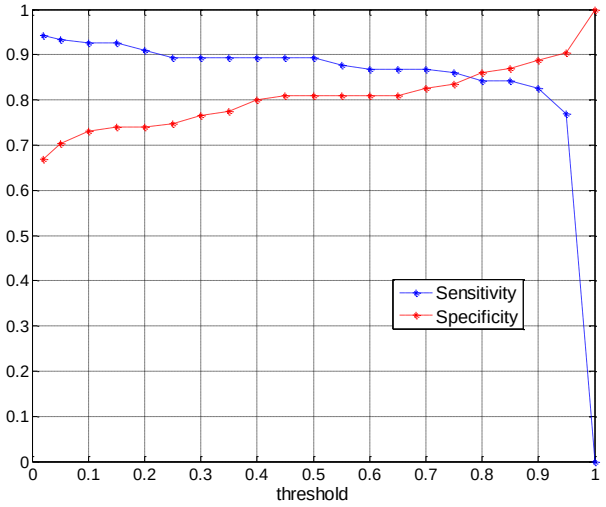

Figure 156- Performance of Bayesian, using the final optimal features, in terms of sensitivity and specificity, for various values of threshold.

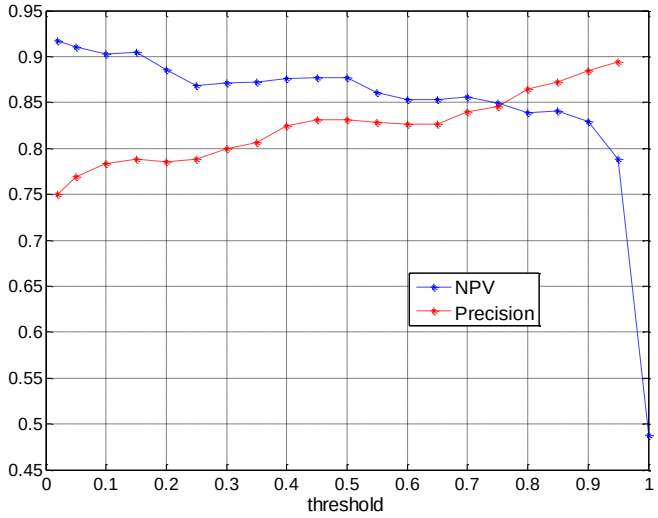

Figure 157- Performance of Bayesian, using the final optimal features, in terms of precision and NPV, for various values of threshold.

Identification of porous layers then enables us to identify porous regions in a layer or identify a whole porous layer associated with bad process parameters. These results would help both with decisions on correcting the region or layer such as remelting, or decide on the acceptance or rejection of the part, or make an overall assessment of the part quality. The results of identification of a porous layer would also provide a feedback to modify the process parameters for the next layer until no porous layer is identified

In addition to providing information on the layer or regional porosity, identification can be used to provide more confidence for detection of individual pores performed in the previous Chapter. Chapter VII showed several results of detection of pores applied to both porous and non-porous layers including two cases of non-porous layers that pore detection algorithms led to detection of some pores which were false positives. Results of identification can be used for two purposes to improve pore detection: The first way which is more confident is to use the results of identification to remove any false positives detected in non-porous layers due to darkly etching regions or surface discolorations. In other words if any pore is identified in a non-porous layer, it

would be regarded as false positives. The second way which is less computational is to apply pore detection to a region or layer only after it is identified as porous.

Figure 158 shows the two cases of porous regions where they were successfully identified as porous using Bayesian identification. Figure 159 shows the two cases of non-porous regions where pores were falsely detected in the regions. Performing Bayesian identification successfully identified both these regions as non-porous. Combining these results with the result of pore detection successfully removed these false positives as seen in the Figure.

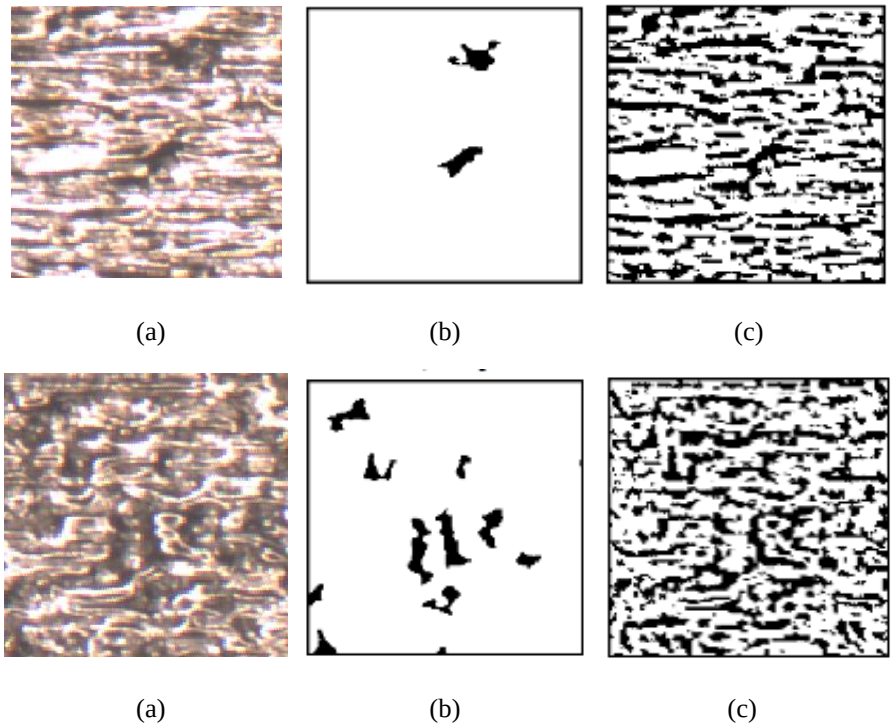

Figure 158- Two examples of porous regions (in each row): (a) original image, (b) result of pore segmentation from Chapter VIII, result of local thresholding applied to the region that was identified as porous using Bayesian network developed in this Chapter.

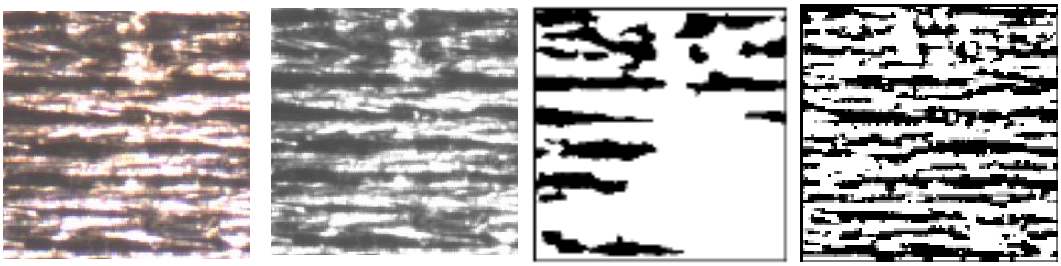

(a) (b) (c) (d)

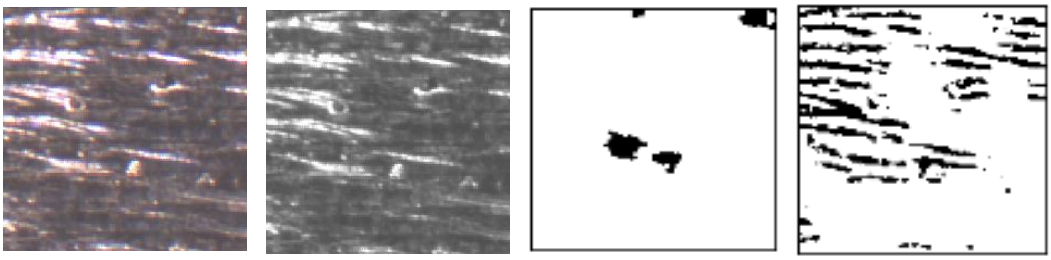

(a) (b) (c) (d)

Figure 159- Two examples of non-porous regions (in each row): (a) original image, (b) gray-scale image, (c) result of pore segmentation from Chapter VIII, (d) result of local thresholding applied to the region that was identified as non-porous using Bayesian network developed in this Chapter. The segmented objects that could be FPs were removed using Bayesian identification.

CHAPTER IX

CONCLUSION

Issues of part quality in terms of quality of fusion and formed porosity as well as dimensional errors are widely known and stated as some of the important challenges with laser powder-bed fusion (LPBF) process. This work addressed the in-situ inspection of layer-wise part quality using visual camera images.

One of the main objectives of this work has been to investigate the efficacy of high-resolution visual imaging for in-situ quality inspection in metal powder-bed AM. The work conducted on using visual camera for inspection in powder-bed AM is as new as 2012 and is at the very preliminary stages of study. As was mentioned in Section 2.4.2, most of the work conducted on inspection using visual camera images, which are mainly performed concurrent to this PhD research, are mostly focused on inspection of process errors such as non-uniform powder distribution, coater wear, and elevated edges for preventing coater collision. There is no prior work on inspection of porosity from camera images in AM. In fact, no prior imaging system was capable of capturing and visualizing porosity due to physical limitations. Therefore, no automated inspection of porosity was seen performed. Nor was any work seen reported on performing and evaluating an automated inspection system for dimensional accuracy of powder-bed AM parts from camera images.

In more details, this work has been seeking to study the efficacy and ability to make some sort of assessment of part quality from visual images in two aspects: porosity and geometry. This assessment could be qualitative even in form of binary (good or bad - porous or non-porous), or quantitative. The level of information that the images provide and can be used for was to be obtained during the study. If this possibility is seen, next

work is to perform an automated inspection system for making this assessment of porosity (or geometry). After automated inspection is performed to make a qualitative or quantitative assessment of porosity or dimensional accuracy, the inspection can be evaluated and specified in terms of some quantitative measures to specify the level of confidence in a mathematical or statistical manner.

9.1 Contributions

In this work, the above objectives were achieved as follows and the following major contributions were made that are expanded in this section.

1) Resolved a major issue with in-situ imaging of detailed surface features of AM part layers by incorporating a movable light source. The movable light was mounted at a desired distance from the build allowing porosity to be visualized in the image while avoiding beam blockage. This was performed using the moving mechanism of the machine and without adding new moving physical hardwares.
2) By analysis of image showing the part geometry and developing an imaging setup visualizing porosity the efficacy of visible-light imaging for in-situ inspection of part quality in terms of geometry and porosity was investigated and the possibility of this work was demonstrated by the results.
3) Developed image segmentation algorithms for detection of fused geometric objects in each layer within a boundary rms error of 81 microns. The algorithms were also tested and led to successful segmentation of other geometries such as polygonal, hollow, and curved objects. Used model-based image processing for extraction of synthetic parameters. The precision of extraction of synthetic parameters was determined, for angles of lines, as

maximum error of 1^{o}, and for locations of vertices, as the maximum error of 50 μm and rms of 21 microns, verified for square objects.

4) Developed pore segmentation algorithms and achieved automatic detection of pores from camera images as a quantitative assessment of porosity. The pore detection matched microscopic porosity by the rms error of 15% for segmentation of porosity area.
5) Performed identification of porous regions for qualitative assessment of porosity. Developed a Bayesian network that identified porous from non-porous layers, based on selected and extracted texture features both in spatial and frequency domain, and achieved a performance of precision of 89% and NPV of 83%.

The detailed aspects of the above contributions are presented below.

An imaging setup was developed to produce high-resolution visual images from each layer of the part during LPBF process. The imaging and illumination setups were developed and modified such that the produced images visualize detailed surface characteristics of each layer of the build such as fused seams, as well as the individual formed pores. This system resolved, to a significant extent, the challenges associated with the illumination and, unlike the previous work on development of imaging setup for powder-bed AM, this system captures images that visualize detailed surface features such as individual pores as they appear in microscopic images. From a rough examination, pores as small as 10 pixels (70 microns) could be seen and visually recognized in the images. The challenges with the imaging and issues with image quality and how higher quality image can be produced were identified and discussed.

It was determined that images can provide different types of information about part quality and characteristics that could be extracted and automatically inspected from camera images that was discussed in Chapters VII and VIII. In this work, the two aspects

of geometry and porosity were considered. To automatically inspect part quality in these two aspects, image processing algorithms were utilized for inspection of part geometry and for assessment of porosity. Porosity was assessed in two manners: 1) qualitative in terms of porous or non-porous and 2) in terms of detection of individual pores that serves to provide a quantitative measure of porosity.

For the automatic detection of individual pores, it was investigated that image processing algorithms can be and were developed that could detect pores of size as small as 11 pixels (77 microns), However, to develop an algorithm that meet some specific performance criteria that could be quantified in terms of true and false detections, an image processing algorithm was developed to detect pores whose performance was quantified as follows. The results of automatic detection of pores was evaluated on 10 randomly selected images compared to microscopic images, and it was observed that pores larger than 100 microns (equivalent diameter) can be detected with 100% sensitivity (TPR), the FPR for objects large than 100 microns was 0. Additionally the area of the automatically detected pores matched the true pore area with only 15% rms error.

In addition to detection of individual pores, an intelligent classification algorithm was developed to identify porous versus non-porous regions that provides a quantitative assessment of porosity. For this purpose, 1.5 mm ×1.5 mm regions and their corresponding images were considered. Image processing algorithms were implemented to convert the image to a binary image from which appropriate features in spatial and frequency domain were identified and extracted that can distinguish porous from non-porous regions. Bayesian inference as a reliable statistical identification method was used to perform the classification. Identification of porous reigns from non-porous regions was achieved with a specificity of 89% and sensitivity of 82% which is regarded

as a very good performance for similar applications of inspection. The precision and NPV of the identification were also quantified as 89% and 83% respectively.

The results of identification, as mentioned earlier, can help with removal of false positives and increase the level of confidence in the results of detection of individual pores. The identification step successfully identified several non-porous layers in which some pores had falsely been detected and removed these false positives. Combining intelligent classification with the result of detection of individual pores therefore improved the performance of pore detection.

The work on identification of porous regions in this research presents the benchmark approach and can simply be generalized to study and assess other part characteristics visible in images such as roughness of the layer, quality of fusion, level of input energy, and also to be used for process calibration.

Inspection of part geometry in each layer from camera images was also investigated. It was seen that the part geometry can be visualized in camera images with sufficient clarity that a human eye can distinguish the fused region from powder region. The confidence of manual observation strongly depends on illumination and resolution. In this research, from the set of camera images that were considered for inspection of geometry, automatic inspection of geometric objects in each layer was performed by developing appropriate image processing algorithms. The performance of detection evaluated in terms of rms error was measured as 81 micros which is smaller than the laser scan width (90 microns). The algorithms were also tested and led to successful segmentation of other geometries such as polygonal, hollow, and curved objects. In addition to detection of object boundary, detection of the synthetic parameters of square objects was also successfully performed using Hough transform. The geometric parameters for angles were detected within precision of 1^{o} and for location of vertices were calculated with maximum error of 50 microns and rms of 21 microns. This

application can simply be applied to other geometries such as all polygons, circles, ellipses, and any other parametric shape, for extraction of the synthetic parameters of geometric objects in each layer.

Other contributions

In addition to the above major contributions of this work, this research serves the existent research in the following ways:

1. This work is the first work on development and implementation of an extensive (addressing fusion quality and porosity, and 2D geometry, and including three processing levels of a MV) machine vision system based on visible light images for inspection in metal powder-bed AM. This work provides a general framework for inspection of geometric errors and defects in powder-bed AM based on metrology and machine vision principles. The developed framework offers a foundation for developing MV systems for powder-bed AM that use any sources of 2D measurements such as visible-light images, height maps, 2D thermal images, etc.

2. The developed imaging setup is the first reported in-situ visible-light imaging system that visualizes defects (pores), as small as 70 microns. The developed imaging and illumination setup solves some of the challenges and offers further important suggestions for capturing images in situ that visualize defects despite the physical constraints, and using only the available mechanical structure in current commercial systems.

3. The image segmentation algorithms developed in this work are the first set of reported algorithms developed and statistically evaluated for detection of geometric objects in metal powder-bed AM that also achieve a precision (based on root-mean-square error) within laser scan width. The image segmentation algorithms developed in this work are the first set of algorithms for detection of pores in camera images of

powder-bed AM (other than simple approximate thresholding for defects). The aforementioned developed imaging setup and algorithms provide a starting point and basis for developing more precise and confident imaging and detection systems for powder-bed AM for visible-light camera images. It also provides a measure of comparison, quantification, and evaluation of any developed algorithms in the future.

4. In this work, a first image database that provides a large set of in-situ (visible-light) images of defects formed at different levels of process parameter was developed. Defect detection algorithms, such as ones discussed in this research, can be applied to this image database to detect defects automatically and fast efficiently from this database or any other future image database to provide a large comprehensive database of binary images for defect patterns. This database of defect patterns is very helpful for development of potentially more precise defect detection techniques based on pattern matching. This pattern database can both be used for direct 2D pattern matching or feature-based defect detection.

5. In this work, for the first time, porous regions are identified from non-porous regions using high-level machine vision. This is the first implementation of high-level MV for identification (of defects) from visible-light images in powder-bed AM. A statistical Bayesian network was developed and used to classify patterns of porous regions versus non-porous regions. The result leads to better confidence in detection. Although the feature-based identification in this work mainly focused on a qualitative binary assessment of porosity, this work can simply be used for multi-level, more detailed assessment of porosity. This work provides the benchmark for other identification systems to assess other important process or part features such as roughness of the layer, quality of fusion, level of input energy, and can be used in process calibration.

9.2 Limitations and Application to Outside of the Scope of This Thesis

Limitations:

Relatively Low Contrast of Images Of Porosity: As mentioned earlier, although the camera images visualize pores, they do not have the clarity of microscopic images due to reasons that were discussed in Section 4.2. Theoretically, it is possible to capture camera images as clear as microscopic images. Approaches that can be taken to improve image quality are suggested as future work in the next section (Section 9.2). The lack of clarity of camera images decreases the contrast and distinguishability of pores from other surface features such as discolorations and interferes with accurate detection of pores.

Small Field of View:

The current developed imaging setup has a small FoV covering about 3cm ×2 cm of the layer. This would allow to inspect small parts or a smaller region of the part. However, it is possible to increase the FoV by using a lens with higher FoV to increase the FoV and a higher-resolution camera to maintain large resolution (small pixel size). This solution is suggested in Section 9.3, as well, as an extension of the current work.

Uncertainties in Statistical Evaluation of Detection of Individual Pores: The algorithms for detection of pores were evaluated by randomly selecting several images from all the image database, since it is too cumbersome to inspect all images manually. If an automatic manner of evaluation of pore detection existed, such as an existent database of images of AM layers where pores are clearly already specified, this information could be used for fast, accurate evaluation of the algorithms.

Application to Outside of the Scope of This Thesis:

Application of the Developed Imaging Setup to Other Processes or Materials: In this research, as will be described in Section 4.2, an imaging setup was developed, to visualize porosity, by using a moveable light source mounted at the moving mechanisms

of the machine itself. The same imaging setup can be implemented to visualize porosity in layers of builds made from other materials or by other processes such as EBM.

Application to Other Camera and illumination Settings: In case of changing illumination settings or any aspect of imaging setup, the characteristics, quality, or intensity of images would change. In these cases, the intensity of images would change and therefore the current algorithms might need to be parameterized again. For using a different camera, for example of higher resolution, the pixel size or image size might be different. However, it is very reasonably expected that the developed algorithms in this thesis would still be well applicable to similar imaging setups and would only need parameterization or minor adjustments to produce satisfactory results. But, of course, as mentioned earlier, image segmentation algorithms are customized, and for an entirely different imaging setup, the algorithms developed in this work, are not applicable, but the same concept or even same design is reasonably applicable.

Application to Other Materials or EBM Process: In this work, the algorithms for detection of fused geometry and pores were designed and evaluated for material Inconel 625 and the process of laser powder-bed fusion. Different materials would show different color and intensity values in images and therefore, the developed algorithms in their exact current form might not produce accurate results. However, it is expected that the algorithms in the same form will be applicable and appropriate parameterization and adjustment would produce satisfactory results. Use of EBM may slightly alter the contrast of fused region and powder region or porosity within the part. However, with similar imaging setup, it is expected that the current algorithms would be applicable and would lead to satisfactory results, after parameterization, adjustment, or potentially minor modification.

9.3 Extensions and Recommendations for Future Work

The following work is suggested as extension of the current research:

1. Work on improving image quality for better and clearer visualization of surface features and pores, based on the discussions made in this research. Some future attempts to improve image quality can be named as follows:

- Better adjustment and parameterization of illumination, light intensity, and saturation effect.
- Adjust the focus of the camera on the top layer: Use of a camera with sharper but smaller depth of focus to exactly focus on the very top layer of the build as in microscopes.
- Limit images only to the effective FoV close to the center of images
- Study the pros and cons of utilizing a ring LED with larger ring illumination that can now be mounted on a fixed fixture as discussed in Chapter III.
- Study the efficacy of mounting a camera on a moveable fixture to reduce the camera distance or increase the coverage of camera by sliding the camera over the build platform and taking multiple pictures.
- Use a lens with larger FoV to increase the camera FoV and a higher-resolution camera to maintain the large resolution (the small pixel size).
- Taking two images at two close but different locations by sliding the camera and use image fusion to increase image quality and give depth to images.
- Further study on the effect of image enhancement algorithms and fusion of multiple images from the same layer in improving results.
- Building parts in lower level of oxygen inside the chamber such as 100 ppm as in more commercial machines. This would significantly alleviate formation of darkly etching regions that interfere with automatic detection of pores.

2. Applying the developed segmentation algorithm and Hough transform for a larger variety of geometric shapes and larger number of builds, for more precise evaluation.

3. Design and development of low-computational pattern matching algorithms for detection of fused objects based on classification of small regions.

4. Reducing the window size in identification of porous regions for even smaller regions to be identified.

5. Development of intelligent algorithms for defect detection based on defect features, or development of pattern-matching algorithms for each pixel based on its intensity and its neighborhood pattern.

6. Implementing the (Bayesian) feature-based identification for assessment of other physical characteristic that can be seen in images or are correlated to some features in images, such as the quality of fusion, level of energy, or the physical roughness.

7. Calibration of such a feature from the image or physical characteristics of the part to process parameters that can be used for process control feedback.

8. Making a 3D geometric model of the as-built part by integrating the results of detection of the fused geometric object from each cross section (layer) of the part.

9. Stacking the results of detection of the pore detection from each layer and make a whole 3D (or also called 2.5 D) model from the as-built part including the internal porosity of the part. Such a model can be used in simulation and evaluation of the properties of the true (as-built) part.

APPENDIX A

DESCRIPTION OF THE UTILIZED IMAGE PROCESSING ALGORITHMS

This section lists and explains some of the image processing concepts and algorithms used in this PhD research. It will cover these algorithms according to the following list:

A.1 Linear spatial filtering and Cross-correlation

A.2 Morphological operations:

Dilation and Erosion

Opening and Closing

Morphological reconstruction

A.3Region-growing

A.4 Hough transform

A.1 Linear Spatial Filtering and Cross-correlation

In this section, we are interested in filtering operations that are performed directly on the pixels of an image. The linear operations of interest consist of multiplying each pixel in the neighborhood by a corresponding coefficient and summing the results to obtain the response at each point (x, y). If the neighborhood is of size m×n, mn coefficients are required. The coefficients are arranged as a matrix, called a filter, mask, filter mask, kernel, template, or window, with the first three terms being the most prevalent. Figure 160 illustrates the mechanics of cross-correlation, the form of linear spatial filtering used in this dissertation. The red dots in the filter represent 1 and the gray

cells in the image f represent 1. Correlation is the process of passing the mask w by the image array f in the manner described in Figure 160. The process consists of moving the center of the filter mask, w, from point to point in an image. At each point (x, y) in image f, the response of the filter at that point is the sum of products of the filter coefficients and the corresponding neighborhood pixels in the area spanned by the filter mask as shown in the following equation:

$$f(x,y) \times w(x,y) = \sum_{i=0}^{W-1} \sum_{j=0}^{H-1} f(i,j)w(x+i,y+j)$$

Equation 27

where W and H are the width and height of the image.

Our principal focus is on masks of odd sizes, with the smallest meaningful size being 3×3. Although it certainly is not a requirement, working with odd-size masks is more intuitive because they have an unambiguous center point. Figure 161 shows the final result of cross-correlation of the filter w with the image f shown in Figure 160.

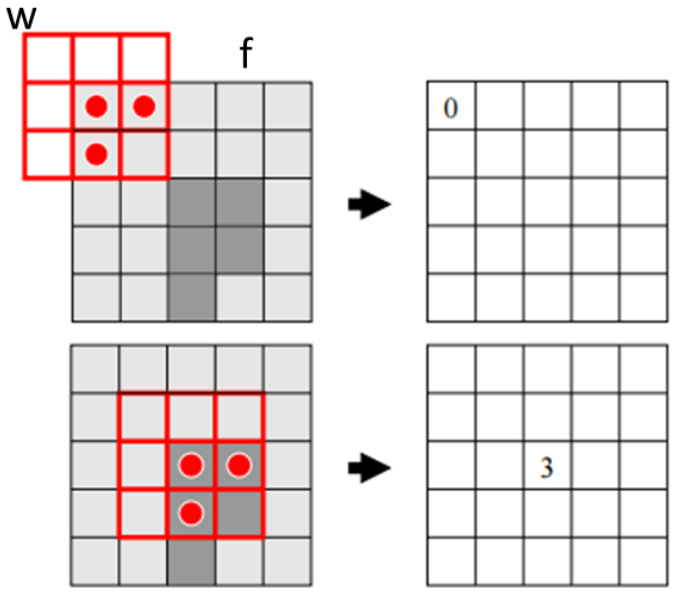

Figure 160- Mechanics of cross-correlation of mask w with image f.

0	0	0	0	0
0	0	1	1	0
0	1	3	2	0
0	1	3	1	0
0	1	1	0	0

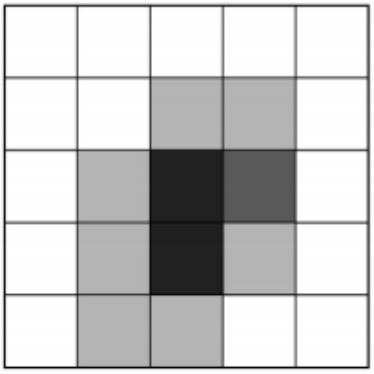

Figure 161- final result of cross-correlation of the filter w with the image f shown in Figure 160.

A.2 Morphological Operations

Dilation and Erosion

The operations of dilation and erosion are fundamental to morphological image processing. The dilation of A by B, denoted A⊕B, is defined as the set operation

$$A \oplus B = \{z \mid (\hat{B})_z \bigcap A \neq \varnothing\}$$ Equation 28

where ∅ is the empty set and B is the structuring element. In words, the dilation of A by B is the set consisting of all the structuring element origin locations where the reflected and translated B overlaps at least one element of A. Figure 162 shows the result of dilation of image A by mask B.

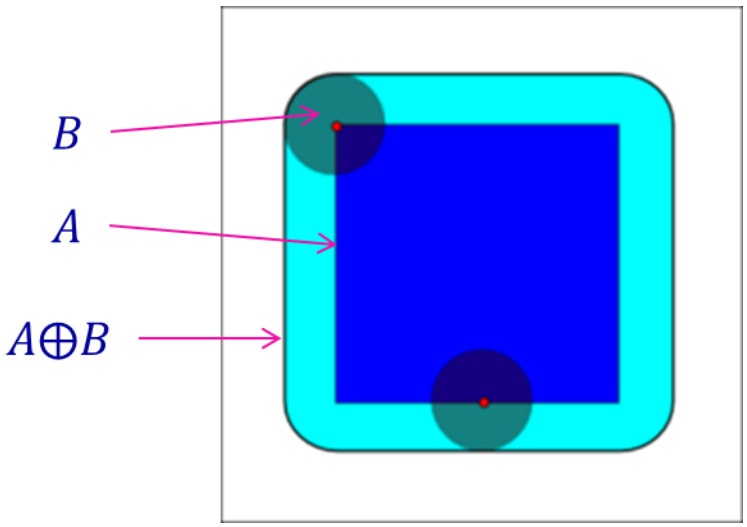

Figure 162- Result of dilation of image A by mask B.

The erosion of A by B, denoted A 8 B, is defined as

$$A \ominus B = \{z \mid (B)_z \subseteq A\}$$

Equation 29

where, as usual, the notation $C \subseteq D$ means that C is a subset of D. This equation says that the erosion of A by B is the set of all points z such that B, translated by z, is contained in A. Because the statement that B is contained in A is equivalent to B not sharing any elements with the background of A , we can say erosion of A by B is the set of all structuring element origin locations where no part of B overlaps the background of A. Figure 163 shows the result of erosion of image A by mask B.

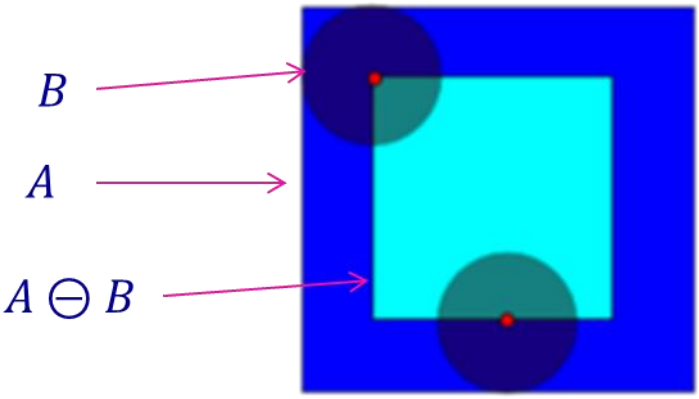

Figure 163- Result of erosion of image A by mask B.

Opening and Closing

The morphological opening of A by B, denoted $A \circ B$, is defined as the erosion of A by B, followed by a dilation of the result by B:

$$A \circ B = (A \ominus B) \oplus B$$

Equation 30

An equivalent formulation of opening is:

$$A \circ B = \cup \{(B)_z | (B)_z \subseteq A$$

Equation 31

where $\cup \{\}$ denotes the union of all sets inside the braces. This formulation has a simple geometric interpretation: $A \circ B$ is the union of all translations of B that fit entirely within A. Figure 164 illustrates this interpretation.

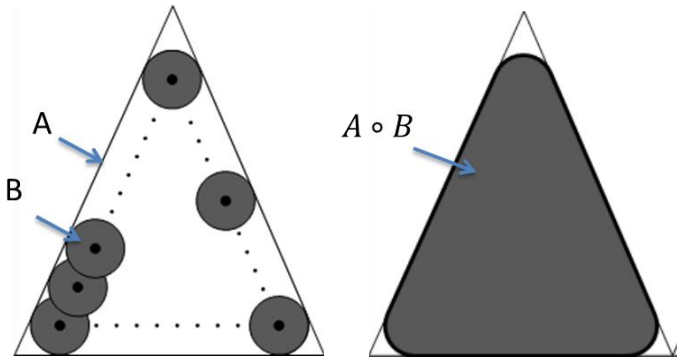

Figure 164- Illustration of the mechanics and final results of opening operation.

The morphological closing of A by B, denoted A • B, is a dilation followed by an erosion:

$$A \bullet B = (A \oplus B) \ominus B$$

Equation 32

Geometrically, A • B is the complement of the union of all translations of B that do not overlap A. Figure 165 (left image) illustrates several translations of B that do not overlap A. By taking the complement of the union of all such translations, we obtain the gray region Figure 165 (left image) which is the complete closing. Like opening, morphological closing tends to smooth the contours of objects. Unlike opening, however, closing generally joins narrow breaks, fills long thin gulfs, and fi lls holes smaller than the structuring element.

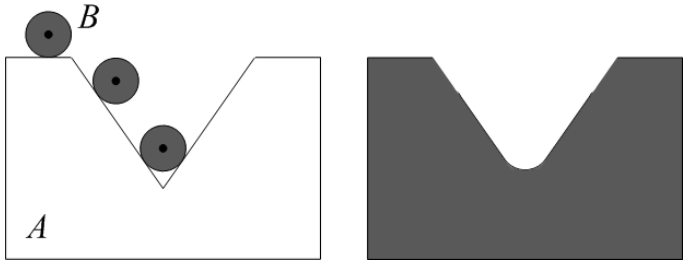

Figure 165- Illustration of the mechanics and final results of closing operation.

Morphological reconstruction

Reconstruction is a morphological transformation involving two images and a structuring element (instead of a single image and structuring element). One image, the marker, is the starting point for the transformation. The other image, the mask, constrains the transformation. The structuring element used defines connectivity, such as 8-connectivity which implies that B in the following discussion is a 3×3 matrix of l s, with the center defined at coordinates (2, 2). In this dissertation we dealt with binary images.

If G is the mask and F is the marker, the reconstruction of G from F, denoted $R_G(F)$, is defined by the following iterative procedure:

1. Initialize h_1 to be the marker image, F. F must be a subset of G (i.e. $F \subseteq G$).

2. Create the structuring element: B = a 3×3 matrix of l s.

3. Repeat: $h_{k+1} = (h_k \oplus B) \cap G$ until $h_{k+1} = h_k$.

4. $R_G(F) = h_{k+1}$.

Figure 166 illustrates the preceding procedure.

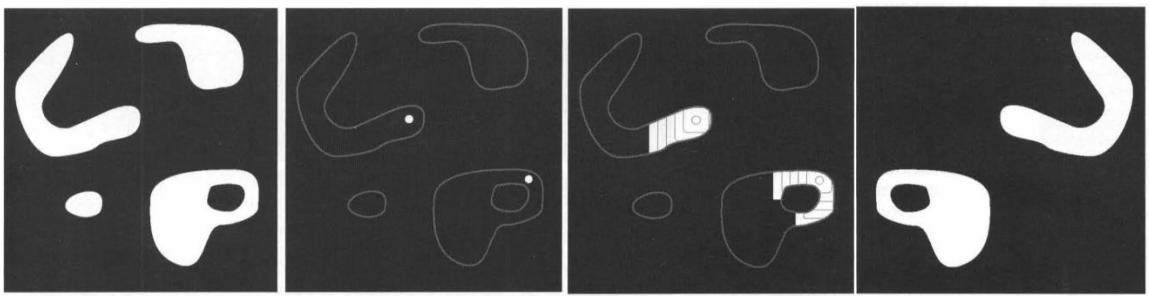

(a) (b) (c) (d)

Figure 166- Procedure and steps for morphological reconstruction [106]: (a) mask, (b) marker, (c) iterative procedure for step 3 described above, (d) final result of reconstruction.

A.3 Region-growing

As its name implies, region growing is a procedure that groups pixels or subregions into larger regions based on predefined criteria for growth. The basic approach is to start with a set of "seed" points and from these grow regions by appending to each seed those neighboring pixels that have predefined properties similar to the seed (such as specific ranges of gray level or color). The procedure can be summarized in the following three steps:

(1) Choose the seed pixels

(2) Check the neighboring pixels and add them to the region if they are similar to the seed based on a similarity predicate

(3) Repeat step 2 for each of the newly added pixels; stop if no more pixels can be added

The similarity predicate can be based on any characteristic of the regions in the image such as average intensity, variance, color, texture, motion, shape, and/or size. The quantities of similarity predicate can be based on pre-determined constant values or a function of the properties of the grown region that gets updated in each step.

Figure 167- Illustration of region-growing algorithm. From left to right: image containing the seed number, image containing a grown region resulted from finding and connecting the seed number neighboring pixels that satisfied a specified similarity predicate to the seed point or to the grown region at the previous step, the image containing the final result where adding any neighboring pixels would no longer satisfy the similarity predicate.

In this dissertation, region-growing was used in Chapter VII to detect pores from camera images and microscopic images. In those algorithms, two types of region-growing, i.e. using two different similarity predicates, were studied. Given the image characteristics, the results of these two different predicates were found to be almost the same. These first studied predicates was the intensity of the examined pixel lies within a certain range around the intensity of thee seed point or some specific intensity, close to that of the seed point. The second studied predicate that was used in the algorithms used in Chapter VII is that the intensity of the examined pixel lies within a specified range of the intensity of the entire region that has grown to that step of iterations. This specified range was determined by the selected similarity parameter.

A.4 Hough transform

The Hough transform is a feature extraction technique used in image processing. The purpose of the technique is to find imperfect instances of objects within a certain class of shapes by a voting procedure. This voting procedure is carried out in a parameter space, from which object candidates are obtained as local maxima in a so-called accumulator space that is explicitly constructed by the algorithm for computing the Hough transform.

The classical Hough transform was concerned with the identification of lines in the image, but later the Hough transform has been extended to identifying positions of arbitrary shapes, most commonly circles or ellipses. In this dissertation, Hough transform was used to extract the lines associated with edges of the square. However, it can similarly be used for extraction other parametric shapes such as circles or ellipses as well as parametric curves or parametric splines. Application of Hough transform to extract

lines is described as below. Same procedure can be generalized for extraction of other geometries.

Consider Figure 168 which show a line with two parameters. Although there is a variety of ways to parameterize a line, the r and θ representation is used in this example. The equation of the line in terms of these two parameters can be described as below:

$$x = rcos(\theta)$$
$$y = rsin(\theta)$$

Equation 33

For each point (x,y), there is an unlimited number of lines passing through the point, but the parameters (r,θ) of all these lines lie on a curve parameterized by the following equations:

$$r = xcos\theta + ysin\theta$$

$$\theta = \text{atan2}(y, x)$$

Equation 34

where x and y are the coordinates of the examined point and atan2 represents the angle between positive x axis and a line connecting origin to point (x,y).

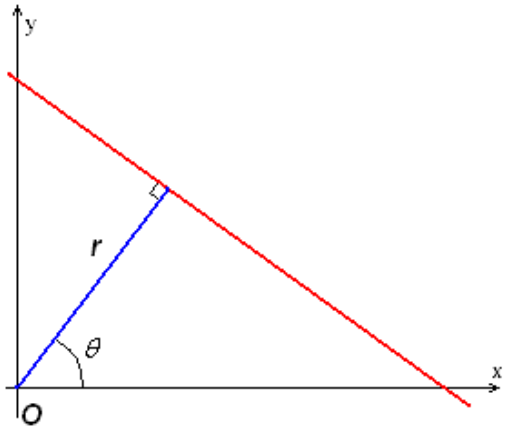

Figure 168- Parametric representation of a line in x-y space with respect to r and θ.

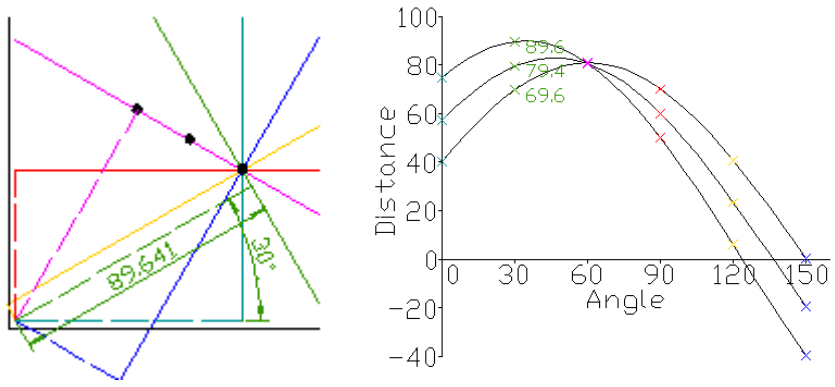

(a) (b)

Figure 169- Example of application of Hough transform to extract lines: (a) an image containing of 3 points in x-y space that lie on a line, approximately with r = 89 and $\theta = 30^o$ (b) locus of the lines passing through each of the three points in parameter space r-θ.

Figure 169 (a) shows an example image containing three points where it is interested to find the parameters of the line passing through these points, or in other words, to find a line that passes through the largest number of existing points in the image. Figure 169 (b) shows the locus of all lines passing each of the three points in parameter space r-θ. Each sinusoidal curve shows the r-θ parameters associated with all the lines passing through each point in the image. The intersection of all these three curves correspond to the r-θ parameters of the line that passes through all these three points, which is the line of interest.

In case of any input image, Hough transform calculates the locus of all lines (or parametric shapes) that pass through each point in the foreground (for binary images for example) and finds the parameter sets associated with the line that passes through a large (or largest) number of points or, in other words, receives a large number of votes.

REFERENCES

1. Kruth, J.P., *Material incress manufacturing by rapid prototyping techniques.* CIRP Annals - Manufacturing Technology, 1991. **40**(2): p. 603-614.
2. Hull, C.W., *Apparatus for production of three-dimensional objects by stereolithography*. 1986, Uvp, Inc.
3. Kruth, J.P., M.C. Leu, and T. Nakagawa, *Progress in additive manufacturing and rapid prototyping.* Cirp Annals 1998 - Manufacturing Technology, Vol 47/2/1998, 1998: p. 525-540.
4. Bourell, D.L., M.C. Leu, and D.W. Rosen, *Roadmap for additive manufacturing: identifying the future of free form processing*. 2009: The University of Texasat, Austin, Laboratory for Freeform Fabrication, Advanced Manufacturing Center.
5. Craeghs, T., et al., *Determination of geometrical factors in Layerwise Laser Melting using optical process monitoring.* Optics and Lasers in Engineering, 2011. **49**(12): p. 1440-1446.
6. Craeghs, T., et al., *Feedback control of Layerwise Laser Melting using optical sensors.* Laser Assisted Net Shape Engineering 6, Proceedings of the Lane 2010, Part 2, 2010. **5**: p. 505-514.
7. Bayle, F. and M. Doubenskaia, *Selective Laser Melting process monitoring with high speed infra-red camera and pyrometer* Fundamentals of Laser Assisted Micro- and Nanotechnologies, 2008. **6985**: p. 98505-98505.
8. Fang, T., et al., *Statistical feedback control architecture for layered manufacturing.* Journal of Materials Processing & Manufacturing Science, 1999. **7**(4): p. 391-404.
9. Kruth, J.-P., et al. *Feedback control of selective laser melting*. in *The 3rd International Conference On Advanced Research In Virtual And Rapid Prototyping*. 2007.
10. Boddu, M.R., R.G. Landers, and F.W. Liou. *Control of laser cladding for rapid prototyping – a review*. in *International Solid Freeform Fabrication Symposium*. 2003. Texas.
11. Clijsters, S., et al., *In situ quality control of the selective laser melting process using a high-speed, real-time melt pool monitoring system.* The International Journal of Advanced Manufacturing Technology, 2014: p. 1-13.
12. Kleszczynski, S., z.J. Joschka, and J.T. Sehrt. *Error detection in laser beam melting systems by high resolution imaging*. in *Proceedings of the Twenty Third Annual International Solid Freeform Fabrication Symposium*. 2012.
13. Barua, S., et al., *Vision-based defect detection in laser metal deposition process.* Rapid Prototyping Journal, 2014. **20**(1): p. 77-85.
14. Clark, D., S.D. Sharples, and D.C. Wright, *Development of online inspection for additive manufacturing products.* Insight - Non-Destructive Testing and Condition Monitoring, 2011. **53**(11): p. 610-613.

15. Sheng, L., I.C. Ume, and A. Achari, *Defects pattern recognition for flip-chip solder joint quality inspection with laser ultrasound and Interferometer.* Electronics Packaging Manufacturing, IEEE Transactions on, 2004. **27**(1): p. 59-66.
16. Tai-Hoon, C. and R.W. Conners. *A neural network approach to machine vision systems for automated industrial inspection*. in *Neural Networks, 1991., IJCNN-91-Seattle International Joint Conference on*. 1991.
17. Labudzki, R. and S. Legutko, *Applications of Machine Vision.*
18. Kumar, A., *Computer-vision-based fabric defect detection: a survey.* Industrial Electronics, IEEE Transactions on, 2008. **55**(1): p. 348-363.
19. Bhandarkar, S.M., T.D. Faust, and M. Tang, *CATALOG: a system for detection and rendering of internal log defects using computer tomography.* Machine Vision and Applications, 1999. **11**(4): p. 171-190.
20. Rahaman, G. and M. Hossain, *Automatic defect detection and classification technique from image: a special case using ceramic tiles.* arXiv preprint arXiv:0906.3770, 2009.
21. Bhandarkar, S.M., et al., *Detection of cracks in computer tomography images of logs.* Pattern Recognition Letters, 2005. **26**(14): p. 2282-2294.
22. Sivabalan, K. and D.D. Ghanadurai, *Detection of defects in digital texture images using segmentation.* International Journal of Engineering Science and Technology, 2010. **2**(10): p. 5187-5191.
23. Martins, L.A., F.L. Pádua, and P.E. Almeida. *Automatic detection of surface defects on rolled steel using computer vision and artificial neural networks*. in *36th annual conference IEEE industrial electronics society*. 2010.
24. Karimi, M.H. and D. Asemani, *Surface defect detection in tiling Industries using digital image processing methods: Analysis and evaluation.* ISA transactions, 2014. **53**(3): p. 834-844.
25. Ramesh, S., B. Gomathy, and T. Sundararajan, *Detection of Defects on Steel Surface for using Image Segmentation Techniques.* International Journal of Signal Processing, Image Processing and Pattern Recognition, 2014. **7**(5): p. 323-332.
26. Talab, A.M.A., et al., *Detection crack in image using Otsu method and multiple filtering in image processing techniques.* Optik - International Journal for Light and Electron Optics, 2016. **127**(3): p. 1030-1033.
27. Tsai, D.-M., P.-C. Lin, and C.-J. Lu, *An independent component analysis-based filter design for defect detection in low-contrast surface images.* Pattern Recognition, 2006. **39**(9): p. 1679-1694.
28. Ai, Y. and K. Xu, *Feature extraction based on contourlet transform and its application to surface inspection of metals.* Optical Engineering, 2012. **51**(11): p. 113605-113605.
29. Zahran, O., et al., *Automatic weld defect identification from radiographic images.* NDT & E International, 2013. **57**: p. 26-35.
30. Sharifzadeh, M., et al. *Detection of steel defect using the image processing algorithms*. in *Multitopic Conference, 2008. INMIC 2008. IEEE International*. 2008.
31. Craeghs, T., et al. *Online quality control of selective laser melting*. in *20th Solid Freeform Fabrication (SFF) symposium*. 2011. Austin (Texas).

32. Jacobsm, J.z., et al. *High resolution imaging for inspection of laser beam melting systems*. in *2013 IEEE International Instrumentation and Measurement Technology Conference (I2MTC)*. 2013.
33. zur Jacobsmühlen, J., et al. *Elevated region area measurement for quantitative analysis of laser beam melting process stability*. in *26th International Solid Freeform Fabrication Symposium; Austin, TX*. 2015.
34. Wohlers, T., *Wohlers report 2012*. 2012: Wohlers Associates, Inc.
35. Commerce, D.o., *Fact Sheet: Additive Manufacturing*. 2012: http://2010-2014.commerce.gov/news/fact-sheets/2012/08/15/fact-sheet-additive-manufacturing.
36. Technology, N.I.o.S.a., *NIST Additive Manufacturing*. 2014: http://www.nist.gov/public_affairs/factsheet/additive-manufacturing.cfm.
37. Press, T.N.A., *3D Printing in Space*. 2012: http://www.nap.edu/catalog/18871/3d-printing-in-space.
38. Advanced Manufacturing Office, U.S.D., *Additive Manufacturing: Pursuing the Promise*. 2013: http://energy.gov/sites/prod/files/2013/12/f5/additive_manufacturing.pdf.
39. Advanced Manufacturing Office, U.S.D., *Materials: Foundation for the Clean Energy Future*. January 2012: http://energy.tms.org/docs/pdfs/Materials_Foundation_for_Clean_Energy_Age_Press_Final.pdf.
40. Sutherland, J.W., et al., *A comparison of manufacturing and remanufacturing energy intensities with application to diesel engine production.* CIRP Annals-Manufacturing Technology, 2008. **57**(1): p. 5-8.
41. Crump, S.S., *Apparatus and method for creating three-dimensional objects*. 1992, Stratasys, Inc.
42. Gausemeier, J., et al., *Thinking ahead the Future of Additive Manufacturing–Analysis of Promising Industries.* Study for the Direct Manufacturing Research Center, Paderborn, 2011.
43. Deckard, C.R., *Method and apparatus for producing parts by selective sintering*. 1989, Google Patents.
44. Meiners, W., K. Wissenbach, and A. Gasser, *Selective laser sintering at melting temperature*. 2001, Google Patents.
45. Toyserkani, E., A. Khajepour, and S. Corbin, *Laser Cladding*. 2004, United States of America: CRC Press LLC.
46. Britannica, E., *Encyclopedia Britannica.* INC. Yayınları, C, 2000. **9**.
47. Thijs, L., et al., *A study of the microstructural evolution during selective laser melting of Ti–6Al–4V.* Acta Materialia, 2010. **58**(9): p. 3303-3312.
48. Gong, H., et al., *Analysis of defect generation in Ti–6Al–4V parts made using powder bed fusion additive manufacturing processes.* Additive Manufacturing, 2014. **1**: p. 87-98.
49. Ahsan, M.N., R. Bradley, and A.J. Pinkerton, *Microcomputed tomography analysis of intralayer porosity generation in laser direct metal deposition and its causes.* Journal of laser applications, 2011. **23**(2): p. 022009.
50. Gong, H., et al. *Defect Morphology in Ti–6Al–4V Parts Fabricated by Selective Laser Melting and Electron Beam Melting*. in *24rd Annual International Solid*

Freeform Fabrication Symposium—An Additive Manufacturing Conference, Austin, TX, Aug. 2013.
51. Prabhu, A.W., *Improving Fatigue Life of LENS Deposited Ti-6Al-4V through Microstructure and Process Control*. 2014, The Ohio State University.
52. Kleszczynski, S., et al., *Mechanical properties of Laser Beam Melting components depending on various process errors*, in *Digital Product and Process Development Systems*. 2013, Springer. p. 153-166.
53. Gong, H., *Generation and detection of defects in metallic parts fabricated by selective laser melting and electron beam melting and their effects on mechanical properties.* 2013.
54. Kruth, J.P., et al., *Consolidation phenomena in laser and powder-bed based layered manufacturing.* CIRP Annals - Manufacturing Technology, 2007. **56**(2): p. 730-759.
55. Kruth, J.-P., et al. *Part and material properties in selective laser melting of metals*. in *16th International Symposium on Electromachining*. 2010. Chicago.
56. Das, S., *Physical aspects of process control in selective laser sintering of metals.* Advanced Engineering Materials, 2003. **5**(10): p. 701-711.
57. Gu, D. and Y. Shen, *Balling phenomena in direct laser sintering of stainless steel powder: Metallurgical mechanisms and control methods.* Materials & Design, 2009. **30**(8): p. 2903-2910.
58. Islam, M., et al., *Temperature profile and imaging analysis of laser additive manufacturing of stainless steel.* Lasers in Manufacturing (Lim 2013), 2013. **41**: p. 828-835.
59. Yang, Y., et al., *Equidistant path generation for improving scanning efficiency in layered manufacturing.* Rapid Prototyping Journal, 2002. **8**(1): p. 30-37.
60. Yasa, E., et al., *Investigation on occurrence of elevated edges in selective laser melting* in *International Solid Freeform Fabrication Symposium*. 2009: Austin, TX. p. 673-85.
61. Boisselier, D. and S. Sankare, *Influence of powder characteristics in laser direct metal deposition of SS316L for metallic parts manufacturing.* Laser Assisted Net Shape Engineering 7, 2012. **39**: p. 455-463.
62. Hirvimäki, M., et al., *Evaluation of different monitoring methods of laser additive manufacturing of stainless steel.* Advanced Materials Research, 2013. **651**: p. 812-819.
63. Reinarz, B. and G. Witt, *Process Monitoring in the Laser Beam Melting Process-Reduction of Process Breakdowns and Defective Parts.* Proceedings of Materials Science & Technology, 2012. **2012**.
64. Craeghs, T., et al., *Detection of process failures in Layerwise Laser Melting with optical process monitoring.* Laser Assisted Net Shape Engineering 7 (Lane 2012), 2012. **39**: p. 753-759.
65. Bi, G., C.N. Sun, and A. Gasser, *Study on influential factors for process monitoring and control in laser aided additive manufacturing.* Journal of Materials Processing Technology, 2013. **213**(3): p. 463-468.
66. Hu, D.M. and R. Kovacevic, *Sensing, modeling and control for laser-based additive manufacturing.* International Journal of Machine Tools & Manufacture, 2003. **43**(1): p. 51-60.

67. Aggarangsi, P., J.L. Beuth, and M. Griffith. *Melt pool size and stress control for laser-based deposition near a free edge*. in *International Solid Freeform Fabrication Symposium*. 2003. Texas, Austin.
68. Kruth, J.-P. and P. Mercelis, *Procedure and apparatus for in-situ monitoring and feedback control of selective laser powder processing*. 2007, Google Patents.
69. Lott, P., et al., *Design of an optical system for the in situ process monitoring of selective laser melting (SLM).* Physics Procedia, 2011. **12**: p. 683-690.
70. Pavlov, M., M. Doubenskaia, and I. Smurov, *Pyrometric analysis of thermal processes in SLM technology.* Physics Procedia, 2010. **5**: p. 523-531.
71. Cheng, Y. and M.A. Jafari, *Vision-based online process control in manufacturing applications.* Ieee Transactions on Automation Science and Engineering, 2008. **5**(1): p. 140-153.
72. Santospirito, S.P., et al., *Defect detection in laser powder deposition components by laser thermography and laser ultrasonic inspections.* Frontiers in Ultrafast Optics: Biomedical, Scientific, and Industrial Applications Xiii, 2013. **8611**.
73. Kleszczynski, S., et al. *Improving process stability of laser beam melting systems*. in *Proceedings of the Frauenhofer Direct Digital Manufacturing Conference*. 2014.
74. Albakri, M., et al., *NON-DESTRUCTIVE EVALUATION OF ADDITIVELY MANUFACTURED PARTS VIA IMPEDANCE-BASED MONITORING.*
75. Schwerdtfeger, J., R.E. Singer, and C. Korner, *In situ flaw detection by IR-imaging during electron beam melting.* Rapid Prototyping Journal, 2012. **18**(4): p. 259-263.
76. Malamas, E.N., et al., *A survey on industrial vision systems, applications and tools.* Image and vision computing, 2003. **21**(2): p. 171-188.
77. Fang, T., et al., *On-line detection of defects in layered manufacturing.* 1998 Ieee International Conference on Robotics and Automation, Vols 1-4, 1998: p. 254-259.
78. Fang, T., et al., *On-line defect detection in Layered Manufacturing using process signature.* 1998 IEEE International Conference on Systems, Man, and Cybernetics, Vols 1-5, 1998: p. 4373-4378.
79. Cheng, Y. and M. Jafari, *Vision-based process control in layered manufacturing.* Sixth International Conference on Quality Control by Artificial Vision, 2003. **5132**: p. 303-313.
80. Fang, T., et al., *Signature analysis and defect detection in layered manufacturing of ceramic sensors and actuators.* Machine Vision and Applications, 2003. **15**(2): p. 63-75.
81. Straub, J., *Initial Work on the Characterization of Additive Manufacturing (3D Printing) Using Software Image Analysis.* Machines, 2015. **3**(2): p. 55-71.
82. Straub, J. *Characterization of 3D printing output using an optical sensing system*. in *SPIE Sensing Technology+ Applications*. 2015. International Society for Optics and Photonics.
83. Yasa, E. and J.-P. Kruth, *Application of laser re-melting on selective laser melting parts.* Advances in Production Engineering & Management Journal, 2011. **4**(4): p. 259-270.

84. zur Jacobsmuhlen, J., et al. *Robustness analysis of imaging system for inspection of laser beam melting systems*. in *Emerging Technology and Factory Automation (ETFA), 2014 IEEE*. 2014. IEEE.
85. Kleszczynski, S., et al. *Position dependency of surface roughness in parts from laser beam melting systems*. in *26th International Solid Free Form Fabrication (SFF) Symposium*. 2015.
86. Foster, B., et al. *Optical, layerwise monitoring of powder bed fusion*. in *26th International Solid Freeform Fabrication Symposium; Austin, TX*. 2015.
87. Alhwarin, F., et al. *Improving additive manufacturing by image processing and robotic milling*. in *Automation Science and Engineering (CASE), 2015 IEEE International Conference on*. 2015. IEEE.
88. Kaufmann, P., G. Medioni, and R. Nevatia, *Visual inspection using linear features.* Pattern Recognition, 1984. **17**(5): p. 485-491.
89. Bodnarova, A., M. Bennamoun, and S. Latham, *Optimal Gabor filters for textile flaw detection.* Pattern Recognition, 2002. **35**(12): p. 2973-2991.
90. Gayubo, F., et al. *On-line machine vision system for detect split defects in sheet-metal forming processes*. in *Pattern Recognition, 2006. ICPR 2006. 18th International Conference on*. 2006. IEEE.
91. Chetverikov, D. and A. Hanbury, *Finding defects in texture using regularity and local orientation.* Pattern Recognition, 2002. **35**(10): p. 2165-2180.
92. Dawson, B., *Applying automated optical inspection.* Ee-Evaluation Engineering, 2005. **44**(7): p. 62-+.
93. Wang, Y., et al., *Detection of line weld defects based on multiple thresholds and support vector machine.* NDT & E International, 2008. **41**(7): p. 517-524.
94. Conners, R.w., D.E. Kline, and P.A. Araman. *A Multiple Sensor Machine Vision System Technology for the Hardwood*. in *The Second International Symposium on Computers in Furniture and Cabinet Manufacturing*. 1995.
95. Conners, R.W., et al., *Machine vision technology for the forest products industry.* Computer, 1997. **30**(7): p. 43-48.
96. Asiegbu, G.O., A.M. Haidar, and K. Hawari. *A Review of Defect Detection on Electrical Components Using Image Processing Technology*. in *Proceedings of the Fourth International Conference on Signal and Image Processing 2012 (ICSIP 2012)*. 2013. Springer.
97. Mavi, A. and M. Kaur, *Identify Defects in Gears Using Digital Image Processing.* International Journal of Engineering Research and Development ISSN, 2012: p. 49-55.
98. GROTH, S.R. and R. ZHONGFEI, *Glass Defect Detection Techniques using Digital Image Processing–A Review*. 2011.
99. Martins, L.A., F.L. Pádua, and P.E. Almeida. *Automatic detection of surface defects on rolled steel using computer vision and artificial neural networks*. in *IECON 2010-36th Annual Conference on IEEE Industrial Electronics Society*. 2010. IEEE.
100. Ng, H.-F., *Automatic thresholding for defect detection.* Pattern recognition letters, 2006. **27**(14): p. 1644-1649.

101. Chackalackal, M.S. and J.P. Basart, *NDE X-ray image analysis using mathematical morphology*, in *Review of Progress in Quantitative Nondestructive Evaluation*. 1990, Springer. p. 721-728.
102. Saravanan, T., et al., *Segmentation of defects from radiography images by the histogram concavity threshold method.* Insight-Non-Destructive Testing and Condition Monitoring, 2007. **49**(10): p. 578-584.
103. Koch, C., et al., *A review on computer vision based defect detection and condition assessment of concrete and asphalt civil infrastructure.* Advanced Engineering Informatics, 2015. **29**(2): p. 196-210.
104. Chady, T. and M. Caryk, *Selected algorithms of background generation used for flaw detection in welded joints.* Review of Progress in Quantitative Nondestructive Evaluation, Vol 27a and 27b, 2008. **975**: p. 453-460.
105. Liao, Z. and J. Sun. *Image segmentation in weld defect detection based on modified background subtraction*. in *Image and Signal Processing (CISP), 2013 6th International Congress on*. 2013.
106. Gonzalez, R.C. and R.E. Woods, *Digital Image Processing*. 3rd ed. 2008: Addison-Wesley Longman Publishing Co., Inc. 716.
107. Ziou, D. and S. Tabbone, *Edge Detection Techniques - An Overview.* INTERNATIONAL JOURNAL OF PATTERN RECOGNITION AND IMAGE ANALYSIS, 1998. **8**(4): p. 537–559.
108. Vernon, D., *Machine Vision; Automated Visual Inspection and Robot Vision*. Pearson Education Limited. 1991.
109. Maragos, P. and R.W. Schafer, *Morphological filters--Part I: Their set-theoretic analysis and relations to linear shift-invariant filters.* Acoustics, Speech and Signal Processing, IEEE Transactions on, 1987. **35**(8): p. 1153-1169.
110. Shapiro, L.G. and G.C. Stockman, *Computer Vision*. 2001, London Prentice Hall.
111. Khurshid, K., et al. *Comparison of Niblack inspired binarization methods for ancient documents*. 2009.
112. Ostu, N., *A threshold selection method from gray-level histograms.* IEEE Transactions on Systems, Man and Cybernetics, 1979. **9**(1): p. 62-66.
113. Leedham, G., et al., *Comparison of Some Thresholding Algorithms for Text/Background Segmentation in Difficult Document Images*, in *Proceedings of the Seventh International Conference on Document Analysis and Recognition - Volume 2*. 2003, IEEE Computer Society. p. 859.
114. Beveridge, J.R., et al., *Segmenting images using localized histograms and region merging.* International Journal of Computer Vision, 1989. **2**(3): p. 311-347.
115. Vincent, L., *Morphological grayscale reconstruction in image analysis: applications and efficient algorithms.* Image Processing, IEEE Transactions on, 1993. **2**(2): p. 176-201.
116. Dougherty, E.R., R.A. Lotufo, and T.I.S.f.O.E. SPIE, *Hands-on morphological image processing*. Vol. 71. 2003: SPIE press Bellingham.
117. Chady, T., M. Caryk, and B. Piekarczyk, *Automated Defect Classification Using an Artificial Neural Network.* Review of Progress in Quantitative Nondestructive Evaluation, Vols 28a and 28b, 2009. **1096**: p. 1591-1598.

118. Nacereddine, N., et al., *Statistical Tools for Weld Defect Evaluation in Radiographic Testing*, in *Proceedings of 12th European conference on non-destructive testing – ECNDT 2006*. 2006.
119. Tsneg, Y.-H. and D.-M. Tsai, *Defect detection of uneven brightness in low-contrast images using basis image representation.* Pattern Recognition, 2010. **43**(3): p. 1129-1141.
120. Kumar, A., *Neural network based detection of local textile defects.* Pattern Recognition, 2003. **36**(7): p. 1645-1659.
121. Cho, T.-H. and R. Conners. *A neural network approach to machine vision systems for automated industrial inspection*. in *Neural Networks, 1991., IJCNN-91-Seattle International Joint Conference on*. 1991. IEEE.
122. Habib, M.T. and M. Rokonuzzaman, *A Set of Geometric Features for Neural Network-Based Textile Defect Classification.* ISRN Artificial Intelligence, 2012. **2012**: p. 16.
123. Wittels, N. and M.A. Gennert. *Optimal lighting design to maximize illumination uniformity*. in *Photonics for Industrial Applications*. 1994. International Society for Optics and Photonics.
124. Brecher, V.H., et al., *Automated defect classification system*. 1996, Google Patents.
125. Yasnoff, W.A., J.K. Mui, and J.W. Bacus, *Error measures for scene segmentation.* Pattern recognition, 1977. **9**(4): p. 217-231.
126. Tripathi, S., et al., *Image segmentation: A review.* International Journal of Computer Science and Management Research, 2012. **1**(4): p. 838-843.
127. Vernon, D., *Machine Vision: Automated Visual Inspection and Robot Vision*. 1991: Prentice Hall.
128. Zhang, Y.-J., *Advances in image and video segmentation*. 2006: IGI Global.
129. Baxes, G.A., *Digital image processing: principles and applications*. 1994: Wiley New York.
130. Sonka, M., V. Hlavac, and R. Boyle, *Image processing, analysis, and machine vision*. 2014: Cengage Learning.
131. Acharya, T. and A.K. Ray, *Image processing: principles and applications*. 2005: John Wiley & Sons.
132. Chan, R.H., C.-W. Ho, and M. Nikolova, *Salt-and-pepper noise removal by median-type noise detectors and detail-preserving regularization.* Image Processing, IEEE Transactions on, 2005. **14**(10): p. 1479-1485.
133. Bovik, A.C., *Handbook of image and video processing*. 2010: Academic press.
134. Aminzadeh, M. and T. Kurfess, *Automatic thresholding for defect detection by background histogram mode extents.* Journal of Manufacturing Systems, 2015. **37, Part 1**: p. 83-92.
135. Rosenfeld, A. and P. De La Torre, *Histogram concavity analysis as an aid in threshold selection.* Systems, Man and Cybernetics, IEEE Transactions on, 1983(2): p. 231-235.
136. Canny, J., *A computational approach to edge detection.* Pattern Analysis and Machine Intelligence, IEEE Transactions on, 1986(6): p. 679-698.
137. Kwon, S.H., *Threshold selection based on cluster analysis.* Pattern Recognition Letters, 2004. **25**(9): p. 1045-1050.

138. Sahasrabudhe, S. and K. GUPTA, *A VALLEY-SEEKING THRESHOLD SELECTION.* Computer vision and image processing, 1992. **55**.
139. Ng, H.-F., et al. *An improved method for image thresholding based on the valley-emphasis method*. in *Signal and Information Processing Association Annual Summit and Conference (APSIPA), 2013 Asia-Pacific*. 2013. IEEE.
140. Bernardo, J.M. and A.F. Smith, *Bayesian theory*. 2001, IOP Publishing.
141. Congdon, P., *Bayesian statistical modelling*. 2002, IOP Publishing.
142. Berger, J.O., *Statistical decision theory and Bayesian analysis*. 2013: Springer Science & Business Media.
143. Lee, P.M., *Bayesian statistics: an introduction*. 2012: John Wiley & Sons.
144. Gelman, A., et al., *Bayesian data analysis*. Vol. 2. 2014: Chapman & Hall/CRC Boca Raton, FL, USA.
145. West, M., *Bayesian forecasting*. 1999: Wiley Online Library.
146. Carlin, B.P. and T.A. Louis, *Bayes and empirical Bayes methods for data analysis.* Statistics and Computing, 1997. **7**(2): p. 153-154.
147. Casella, G. and R. Berger, *L.(2001). Statistical Inference.* Duxbury Press.
148. Sauvola, J. and M. Pietikäinen, *Adaptive document image binarization.* Pattern recognition, 2000. **33**(2): p. 225-236.

VITA

MASOUMEH AMINZADEH

Masoumeh Aminzadeh grew up in Rafsanjan, Kerman, Iran. She received a B.Sc. degree in Aerospace Engineering in 2007 and a M.Sc. degree in Aerospace Engineering in 2009 from Amirkabir University of Technology (Tehran Polytechnique), Tehran, Iran. She received another M.Sc. in Mechanical Engineering from Georgia Institute of Technology in 2014. Her PhD research focus was on machine vision, automated visual inspection, and in-situ quality monitoring in additive manufacturing processes and manufactured parts. Her recent research involves a combination of scientific areas such as computer vision, machine learning, signal and image processing, identification and diagnosis, statistical analyses, uncertainty analysis, and manufacturing processes. Prior to Georgia Tech, she conducted several years of research in academia and industry on design, dynamic analysis, simulation, system identification and control of mechanical systems especially robotics and motion systems. She has authored fifteen scholarly articles in prestigious journals and conferences, such as IEEE, ASME, and by SME. She has also authored several industrial technical reports. She is a member of several professional organizations such as ASME, APS, and SPIE.